A Density Functional Study of the Magnetic Interactions in Transition Metal Phthalocyanines

James Broadhurst
Department of Chemistry
Imperial College London

A thesis submitted in fulfilment of the requirements
for the degree of
Doctor of Philosophy

26th July 2025

Abstract

In recent years, molecular and low-dimensional magnetic materials have drawn considerable interest within the field of spintronics, with the opportunity to use such materials to fabricate next-generation electronics. However, to be considered for use in these devices, candidates must exhibit near room temperature magnetism. With this in consideration, the family of transition metal phthalocyanines (TMPcs) has demonstrated potential in fulfilling this objective. In particular, the alpha polymorph of cobalt (II) phthalocyanine (α-CoPc) exhibits strong antiferromagnetic ordering, with a transition temperature of approximately $100\,\mathrm{K}$. Improvement of the coupling in such systems is restricted, however, by limited understanding of both the underlying exchange mechanisms and structure-property relationships.

The work presented here aims to provide insight into these mechanisms, thereby, offering routes to the design of novel phthalocyanine systems with specific characteristics. These investigations are carried out using first-principles theoretical electronic structure methods, employing hybrid exchange density functional theory. The respective results indicate that the strong antiferromagnetic coupling in α-CoPc arises due to a dominant kinetic exchange interaction between adjacent singly occupied, d_{z^2}-derived magnetic orbitals. By mapping the dynamics of this interaction to the parameters of the Hubbard Hamiltonian, subsequent calculations indicate that, by replacing the central cobalt with its second-row counterpart, rhodium, the strength of the interaction could be significantly increased, with evaluated coupling magnitudes exceeding room temperature within α-phase crystal configurations.

This work also provides a comprehensive examination of the electronic structure and emergent magnetic properties within the class of two-dimensional polymeric TMPcs. Significant variation in the exchange coupling is observed across the first-row group of these systems. Most consequently, polymeric manganese (II) phthalocyanine is predicted to exhibit strong ferromagnetic coupling, with a calculated Curie transition temperature, $T_C \sim 130\,\mathrm{K}$. This ferromagnetism is shown to originate in the system's electronic structure.

Certification of Originality

I hereby declare that the work presented in this thesis is my own original research and has not been submitted for a degree or diploma qualification at this University or any other institute of higher learning. Material or contributions from others, where included, have been appropriately referenced within the work. This research has been carried out at Imperial College London under the supervisorial guidance of Professor Nicholas Harrison and Doctor Giuseppe Mallia.

James Broadhurst
26/07/2025

Copyright Declaration

The copyright of this thesis rests with the author. Unless otherwise indicated, its contents are licensed under a Creative Commons Attribution-Non Commercial 4.0 International Licence (CC BY-NC). Under this licence, you may copy and redistribute the material in any medium or format. You may also create and distribute modified versions of the work. This is on the condition that: you credit the author and do not use it, or any derivative works, for a commercial purpose. When reusing or sharing this work, ensure you make the licence terms clear to others by naming the licence and linking to the licence text. Where a work has been adapted, you should indicate that the work has been changed and describe those changes. Please seek permission from the copyright holder for uses of this work that are not included in this licence or permitted under UK Copyright Law.

Acknowledgements

This thesis would not be complete without acknowledging all those who have supported, guided and inspired me throughout this journey. Firstly, I would like to extend my whole-hearted gratitude to my two supervisors, Prof. Nicholas Harrison and Dr. Giuseppe Mallia. Without their mentorship and guidance, this work would not have been possible, and I am truly grateful for the countless discussions and invaluable advice they have provided along the way.

Secondly, I would like to extend my appreciation to all my colleagues whom I have had the fortune of working alongside for the past three and a half years. In particular, I would like to thank Kipras, Fei, Huanyu, Felix, Luke, Margherita, Rashid, Ayse and Xinyue. This research project would not have been the same without their friendship, and I will miss the post-lunch coffees in the office tea room. I wish all of them the best of luck with their future endeavours.

Finally, I would like offer my eternal gratitude to my family, and to my partner. To my mother and father, thank you for being endlessly supportive throughout this journey. I would not be where I am today if it were not for all your encouragement and care. To my brother, Sam, thank you for all your friendship and loyalty. I am always grateful to have such a dependable person by my side. To my partner, Ellie, thank you for all the kindness, compassion and belief you have shown me during this time. I am truly appreciative of the companionship and support that you bring into my life.

Publications

J. Broadhurst, G. Mallia and N. M. Harrison. A prediction of high temperature magnetic coupling in transition metal phthalocyanines. *J. Chem. Phys.*, 2024, 161, 114703.

J. Broadhurst, G. Mallia and N. M. Harrison. The quantum origin of magnetic coupling in molecular crystals for spintronics. *J. Chem. Phys.*, 2025, 162, 244708.

Presentations

TALKS:

Global Congress on Magnetism & Magnetic Materials, Renaissance London Heathrow Hotel, August 2023.

Condensed Matter and Quantum Materials, St Andrews University, July 2024.

Postgraduate Symposium, Imperial College London, June 2024. (Awarded "Best Presentation Award")

MSSC2024: Ab Initio Modelling in Solid-State Chemistry, Imperial College London, September 2024.

APS Global Physics Summit, California, March 2025.

POSTERS:

Postgraduate Symposium, Imperial College London, July 2023. (Awarded "Best Poster Award")

Contents

Introduction **23**

1 Contextual Framework **25**

1.1 Core Motivations 25

1.2 Spintronics 26

1.2.1 Giant Magnetoresistance 26

1.2.2 Tunnelling Magnetoresistance 28

1.2.3 Spin Field Effect Transistors 29

1.3 Molecular Nanomagnets 30

1.4 Phthalocyanines 31

1.5 Principle Challenge 40

2 Theoretical Concepts **41**

2.1 Schrödinger Equation 42

2.2 Wavefunction Methods 43

2.3 Density Functional Theory 46

2.3.1 Local Density Approximation 49

2.3.2 Generalised Gradient Approximation 50

2.3.3 Meta-Generalised Gradient Approximation 51

2.3.4 Hybrid Exchange Functionals 52

2.4 Periodicity 53

2.5 The Basis Set Approximation 54

2.5.1 Plane Waves 55

2.5.2 Pseudopotentials 56

2.5.3 Localised Basis Sets 56

2.6 Geometry Optimisation . . . 57
2.7 Properties . . . 59
2.7.1 Band Structure . . . 59
2.7.2 Mulliken Population Analysis . . . 59

3 Principles of Magnetism 61
3.1 Microscopic Foundation of Magnetism . . . 62
3.1.1 Exchange Interactions . . . 63
3.1.2 Paramagnetism . . . 65
3.1.3 Diamagnetism . . . 65
3.2 Macroscopic Ordering in Magnetic Materials . . . 65
3.2.1 Ferromagnetism . . . 66
3.2.2 Antiferromagnetism . . . 66
3.2.3 Ferrimagnetism . . . 67
3.3 Magnetic Anisotropy . . . 68
3.4 Quantum Spin Models . . . 69
3.4.1 Heisenberg Model . . . 70
3.4.2 Ising Model . . . 70
3.4.3 Hubbard Model . . . 71
3.5 Mapping Strategies for Quantum Simulations . . . 72

4 The Magnetic Coupling in CoPc and CuPc 75
4.1 Theoretical Background . . . 76
4.2 Computational Details . . . 77
4.3 Single Molecules . . . 79
4.3.1 CoPc . . . 80
4.3.2 CuPc . . . 83
4.4 Periodic Chains . . . 85
4.4.1 Unit Cell . . . 86
4.4.2 CoPc . . . 87
4.4.2.1 α-CoPc . . . 88
4.4.2.2 β-CoPc . . . 90
4.4.3 CuPc . . . 92
4.4.3.1 α-CuPc . . . 92
4.4.3.2 β-CuPc . . . 94

4.5 Conclusions 96

5 The Magnetic Coupling in RhPc **98**

5.1 Computational Details 100
5.2 Single Molecule 100
5.3 Periodic Chains 103
5.3.1 Unit Cell 104
5.3.2 α-RhPc 105
5.3.3 β-RhPc 108
5.3.4 Additional Chain Geometries 109
5.4 Conclusions 112

6 Decomposition of the Exchange Interactions **114**

6.1 Decomposition Procedure 116
6.2 Computational Details 118
6.3 Decomposition of the H_2 Molecule 118
6.3.1 Direct Exchange 119
6.3.2 Kinetic Exchange 127
6.3.3 Total Exchange 128
6.3.4 Summary 128
6.4 Single TMPc Molecules 129
6.4.1 CoPc 130
6.4.2 CuPc 131
6.4.3 RhPc 132
6.5 Decomposition of the Exchange Interactions 133
6.5.1 CoPc 134
6.5.2 CuPc 137
6.5.3 RhPc 139
6.6 Conclusions 142

7 The Magnetic Coupling in Polymeric Phthalocyanines **144**

7.1 Computational Details 145
7.2 Unit Cell 145
7.3 Electronic Structure 147
7.3.1 poly-CoPc 147

7.3.2 poly-CuPc . . . 148
7.3.3 poly-MnPc . . . 149
7.3.4 poly-FePc . . . 154
7.3.5 poly-CrPc . . . 155
7.4 Magnetic Interactions . . . 155
7.5 Conclusions . . . 163

8 Conclusions & Future Work **165**

Bibliography **169**

A Basis Sets **194**
A.1 Cobalt . . . 195
A.2 Copper . . . 197
A.3 Manganese . . . 199
A.4 Iron . . . 201
A.5 Chromium . . . 203
A.6 Rhodium . . . 205
A.7 Carbon . . . 207
A.8 Nitrogen . . . 208
A.9 Hydrogen . . . 209

B Mathematical Formalisms **210**
B.1 Two Component SCF Procedure . . . 211
B.2 Direct Inversion of the Iterative Subspace . . . 212
B.3 Local Self Consistent Field Procedure . . . 213
B.4 Pipek-Mezey Localisation Procedure . . . 214

C Supplementary Data **215**
C.1 Delocalised Magnetic State in RhPc Chains . . . 216
C.2 H_2 Basis Set Analysis . . . 219
C.3 Poly-TMPc Spin Density Isosurfaces . . . 220

List of Figures

1.1 Schematic of the GMR effect in a ferromagnetic/non-magnetic/ferromagnetic (FM-NM-FM) layered structure in the (a) high resistance state and (b) low resistance state. Red arrows represent the motion of majority (up-spin, $\uparrow$) electrons through the device, blue arrows represent the motion of minority (down-spin, $\downarrow$) electrons through the device. Black arrows indicate the direction of magnetisation of each FM layer of the device. Note that the vertical position of the electron movement through the device is arbitrary. . 27

1.2 Geometrical structure of (a) metal-free phthalocyanine (H_2Pc) and (b) metal phthalocyanine (MPc). 32

1.3 Structural depiction of the stacking angle, ϕ (top), and sliding angle, ψ (bottom). Figure reproduced from Ref. [46] with permission from the authors. 33

1.4 Visualisation of the d-derived orbitals: (a) b_{2g} (d_{xy}), (b) e_{gx} (d_{xz}), (c) a_{1g} (d_{z^2}), (d) e_{gy} (d_{yz}) and (e) b_{2g} $(d_{x^2-y^2})$. 36

4.1 Geometry of a metal phthalocyanine molecule with labelled atoms. Atom colours refer to those defined in Fig. 1.2(b). Figure reproduced from Ref. [46] with permission from the authors. 78

4.2 Spin density isosurface plot for the single molecule of (a) CoPc and (b) CuPc. An isovalue of $0.001\ |e|$ Å^{-3} is used. Yellow (blue) shading indicates regions of up-spin (down-spin) electron density. 79

4.3 Diagrammatic representation of the eigenvalues of the fronter MOs for (a) single molecule CoPc and (b) single molecule CuPc. Black plain-text labels refer to the d-derived MOs, whilst blue bold-text labels refer to the ligand derived MOs. Note that in (a) the b_{1g} MOs are energetically positioned above the unoccupied a_{1g} MO and are omitted for clarity. Fig. 4.3(a) reproduced from Ref. [184] with permission from the authors. 83

4.4 Structural depiction of the dimeric unit cell for the (a) α-phase and (b) β-phase. 87

4.5 Plots of the (a) AFM and (b) FM band structures, and (c) AFM and (d) FM spin density isosurfaces for single chain structures of α-CoPc. In (a) and (b), the magnetic a_{1g} bands are highlighted in red. In (c) and (d), an isovalue of $0.001\,|e|$ Å^{-3} is used. Yellow (blue) shading indicates regions of up-spin (down-spin) electron density. Figs. 4.5(a) and 4.5(b) reproduced from Ref. [184] with permission from the authors. 89

4.6 Plots of the (a) AFM and (b) FM band structures, and (c) AFM and (d) FM spin density isosurfaces for single chain structures of β-CoPc. In (a) and (b), the magnetic a_{1g} bands are highlighted in red. In (c) and (d), an isovalue of $0.001\,|e|$ Å^{-3} is used. Yellow (blue) shading indicates regions of up-spin (down-spin) electron density. Figs. 4.6(a) and 4.6(b) reproduced from Ref. [184] with permission from the authors. 91

4.7 Plots of the (a) AFM and (b) FM band structures, and (c) AFM and (d) FM spin density isosurfaces for single chain structures of α-CuPc. In (a) and (b), the magnetic b_{1g} bands are highlighted in red. In (c) and (d), an isovalue of $0.001\,|e|$ Å^{-3} is used. Yellow (blue) shading indicates regions of up-spin (down-spin) electron density. 93

4.8 Plots of the (a) AFM and (b) FM band structures, and (c) AFM and (d) FM spin density isosurfaces for single chain structures of β-CuPc. In (a) and (b), the magnetic b_{1g} bands are highlighted in red. In (c) and (d), an isovalue of $0.001\,|e|$ Å^{-3} is used. Yellow (blue) shading indicates regions of up-spin (down-spin) electron density. 95

5.1 Depiction of (a) eigenvalues of the frontier MOs and (b) spin density isosurface plot for the single molecule RhPc. In (a), black plain-text labels refer to d-derived MOs whilst blue bold-text labels refer to ligand derived MOs. Note that the b_{1g} MOs are energetically positioned above the ligand e_g orbitals and are omitted for clarity. In (b), an isovalue of $0.001\,|e|$ Å^{-3} is used. Yellow (blue) shading indicates regions of up-spin (down-spin) electron density. Fig. 5.1(a) reproduced from Ref. [184] with permission from the authors. 101

5.2 Structural depiction of the dimeric unit cell for the (a) α-phase and (b) β-phase. 105

5.3 Plots of the (a) AFM and (b) FM band structures, and (c) AFM and (d) FM spin density isosurfaces for single chain structures of α-RhPc. In (a) and (b), the magnetic a_{1g} bands are highlighted in red. In (c) and (d), an isovalue of $0.001\,|e|$ Å^{-3} is used. Yellow (blue) shading indicates regions of up-spin (down-spin) electron density. Figs. 5.3(a) and 5.3(b) reproduced from Ref. [184] with permission from the authors. 107

5.4 Plots of the (a) AFM and (b) FM band structures, and (c) AFM and (d) FM spin density isosurfaces for single chain structures of β-RhPc. In (a) and (b), the magnetic a_{1g} bands are highlighted in red. In (c) and (d), an isovalue of $0.001\,|e|$ Å^{-3} is used. Yellow (blue) shading indicates regions of up-spin (down-spin) electron density. 108

5.5 Magnitude of J^{BS} and J^{KE} as a function of the interplanar distance for single periodic chains of RhPc in the α-phase configuration ($\phi = 65°; \psi = 0°$) (top panel) and β-phase configuration ($\phi = 45°; \psi = 45°$) (bottom panel). 110

5.6 Magnitude of J^{BS} as a function of the stacking angle, ϕ, and sliding angle, ψ, for single periodic chains of RhPc at a fixed interplanar distance of 3.70 Å. Figure reproduced from Ref. [184] with permission from the authors. 111

6.1 Figurative depiction of the decomposition scheme. Green and red spheres represent individual SOMOs localised on adjacent metal centres, whilst core (doubly occupied) MOs are pictured beneath. J^{DE}, J^{KE}, J^{SP} and J^{Total} refer to respective coupling constants as defined in Sec. 6.1. Figure reproduced from Ref. [46] with permission from the authors. 119

6.2 Variation in J^{DE}, J^{KE}, J^{Σ} (where $J^{\Sigma} = J^{DE} + J^{KE}$) and J^{Total} as a function of bond distance in H_2. Calculations carried out using the B3LYP functional. 120
6.3 Variation in J^{DE} as a function of bond distance in H_2 for calculations carried out using the B3LYP, B3LYP-REF and B3VWN-REF approaches. . 123
6.4 Variation in J^{DE} as a function of bond distance in H_2 for calculations carried out using the B3LYP-EX approach. 126
6.5 Variation in J^{DE}, J^{KE}, J^{Σ} (where $J^{\Sigma} = J^{DE} + J^{KE}$) and J^{Total} as a function of bond distance in H_2. Calculations carried out using the B3LYP-EX approach. 127
6.6 Spin density isosurface plots for single molecule structures of (a) CoPc, (b) CuPc and (c) RhPc. An isovalue of $0.001\,|e|$ Å^{-3} is used. Yellow (blue) shading represents regions of up-spin (down-spin) electron density. 129
6.7 Dimeric molecular geometry of the (a) α-phase and (b) β-phase configurations. 133
6.8 Isosurface plots of the magnetic orbital extracted from the $\Phi_{UFC,BS}$ determinant for (a) α-CoPc and (b) β-CoPc. An isovalue of $0.003\,|e|$ Å^{-3} is used. Blue and yellow shading indicates relative phase. Figures reproduced from Ref. [46] with permission from the authors. 135
6.9 Spin density isosurface plots of the $\Phi_{UFM,HS}$ determinant for (a) α-CoPc and (c) β-CoPc and, the $\Phi_{UFM,BS}$ determinant for (b) α-CoPc and (d) β-CoPc. An isovalue of $0.0005\,|e|$ Å^{-3} is used. Yellow (blue) shading indicates regions of up-spin (down-spin) electron density. Figures reproduced from Ref. [46] with permission from the authors. 136
6.10 Isosurface plots of the magnetic orbital extracted from the $\Phi_{UFC,BS}$ determinant for (a) α-CuPc and (b) β-CuPc. An isovalue of $0.003\,|e|$ Å^{-3} is used. Blue and yellow shading indicates relative phase. Figures reproduced from Ref. [46] with permission from the authors. 138
6.11 Spin density isosurface plots of the $\Phi_{UFM,HS}$ determinant for (a) α-CuPc and (c) β-CuPc and, the $\Phi_{UFM,BS}$ determinant for (b) α-CuPc and (d) β-CuPc. An isovalue of $0.0005\,|e|$ Å^{-3} is used. Yellow (blue) shading indicates regions of up-spin (down-spin) electron density. Figures reproduced from Ref. [46] with permission from the authors. 139

6.12 Isosurface plots of the magnetic orbital extracted from the $\Phi_{UFC,BS}$ determinant for (a) α-RhPc and (b) β-RhPc. An isovalue of $0.003\,|e|$ Å^{-3} is used. Blue and yellow shading indicates relative phase. 140
6.13 Spin density isosurface plots of the $\Phi_{UFM,HS}$ determinant for (a) α-RhPc and (c) β-RhPc and, the $\Phi_{UFM,BS}$ determinant for (b) α-RhPc and (d) β-RhPc. An isovalue of $0.0005\,|e|$ Å^{-3} is used. Yellow (blue) shading indicates regions of up-spin (down-spin) electron density. 141

7.1 Structural geometry of the unit cell for the poly-TMPc systems with labelled atoms. These systems are laterally periodic and extend as a 2D surface. Note that atom colours refer to those defined in Fig. 1.2(b). 146
7.2 Band structure plots for (a) poly-CoPc and (b) poly-CuPc. E_F is set to $0\mathrm{eV}$ and denoted by a blue highlighted line. 150
7.3 Band structure plots for (a) poly-MnPc and (b) poly-FePc. E_F is set to $0\mathrm{eV}$ and denoted by a blue highlighted line. 151
7.4 Band structure plot for poly-CrPc. E_F is set to $0\,\mathrm{eV}$ and denoted by a blue highlighted line. 152
7.5 Spin density isosurface plots for the unit cell of (a) poly-CoPc, (b) poly-CuPc, (c) poly-MnPc, (d) poly-FePc and (e) poly-CrPc. An isovalue of $0.001\,|e|$ Å^{-3} is used. Yellow (blue) shading indicates regions of up-spin (down-spin) electron density. 153
7.6 Graphical depiction of (a) the ferromagnetic (FM) phase, (b) the collinear antiferromagnetic (CAF) phase and (c) the Néel antiferromagnetic (NAF) phase. Arrows indicate the direction of the total magnetic moment at each metal centre. 156
7.7 Graphical depiction of the two unique coupling interactions in the (2×2) unit cell of a poly-TMPc system. Here J_1 denotes the interaction between nearest neighbour pairs, whilst J_2 captures the interaction between next-nearest neighbour pairs. 157
7.8 Graphical plots of the transcendental average magnetisation equation. $f(m)$ refers to the right hand side of Eq. 7.12. 162

C.1 Spin density isosurface plots for the (a) FM and (b) AFM configurations of Chain B. An isovalue of $0.001\,|e|$ Å^{-3} is used. 217

C.2 Variation in J^{DE} as a function of bond distance in H_2 for calculations carried out using the B3LYP approach alongside the DZVP (see Appendix A.9), def2-SVP [245] and def2-TZVP [245] basis sets. 219
C.3 Spin density isosurface plots for poly-CoPc in (a) the FM phase, (b) the CAF phase and (c) the NAF phase. An isovalue of $0.001\,|e|$ Å^{-3} is used. Yellow (blue) shading indicates regions of up-spin (down-spin) electron density. . . 221
C.4 Spin density isosurface plots for poly-CuPc in (a) the FM phase, (b) the CAF phase and (c) the NAF phase. An isovalue of $0.001\,|e|$ Å^{-3} is used. Yellow (blue) shading indicates regions of up-spin (down-spin) electron density. . . 222
C.5 Spin density isosurface plots for poly-MnPc in (a) the FM phase, (b) the CAF phase and (c) the NAF phase. An isovalue of $0.001\,|e|$ Å^{-3} is used. Yellow (blue) shading indicates regions of up-spin (down-spin) electron density. 223
C.6 Spin density isosurface plots for poly-FePc in (a) the FM phase, (b) the CAF phase and (c) the NAF phase. An isovalue of $0.001\,|e|$ Å^{-3} is used. Yellow (blue) shading indicates regions of up-spin (down-spin) electron density. . . 224
C.7 Spin density isosurface plots for poly-CrPc in (a) the FM phase, (b) the CAF phase and (c) the NAF phase. An isovalue of $0.001\,|e|$ Å^{-3} is used. Yellow (blue) shading indicates regions of up-spin (down-spin) electron density. . . 225

List of Tables

1.1 Moments and ground state configurations for the set of air-stable, divalent, magnetic first-row transition metal phthalocyanines, with respective references. 37

4.1 Optimised bond lengths and angles (Calc.) for single molecule CoPc, with respective experimental (Exp.) bond lengths and angles obtained from Ref. [209]. Labels refer to those defined in Fig. 4.1. 80

4.2 Mulliken population analysis for the charge and spin density in single molecule CoPc. Labels refer to those defined in Fig. 4.1. 81

4.3 Mulliken population analysis of the spin and charge density for the d AOs in single molecule CoPc. 81

4.4 Energies of the three electronic configurations in CoPc relative to the ground $^2A_{1g}$ state. 82

4.5 Optimised bond lengths and angles (Calc.) for single molecule CuPc, with respective experimental (Exp.) bond lengths and angles obtained from Ref. [208]. Labels refer to those defined in Fig. 4.1. 84

4.6 Mulliken population analysis for the charge and spin density in single molecule CuPc. Labels refer to those defined in Fig. 4.1. 85

4.7 Mulliken population analysis of the spin and charge density for the d AOs in single molecule CuPc. 85

4.8 Lattice parameters for the periodic single chain models of the two polymorphic phases of both CoPc and CuPc. 86

4.9 Full set of exchange energy data for the two polymorphic phases of CoPc and CuPc. J^{BS} refers to the coupling energies obtained using Eq. 4.4; J^{KE} refers to the coupling energies obtained using the values of t and U employed in Eq. 4.2; J^{Exp} refers to respective experimental data for each system. 88

5.1 Optimised bond lengths and angles for single molecule RhPc, with respective optimised CoPc bond lengths and angles for comparison. Labels refer to those defined in Fig. 4.1. 102
5.2 Mulliken population analysis for the charge and spin density in single molecule RhPc. Labels refer to those defined in Fig. 4.1. 103
5.3 Mulliken population analysis of the spin and charge density for the d AOs in single molecule RhPc. 103
5.4 Lattice parameters for the periodic single chain models of the two polymorphic phases of RhPc. 104
5.5 Exchange energy data for the two polymorphic phases of CoPc and RhPc. J^{BS} refers to the coupling energies obtained using Eq. 4.4; J^{KE} refers to the coupling energies obtained using the values of t and U employed in Eq. 4.2; J^{Exp} refers to respective experimental data for the CoPc systems. . 106

6.1 Exchange ($E_x[\rho]$), correlation ($E_c[\rho]$) and total exchange-correlation ($E_{xc}[\rho]$) energy for the RO,HS and RO,BS determinants ($\Phi_{RO,HS}$ and $\Phi_{RO,BS}$, respectively) as a function of interatomic distance in H_2. Calculations carried out using B3LYP. * indicates the optimised $\mathrm{H-H}$ bonding distance for the singlet ground state. 121
6.2 Exchange ($E_x[\rho]$), correlation ($E_c[\rho]$) and total exchange-correlation ($E_{xc}[\rho]$) energy for the RO,HS and RO,BS determinants ($\Phi_{RO,HS}$ and $\Phi_{RO,BS}$, respectively) as a function of interatomic distance in H_2. Calculations carried out using the B3LYP-REF method. * indicates H_2 singlet ground state bonding distance optimised using the B3LYP approach. 123
6.3 Exchange ($E_x[\rho]$), correlation ($E_c[\rho]$) and total exchange-correlation ($E_{xc}[\rho]$) energy for the RO,HS and RO,BS determinants ($\Phi_{RO,HS}$ and $\Phi_{RO,BS}$, respectively) as a function of interatomic distance in H_2. Calculations carried out using the B3VWN-REF method. * indicates H_2 singlet ground state bonding distance optimised using the B3LYP approach. 124

6.4 Optimised bond lengths and angles for single molecule CoPc, CuPc and RhPc. Labels refer to those defined in Fig. 4.1. Note that experimental bond distances and angles for CoPc and CuPc have been omitted for clarity. These respective values may be found in Tables 4.1 and 4.5. 130
6.5 Mulliken population analysis of the charge and spin density for the single molecule structures of CoPc, CuPc and RhPc. Labels refer to those defined in Fig. 4.1. 131
6.6 Mulliken population analysis of the charge and spin density for d AOs of the single molecule structures of CoPc, CuPc and RhPc. 132
6.7 Decomposition data for the α and β-phase polymorphs of CoPc, CuPc and RhPc. All values are given in units of temperature (K). 134

7.1 Lattice dimensions for the unit cell of each poly-TMPc. 147
7.2 Structural data for both bond lengths and angles for all poly-TMPc systems studied. Labels refer to those of Fig. 7.1. 148
7.3 Total magnetic moment and spin density localised to each metal, and electronic ground state configuration for each poly-TMPc. 149
7.4 Magnetic data for each studied poly-TMPc system. ΔE^{CAF} (ΔE^{NAF}) is the energy difference per unit cell for the CAF (NAF) phase with respect to the FM phase. Note that a positive (negative) value indicates that the FM phase is lower (higher) in energy than the respective CAF or NAF phase. J_1 and J_2 are the respective nearest neighbour and next-nearest neighbour coupling constants. A positive sign indicates FM coupling, a negative sign indicates AFM coupling. 158

C.1 Structural parameters defining two RhPc periodic chains. Here, $\mathrm{M}-\mathrm{M}$ is the metal-metal distance between adjacent molecules, ϕ is the stacking angle and ψ is the sliding angle. Please refer to Fig. 1.3 for the definition of these two latter parameters. 216
C.2 Mulliken population analysis of the charge density localised in the d AOs for the FM (HS) and AFM (BS) states of Chain A and Chain B. 217

List of Abbreviations

2c-SCF - Two-Component Self-Consistent Field
AFM - Antiferromagnetic
AO - Atomic Orbital
BF - Bloch Function
BO - Born-Oppenheimer
BS - Broken Symmetry
CAF - Collinear Antiferromagnetic
CC - Coupled Cluster
CI - Configuration Interaction
CO - Crystalline Orbital
DE - Direct Exchange
DFT - Density Functional Theory
DIIS - Direct Inversion of the Iterative Subspace
DSSC - Dye Sensitised Solar Cell
FBZ - First Brillouin Zone
FM - Ferromagnetic
FO - Frozen Orbital
GGA - Generalised Gradient Approximation
GMR - Giant Magnetoresistance
GTO - Gaussian Type Orbital
HDD - Hard Disk Drive
HEG - Homogeneous Electron Gas
HF - Hartree-Fock
HOMO - Highest Occupied Molecular Orbital
HS - High Spin

IC - Integrated Circuit
KE - Kinetic Exchange
KS - Kohn-Sham
LCAO - Linear Combination of Atomic Orbitals
LDA - Local Density Approximation
LS - Low Spin
LSCF - Local Self-Consistent Field
LSDA - Local Spin Density Approximation
LUMO - Lowest Unoccupied Molecular Orbital
MAE - Magnetic Anisotropy Energy
MC - Monte Carlo
MCA - Magnetocrystalline Anisotropy
MF - Mean Field
ML - Machine Learning
MO - Molecular Orbital
MOSFET - Metal Oxide Semiconductor Field Effect Transistor
MP - Møller-Plesset
MPA - Mulliken Population Analysis
MPc - Metal Phthalocyanine
MR - Magnetoresistance
MRAM - Magnetoresistive Random Access Memory
MTJ - Magneto Tunnelling Junction
mGGA - Meta Generalised Gradient Approximation
NAF - Néel Antiferromagnetic
NM - Non-Magnetic
NR - Newton-Raphson
OFO - Orthogonalised Frozen Orbital
oFET - Organic Field Effect Transistor
PDOS - Projected Density of States
PES - Potential Energy Surface
PP - Pseudopotential
PW - Plane-Wave
QIP - Quantum Information Processing
QMC - Quantum Monte Carlo

QM/MM - Quantum Mechanics/Molecular Mechanics
QN - Quasi Newton
RKKY - Ruderman-Kittel-Kasuya-Yosida
RT - Room Temperature
SCF - Self-Consistent Field
SCM - Single Chain Magnet
SDFT - Spin Density Functional Theory
SIE - Self Interaction Error
SMM - Single Molecule Magnet
SOMO - Singly Occupied Molecular Orbital
SOC - Spin-Orbit Coupling
SP - Spin Polarisation
SPE - Single Point Energy
SQUID - Superconducting Quantum Interference Device
STO - Slater Type Orbital
TMR - Tunnelling Magnetoresistance
TM - Transition Metal
TMPc - Transition Metal Phthalocyanine
VO - Variational Orbital
XAS - X-Ray Absorption Spectroscopy

Introduction

Magnetic materials permeate through numerous facets of modern society, with broad technological and industrial uses. Since their earliest acknowledgment in the 6th Century BC, there has been continual development of such materials and their associated practical applications. These include utilisation within power generation, medical imaging, smartphone devices, digital memory storage and acoustic engineering. Much emphasis has also been placed upon their critical role in the transition to a more environmentally sustainable economy. In particular, their magneto-mechanical properties render them indispensable in renewable energy generators and electric vehicle (EV) motors [1].

In addition to these applications, magnetic materials have also been the source of much interest within research and academic fields. One such area that has seen significant growth in the last few decades is that of molecular magnetism. The design and implementation of low dimensional magnetic materials into next-generation electronic devices has been presented as an intriguing and potentially transformative opportunity. Not only do such systems have the capability of revolutionising computational hardware, but may also offer sustainable alternatives to the energy intensive fabrication processes currently required in the production of modern silicon-based chips. In this thesis, one such promising candidate - the metal phthalocyanine - has been studied extensively within the context of its emergent magnetic properties. The aim of this investigation is to further elucidate the underlying mechanisms through which the coupling interactions of the materials emerge and, in doing so, provide comprehensive structure-property relationships that may aid in the design and synthesis of novel phthalocyanine species with desirable characteristics. This investigation is carried out theoretically, using first-principles electronic structure methods, and the results are communicated within this report. These results are intended to compliment material synthesis and aid in the characterisation and design of novel molecular electronic devices.

The remainder of this thesis is organised into eight chapters. In Chapter 1, background

information pertaining to spintronics, molecular nanomagnets and phthalocyanines is provided. In addition, the core motivations and challenges underpinning the work presented in this report are articulated. Chapter 2 provides a comprehensive description of the theory related to the electronic structure methods used in the subsequent studies. A brief overview of magnetism, including its microscopic quantum origin as well as the emergent cooperative macroscopic behaviour, is outlined in Chapter 3. In Chapter 4, the results from an examination of the magnetism within cobalt (II) phthalocyanine and copper (II) phthalocyanine are presented. The study provides a broad analysis of the coupling interactions in the two materials, offering explanatory insight into the underlying exchange mechanisms and structure-property relationships. The conclusions of this study facilitate the prediction of a novel phthalocyanine system - rhodium (II) phthalocyanine - that is predicted to exhibit room temperature magnetic coupling. The investigation and related results of the study into this material is detailed in Chapter 5. In Chapter 6, the coupling mechanisms of the three previously studied materials is further examined. Quantitative values of each individual component of the magnetic interaction are extracted, enabling an intricate understanding of the nature of the respective material's ordering. In Chapter 7, the analysis of magnetic properties is extended to the class of polymeric transition metal phthalocyanines. The aim of this final study is to provide the reader with a comprehensive and complete understanding of the emergent ordering within the family of metal phthalocyanine systems. Finally, holistic conclusions of the thesis are drawn in Chapter 8 and potential avenues for future investigations are outlined.

1

Contextual Framework

In this chapter, an overview of the background and context underpinning the research of this thesis is provided. The aim is to give the reader a foundation to understand the primary justifications behind the studies carried out here. The chapter is divided as follows: in Sec. 1.1, the core motivations of the project are outlined; in Sec. 1.2, a description of the field of spintronics is provided; an overview of molecular nanomagnetic materials is presented in Sec. 1.3; information related to phthalocyanines - the principle class of materials studied in this report - is provided in Sec. 1.4; finally, the primary challenges that the studies reported here have attempted to address, are articulated in Sec. 1.5.

1.1 Core Motivations

Moore's law - the general observation that the number of transistors that could be placed onto an integrated circuit (IC) chip doubles each year - has, for almost 60 years, underpinned the consistent progression in computational capabilities and facilitated accessibility to powerful yet economically viable personal computers (PCs). However, as this lithographically-enabled shrinking of transistor size approaches single nm length scales, the requirements to yield further decreases have become ever-more complex. Today, the most sophisti-

cated semiconductor manufacturing processes, including the most advanced $3\,\mathrm{nm}$ process node [2], are only sustained through a complex web of supply chains with the fabrication technologies and manufacturing capabilities resting with a handful of companies, imposing significant risks on the supply of IC chips to the global economy [3]. Additionally, at these process node length scales, quantum tunnelling effects begin to significantly impact the reliability and accuracy of charge conductance across the transistor channel. Furthermore, as the number of IC chip transistors increases, a reductive scaling in the threshold voltage, V_T, (the voltage at which a transistor switches from an OFF state to an ON state) is necessitated in order to maintain a similar power consumption. However, with an ideal sub-threshold swing limit of $60\,\mathrm{mV/dec}$[1] for metal oxide semiconductor field effect transistors (MOSFETs), reductions in V_T result in increases in static power dissipation [4]. Thus, it may be reasoned that an alternative approach to carrying out computational logic tasks is required. This approach should be scalable, address the aforementioned issues with conductance accuracy at low length scales and operate within a low power consumption environment. Furthermore, certain material characteristics such as sustainable fabrication and flexibility in design would also be desirable. Thus, the core motivation underpinning the research presented in this report is related to the design, and characterisation of candidate materials that have the potential to address these requirements. In particular, molecular nanomagnetic systems that may be implemented within *spintronic* applications are, here, the primary focus of study.

1.2 Spintronics

In the field of spin electronics or spintronics, both the charge *and* spin degrees of freedom of an electron are manipulated. The inception of the field occurred with the discovery of the giant magnetoresistance (GMR) effect [5, 6], and in subsequent years has developed into a broad field encompassing many different technologies.

1.2.1 Giant Magnetoresistance

In 1988, the groups of Albert Fert and Peter Grünberg independently discovered the GMR effect [5, 6] (for which they jointly won the Nobel Prize in Physics in 2007 [7]). In the

[1]The sub-threshold swing defines the efficiency of a transistor at switching from an OFF state to an ON state as a voltage is applied across the gate. In MOSFETs, the $60\,\mathrm{mV/dec}$ swing indicates that for each increase of $60\,\mathrm{mV}$ in gate voltage, the current across the device increases by a factor of 10.

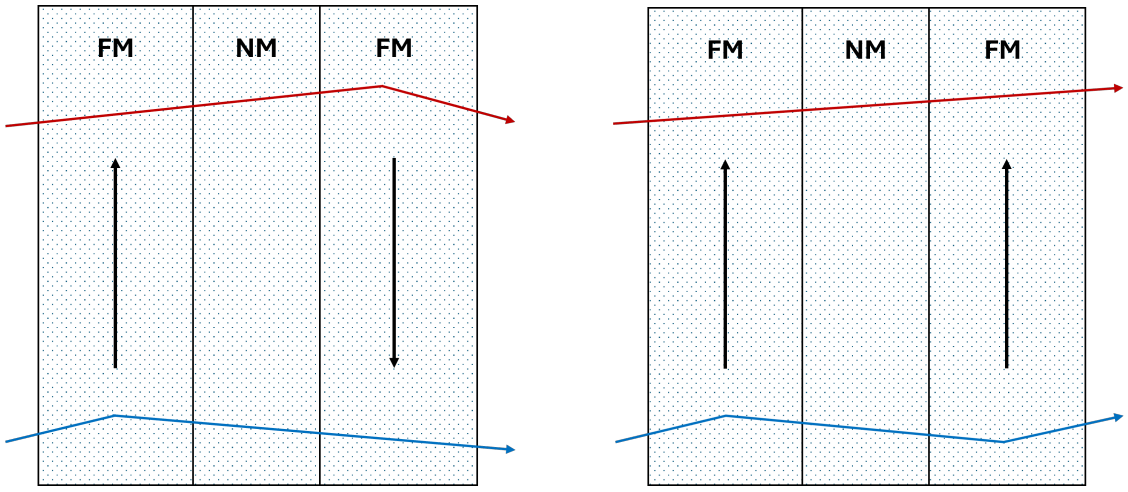

(a) (b)

Figure 1.1: Schematic of the GMR effect in a ferromagnetic/non-magnetic/ferromagnetic (FM-NM-FM) layered structure in the (a) high resistance state and (b) low resistance state. Red arrows represent the motion of majority (up-spin, $\uparrow$) electrons through the device, blue arrows represent the motion of minority (down-spin, $\downarrow$) electrons through the device. Black arrows indicate the direction of magnetisation of each FM layer of the device. Note that the vertical position of the electron movement through the device is arbitrary.

GMR effect, a variable resistance may be augmented by aligning the magnetisation of ferromagnetic (FM) conducting layers either parallel (low resistance) or antiparallel (high resistance) to one another. Free moving electrons whose spins are aligned parallel with the magnetisation of the FM material experience a lower resistance than those whose spins are aligned antiparallel. The origin of this phenomena may be understood through the "two current" model developed by Nevill Mott in 1936 [8]. According to the model, the principal origin of electron scattering (resistance) in transition metal (TM) conductors arises due to $s \rightarrow d$ transitions. Within the d-band of an FM TM material, there are fewer empty orbitals (here referred to as "holes") that may accommodate scattered s-band electrons with spins parallel (majority spin) to the material magnetisation than respective electrons that are oppositely spin polarised (minority spin). Therefore, in the absence of spin-flip scattering events, the mean free path of the majority spin electrons is greater than that of the minority spin electrons [9] and, consequently, there is a resistive difference between oppositely spin polarised currents. This phenomena underpinned the GMR effect induced by both Fert and Grünberg in iron-chromium-iron (Fe/Cr/Fe) superlattices [5, 6]. Within these structures, the magnetisation of the Fe layers were aligned antiparallel to one another and the current

was passed through the plane of the material. With the central Cr layer thickness fabricated to be less than the mean free path of the conduction electrons, transmission between the Fe layers was ballistic [10]. Within this antiparallel configuration of the Fe layers, both majority and minority spin electrons experience a resistance due to scattering. However, when an external magnetic field was applied so as to align the magnetisation of the Fe layers in parallel, a significant reduction in the conductive resistance was observed. The magnetoresistance (MR), denoted by $\Delta R/R$, is given by,

$$\frac{\Delta R}{R} = \frac{R_P - R_{AP}}{R_{AP}} \tag{1.1}$$

where R_P and R_{AP} are the resistances in the parallel and antiparallel configurations, respectively.

The downsizing of the ferromagnetic/non-magnetic/ferromagnetic (FM-NM-FM) layers resulted in a significant reduction in the size of the magnetic field required to magnetise the layers into a parallel configuration. As a result, the GMR effect was implemented within spin-valve systems that formed the basis of the "read" functionality in the read-write heads of magnetic disk-drives. These spin-valves consist of an NM spacer enclosed between two FM conducting layers. The magnetisation of one of the FM layers is "pinned" whilst the other is free to respond to an external magnetic field. As the field modifies the magnetisation of the free layer from an antiparallel state to a parallel state (with respect to the pinned layer) the electrical resistance through the valve decreases. The implementation of this in the read-write heads of disk drives facilitated a significant contraction in the size of each domain on the magnetic disk, resulting in an increased areal density [10]. However, most modern hard disk drives (HDD) use an alternative spin-valve system known as a magnetic tunnel junction (MTJ) which makes use of a variant of the GMR effect known as tunnelling magnetoresistance (TMR).

1.2.2 Tunnelling Magnetoresistance

In an MTJ, transport of the spin-polarised current from one FM layer to the other occurs via *quantum tunnelling* of the electrons rather than electrical conductance. As a result, the NM spacer is formulated from an insulating material. As in the GMR effect, the relative alignment of the magnetisation of the FM layers induces either a high or low resistive state, known as the TMR effect. The specific insulating layer plays an important role in the strength of the MR effect, with MTJs made using an Al_2O_3 NM spacer exhibiting an MR of 18% at room temperature (RT) [11], whilst an MR of 57% at RT was found in a system

made with a MgO NM spacer [12]. The advantages of the MTJ systems over those relying upon the traditional GMR effect is twofold. Firstly, the MR arising from the TMR effect is often much greater than that arising from the GMR effect and secondly, the MTJs are often easier to fabricate owing to the insulating nature of the NM spacer [13]. As a result, MTJs have replaced the traditional spin-valves in many applications including the read-write heads of HDDs. From the theoretical first-principles calculations of Butler *et al*. (2001) and Mathon & Umerski (2001), the mechanism underpinning the TMR effect has been detailed [14, 15]. A coupling at the interfacial region between the propagating Bloch bands of the FM conductor and the exponentially decaying electronic levels in the insulating layer occurs [14], with the strength of the coupling being dictated by the respective symmetries of the two states. A particular Bloch band in the majority spin channel was shown to most effectively couple with the evanescent states in the insulating layer, and, thus, was optimal at tunnelling through the barrier [14]. In the parallel configuration of the two FM layers, this majority spin channel is identical, therefore inducing a low electrical resistance, whilst in the antiparallel configuration, the majority spin channel of one FM layer corresponded with the minority spin channel of the other and, therefore, a high resistive state is present. The greater sensitivity of the TMR effect has led to ever more powerful disk drive memory devices as well facilitating the development of non-volatile random access memory devices, commonly referred to as MRAM [16].

1.2.3 Spin Field Effect Transistors

Additional spintronic-based advancements have also been made within other technological areas. One of the most rigorously explored of these areas is computational transistors. The spin-field effect transistor (spin-FET), originally conceived by Datta & Das (1990) [17], is seen as a possible replacement for conventional MOSFETs. In the spin-FET, two FM conductors act as a source and drain for the device, with a semiconducting material interposed between them. The source injects a spin-polarised current into the semiconducting channel, whilst the drain acts a spin filter, with conductance across the system occurring when the spins of the exiting current align with its magnetisation. Due to the structural inversion asymmetry of the channel, spin-orbit coupling (SOC) interactions arising from the Rashba effect[2] induce spin precessions in the polarised current. A gate voltage applied

[2]In materials exhibiting a structural asymmetry, such as that of an interface or surface, the crystal field is not symmetric in all directions. This produces an electric field which couples with the electron momentum generating an effective magnetic field that removes the degeneracy between the spin-up and spin-down

on the surface of the channel modulates the strength of the Rashba field and, therefore, the degree of precession [18]. Thus, action of the gate allows for the switching between ON and OFF states [19]. There are a number of advantages that spin-FET devices posses including lower power consumption, reduced static power leakage and intrinsic non-volatility [20,21]. Although a commercially available spin-FET device has yet to be realised, there has been much progress within the field [22–24].

1.3 Molecular Nanomagnets

Until the late twentieth century, magnetic materials were derived solely from metallic or ionic-based lattice structures. In 1991, Tamura *et al*. reported long range FM ordering at $0.6\,\mathrm{K}$ in a β-phase crystal of *para*-nitronyl nitroxide [25] - the first instance[3] in which a purely organic molecular-based material had exhibited long-range magnetism [27]. In the subsequent years, the fields of organic, molecular and nano-magnetism have advanced considerably and now encompass a broad spectrum of different materials. One of the key benefits to the use of such materials is that their synthesis requires a substantially less energy intensive and environmental harmful fabrication process, relative to the more demanding methods required for metallurgical assembly. Additionally, the elemental components of such devices are often Earth abundant and more financially accessible. Within the class of nanomagnetism, the families of single molecule magnets (SMMs) and single chain magnets (SCMs) have accrued substantial interest within a wide range of different fields.

SMMs were first characterised with the discovery of magnetic bistability and strong anisotropy in a manganese-based molecular cluster - $[\mathrm{Mn_{12}O_{12}(CH_3COO)_{16}(H_2O)_4}]$ (commonly simplified to $\mathrm{Mn_{12}}$) - arising *only* from the intramolecular interactions of the paramagnetic ions [28]. Additional SMM systems have been subsequently developed including those similar to $\mathrm{Mn_{12}}$ [29,30] as well as more complex lanthanide-based "sandwich" structures [31, 32]. These materials do not exhibit phase transitions and exist only within a single magnetic domain. They exhibit strong magnetic anisotropy energies, which, alongside the large moment of the molecule and bistable ground state, generates the observed slow magnetic dynamics. The systems represent a "bottom-up" approach to magnetic material design [33] and have potential applications in high density magnetic memory [34],

electrons due to spin-orbit coupling interactions. This is known as the Rashba effect.

[3] It is important to note that there were previous reports of molecular based magnetic materials, derived from a combination of transition metals and organic components, including the room temperature, ferrimagnetic material $[\mathrm{V(TCNE)_2}]$ [26].

molecular spintronics [35] and quantum information processing (QIP) [36].

If SMMs are zero dimensional (0D) molecular magnets, SCMs are the one dimensional (1D) equivalent. These materials are characterised by strong *intrachain* and very weak or negligible *interchain* interactions. The field has principally been focused upon systems exhibiting FM or ferrimagnetic (see Sec. 3.2.3) interactions, with their related relaxation dynamics being described by Glauber dynamics [37]. Within this theory, the magnetic relaxation of the SCMs is dependent upon the surpassing of an energy barrier arising from the exchange interactions between one spin moment and its nearest neighbours within the chain. Thus, the strategy for fabricating SCMs with slow relaxation times is to maximise the strength of this exchange coupling between adjacent spin centres, whilst minimising the interchain interactions so as to prevent the system transitioning into a three dimensional (3D) magnetically ordered system. In 2001, the first example of an SCM exhibiting slow Glauber dynamics was reported: the ferrimagnetic CoPhMe[4] system, with remanent magnetisation measured below $4\,\mathrm{K}$ [38, 39]. Following this discovery, the first homogenous FM SCM was reported - the cobalt-based species $[\mathrm{Co}(2,2'-\mathrm{bithiazoline})(\mathrm{N_3})_2]_\mathrm{n}$ - exhibiting an intrachain coupling strength of $J/k_B = 14.4\,\mathrm{K}$[5] [40]. In subsequent years, a number of different SCMs have been successfully synthesised including heteronuclear systems [41,42] and species comprising of rare earth elements [43, 44]. Another important class of SCMs, relevant to the work presented in this report, is the family of metal phthalocyanines. In the following section, an overview of this group is provided.

1.4 Phthalocyanines

Phthalocyanines are a class of materials, with chemical formula $(\mathrm{C_{32}H_{18}N_8})$ that belong to the family of porphyrin-type systems. The molecule is constructed from four isoindole units connected together by "bridging" nitrogen atoms, forming a planar aromatic D_{2h} structure (see Fig. 1.2(a)) with 18 π-electrons. Following the loss of the two central hydrogens to

[4] $\mathrm{CoPhOMe}$ is a shorthand notation used by the original authors. The full complex is given by $[\mathrm{Co(hfac)_2[NIT(C_6H_4}p\text{-}\mathrm{OMe})]$ where hfac is hexafluoroacetylacetonate and $\mathrm{NIT(C_6H_4}p\text{-}\mathrm{OMe})$ is a 4'-methoxy-phenyl-4,4,5,5-tetramethylimidazoline-1-oxyl-3-oxide radical.

[5] Here, J is the standard notation for the coupling strength between two local spin operators. A value of $J > 0$ is indicative of ferromagnetic coupling, whilst a value of $J < 0$ denotes antiferromagnetic coupling. The parameter is derived from the Heisenberg Dirac van Vleck (HDvV) Hamiltonian. The inclusion of the Boltzmann term, k_B, indicates that the constant is in units of temperature (K). For further information the reader is directed to Sec. 3.4.1.

form the conjugate base Pc^{2-}, the central cavity may accommodate a metal ion to form a metal phthalocyanine (MPc) with D_{4h} symmetry (see Fig. 1.2(b)). Over seventy different ions have been placed within this cavity, resulting in an extensive set of phthalocyanine systems exhibiting a diverse array of properties [45]. This section provides an overview of the most important information related to the structural and electronic characteristics of phthalocyanine systems, including details related to the magnetic properties of MPcs, which is directly relevant to the respective research that is detailed in this work.

Although the first metal-free phthalocyanine was made in 1907 by Braun and Tcherniac [47], and the first metal phthalocyanine (copper (II) phthalocyanine (CuPc)) in 1927 by De Diesbach and von der Weid [48], neither were characterised in the scientific literature. The first accepted characterisation of phthalocyanines was of iron (II) phthalocyanine (FePc), by chemists at Scottish Dyes Ltd., with later confirmational clarification by Linstead in 1934 [49]. The system was patented in 1928 [50]. Phthalocyanines crystallise into a number of different polymorphs, with the most common being the stable β-phase and the meta-stable α-phase, although other forms have been observed experimentally including an η-phase in CuPc [51] and the x-phase in lithium phthalocyanine (LiPc) [52]. The β-phase is mostly observed in bulk crystal structures of the respective phthalocyanine, while the α-phase emerges in thin films. A transition between the two phases is achieved through an annealing process at approximately $300\,^{\circ}\mathrm{C}$ [53]. These phases are characterised by

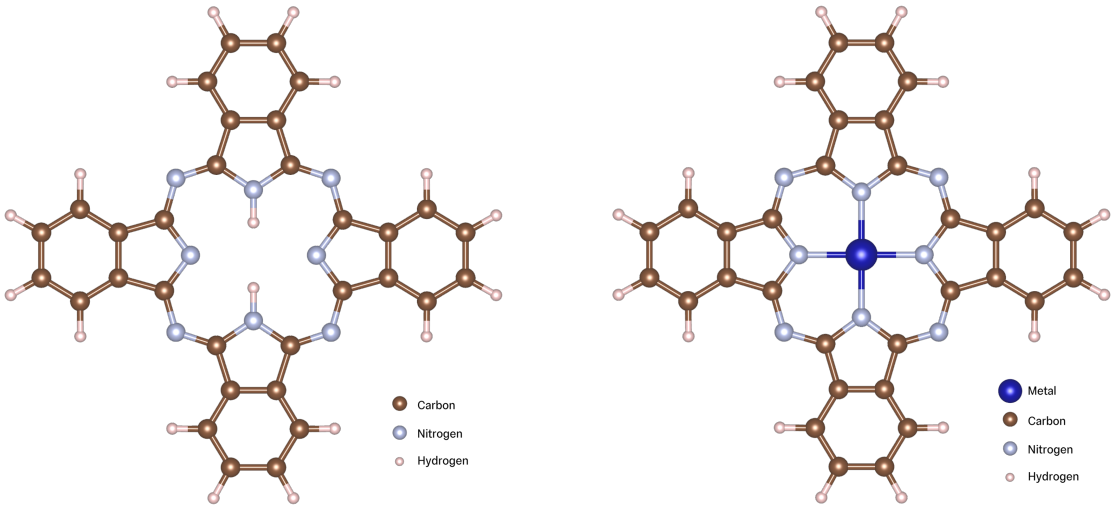

(a) (b)

Figure 1.2: Geometrical structure of (a) metal-free phthalocyanine (H_2Pc) and (b) metal phthalocyanine (MPc).

the specific structural orientation of the respective molecules which arise from their self-assembly into stacked chains held together by π-π dispersion interactions. The specific geometry of the phase may be characterised either by reference to its respective crystal lattice parameters or, more intuitively, through the use of two structural variables: the stacking angle, ϕ, and the sliding angle, ψ. ϕ quantifies the angle between the metal-metal stacking axis and the molecular plane, whilst ψ determines the orientation of the chain stacking with respect to the molecular axes (see Fig. 1.3). An additional parameter, the interplanar distance, measures the intrachain spacing normal to the plane of two adjacent molecules. In the bulk, individual chains of phthalocyanine molecules most commonly adopt a herringbone arrangement [54]. However, brickstone packing motifs have also been reported for CuPc [55], and in thin film templated configurations the chains stack next to one another along the same lattice direction [53].

With regards to the optoelectronic structure of phthalocyanines, the most prominent feature in its energy spectrum is the characteristic Q-band, which resides at approximately $650\,\mathrm{nm}$ $(1.9\,\mathrm{eV})$ [56]. In metallated phthalocyanines, this feature is a single band, whilst in metal-free phthalocyanines, owing to the lower D_{2h} symmetry, the band is split. UV-Vis

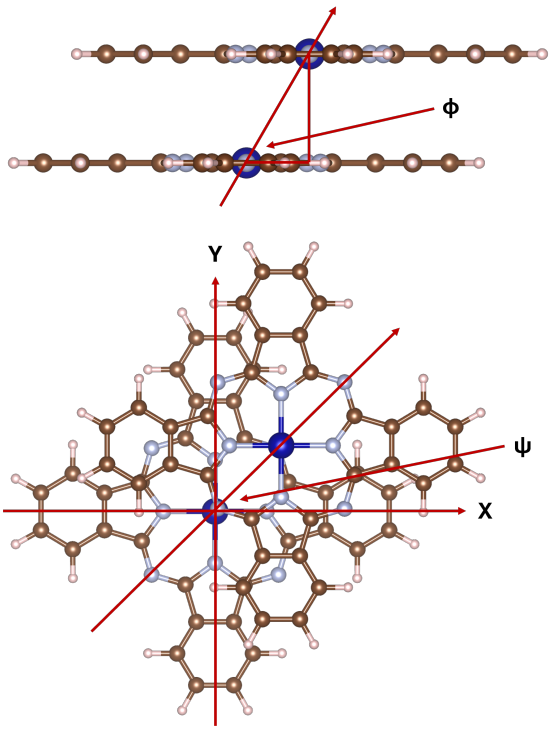

Figure 1.3: Structural depiction of the stacking angle, ϕ (top), and sliding angle, ψ (bottom). Figure reproduced from Ref. [46] with permission from the authors.

spectroscopic measurements of phthalocyanine thin film complexes indicated that this Q-band arises due to an $n \rightarrow \pi^*$ [6], valence to conduction band electronic transition [57]. Both of these bands are ligand-derived and, as such, there is a distinct lack of variance observed in the band gap between different phthalocyanine systems where the only modification has been the central metal. Given this $\sim 2\,\mathrm{eV}$ band gap, phthalocyanines are also classified as medium band gap semiconductors and, as such, have found applications within spintronic FET technologies (see below).

An important facet of phthalocyanine chemistry relates to the functionalisation of the peripheral positions of the ring. In particular, substitution of the outer hydrogen atoms with a different functional group can induce both electronic and steric effects on the system. One of the of the most common functionalisations is that of halogenation, and, in particular, the addition of fluorine atoms to the peripheral of the ring. One extensively studied example is the fully substituted copper hexadecaphthalocyanine (F_{16}CuPc) which is an air-stable *n*-type semiconductor. A combined theoretical and experimental treatment of F_{16}CuPc thin films found that, whilst there were negligible differences in the band gap and magnetic interactions between the fluorinated and non-fluorinated systems, there was a shift of approximately $1\,\mathrm{eV}$ in the energy levels of the former system [58]. As a result of the augmentation in these energy levels, strong charge transfers can be induced in F_{16}CuPc/CuPc heterojunctions providing them with applicability in photovoltaic applications [59]. This trend was also observed in fluorinated zinc (II) phthalocyanine (ZnPc) systems in which an increasing energy shift of the highest occupied molecular orbital (HOMO) and lowest unoccupied molecular orbital (LUMO) was induced by an increasing degree of fluorination [60]. Extension of the aromatic π system through the fusing of additional benzene rings to the outer periphery of the system has been found to induce bathochromic shifts in the Q-band, with the magnitude of this shift increasing with an increasing number of benzene rings [56]. Larger steric-like substituents may also be added to the peripheral positions of the ring. The addition of long alkyl chains to the phthalocyanine system has been shown to increase its lipophilicity, making them highly useful as reaction catalysts [61]. More exotic substituents have been used to functionalise the ring in order to induce particular structural configurations between molecules. One notable example of this is the family of crown-ether phthalocyanines. These systems are characterised by the fusing of a crown-ether, of variable ring size, to the outer benzene rings. The addition of cations, whose atomic diameter is larger than that of the ring cavity, leads to the formation of stable cofacial dimers in which each pair

[6] Here n defines a non-bonding orbital, whilst π^* denotes an antibonding π-type orbital.

of crown-ethers on adjacent molecules are chelated by the ion [62]. In addition to the crown-ether functionalisation, other types of "bridging" substituents have been added so as to induce a cofacial alignment of the phthalocyanines. Yamada *et al.* (2018) reported on the synthesis of a rigid phthalocyanine dimer held in a coplanar alignment by a complex linker that attached to both rings [63].

Moving from one to two dimensional periodic systems, polymerisation of the phthalocyanines has also been reported. Here, a single 2D layer is generated in which adjacent phthalocyanine units are linked through the sharing of a benzene ring. In 2010, Abel *et al.* (2011) fabricated a polymeric iron phthalocyanine (poly-FePc[7]) system, grown on a Ag(111) surface [64]. Subsequently, Koudia & Abel (2014) successfully synthesised a polymeric manganese phthalocyanine (poly-MnPc) system, again on an Ag(111) surface, highlighting the complete delocalisation of the respective π-system [65]. In a separate theoretical characterisation of a series of polymeric first-row transition metal phthalocyanines (poly-TMPc), the electronic properties of each systems were highlighted. Perhaps most interestingly, poly-MnPc exhibited half-metallicity with a conduction band in the down-spin channel [66]. Additionally, all first-row poly-TMPc systems reported upon in the study displayed a reduction in the size of the band gap relative to that of the periodic crystal chain systems, likely due to the increased delocalisation of the ligand crystalline orbitals that constitute the respective valence and conduction bands. The systems also exhibit interesting magnetic properties. A first-principles DFT study carried out by Zhou & Sun (2011), using a PBE density functional, calculated the exchange energies for the same series of first-row poly-TMPcs, reporting relatively strong antiferromagnetic (AFM) interactions in polymeric chromium and iron phthalocyanine (poly-CrPc and poly-FePc, respectively) and strong FM coupling in poly-MnPc [67]. The coupling in the latter system was assigned to strong $d-p$ exchange interactions arising from hybridisation of the $d_{xz/yz}$ atomic orbitals (AOs) in the down-spin conduction band.

With regards to their applications, phthalocyanines play a particularly important role as pigments for industrial colourants. Indeed, CuPc is the most used pigment by volume-sold [50]. Gregory (2000) cites three principle reasons for their widespread use within this commercial sector: firstly, the materials have bright vivid colours and impart this colour to host materials easily; secondly, they exhibit strong thermal and chemical stability; and

[7]Within this report, both single chain periodic and two dimensional polymeric TMPc systems are studied. These are explicitly distinguished by their respective nomenclature: periodic single chain structures are referred to as "TMPc", whilst polymeric systems are denoted as "poly-TMPc", where TM characterises the specific transition metal.

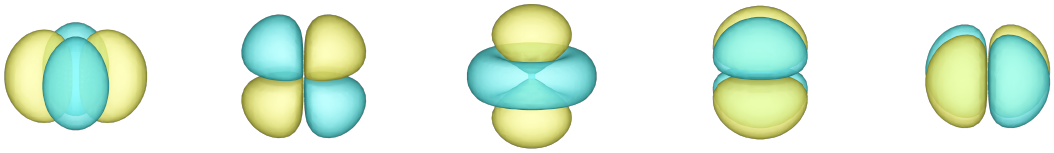

(a) (b) (c) (d) (e)

Figure 1.4: Visualisation of the d-derived orbitals: (a) b_{2g} (d_{xy}), (b) e_{gx} (d_{xz}), (c) a_{1g} (d_{z^2}), (d) e_{gy} (d_{yz}) and (e) b_{2g} $(d_{x^2-y^2})$.

thirdly, they show exceptional resistance to light exposure over time [50]. Phthalocyanines have also found more specialised applications within a variety of different scientific and technological fields. A functionalised lead (II) phthalocyanine (PbPc) derivative was used as the active material in the conductance channel of an organic field effect transistor (oFET) device, displaying an on-state retention time of more than five hours [68]. In addition to this, crystals of CuPc were used within a p-type oFET [69]. Both examples highlight the potentiality of organic molecular electronic devices with the potential to exhibit desirable properties not found within conventional MOSFETs. Due to their optoelectronic properties, arising principally from the aromaticity of the ligand, phthalocyanines and related derivatives have also found applications within dye sensitised solar cells (DSSCs), where the ability to functionalise both axial and peripheral positions of the ring facilitates strong binding to the TiO_2 surface [70]. In addition to their semiconducting and optoelectronic properties, phthalocyanine materials also exhibit a variety of magnetic properties. These are particularly prevalent within the class of transition metal phthalocyanines (TMPcs), in which the divalent metal ion contains a single, or set, of unpaired electrons, generating a paramagnetic molecular species[8] with potential utility within spintronic-based devices. Examples of such applications include multifunctional devices in which the insertion of paramagnetic TMPc molecules between graphene nano-ribbons [72] and carbon nanotubes [73, 74] results in highly effective spin filtering of conducting electrons, and organic semiconductors, where the fabrication of a ferromagnetic/TMPc heterojunctions facilitates efficient spin injection [75]. The remainder of this section focuses on the specific magnetic properties of these MPc systems and, in particular, those related to the first-row transition metals.

[8]Whilst the most prominent paramagnetic metal phthalocyanine species derive themselves from the transition metals, LiPc has been previously shown to exhibit a spin, $S = 1/2$ molecular electronic ground state and weak intrachain AFM coupling within periodic structures [71]. However, this particular system is not of relevance to the studies carried out in this report, and is, thus, excluded from the discussion here.

System	Moment [μ_B]	Configuration
CrPc	4	$(a_{1g})^1(e_g)^2(b_{2g})^1$ [76]
MnPc	3	$(a_{1g})^1(e_g)^2(b_{2g})^2$ [77]
FePc	2	$(a_{1g})^1(e_g)^3(b_{2g})^2$ [78]
CoPc	1	$(a_{1g})^1(e_g)^4(b_{2g})^2$ [79]
CuPc	1	$(a_{1g})^2(e_g)^4(b_{2g})^2(b_{1g})^1$ [80]

Table 1.1: Moments and ground state configurations for the set of air-stable, divalent, magnetic first-row transition metal phthalocyanines, with respective references.

Within the $\mathrm{D_{4h}}$ symmetry environment, the crystal field transforms the d AOs into molecular orbitals (MOs) of the following symmetry: $a_{1g}(d_{z^2})$, $e_g(d_{xz/yz})$, $b_{1g}(d_{x^2-y^2})$ and $b_{2g}(d_{xy})$ (see Fig. 1.4). Given the alignment of the b_{1g} MO along the metal-nitrogen bonding axes, the d-electrons will preferentially occupy the a_{1g}, e_g and b_{2g} MOs first. Table 1.1 shows the respective ground state electronic configurations for the set of air-stable divalent first-row TMPcs. For nickel (II) phthalocyanine (NiPc) and zinc (II) phthalocyanine (ZnPc), the ground state electronic configuration generates diamagnetic systems with no singly occupied d-derived MOs. As a result, these two species are not of interest with regard to metal phthalocyanine magnetic coupling.

CrPc has been reported in both the α and β-polymorphic phases [81]. The molecular species has a spin, $S = 2$, with four unpaired electrons residing within the d-derived MOs. Theoretical hybrid exchange density functional theory (DFT) calculations determined that these four electrons were distributed equally amongst the a_{1g}, e_g and b_{2g} MOs [76], as presented in Table 1.1. Analysis of the temperature dependence of the magnetic moment indicated moderate AFM ordering with a coupling strength of $J/k_B = -38.2\,\mathrm{K}$ in α-CrPc [82]. This was confirmed by DFT-based calculations carried out by Wu *et al.* (2013), which reported values of $J/k_B = -30\,\mathrm{K}$ ($J/k_B = -1\,\mathrm{K}$) for α-CrPc (β-CrPc) [76].

Manganese (II) phthalocyanine (MnPc) exhibits a spin, $S = 3/2$, with three unpaired electrons distributed amongst the d-derived MOs. Magnetic susceptibility measurements of MnPc crystals indicated the presence of a ${}^4A_{2g}$ ground electronic state with a configuration of $(a_{1g})^1(e_g)^2(b_{2g})^2$ [77]. This configuration was also confirmed by theoretical density functional calculations of the single molecule structure [83]. However, the ground state of single MnPc molecules, isolated within an argon matrix, was found to be ${}^4E_g$ with a configuration of $(a_{1g})^1(e_g)^3(b_{2g})^1$ [84]. The discrepancy has been ascribed to the axial coordination of the central metal to the isoindole nitrogen atoms of adjacent molecules in

the crystal bulk, which is thought to stabilise the ${}^4A_{2g}$ state [85]. Wu *et al.* (2008) suggested that Jahn-Teller distortion should be present if the state was indeed that of E_g [83], a finding not supported by structural characterisation of the bulk crystal [77]. With regards to the magnetic properties of crystalline MnPc, ferromagnetism has been measured in β-MnPc, with a Curie temperature, $T_C = 8.3\,\mathrm{K}$ [86], whilst in the α-phase weak antiferromagnetism has been reported with a Curie-Weiss[9] temperature, $\theta = -1.6\,\mathrm{K}$ [53]. Yamada *et al.* (1998), building upon earlier work by Barraclough *et al.* (1970) [77], offered an orbital focused mechanism to explain this characteristic "switching" in magnetic ordering between the two respective polymorphs [88]. However, a Green's function perturbative study of the MnPc molecular dimer concluded that the posited interaction would result in AFM coupling in *both* polymorphs [83]. As a result, a comprehensive mechanism for the ordering in MnPc crystals has yet to be fully elucidated.

Using accurate x-ray diffraction data, Coppens *et al.* (1983) determined that the ground electronic state FePc ($S = 1$) was ${}^3E_g$ with a configuration of $(a_{1g})^1(e_g)^3(b_{2g})^2$ [78]. This was also supported by theoretical first-principles calculations of the frontier energy spectrum of molecular FePc [89]. With regards to the emergent exchange properties, magnetic susceptibility measurements indicated that α-FePc thin film structures exhibited FM ordering with a Curie-Weiss temperature of $\theta = 24\,\mathrm{K}$ and associated coupling strength of $J/k_B = 11\,\mathrm{K}$, whilst respective characterisation of the β-FePc polymorph revealed a paramagnetic state [90]. The study also highlighted the ability to modulate this coupling strength by templating the thin film structures on a layer of 3, 4, 9, 10-perylenetetracarboxylic dianhydride (PTCDA), with the magnetic coupling being reported to be $J/k_B = 13\,\mathrm{K}$.

Given its prominence within industrial and commercial based applications, the magnetic properties of CuPc have been studied extensively. The molecule exhibits a spin, $S = 1/2$ ground state. The prior double occupation of the a_{1g}, e_g and b_{2g} MOs results in the single electron residing within the higher energy $d_{x^2-y^2}$-derived b_{1g} orbital, giving rise to a ${}^2B_{1g}$ state [80, 91]. Using superconducting quantum interference device (SQUID) measurements, Heutz *et al.* (2007) reported on AFM coupling in the α-polymorph of CuPc,

[9]The Curie-Weiss law characterises the dependence of the magnetic susceptibility on temperature with following formula,

$$\chi = \frac{C}{(T - \theta_p)} \tag{1.2}$$

where χ is the susceptibility, C is the empirical, system-specific Curie constant per unit mass, T is the temperature and θ_p is the paramagnetic temperature [87]. For ferromagnetic materials, this value is positive, whilst for antiferromagnets it is negative.

with a coupling strength, determined by fitting the data to the Bonner-Fisher model [92], of $J/k_B = -1.4\,\mathrm{K}$ [53]. Additional DFT based calculations also reported on a coupling parameter value of $J/k_B = -1.3\,\mathrm{K}$ and, using projected density of states (PDOS) of the single periodic α-CuPc chain, suggested that an indirect exchange mechanism, arising from the polarisation of ligand MOs, underpinned the weak AFM ordering [91]. With respect to the β-phase of CuPc, a paramagnetic state was ascertained [53].

The final important magnetic TMPc system of note is that of cobalt (II) phthalocyanine (CoPc). Like CuPc, CoPc exhibits a spin, $S = 1/2$ ground electronic state. Previous theoretical first-principles calculations of the single molecule structure have determined a $^2A_{1g}$ configuration, with the single electron residing within the d_{z^2}-derived a_{1g} MO [93,94]. These findings supported the investigative work by Kroll *et al.* (2009) who compared x-ray absorption spectroscopic (XAS) measurements of CoPc thin films with respective simulations of the spectra, concluding that a $^2A_{1g}$ ground state was present [79]. Within the self-assembled crystal polymorphs, CoPc has been shown to exhibit exceptionally strong AFM coupling. In particular, Serri *et al.* (2014) carried out temperature-dependent magnetic susceptibility measurements of α-CoPc, reporting an AFM coupling strength of $J/k_B = -78\,\mathrm{K}$ in a powder morphology and $J/k_B = -80\,\mathrm{K}$ and $J/k_B = -107\,\mathrm{K}$ in templated and non-templated thin film structures, respectively [93]. These findings were also supported by DFT-based calculations of the intrachain exchange interaction, which determined a value of $J/k_B = -85\,\mathrm{K}$ [94]. Comparatively weaker AFM interactions were measured in the β-polymorph of CoPc, with a $J/k_B = -1.5\,\mathrm{K}$ calculated by fitting magnetisation data to the Bonner-Fisher model [95]. This measurement was also supported by the DFT calculations of Ref. [94], who reported a value of $J/k_B = -2\,\mathrm{K}$.

The exceptionally strong magnetic coupling observed in α-CoPc (relative to that of both its polymorphic and transition metal counterparts) has led to much interest about its potential uses within operable spintronic devices. However, the underlying mechanism through which this strong coupling emerges is not fully understood. A previous study has suggested that the AFM coupling arises from a superexchange (see Sec. 3.1.1) interaction through the bonding nitrogen atoms which, in the α-phase, are aligned in the axial position of the metal atom of the neighbouring molecules [96]. However, according to the Goodenough-Kanamori-Anderson (GKA) rules for superexchange interactions [97–99], electron exchange proceeding through a 90° angle results in weak FM interactions. This is because the superexchange transfers electrons between the two paramagnetic atoms *via* the *same* diamagnetic ligand orbital. In a 90° configuration, this intermediary ligand orbital is orthogonal to at least one of

the paramagnetic atoms and, thus, electron transfer is symmetry forbidden. Furthermore, the theoretical calculations carried out in Ref. [94], in which the stacking angle, ϕ, was systematically varied, reported a maximum AFM exchange coupling of $J/k_B = -400\,\mathrm{K}$ in the co-facial ($\phi = 90°$) configuration. If the underlying mechanism was governed by an Anderson type superexchange interaction [99], this trend would not be expected to emerge. Thus, alternative mechanistic pathways are likely required in order to not only better understand the nature of the coupling within α-CoPc, but also direct chemical and structural modifications that may further improve this exchange strength. This is addressed within the studies presented in this work.

1.5 Principle Challenge

The principle challenge related to TMPc systems may be articulated as follows: molecular spintronic devices present themselves as possible "next-generation" alternatives to traditional silicon-based technologies. However, the realisation of a viable system is dependent upon a strong magnetic coupling in the candidate material. First-row TMPc crystals show some promise towards fulfilling this requirement, exhibiting a diverse range of magnetic properties. In particular, the high temperature AFM coupling observed in α-CoPc positions this system as suitable for spintronic applications. As discussed in the previous section, the pathway through which this coupling interaction proceeds is not well understood. Thus, a robust model, supported by theoretical first-principles calculations, would offer not only a deeper comprehension of the reasons underpinning this strong magnetism, but also provide the tools to chemically or structurally modify the system in such a way as to increase the interaction strength further. In order to do this, it is vital that the coupling is deconstructed into simple electron interaction terms that may be evaluated using computational methods. This is the primary focus of Chapters 4, 5 and 6, in which a mechanistic pathway is rigorously examined leading to the design of a novel TMPc system - rhodium (II) phthalocyanine - predicted to exhibit RT magnetic coupling. In addition to this, as outlined above, poly-TMPc systems also show much promise as materials for 2D single layer electronic devices. In Chapter 7, an examination of the first-row poly-TMPc systems is carried out so as to further elucidate the exchange mechanisms underpinning the observed magnetic behaviour. By providing this additional research to the current scientific understanding of these systems, it is hoped that specific and directed modifications to the systems can be made with the goal of realising viable 2D systems with molecular electronic applications.

2

Theoretical Concepts

Modern electronic structure methods provide an indispensable tool to both investigate and elucidate the chemistry and physics underpinning numerous emergent properties in both molecular systems and solid-state periodic structures. They provide the ability to probe deeply into materials, identifying the microscopic origins of macroscopic features [100]. In addition to this, they are invaluable in the design of novel systems, particularly in circumstances where specific characteristics are desired. The capacity to investigate the properties of such materials without the requirement of an initial synthesis or fabrication, not only provides a pathway for more efficient breakthroughs, where only the most promising of candidate materials are eventually constructed, but also minimises the potential for unnecessary resource expenditure and environmental harm [101]. Furthermore, the augmentation of these computational methodologies with evermore powerful and sophisticated machine learning (ML) models, only serves to further enhance the capabilities of such materials design [102, 103].

The plethora of different quantum simulation methods and tools available for both commercial and research applications offers users a broad and extensive range of options. The choice of a specific approach over another is often dictated by the system requirements or available computational resources. Whilst some quantum simulation techniques require

enormous data processing capabilities even for the smallest of systems, a number of others are more resource-efficient, offering the ability to obtain accurate solutions to the electronic structure problems of medium-sized systems on most modern desktop PCs. Not only has this expanded the research-based utility of these tools, but it has also facilitated their use for educational purposes, offering the capacity to understand the quantum structure of systems in a way not available through traditional experimental methods.

This chapter offers a summary of these electronic structure methods. Sec. 2.1 provides an outline of the Schrödinger equation - the principle formula underpinning the electronic structure of all quantum systems. In Sec. 2.2 and Sec. 2.3, an overview of the two most widely used computational methodologies - wavefunction methods and density functional theory - is communicated. Sec. 2.4 details the framework for treating periodicity within electronic structure methods. Sec. 2.5 introduces the concept of the basis set approximation. Sec. 2.6 summarises the operation of the geometry optimisations protocols. Finally, in Sec. 2.7 an outline of the different properties extracted from electronic structure calculations is provided.

2.1 Schrödinger Equation

In quantum mechanics[1], for every well-defined observable in classical mechanics, there exists a corresponding operator [105]. Measurement by action of this operator (here referred to as $\hat{A}$) on a system (here referred to as ψ) yields values (here referred to as a) that satisfy the following eigenvalue equation,

$$\hat{A}\psi = a\psi \tag{2.1}$$

where ψ and a are the *eigenfunction* and *eigenvalue* of the operator, $\hat{A}$, respectively. The operator that relates to the measurement of the energy of a quantum system is the Hamiltonian, $\hat{H}$. The quantum system itself is represented by the many-body wavefunction $|\Psi\rangle$[2], which, under Born-Oppenheimer (BO) conditions[3], is explicitly dependent on the four coordinates

[1]Theoretical information within this section is drawn from Ref. [104], which readers are directed to for a more detailed discussion.

[2]The bracketed notation, $|\Psi\rangle$, is a ket. The opposite notation, $\langle\Psi|$, is a bra and represents the complex conjugate of the ket. The notation, $\langle\Psi|\Psi\rangle$, is the *inner product* which is defined as the integral over all space of the product of the two functions.

[3]The mass of a nucleus is over a thousand times more than the mass of an electron. The corollary of this is that the motion of the electron is instantaneous on the timescale of nuclei motion and, therefore, the nuclei

(three spatial and one spin) of each electron and parametrically dependent on the positions of the nuclei [104]. For the action of the Hamiltonian on such a system, the corresponding eigenvalue equation is given by,

$$\hat{H}|\Psi\rangle = E|\Psi\rangle \tag{2.2}$$

where E is energy of the system. Eq. 2.2 is known as the *time-independent Schrödinger equation*. Under non-relativistic conditions, the Hamiltonian, in atomic units[4], is given by,

$$\begin{aligned}\hat{H} &= \hat{T}_e + \hat{V}_{ne} + \hat{V}_{ee} + \hat{V}_{nn} \\ &= -\frac{1}{2}\sum_{i=1}^{N}\nabla_i^2 - \sum_{i=1}^{N}\sum_{A=1}^{M}\frac{Z_A}{|r_i - R_A|} + \sum_{i<j}^{N}\frac{1}{|r_i - r_j|} + \sum_{A<B}^{M}\frac{Z_A Z_B}{R_A - R_B}\end{aligned} \tag{2.3}$$

Here, the first term, $\hat{T}_e$ relates to the kinetic energy of each of the N electrons, the second term, $\hat{V}_{ne}$, to the attractive potential interaction between each of the N electrons and each of the M nuclei, the third term, $\hat{V}_{ee}$, to the repulsion between each pair of the N electrons and the fourth term, $\hat{V}_{nn}$, to the repulsion between each pair of the M nuclei. ∇_i^2 is the Laplacian second-order differential operator acting on each electron i, Z_A is the atomic charge of nucleus A, and r_i and R_A are the coordinates of electron i and nucleus A, respectively. Due to the restrictions imposed by BO conditions, the nuclei do not contribute any kinetic energy terms. The repulsive interaction between each pair of the M nuclei is a constant term in the total energy expression.

However, even under these conditions, for all but the most simple single electron systems, the Schrödinger equation cannot be solved analytically. Consequently, numerical solutions to the equation are necessary. In modern electronic structure methods, there are two principal approaches used to obtain numerical solutions to the Schrödinger equation: wavefunction methods and density functional methods.

2.2 Wavefunction Methods

Wavefunction methods offer numerical solutions to the Schrödinger equation by systematically optimising a trial wavefunction until a reasonable approximation to the ground state

may be treated as maintaining stationary positions, with only the *electronic* Schrödinger equation requiring resolution.

[4]Throughout this chapter, unless specifically stated, relevant equations have been derived in atomic units.

energy of the system is obtained. The fundamental theorem that facilitates this procedure is known as the variational principle. This states that, for any ortho-normalised[5] trial wavefunction, $|\Psi_{tr}\rangle$, the energy obtained from the expectation value of the Hamiltonian will always be greater than or equal to the true ground state energy, E_{GS},

$$\langle\Psi_{tr}|\hat{H}|\Psi_{tr}\rangle = E[\Psi_{tr}] \geq E_{GS} \tag{2.4}$$

Here, $E[\Psi_{tr}]$ indicates that the energy of the system is a *functional* of $|\Psi_{tr}\rangle$. In general, $|\Psi_{tr}\rangle$ is defined as a function of a set of N fixed basis functions, $|\psi_i\rangle$ [104], given by

$$|\Psi_{tr}\rangle = f(|\psi_i\rangle) \tag{2.5}$$

Orthonormality conditions are satisfied if,

$$\langle\psi_i|\psi_j\rangle = \delta_{ij} \tag{2.6}$$

where δ_{ij} is defined as,

$$\delta_{ij} = \begin{cases} 1 & \text{if } i = j \\ 0 & \text{if } i \neq j \end{cases} \tag{2.7}$$

Additionally, the wavefunction must be antisymmetric upon the interchange (exchange) of coordinates of any two electrons,

$$\Psi_{tr}(\mathbf{r}_1, \ldots, \mathbf{r}_i, \ldots, \mathbf{r}_j \ldots, \mathbf{r}_N) = -\Psi_{tr}(\mathbf{r}_1, \ldots, \mathbf{r}_j, \ldots, \mathbf{r}_i \ldots, \mathbf{r}_N) \tag{2.8}$$

where the set of electron coordinates, $\{\mathbf{r}_i\}$, define both a spatial and spin component [104].

The simplest wavefunction method is the *Hartree-Fock* (HF) approximation. In this approach, each electron is evaluated within a mean-field (MF) derived from the potential of all other electrons and nuclei. The associated Hamiltonian, known as the Fock operator, $\hat{F}$, is given by,

$$\hat{F} = \hat{T}_e + \hat{V}_{ext} + \hat{V}_H + \hat{V}_x \tag{2.9}$$

where $\hat{T}_e$ is the kinetic energy term for each electron, $\hat{V}_{ext}$ is the external potential term arising from the nuclei of the system, $\hat{V}_H$ - the Hartree potential - is a classical Coulombic term arising from electron-electron repulsion in the system, and $\hat{V}_x$ is the exchange term arising

[5]Orthonormality for a given wavefunction, Ψ is satisfied if $\langle\Psi|\Psi\rangle = 1$.

from the exchange interaction between electrons. In the HF method, the wavefunction of the system is constructed from a single *Slater determinant*, given by

$$\Psi(\mathbf{r}_1, \mathbf{r}_2, \ldots, \mathbf{r}_N) = \frac{1}{\sqrt{N!}} \begin{vmatrix} \chi_1(\mathbf{r}_1) & \chi_2(\mathbf{r}_1) & \ldots & \chi_N(\mathbf{r}_1) \\ \chi_2(\mathbf{r}_2) & \chi_2(\mathbf{r}_2) & \ldots & \chi_N(\mathbf{r}_2) \\ \vdots & \vdots & \ddots & \vdots \\ \chi_1(\mathbf{r}_N) & \chi_2(\mathbf{r}_N) & \ldots & \chi_N(\mathbf{r}_N) \end{vmatrix} \tag{2.10}$$

where $\chi_i(\mathbf{r}_n)$ is the i^{th} spin orbital of the n^{th} electron. This is an antisymmetric function, and, therefore, inherently accounts for the exchange term in $\hat{F}$.

Within the HF method, the Coulomb and exchange interactions of an electron with itself completely cancel each other and, therefore, no self-interaction error (SIE) is present in the theory. However, whilst exchange between electrons is explicitly considered, the theory does not account for electron correlation, which arises due to both the static and dynamic Coulomb interactions between electrons. The associated energy, E_c, is defined as the difference in energy between the exact solution to the non-relativistic Schrödinger equation (E_{SE}) and that of the HF limit (E_{HF})[6],

$$E_c = E_{SE} - E_{HF} \tag{2.11}$$

Wavefunction methods that include the energy related to electron correlation effects are referred to as post-HF methods. The most common methods include the coupled cluster (CC) and configuration interaction (CI) schemes, and Møller-Plesset (MP) perturbation theory. In general, these methods offer more accurate approximations to the Schrödinger equation, provided that an appropriately sized basis set is used.

In the CC scheme[7], the total wavefunction of the system, $|\Psi_{CC}\rangle$, is defined as,

$$|\Psi_{CC}\rangle = e^{\hat{T}}|\phi_0\rangle \tag{2.12}$$

Here, $|\phi_0\rangle$ is the HF single Slater determinant and $e^{\hat{T}}$ is an exponential cluster operator [106]. By acting on $|\phi_0\rangle$, this operator generates a linear combination of single (S), double (D), triple (T) and higher order excitations. In general, the excitations are truncated at a

[6]The HF limit is the lowest possible energy attainable using the HF approximation. It is obtained within a compete basis set regime.

[7]The information outlined in this section related to CI, CC and MP methods is obtained from Refs. [104, 106], which the reader is directed to for a more detailed and comprehensive description.

desired level of accuracy such as CCSD (single and double excitations only) or CCSDT (single, double and triple excitations).

CI schemes account for electron correlation effects by replacing the HF single Slater determinant with a set of many Slater determinants [106]. The CI wavefunction, $|\Psi_{CI}\rangle$, is formulated in terms of different excitations to the HF reference determinant, $|\Phi_0\rangle$, given by,

$$|\Psi_{CI}\rangle = c_0|\Phi_0\rangle + \sum_{ra} c_a^r|\Phi_i^r\rangle + \sum_{a<b,r<s} c_{ab}^{rs}|\Phi_{ab}^{rs}\rangle + \cdots \tag{2.13}$$

where $|\Phi_a^r\rangle$ indicates an excitation from the occupied orbital, a, to the virtual orbital, r, and c_a^r is the associated coefficient. As with CC, the excitations are often truncated at a desired level of accuracy such as double excitations (CID).

MP perturbation theory is less computationally intensive relative to CC and CI methods. The procedure constructs an unperturbed Hamiltonian, $\hat{H}_0$, as a sum of the Fock operators for the system, with the correlation effects included as a perturbation, $\hat{V}$,

$$\hat{H} = \hat{H}_0 + \lambda\hat{V} \tag{2.14}$$

where λ is a parameter that weights the perturbation. At the second-order (MP2), electron correlation is included through double excitations of the HF determinant (the zero-order and first-order perturbations are the sum of the eigenvalues and the HF energy, respectively). Further excitations may be progressively included and are labelled accordingly.

Whilst post-HF methods, including those addressed here, provide very accurate approximations to the Schrödinger equation, they are computationally intensive, with the demand arising from the multi-determinental nature of the methods. Whilst HF scales as M^4, where M is the number of basis functions, MP2 scales as M^5 and MP3, CISD and CCSD scale as M^6 [107]. Consequently, such multi-determinental methods are restricted to small molecular systems or utilised in the benchmarking of other computational approaches [108–110].

2.3 Density Functional Theory

An alternate approach to the wavefunction based methods outlined above is density functional theory (DFT)[8]. In DFT, the variable that is used to find solutions to the Schrödinger equation is the electron density (as opposed to the wavefunction). This reduces the dimensionality of the problem from $3N$ to 3 spatial coordinates, where N is the number of

[8]General information related to this section is obtained from Refs. [111–113].

electrons in the system. The principles of DFT are grounded in two fundamental theorems proved by Hohenberg and Kohn [114] in 1964. The first theorem states that the ground state energy of a system is a unique functional of the electron density. Consequently, all observables of a quantum system may be obtained from this functional *without* any knowledge of the wavefunction. The second theorem explicates that the electron density that minimises the energy of this functional corresponds to the ground state solution of the Schrödinger equation. This implies that the ground state energy of the system can be obtained variationally,

$$E[\rho_{tr}] \geq E[\rho_{GS}] \tag{2.15}$$

where $E[\rho_{tr}]$ and $E[\rho_{GS}]$ are the energies as functionals of the trial and ground state electron density, respectively. This condition is fulfilled provided that,

$$N = \int \rho(\mathbf{r}) d\mathbf{r} \tag{2.16}$$

where N is the number of electrons in the system. The energy functional may be expressed as,

$$E[\rho] = \hat{T}[\rho] + \hat{E}_{ext}[\rho] + \hat{E}_{ee}[\rho] \tag{2.17}$$

where $\hat{T}[\rho]$, $\hat{E}_{ext}[\rho]$ and $\hat{E}_{ee}[\rho]$ are the kinetic energy, external electron-nuclei potential and inter-electronic potential terms as functionals of the electron density, respectively. Minimisation of this functional with respect to the electron density,

$$\frac{\delta E[\rho]}{\delta \rho(\mathbf{r})} = \frac{\delta \hat{T}[\rho]}{\delta \rho(\mathbf{r})} + \frac{\delta \hat{E}_{ext}[\rho]}{\delta \rho(\mathbf{r})} + \frac{\delta \hat{E}_{ee}[\rho]}{\delta \rho(\mathbf{r})} = 0 \tag{2.18}$$

provides a ground state solution to the Schrödinger equation. However, whilst the form of $\hat{E}_{ext}[\rho]$ is trivial,

$$\hat{E}_{ext}[\rho] = \int \hat{V}_{ext} \rho(\mathbf{r}) d\mathbf{r} \tag{2.19}$$

where the potential $\hat{V}_{ext}$ is system dependent, the forms of both $\hat{T}[\rho]$ and $\hat{E}_{ee}[\rho]$ are unknown. In 1965, Kohn and Sham established a procedure to approximate the unknown functionals in Eq. 2.17 [115]. By using a fictitious system of non-interacting electrons occupying a set of orbitals described by a single Slater determinant, an approximation to the kinetic energy may be obtained from,

$$\hat{T}_s[\rho] = -\frac{1}{2}\sum_{i=1}^{N}\langle\phi_i|\nabla^2|\phi_i\rangle \tag{2.20}$$

where the subscript "s" of $\hat{T}_s[\rho]$ indicates that the functional is the approximate kinetic energy arising from the non-interacting (single-particle) system [112] and ϕ_i are a set of occupied orbitals that describe the true ground state electron density,

$$\rho(\mathbf{r}) = \sum_{i=1}^{N}|\phi_i(\mathbf{r})|^2 \tag{2.21}$$

From the approximation, the classical Coulombic repulsion between electrons - the Hartree potential ($\hat{E}_H[\rho]$) - may also be obtained, given by

$$\hat{E}_H[\rho] = \frac{1}{2}\int\frac{\rho(\mathbf{r})\rho(\mathbf{r}')}{|\mathbf{r}-\mathbf{r}'|}d\mathbf{r}d\mathbf{r}' \tag{2.22}$$

where $\rho(\mathbf{r})$ and $\rho(\mathbf{r}')$ are the electron densities at positions $\mathbf{r}$ and $\mathbf{r}'$, respectively. Using Eqs. 2.20 and 2.22, the energy functional may be reformulated as

$$E[\rho] = \hat{T}_s[\rho] + \hat{E}_{ext}[\rho] + \hat{E}_H[\rho] + \hat{E}_{xc}[\rho] \tag{2.23}$$

where $\hat{E}_{xc}[\rho]$ is the exchange-correlation functional, defined as

$$\hat{E}_{xc}[\rho] = (\hat{T}[\rho] - \hat{T}_s[\rho]) + (\hat{E}_{ee}[\rho] - \hat{E}_H[\rho]) \tag{2.24}$$

Using the functional defined in Eq. 2.23, the Kohn-Sham (KS) equations may be derived as follows,

$$\left[-\frac{1}{2}\nabla^2 + \hat{v}_s(\mathbf{r})\right]\phi_i(\mathbf{r}) = \epsilon_i\phi_i(\mathbf{r}) \tag{2.25}$$

where $\phi_i(\mathbf{r})$ are a set of one electron orbitals, ϵ_i are the corresponding eigenvalues and $\hat{v}_s(\mathbf{r})$, the KS potential, is given by,

$$\hat{v}_s(\mathbf{r}) = \hat{v}_{ext}(\mathbf{r}) + \int\frac{\rho(\mathbf{r}')}{|\mathbf{r}-\mathbf{r}'|}d\mathbf{r}' + \hat{v}_{xc}(\mathbf{r}) \tag{2.26}$$

where the first term is the external potential, the second, the Hartree potential and the final, the exchange-correlation potential. Due to the dependence of $v_s(\mathbf{r})$ on the density, $\rho(\mathbf{r})$, no closed-shell solution is available and the KS equations must be solved self-consistently. Using an initial electron density, the potentials may be formulated. The eigenvalue equation,

Eq. 2.25, is then solved to obtain a set of eigenvectors which correspond to the single-particle orbitals. From this set of eigenvectors, a new electron density is constructed and the potentials are updated. This cycle is then iteratively repeated until self-consistency is achieved. In practice, iterative thresholds are set for changes in both the total energy of the system and the electron density, with the tolerance of this threshold defining the accuracy of the calculation.

For open-shell systems containing one or more unpaired electrons, an extension of DFT known as *spin density functional theory* (SDFT) must be used. Here, the total electron density is considered to be a composition of two independent densities,

$$\rho = \rho_{\uparrow} + \rho_{\downarrow} \tag{2.27}$$

Each density is constructed from a set of occupied spin orbitals, $\{\phi_{i,\sigma}(\mathbf{r})\}$, given by,

$$\rho_{\sigma}(\mathbf{r}) = \sum_{i=1}^{N_{\sigma}} |\phi_{i,\sigma}(\mathbf{r})|^2 \tag{2.28}$$

where σ denotes the specific spin projection ($\uparrow$ or $\downarrow$) of the respective orbital. Reformulation of Eq. 2.25 to account for the two separate densities, results in,

$$\left[-\frac{1}{2}\nabla^2 + \hat{v}_{s,\sigma}(\mathbf{r})\right]\phi_{i,\sigma}(\mathbf{r}) = \epsilon_{i,\sigma}\phi_{i,\sigma}(\mathbf{r}) \tag{2.29}$$

where

$$\hat{v}_{s,\sigma}(\mathbf{r}) = \hat{v}_{ext}(\mathbf{r}) + \int \frac{\rho(\mathbf{r}')}{|\mathbf{r} - \mathbf{r}'|} d\mathbf{r}' + \hat{v}_{xc,\sigma}(\mathbf{r}) \tag{2.30}$$

Solutions to Eqs. 2.25 and 2.29 are exact, but for the exchange-correlation functional whose true form is not known. As a result, a number of different methods have been formulated to provide an approximation to this functional.

2.3.1 Local Density Approximation

In the local density approximation (LDA), the inhomogeneous electron density of the system is treated to be locally homogeneous. The corollary of this is that, at each point, $\mathbf{r}$, in space, the exact exchange-correlation hole[9] is approximated to be that corresponding to

[9]The exchange-correlation hole is a fictitious depletion of charge density at a point $\mathbf{r}$ where an electron is located. It accounts for the reduction in the probability of finding a second electron at point $\mathbf{r}'$, located in the local vicinity of the first electron, due to the inherent nature of electrons to avoid one another.

an homogeneous electron gas (HEG), the form of which is known to a great accuracy [111]. The functional, $\hat{E}_{xc}[\rho]$, is then rewritten as,

$$\hat{E}_{xc}^{LDA}[\rho] = \int \epsilon_{xc}^{LDA}(\rho(\mathbf{r}))\rho(\mathbf{r})d\mathbf{r} \tag{2.31}$$

where $\epsilon_{xc}^{LDA}(\rho(\mathbf{r}))$ is the exchange-correlation energy per electron in an HEG with density ρ. For the exchange portion of the functional, the energy for an electron in an HEG is known exactly, given by

$$\epsilon_{x}^{HEG}[\rho] = -\frac{3}{4}\left(\frac{3}{\pi}\right)^{1/3}\rho^{1/3} \tag{2.32}$$

whilst the correlation energy has been approximated to an excellent degree of accuracy using quantum Monte Carlo (QMC) simulations [116, 117].

For open-shell systems, described by SDFT, the local spin density approximation (LSDA) may be used, in which $\epsilon_{xc}^{LDA}(\rho(\mathbf{r}))$ is replaced by an expression that separates the two spin densities,

$$\hat{E}_{xc}^{LSDA}[\rho_{\uparrow}, \rho_{\downarrow}] = \int \epsilon_{xc}^{LSDA}(\rho_{\uparrow}(\mathbf{r}), \rho_{\downarrow}(\mathbf{r}))[\rho_{\uparrow}(\mathbf{r}) + \rho_{\downarrow}(\mathbf{r})]d\mathbf{r} \tag{2.33}$$

Whilst LDA has proven to be a successful approximation, particularly for systems with smooth or uniform electron density distributions, there are several important limitations. Firstly, LDA offers a poor description of systems or environments where the electron density is inhomogeneous and varying. This is particularly relevant for the binding energy in molecules or cohesive energy in solids, where LDA overestimates their respective strengths [111]. Secondly, inherent in LDA is the self-interaction error (SIE) - the error arising from the electron interaction with its own contribution to the MF. In the HF method, the Coulomb and exchange self-interactions are exactly cancelled, but in LDA they are not. This results in poor representations of the charge density in regions where electrons are strongly localised. A number of improvements have thus been offered to enhance the accuracy of the LDA method.

2.3.2 Generalised Gradient Approximation

LDA may be considered as the zeroth-order approximation to the density matrix. Therefore, a natural progression to obtain an improvement in the performance of the functional, including the reconciliation of issues related to inhomogeneities in the electron density, is to expand in terms of the gradient and higher order derivatives [112]. However, when carrying

out a gradient expansion without the imposition of any constraints, severe deficiencies in the estimation of the exchange hole were identified, including violations in the normalisation and negative definite conditions[10] [111]. As a result, Perdew (1985) showed that a gradient expansion of the density, whilst mandating the fulfilment of these exact constraints, produced a more accurate functional [118]. This set of functionals belong to the family of generalised gradient approximations (GGAs).

In GGA, the exchange correlation functional is given by,

$$\hat{E}_{xc}^{GGA}[\rho] = \int \epsilon_{xc}^{GGA}(\rho(\mathbf{r}), \nabla\rho(\mathbf{r}))\rho(\mathbf{r})d\mathbf{r} \tag{2.35}$$

where $\epsilon_{xc}^{GGA}(\rho(\mathbf{r}), \nabla\rho(\mathbf{r}))$ is the exchange correlation energy functional dependent upon both the electron density, $\rho(\mathbf{r})$ and its first order derivative (gradient), $\nabla\rho(\mathbf{r})$. The expression can be extended to SDFT in a comparable manner to that of LSDA. Here, the functional is dependent upon both the spin-specific electron density *and* its respective gradient. In general, there are two principle ways in which the GGA functionals are formulated. The first is by fitting the parameters of the functional with the aim of reproducing experimental metrics, such as formation energies or structural data [111]. Alternatively an analytic form of the expression may be derived by requiring the function to fulfil a number of formal constraints. As a result, there can be significant variance in the form of each functional. BLYP, composed of the Becke '88 (B88) [119] exchange and Lee Yang Parr (LYP) [120] correlation functionals, is a notable example of the first approach, whilst PBE [121] is a well-known demonstration of the second. In general, GGA functionals improve upon the performance of LDA across a number of different metrics, including binding and atomisation energies [122], although deficiencies, such as correctly modelling dispersion interactions or highly correlated systems, are still present.

2.3.3 Meta-Generalised Gradient Approximation

Meta-generalised gradient approximation (mGGA) functionals expand on GGA by including both the Laplacian of the electron density and the kinetic energy density, $\tau(\mathbf{r})$,

[10]The exchange hole defines the local spatial region around an electron in which there is diminished electron density due to the Pauli exclusion principle. Therefore, evaluation of the exchange hole must be negative definite (there must always be a *decrease* in density). Additionally, the normalisation condition,

$$\int \rho_x(\mathbf{r}, \mathbf{r}')d\mathbf{r}' = -1 \tag{2.34}$$

where $\rho_x(\mathbf{r}, \mathbf{r}')$ is the exchange hole at position $\mathbf{r}'$ due to an electron at position $\mathbf{r}$, must be fulfilled.

$$\hat{E}_{xc}^{mGGA}[\rho] = \int \epsilon_{xc}^{mGGA}(\rho(\mathbf{r}), \nabla\rho(\mathbf{r}), \nabla^2\rho(\mathbf{r}), \tau(\mathbf{r}))\rho(\mathbf{r})d\mathbf{r} \tag{2.36}$$

where $\nabla^2\rho(\mathbf{r})$ is the second order derivative of the density and $\tau(\mathbf{r})$ is given by,

$$\tau(\mathbf{r}) = \frac{1}{2}\sum_{i}^{N} |\nabla\phi_i|^2 \tag{2.37}$$

where the sum runs over all N occupied KS orbitals. By including these additional degrees of freedom, the mGGA functionals are found to improve upon the performance of both GGA and LDA, particularly with regards to atomisation energies [123]. Examples of mGGAs include the TPSS [124], SCAN [125] and M06-L [126] functionals. However, mGGA functionals still suffer from the SIE also inherent in LDA and GGA.

2.3.4 Hybrid Exchange Functionals

According to the adiabatic connection[11], there exists a continuum of states of the same electron density that "connect" the non-interacting KS eigenstates with the fully interacting real system. This continuum is characterised by the coupling-strength parameter, λ, which takes values between 0 and 1. This theory may be applied to the exchange-correlation energy, E_{xc}, only, which can approximated by a linear interpolation of the two boundary values of λ,

$$E_{xc} \simeq \frac{1}{2}E_{xc}^{0} + \frac{1}{2}E_{xc}^{1} \tag{2.38}$$

where E_{xc}^{0} and E_{xc}^{1} are the exchange-correlation energies for the non-interacting ($\lambda = 0$) and fully interacting ($\lambda = 1$) systems, respectively [128]. Becke (1993) argued that the exchange-correlation energy at the $\lambda = 1$ upper limit was better approximated by the pure HF exchange energy arising from the Slater determinant of the KS orbitals, whilst at $\lambda = 0$, the energy could be derived from the LSDA exchange-correlation energy[12] of the HEG [129]. This resulted in the development of hybrid functionals consisting of a portion of exact (HF) exchange and exchange-correlation arising from LSDA. In general, the exchange-correlation portion of the functional takes the form,

$$E_{xc}^{Hybrid} = \alpha E_{x}^{HF} + (1-\alpha)E_{x}^{LSDA} + E_{c}^{LSDA} \tag{2.39}$$

[11] Readers are directed to Ref. [127] for a detailed description of the adiabatic connection principle and its specific application to KS-DFT.

[12] This was also extended to gradient approximated density functionals (GGAs) [128].

where E_x^{HF} and E_x^{LSDA} are the energies arising from the HF and LSDA exchange, respectively, E_c^{LSDA} is the correlation energy of LSDA and α is an adjustable parameter that modulates the respective proportion of HF and LSDA exchange present in the functional. It is important to note that the above formulation may also be extended to GGA functionals in an identical manner. Generally, hybrid functionals may be divided into range-separated hybrids, which utilise a distance screening of the HF exchange contribution, and global hybrids, which evaluate the exact exchange between all KS orbitals. Noteworthy examples of the former group include the short-range corrected HSE06 [121, 130] and medium-range corrected HISS [131, 132] functionals, whilst the B3LYP [120, 129] and PBE0 [133] functionals are two of the principle global hybrids commonly employed.

With the inclusion of a portion of Fock exchange into the density functional (DF) formalism, hybrids partially compensate for the SIE inherent within local DFs. In general, hybrid functionals yield a better performance than their LDA and GGA counterparts across a number of metrics, including atomisation enthalpies [134] and band gap predictions [135, 136]. As stipulated in later chapters, the B3LYP functional has been employed throughout the studies reported upon in this work.

2.4 Periodicity

To simulate the quantum properties of large, macroscopic materials, system sizes on the order of magnitude of Avogadro's number ($N_A = 6.02 \times 10^{23}$) need to be considered - an infeasible problem for practically all computational assemblies. In order to offer a solution to this problem, the periodic nature of the solid-state structure is exploited. A crystal system may be characterised by the translational repetition of a single unit known as the *primitive cell*. In three dimensions, the translational symmetry operations that define the periodic lattice structure may be written as,

$$\mathbf{R} = n_1\mathbf{a}_1 + n_2\mathbf{a}_2 + n_3\mathbf{a}_3 \tag{2.40}$$

where n_i are integers and $\{\mathbf{a}_i\}$ are a set of real space basis vectors which links a point in the primitive cell with three equivalent points in the lattice [137]. The infinite array of points generated by action of $\mathbf{R}$ on the primitive cell is known as a Bravais lattice, of which there are 14 in three dimensional space. For each unique lattice there is a corresponding set of reciprocal lattice vectors, $\{\mathbf{b}_i\}$, that are defined by the relationship,

$$\mathbf{a}_i \cdot \mathbf{b}_j = 2\pi\delta_{ij} \tag{2.41}$$

In three dimensions, these lattice vectors are given by,

$$\mathbf{b}_1 = 2\pi\frac{\mathbf{a}_2 \times \mathbf{a}_3}{V};\ \mathbf{b}_2 = 2\pi\frac{\mathbf{a}_1 \times \mathbf{a}_3}{V};\ \mathbf{b}_3 = 2\pi\frac{\mathbf{a}_1 \times \mathbf{a}_2}{V} \tag{2.42}$$

where V is the volume of the primitive cell. This set of lattice vectors define a unit cell in reciprocal space, the *first Brillouin zone* (FBZ) corresponds to an equivalent cell with the same volume, but centred with respect to the origin (Γ-point) [111]. Like its direct space counterpart, translational symmetry operations acting on the FBZ generate the reciprocal lattice structure,

$$\mathbf{G} = m_1\mathbf{b}_1 + m_2\mathbf{b}_2 + m_3\mathbf{b}_3 \tag{2.43}$$

where m_i are integers. In order to solve the electronic Schrödinger equation for a periodic system, one makes use of Bloch's theorem [138] which states that the wavefunction of an electron in an external periodic potential,

$$v(\mathbf{r}) = v(\mathbf{r} + \mathbf{R}) \tag{2.44}$$

may be formulated as,

$$\psi_{n,\mathbf{k}}(\mathbf{r}) = e^{i\mathbf{k}\cdot\mathbf{r}}u_n(\mathbf{r}) \tag{2.45}$$

where $u_n(\mathbf{r})$ is a function of the n^{th} eigenstate, that has identical periodicity to $v(\mathbf{r})$ and $e^{i\mathbf{k}\cdot\mathbf{r}}$ is a phase factor dependent upon a reciprocal lattice vector, $\mathbf{k}$. Thus, the eigenstate solutions to the infinite periodic lattice is mapped onto the wavefunction of the electrons in the FBZ [111]. Therefore, the challenge in electronic structure calculations is to express the periodic potential using a finite set of functions - the so-called basis set approximation.

2.5 The Basis Set Approximation

In both HF and DFT approaches, the single-particle orbitals are formulated in terms of a set of basis functions. Theoretically, an infinite number of these functions are required to completely model the orbitals. However, in practice, the number of functions used is truncated to a desired size. The choice of both the size and type of basis set is heavily dependent upon the system and desired variables under study. In general, there are two

principle types of basis sets: plane wave (PW) expansions and atom centred localised basis functions.

2.5.1 Plane Waves

PW basis sets are almost exclusively employed for the modelling of periodic systems. In this approach, the periodic portion of Eq. 2.45, $u_n(\mathbf{r})$, is expanded over a set PWs, given by

$$u_{n,\mathbf{k}}(\mathbf{r}) = \sum_{\mathbf{G}} c_{n,\mathbf{k},\mathbf{G}} e^{i\mathbf{G}\cdot\mathbf{r}} \tag{2.46}$$

where the sum runs over a set of reciprocal lattice vectors, $\mathbf{G}$ (as defined in Eq. 2.43) and $c_{n,\mathbf{G}}$ are the related coefficients for each PW, $e^{i\mathbf{G}\cdot\mathbf{r}}$ [139]. Therefore, the electron wavefunction, as defined in Eq. 2.45, may be reformulated as,

$$\psi_{n,\mathbf{k}}(\mathbf{r}) = \sum_{\mathbf{G}} c_{n,\mathbf{k},\mathbf{G}} e^{i(\mathbf{k}+\mathbf{G})\cdot\mathbf{r}} \tag{2.47}$$

Theoretically, in order to completely capture the electron wavefunction, an infinite expansion of PWs is required. However, whilst this is not feasible, the accuracy may be systematically improved by increasing the number of PWs in the expansion. Thus, the precision may be calibrated by truncating the summation in Eq. 2.47 to the set of PWs whose kinetic energy is below a defined threshold, E_{cut}, given by

$$\frac{1}{2}|\mathbf{k}+\mathbf{G}|^2 \leq E_{cut} \tag{2.48}$$

PW expansions provide a simple set of basis functions that may be *easily* adjusted for a desired level of accuracy. This is in contrast with other basis set approximations, such as atom-centred localised basis sets (see Sec. 2.5.3) where the accuracy of the wavefunction is not necessarily improved by simply increasing the number of functions. However, there are two distinct disadvantages to the use of PWs. Firstly, in systems of low dimensionality such as molecules, chains or surfaces, the surrounding vacuum must also be captured by a PW expansion, thereby utilising unnecessary computational resources. Secondly, wavefunctions that vary sharply close to the nuclei, such as core and d-electrons, require a high E_{cut} which, again, increases the computational demands for such calculations, although, for the core electrons, this limitation is often rectified through the use of pseudopotentials (PPs).

2.5.2 Pseudopotentials

Core electrons (i.e. electrons not occupying valence shells) do not take part in bonding within molecular or periodic systems. Therefore, these *unused* degrees of freedom may be eliminated from the electronic Schrödinger equation by replacing the atomic nuclear charge, Z, with an effective nuclear charge, Z_{eff}, that takes into account the screening from the core electrons. This Z_{eff} may then replace Z in the evaluation of the external potential $\hat{V}_{ext}$ [111]. This is the core principle behind the PP approach. Often PPs are included within a PW approach to replace the core electrons that require high thresholds of E_{cut} to capture. This greatly increases the computational efficiency of the PW calculation.

2.5.3 Localised Basis Sets

In the localised basis set approach, the one electron HF or KS MOs are formulated in terms of a *linear combination of atomic orbitals* (LCAOs). These AOs can be written in terms of a *radial* part and a *spherical harmonic* part,

$$\varphi_{nlm}(\mathbf{r}, \theta, \phi) = f_n(\mathbf{r}) Y_{lm}(\theta, \phi) \tag{2.49}$$

and are represented by an individual basis function. Here n, l and m are the principle, azimuthal and magnetic quantum numbers, respectively, and $(\mathbf{r}, \theta, \phi)$ are the spherical coordinates with the origin centred at a respective nucleus [140]. The spherical harmonics relate to the orbital angular momentum of the electrons and define the respective shape of the AO. $f_n(\mathbf{r})$ specifies the radial extent of the AO from the centre of the nucleus. In general, the set of spherical harmonics are pre-determined for each AO and the role of the basis set is to establish the radial component of each function. There are two principle mathematical representations for the AO that differ in their formulation of $f_n(\mathbf{r})$: Slater-type orbitals (STOs) and Gaussian-type orbitals (GTOs). Whilst STOs provide a more accurate short and long-range representation of the orbital radial distribution, they produce more mathematically complex two electron integral functions resulting in considerable inefficiency. Most modern electron structure implementations instead adopt GTO basis sets. Although they do not provide as accurate a description of the AO as STOs, they are more computationally efficient, particularity with regards to the electron integrals. This is due to the "Gaussian Product Theorem" which states that the product of two gaussian functions localised at two separate points may be expressed as a new gaussian function centred at point between the two original functions. In general, the inaccuracy in GTOs (relative to

STOs) is rectified by approximating a single basis function from a linear combination of gaussian functions.

Local basis sets are most commonly used in molecular and atomic based quantum calculations. However, their use may be extended to periodic systems by describing each crystalline orbital (CO)[13] as a linear combination of Bloch functions (BFs),

$$\psi_i(\mathbf{r},\mathbf{k}) = \sum_{\mu} a_{\mu,i}(\mathbf{k})\phi_{\mu}(\mathbf{r},\mathbf{k}) \tag{2.50}$$

where $a_{\mu,i}(\mathbf{k})$ is a coefficient for the BF and $\phi_{\mu}(\mathbf{r},\mathbf{k})$ is given by,

$$\phi_{\mu}(\mathbf{r},\mathbf{k}) = \sum_{\mathbf{g}} \varphi_{\mu}(\mathbf{r}-\mathbf{A}_{\mu}-\mathbf{g})e^{i\mathbf{k}\cdot\mathbf{g}} \tag{2.51}$$

where $\mathbf{A}_{\mu}$ are the coordinates of the nucleus in the primitive cell, on which the AO, φ_{μ}, is centred, and $\mathbf{g}$ are a set of lattice vectors [141].

For both periodic and non-periodic materials, local basis sets can be preferable over other methods such as the PW approach. With respect to periodic systems, localised basis sets can offer a better description of localised electron environments than that of PWs. Furthermore, local basis sets are often much smaller in size and, therefore, offer enhanced efficiency, particularly within methodologies employing the HF approach or hybrid-based functionals where two electron integrals must be explicitly evaluated. Given the molecular nature of the phthalocyanine systems as well as the local magnetic moments of the metal ions, in the calculations carried out in this report, atom-centred all-electron GTO basis sets are used.

2.6 Geometry Optimisation

Optimisation of the structural degrees of freedom in both molecular and periodic systems is an important facet of quantum calculations. The total energy of a system may be expressed as a function of its atomic coordinates with minima on the resulting potential energy surface (PES) corresponding to stable geometries. This minima region of the PES can be approximated as a quadratic function using a second order Taylor expansion [142], given by

$$E(\mathbf{x}_{n+1}) = E(\mathbf{x}_n) + \mathbf{g}_n^T(\mathbf{x}_{n+1}-\mathbf{x}_n) + \frac{1}{2}(\mathbf{x}_{n+1}-\mathbf{x}_n)^T\mathbf{H}_n(\mathbf{x}_{n+1}-\mathbf{x}_n) \tag{2.52}$$

[13] The crystalline orbital is the periodic counterpart of a non-periodic molecular orbital.

where $E(\mathbf{x}_n)$ and $E(\mathbf{x}_{n+1})$ are the total energies as functions of the atomic coordinates at points n and $n+1$ on the PES, respectively. $\mathbf{g}_n$ is the first derivative of the energy at point n, given by

$$\mathbf{g}_n = \frac{dE(\mathbf{x}_n)}{d\mathbf{x}_n} \tag{2.53}$$

and $\mathbf{H}_n$ is the Hessian or second derivative of the energy at point n, given by

$$\mathbf{H}_n = \frac{d^2E(\mathbf{x}_n)}{d{\mathbf{x}_n}^2} \tag{2.54}$$

Differentiating Eq. 2.52 and setting $\mathbf{g}_{n+1} = 0$ (corresponding to the stationary point on the PES) the following identity is derived,

$$\mathbf{x}_{n+1} = \mathbf{x}_n - \mathbf{H}_n^{-1}\mathbf{g}_n \tag{2.55}$$

known as the *Newton-Raphson* (NR) method [143].

Unless the PES is harmonic with respect to the atomic coordinates (in which case the stationary point is obtained in a single step) [142], Eq. 2.55 must be solved iteratively. In the NR method, $\mathbf{H}_n$ must be calculated at each step, which can be computationally expensive. As a result, *Quasi-Newton* (QN) methods were developed in order to expedite the process. QN methods use an approximate Hessian which is updated and improved at each iterative cycle without requiring its analytical recalculation. A number of different QN methods exist. One of the most commonly used is the Broyden-Fletcher-Goldfarb-Shanno (BFGS) method [144–148] (both the CRYSTAL and ORCA quantum simulation packages, employed in the studies presented in this report, make use of this QN method for geometry optimisations). Within this method, the Hessian approximation is updated using the following equation [143],

$$\mathbf{H}_{n+1} = \mathbf{H}_n + \frac{\Delta\mathbf{g}\Delta\mathbf{g}^T}{\Delta\mathbf{g}^T\Delta\mathbf{x}} - \frac{\mathbf{H}_n\Delta\mathbf{x}\Delta\mathbf{x}^T\mathbf{H}_n}{\Delta\mathbf{x}^T\mathbf{H}_n\Delta\mathbf{x}} \tag{2.56}$$

where

$$\begin{aligned} \Delta\mathbf{g} &= \mathbf{g}_{n+1} - \mathbf{g}_n, \\ \Delta\mathbf{x} &= \mathbf{x}_{n+1} - \mathbf{x}_n \end{aligned} \tag{2.57}$$

2.7 Properties

Once the wavefunction or total electron density of a system has been obtained, a number of different properties pertaining to that structure may be measured. Within the calculations presented in the subsequent chapters of this report, two principle properties of the wavefunction are analysed: the band structure and the Mulliken population.

2.7.1 Band Structure

The band or dispersion plot of a periodic crystal is an important analytical tool for understanding the arrangement and relative energies of the system's respective electronic structure. As outlined in Sec. 2.4, the wavefunction of a periodic system is described by Bloch's theorem, in which the respective eigenstates are characterised by two indices, n and $\mathbf{k}$ (see Eq. 2.45). These eigenstates are referred to as *bands* and are analogous to the electron orbitals of molecular systems (MOs). Each individual band is indexed by a discreet value of n. However, unlike molecular systems, where the interaction between two AOs results in the formation of pair of bonding and antibonding MOs, in crystals, the interaction of a periodic array of AOs, situated along the lattice, generates a continuum of orbital configurations that are distributed across the spectrum defined by the bonding and antibonding limits [149]. These configurations are described by the index $\mathbf{k}$ which is a continuous variable. In practice, only the primitive cell is considered and the eigenstate solutions are mapped onto the wavefunction defined within the FBZ. The resulting electronic dispersion diagrams plot the energy of each band as a function of $\mathbf{k}$. In addition to 3D crystals, band structures may also be generated for lower dimensional 2D and 1D systems, although the bands may only be plotted along the periodic direction. Indeed the band structures of lower dimensional systems are included within the studies presented in this report, with respective plots constructed for the single periodic TMPc chains (1D) and poly-TMPc sheets (2D).

2.7.2 Mulliken Population Analysis

Population analysis, in which the the proportion of charge (and spin) density localised on particular atoms or molecular regions is quantised, serves as an effective tool in the examination of quantum systems. It is particularly important in the analysis of magnetic systems, aiding in the identification of system spin states and exchange pathways. There are a number of different methods that have been devised to segregate both the charge and spin

density amongst the atomic subunits of a system. Amongst these, the Mulliken population analysis (MPA) method, proposed by Robert Mulliken in 1955 [150], has proven to be one of the most widely used within computational quantum chemistry. Within the LCAO approximation, the total number of electrons, N, of a system is given by,

$$N = \sum_{\mu\nu} P_{\mu\nu} S_{\mu\nu} \tag{2.58}$$

where the sum runs over all basis functions (AOs) of the system, and μ and ν label the specific element in both the density matrix, $\mathbf{P}$, and overlap matrix, $\mathbf{S}$, corresponding to AOs, φ_μ and φ_ν [142]. Diagonal terms, where $\mu = \nu$, quantify the population of φ_μ, whilst off-diagonal terms are associated with the population shared between the two AOs. In MPA, this population is shared *evenly* between the two orbitals. Thus, the total electron population of a specific AO, here denoted as a_μ, may be obtained by the following,

$$a_\mu = \sum_{\nu} P_{\mu\nu} S_{\mu\nu} \tag{2.59}$$

From this, the gross atomic population, q_A, is evaluated as follows,

$$q_A = Z_A - \sum_{\mu \in A} a_\mu \tag{2.60}$$

where Z_A is the nuclear charge of atom A [142].

Whilst MPA presents itself as a powerful analytical tool that may be used to more deeply probe the composition of the mono-determinant wavefunction, it is limited by its basis set dependency, with results that may significantly vary between different sets of functions. Furthermore, the equal partitioning of charge between two overlapping AOs may not provide an accurate physical description of the charge (or spin) density distribution. Other available population analysis methods have addressed these limitations. For example, Löwdin population analysis [151] constructs a set of orthogonalised AOs prior to the population analysis and, in doing so, can correct for some of the sensitivity issues of MPA. Nevertheless, MPA remains one of the most widely implemented and extensively employed population analysis procedures, and is used throughout all studies presented in this report.

3

Principles of Magnetism

The phenomena of magnetism has been recognised as far back as the late 7th Century BC, with the pre-Socratic philosopher Thales of Miletus (623-545 BC) reporting his observations of the magnetic effects between iron and the mineral magnetite [152]. During the early Han dynasty (202 BC - 9 AD), rudimentary compasses were constructed by balancing a lodestone spoon on a bronze plate [153] and by the 11th Century, these compasses had been refined and were used for maritime navigation in China. The first rigorous study of magnetism was published by William Gilbert in 1600 in his treatise *De Magnete* [154]. Within this work, Gilbert proposed that the Earth was itself a magnet with poles at its northern and southern extremities. In addition, he noted that these poles do not coincide with those defined by the rotational axis of the Earth [152].

In 1819, Hans Christian Ørsted (1777-1851) noted that an electric current flowing through a wire induced a magnetic force on a nearby compass needle. The following year, he reported upon the rotation of the magnetic field around a current carrying wire [155]. From this initial observation, the field of electromagnetism was established, with many important contributions over the subsequent years. This culminated in James Clerk Maxwell's seminal work, *A Treatise on Electricity and Magnetism* in 1873 [156]. In this work, Maxwell deduced four fundamental equations that describe the propagation of and interaction between the

electric and magnetic fields.

However, whilst the classical theory of electromagnetism accounts for the transmission of and interrelation between the electric and magnetic fields and, indeed, unifies the two into a single electromagnetic field, it cannot account for the magnetisation of a system nor the microscopic origin of magnetism. This was illustrated in the *Bohr–Van Leeuwen theory* [157, 158], which showed that there is no thermal equilibrium magnetisation in a non-rotational classical system. The full proof of this is beyond the scope of the work presented here[1], however, the consequence of the theorem is that a quantum mechanical treatment of the microscopic origin of magnetism is required to account for the spontaneous or perpetual magnetisation of a system.

This remaining chapter is structured as follows: in Sec. 3.1, the microscopic origin of magnetism in quantum systems is outlined; in Sec. 3.2, information related to cooperative macroscopic magnetic behaviour is provided; in Sec. 3.3, an overview of the magnetic anisotropy energy is provided, including the computational approach used to quantify it; in Sec. 3.4, a brief summary of the three quantum spin models relevant to this work are detailed; finally in Sec. 3.5, mapping strategies for quantum simulations are discussed.

3.1 Microscopic Foundation of Magnetism

In magnetism, the principle entity is the magnetic moment [159]. In quantum theory, this moment arises due to the angular momentum of an electron. This angular momentum is comprised of two principle components: the orbital angular momentum of the electron around a nucleus and the intrinsic spin angular momentum of the electron itself. Both quantities are well defined by a set of quantum numbers which characterise the occupied electron orbital. The total magnetic moment of the electron is given by the sum of these two components. The macroscopic long-range order observed in magnetic materials may be attributed to interactions between these magnetic moments. In general, these interactions may be bifurcated into one of two types: magnetic dipolar and exchange. Magnetic dipole interactions arise from the influence of the magnetic field generated by one moment on another. The strength of the interaction is both distance and orientation dependent, with repulsion between dipoles aligned parallel and attraction between dipoles aligned antiparallel. However, the interactions are typically weak (on the order of $1\,\mathrm{K}$ [159]) and cannot account for the macroscopic order of materials at high temperatures. Instead,

[1] For a detailed derivation of the theorem the reader is directed to Ref. [159].

the major energy component relating to the cooperative behaviour of magnetic moments in materials arises as a result of the exchange interaction between electrons. Broadly speaking, within molecular and band-gap magnetic materials, such as those studied in this report, there are three distinct exchange interactions: direct exchange, kinetic or superexchange and spin polarisation. In the remaining portion of this section, an overview of each of these three interactions is be provided. Information in this section has been drawn from Refs. [87, 159–161], and readers are directed to these sources for further details.

3.1.1 Exchange Interactions

The exchange interaction is a purely quantum mechanical phenomenon that arises from the antisymmetric nature of the wavefunction. In order to maintain the indistinguishability of electrons upon their exchange with one another, the total electron wavefunction is written as an antisymmetric function[2] (see Sec. 2.1). Therefore, if the spin portion of the function is symmetric (i.e. spins aligned parallel), then the spatial portion must be antisymmetric and vice versa. When the spatial part of the wavefunction is antisymmetric the constituent electrons are maximally separated from one another (relative to the symmetric configuration). Thus by aligning their spins parallel to one another, electrons may reduce their mutual Coulombic repulsion. The energy stabilisation gained by this separation is termed *direct exchange* (DE) and always acts to align the spins of (unpaired) electrons parallel to one another. However, if the respective single electron orbitals are non-orthogonal to one another, then they also have the ability to overlap. This allows the tails of the respective wavefunctions to delocalise onto one another and, in doing so, lower the associated kinetic energy of the system. However, due to Pauli repulsion between unpaired electrons of the same spin, this delocalisation effect is only possible if the electrons are aligned antiparallel to one another. The kinetic energy stabilisation gained through this antiparallel alignment is known as the *kinetic exchange* (KE) interaction and is in direct competition with DE. In general, for localised electron systems (such as those studied in this report), the DE interaction dominates in systems where the singly occupied orbitals are orthogonal with respect to one another, whilst the KE interaction dominates in systems where the orbitals are respectively non-orthogonal.

It is important to note that a "KE-type" interaction also extends to systems in which there is a diamagnetic intermediary that separates the two paramagnetic atoms. This interaction

[2] In single particle theories the antisymmetric nature of the wavefunction is captured through the use of a Slater determinant.

is termed the *superexchange* interaction and is most commonly observed in metal-oxide insulators [99]. Like the KE interaction, the particular relative alignment of the unpaired electrons is governed by the kinetic energy stabilising effect that such a configuration can induce. In general, according to the GKA rules for the superexchange interaction [97–99], if the bonding angle between the three interacting atoms is $180°$, then an antiparallel configuration of the unpaired electrons will be most stable. However, if the respective bonding angle is $90°$, the single electrons will align parallel to one another. This is due to requirement that the singly occupied orbitals must interact through the *same* orbital of the diamagnetic intermediary. When the bonding angle is $180°$, this set of interactions is possible, whilst in the $90°$ configuration only one of the set of interactions will be symmetry allowed. The superexchange interaction is often defined as an *indirect* exchange interaction as the respective magnetic moments couple indirectly through an intermediary. Whilst this interaction is an important facet of many bulk crystal insulating materials, it is of less relevance to the systems studied in this report, where direct interactions such as KE and DE are predicted to play a far more important role due to the proximity of the metal ions within the crystal chain.

The final component of the exchange interaction is that of the spin polarisation (SP) of the doubly occupied MOs through interaction with the localised magnetic moments. In a magnetic system, there is a unique exchange field generated by each of the two spin configurations. In insulating and molecular magnetic systems, each of these fields interacts with the core (doubly occupied) orbitals in a separate way, generating a differential polarising effect on these electrons. The induction of this effect can be more stabilising for either of the two configurations and, therefore, its presence is not an *a priori* prediction of one spin state or the other. In general, within the doubly occupied orbitals located in the vicinity of the magnetic moment, electrons of the same spin as that of the moment will concentrate closer to the unpaired electron so as to maximise their respective exchange integral. Conversely, electrons of opposite spin will localise further from the moment so as to minimise the inter-electronic repulsion that is not stabilised in the absence of an exchange term.

In metallic systems, this polarising effect is most prevalent amongst the conduction band electrons. Here, the delocalised electrons within the vicinity of the local unpaired electron mix in higher energy states of the same spin such that the respective wavefunction becomes spin polarised around the moment and the exchange terms are maximised. This induces an oscillatory character to the conduction electron spin as a function of distance, with the result being the coupling of two local moments through the polarised conduction band [87].

This specific exchange interaction is known as Ruderman-Kittel-Kasuya-Yosida (RKKY) coupling [162–164] and, whilst important for many conducting systems, is less relevant in medium band-gap semiconductors and insulators as well as many molecular magnetic systems in which the crystalline orbitals exhibit an atomic-like character.

3.1.2 Paramagnetism

Paramagnetism refers to materials that contain unpaired electrons, but do not show spontaneous magnetisation as a result of cooperative exchange interactions. The magnetic moments associated with each single electron are aligned randomly and no overall magnetisation is realised. However, upon the application of an external magnetic field, the moments align parallel with the field axis and the material exhibits a net magnetisation. This magnetisation is linearly dependent on the field strength with its respective rate of change referred to as the paramagnetic susceptibility [87].

3.1.3 Diamagnetism

Diamagnetism is an effect observed in all systems. The orbits of electrons within the atoms of a material may be considered as an electric current with an associated magnetic moment. When an external field is applied to the material, the motion of these electrons is disrupted, generating a small moment. According to Lenz's law, this induced moment will act in the opposite direction to the applied field and, thus, diamagnetic responses induce a negative susceptibility. Diamagnetism is approximately one order of magnitude smaller than the effects induced from paramagnetic susceptibilities and, therefore, generally appears as a minor correction to the material magnetisation response [87].

3.2 Macroscopic Ordering in Magnetic Materials

The microscopic, individual interactions between electrons, and in particular those related to their exchange, induce macroscopic cooperative behaviour in the associated materials. This cooperative behaviour is observed in the material response to applied magnetic fields known as the magnetic susceptibility of the material. In this section, the three principle types of magnetic ordering - ferromagnetism, antiferromagnetism and ferrimagnetism - are outlined.

3.2.1 Ferromagnetism

In a ferromagnetically ordered material, the unpaired electrons are aligned parallel to one another such that the material exhibits spontaneous magnetisation. It is important to note that, in most materials, the uniform magnetisation is not homogenous due to magnetic domains. Instead there is a uniform magnetisation inside the domain, but each domain may align in a different direction. FM materials may be characterised by their response to an external magnetic field. In the absence of any field, the material may exhibit remanent magnetisation within domains. As the external magnetic field is applied and increased, the material magnetisation also increases as the individual domains align with the field direction. At a critical field value, the material magnetisation becomes saturated, and does not continually increase with an increasing applied field. As the field is returned to zero, the material maintains some degree of remanent magnetisation. Reversing the field direction initially causes a decrease in this magnetisation and, with increasing field magnitude, eventually reverses its direction, leading to saturation of the magnetisation in the opposite direction. The material response to this "sweeping" of the field is known as a hysteresis loop and characterises an FM material.

Once magnetised, FM materials maintain this alignment even in the absence of an applied field. This spontaneous magnetisation is temperature dependent. The characteristic temperature at which the material transitions from an ordered FM state into a disordered paramagnetic state is known as the Curie temperature, T_C. A higher T_C is indicative of a stronger coupling between the respective magnetic moments in the material. With regards to the specific exchange interactions discussed in Sec. 3.1.1, a dominant DE interaction in a material leads to the emergence of FM ordering and in band-gap and molecular magnetic materials, this is often achieved only when the respective singly occupied orbitals are both orthogonal and directly interacting. This ensures that the KE interaction, which favours antiparallel alignment of the moments, is suppressed.

3.2.2 Antiferromagnetism

Antiferromagnetism is characterised by the antiparallel alignment of nearest neighbour unpaired electrons. This type of ordering may be understood as the interaction between two sublattices of opposite spin alignment containing every other magnetic moment. With this model, the magnetisation of one sublattice exactly cancels the magnetisation of the other, resulting in no net magnetisation. The application of an external field to the AFM material

presents a more complex interaction than that observed in FM systems. This is due to the fact that any energetic advantage that one sublattice gains by aligning with the field direction is at a disadvantage to other sublattice aligned antiparallel to the field direction. Therefore, the magnetisation exhibits a linear response to the external field and returns to zero upon the removal of the respective field. In addition, the two sublattices exhibit a differential response depending upon whether the external field is applied parallel or perpendicular to the AFM magnetisation axis[3]. In the case where the field direction is aligned perpendicular to the axis, the axes of the two sublattices begin to cant towards to field direction, eventually aligning with the external magnetisation. However, if the direction is aligned parallel to the axis, no rotation or canting is observed below a critical field. Above this critical value, the ordering undergoes a spin-flop transition in which the moments reorder into a new configuration. A continual increase in the field strength eventually aligns the moments with the external magnetisation axis [159].

Just as T_C defines the temperature at which an FM system transitions from an ordered to disordered state, in AFM systems the analogous transition temperature is known as the Néel temperature, T_N, the magnitude of which characterises the strength of the AFM coupling. For temperatures, $T \leq T_N$, an antiferromagnet maintains its respective ordering, whilst for $T > T_N$, the system adopts a paramagnetic state. A number of transition metal oxides exhibit AFM behaviour arising from a superexchange interaction between two cations and a diamagnetic intermediary. Additionally, as outlined in the following chapters, the AFM ordering observed in some TMPc systems is believed to arise from a direct KE interaction between the metal cations of the molecules.

3.2.3 Ferrimagnetism

As outlined above, antiferromagnetism arises due to the interaction between two equal sublattices that completely cancel the magnetisation of the other. However, if the two oppositely aligned sublattices are not equal, the respective material can exhibit a net magnetisation. This phenomena is known as ferrimagnetism. The spontaneous magnetisation of these two sublattices can display quite different temperature dependencies causing the thermal profile of the net magnetisation to be more complex than that observed in AFM or FM materials [159]. A number of materials with reported ferromagnetism are instead ferrimagnetic. The most notable example with regards to molecular magnetic materials

[3]In the case of AFM materials this refers to the direction that the spins are aligned along. However, the moments of the sublattices will point in opposite directions.

is vanadium tetracyanoethylene ($[\mathrm{V(TCNE)_2}]$) periodic which exhibits room temperature spontaneous magnetisation as a result of the ferrimagnetic ordering between the vanadium cations and tetracyanoethylene radicals [26, 165].

3.3 Magnetic Anisotropy

Magnetic anisotropy (MA) refers to the directional dependence of a system magnetisation. These systems are characterised by an *easy* and *hard* axis. The easy axis denotes the preferred (low energy) direction of the magnetisation, whilst the hard axis refers to the unfavourable (high energy) direction. The MA energy (MAE) is the energy required to realign the material magnetisation axis from the easy to hard axis. Whilst MA generally refers to a preferable magnetisation direction, in the context of periodic magnetic systems, the specific form of anisotropy is known as the *magnetocrystalline anisotropy* (MCA), although the two terms may be used interchangeably. MCA occurs as a result of the coupling between the spin moments and the crystal lattice in a magnetic material. In first-row TM systems, such as those studied in this report, the coupling emerges as a result of a spin-orbit coupling (SOC) interaction. SOC is a relativistic effect that arises due to the coupling between the electron spin and its orbital motion around the nuclei. In the rest frame of the electron, the nucleus orbits the electron inducing a magnetic field at the origin of this orbit. This induced magnetic field interacts with the moment generated from the electron intrinsic spin [159]. This has the effect of mixing spin and orbital angular momentum states and inducing energy level splitting. SOC may also interact with the anisotropy generated by the crystal field of the surrounding periodic structure, further splitting the energy levels. This has the effect of inducing an easy axis of alignment for the magnetic moments of the single electrons.

In quantum simulations, MA and MCA are introduced through use of the Dirac equation which reformulates the Schrödinger equation so as to account for relativistic effects (see Appendix B.1). In general, there are two principle ways in which the SOC interaction is evaluated: the perturbative or "second variational" approach and the non-perturbative approach. In the second variational approach [166], a scalar-relativistic wavefunction is obtained in which only relativistic effects related to the electron kinetic energy and associated orbit have been accounted for. The SOC interaction is then included as a perturbation to this scalar-relativistic wavefunction. This approach is particularly useful for systems in which SOC is not expected to be a dominant interaction and facilitates an efficient implementation

of relativistic effects. The second approach includes SOC in a non-perturbative way by solving the fully relativistic Hamiltonian. Whilst this method provides a more accurate description of the SOC and, therefore, the respective anisotropy, it can be computationally intensive and difficult to solve for larger complex systems. Furthermore, when applied at the single-determinant level using DFT, for some open-shell strongly correlated systems, there can difficulties converging the self-consistent procedure [141, 167].

In order to evaluate the energy related to the anisotropy, the relativistic energy of the system is obtained (using one of the two above methods) with the magnetisation aligned along both the easy and hard axes. At the single determinant DFT level - the level at which the calculations in this report have been carried out - in order to account for the different directions of moment alignment, a non-collinear approach is required. In standard collinear DFT, the magnetisation is always quantised along the z cartesian direction. However, in the non-collinear approach, the exchange correlation functional is reformulated so as to include values of magnetisation along all three cartesian directions, thus allowing the direction of the axes of magnetisation to be modified, facilitating the evaluation of its respective energy. The MAE is then evaluated using the following formula [160, 168],

$$\Delta E_{MAE} = E(\theta_0, \tau_0) - E(\theta, \tau) \tag{3.1}$$

where θ and τ refer to the polar and azimuthal angles, respectively. $E(\theta, \tau)$ is the total DFT energy of the system magnetised along an axes defined by the two respective angles. θ_0 and τ_0 define the magnetisation axes aligned along the z cartesian direction. Thus, the magnetisation axes and the related energy may be obtained by varying θ and τ in the initial configurations for the DFT calculation.

3.4 Quantum Spin Models

In systems where the magnetic behaviour is dominated by the interactions between localised moments, the respective energy spectrum can be captured through the use of quantum spin models. Although this section focuses only on the three quantum spin models relevant to the studies carried out in this report, many different prescriptions exist with the choice of a specific model being dependent upon both the type of system and interaction that is being investigated.

3.4.1 Heisenberg Model

For systems in which unpaired electrons are well localised and interact in a correlated way by mutually exchanging with one another, the ground state and low energy spectrum can be captured by a Hamiltonian which takes into account these interactions. Given the exponential decay of the exchange interaction with distance, for many systems of interest, only nearest neighbour interactions are of importance in defining the low energy magnetic states. These interactions are captured within the *Heisenberg Dirac van Vleck* (HDvV) Hamiltonian [169–171], given by

$$\hat{H} = -\sum_{\langle i,j \rangle}^{N} J_{ij} \hat{\mathbf{S}}_i \cdot \hat{\mathbf{S}}_j \tag{3.2}$$

where $\hat{\mathbf{S}}_i$ is the spin operator associated with the moment at the i^{th} lattice site, and J_{ij} is the interaction strength between the i^{th} and j^{th} spin operators[4]. The sum runs over all N pairs of nearest neighbours (as indicated by $\langle i, j \rangle$). The magnitude and sign of each J_{ij} indicates both the strength *and* type of coupling, with values of $J_{ij} > 0$ ($J_{ij} < 0$) being FM (AFM). In the HDvV model, the spin operators, $\hat{\mathbf{S}}_\mathbf{i}$ are three dimensional vectors with an associated order parameter $D = 3$ [159].

3.4.2 Ising Model

In the Ising model, the HDvV Hamiltonian is reformulated such that the order parameter of the operators is reduced to $D = 1$ and, as such, are only described by the z-component of the spin. This reformulated Hamiltonian, known as the Ising Hamiltonian, is given by

$$\hat{H} = -\sum_{\langle i,j \rangle}^{N} J_{ij} \hat{\mathbf{S}}_i^z \cdot \hat{\mathbf{S}}_j^z \tag{3.3}$$

where $\hat{\mathbf{S}}_i^z$ is the z-component of the spin on i^{th} lattice site. J_{ij} measures the coupling between the spins in the same way as in Eq. 3.2. Within the DFT or HF approach, the FM and AFM configurations are represented as single determinant states and are eigenfunctions of the Ising Hamiltonian. Thus the coupling constant J_{ij} may be evaluated from the difference in the total energies of these two states (see Sec. 3.5).

[4]It should be noted that the full HDvV Hamiltonian also includes a term related to the interaction between an external magnetic field and each spin centre of the system. However, all calculations in this report are carried out in the absence of any external field and, as such, this term is omitted for clarity.

3.4.3 Hubbard Model

The Hubbard model [172] is a theoretical framework for treating electron correlation in a system. The model accounts for the competition between electron kinetic energy which favours the transfer of electrons between lattice sites, and the electron-electron repulsion arising from the double occupation of a previously singly occupied site. In second quantised form, the respective Hamiltonian is given by,

$$\hat{H}^{Hubbard} = -t \sum_{\sigma} \sum_{\langle i,j \rangle} (c^{\dagger}_{i\sigma} c_{j\sigma} + h.c) + U \sum_{i} \hat{n}_{i\uparrow} \hat{n}_{i\downarrow} \tag{3.4}$$

Here, t is the transfer integral, given by $\langle i|\hat{H}|j\rangle$, $c^{\dagger}_{i\sigma}$ ($c_{i\sigma}$) are creation (annihilation) operators of spin σ at site i, $h.c$ is the hermitian conjugate, U is the on-site Coulombic repulsion arising from the double occupation of an orbital and $\hat{n}_{i\sigma}$ is the number operator defined as $\hat{n}_{i\sigma} = c^{\dagger}_{i\sigma} c_{i\sigma}$. The Hamiltonian only acts between nearest neighbour spin sites. The dynamics of the model arise from the interplay between t and U. At half-filling (one electron at each lattice site), in the regime where U is small, there is suppressed on-site inter-electronic repulsions, and electrons transfer freely between sites. At the boundary of $U = 0$, the Hamiltonian collapses into the *tight-binding* limit, where a set of short range bonds form between each lattice site. In the opposite regime, where $U >> t$, the energy cost arising from the double occupation of a site greatly outweighs any kinetic energy stabilisation gained from electron transfer. Here, the ground state of the system is that of a set of singly occupied lattice sites and the transfer of electrons between the sites acts as a perturbation to this ground state. Within this regime, it may be shown through a second-order perturbative expansion[5] that the Heisenberg coupling constant, $J = -4t^2/U$. As U increases, electron transfer becomes increasingly energetically unfavourable. At the limit of $U = \infty$, no electron transfer between sites is possible and the system adopts a so-called Mott insulating state. The Hubbard model is particularly useful as a model to describe kinetic exchange and superexchange interactions within respective magnetic systems and is utilised within the studies presented in Chapters 4 and 5.

[5]The derivation of this expansion is beyond the scope of this report. For further information readers are directed Ref. [173].

3.5 Mapping Strategies for Quantum Simulations

In order to obtain quantitative estimates of the exchange coupling within magnetic systems, quantum simulation methods may be employed. The most common strategy is to evaluate the energy difference between the high spin (HS) configuration and lower spin states. Taking the most simple example of system in which a single unpaired electron resides at each magnetic centre, the coupling between each pair of spins may be equated through the energy difference between the singlet (low spin (LS)) and triplet (HS) configurations. However, whilst the triplet configuration may be defined within a single determinant framework, the singlet state is multideterminental. For simple systems, in which there are two magnetic centres, it is possible to evaluate the energy difference between the HS and LS states using a multiconfigurational method. However for larger systems or periodic crystals, such as those studied in this report, one is limited to the use of single determinant MF methodologies such as DFT or HF [174].

In order to provide a mapping between the single determinant energies arising from the DFT or HF solutions and the HDvV Hamiltonian, an MF strategy is adopted. It should be noted that the mapping strategy provided here is applicable to homogenous spin systems in which only the nearest neighbour interactions are evaluated. For the Hamiltonian given by,

$$\hat{H} = -\sum_{\langle i,j \rangle}^{N} J_{ij} \hat{\mathbf{S}}_i \cdot \hat{\mathbf{S}}_j \tag{3.5}$$

the MF approximation of the interaction between the two spin centres is given by,

$$\hat{\mathbf{S}}_i \cdot \hat{\mathbf{S}}_j \simeq \hat{\mathbf{S}}_i^z \cdot \langle \hat{\mathbf{S}}_j^z \rangle + \langle \hat{\mathbf{S}}_i^z \rangle \cdot \hat{\mathbf{S}}_j^z - \langle \hat{\mathbf{S}}_i^z \rangle \cdot \langle \hat{\mathbf{S}}_j^z \rangle \tag{3.6}$$

Here, fluctuations of each spin is ignored (indicted through the use of $\hat{\mathbf{S}}_i^z$) and Eq. 3.5 collapses to the Ising Hamiltonian. Each spin interacts with the average magnetisation of its nearest neighbour (denoted $\langle \hat{\mathbf{S}}_i^z \rangle$). Substituting the identity defined in Eq. 3.6, Eq. 3.5 is reformulated as follows

$$\hat{H} = -J \sum_{\langle i,j \rangle}^{N} (\hat{\mathbf{S}}_i^z \cdot \langle \hat{\mathbf{S}}_j^z \rangle + \langle \hat{\mathbf{S}}_i^z \rangle \cdot \hat{\mathbf{S}}_j^z - \langle \hat{\mathbf{S}}_i^z \rangle \cdot \langle \hat{\mathbf{S}}_j^z \rangle) \tag{3.7}$$

where, given the homogenous nature of the system, the subscript of J has been dropped. In the FM spin configuration,

$$\langle \hat{\mathbf{S}}_i^z \rangle = \langle \hat{\mathbf{S}}_j^z \rangle = m \tag{3.8}$$

whilst for the AFM configuration,

$$\begin{aligned} \langle \hat{\mathbf{S}}_i^z \rangle &= m \\ \langle \hat{\mathbf{S}}_j^z \rangle &= -m \end{aligned} \tag{3.9}$$

where m is the spin on each magnetic centre. For the FM system, Eq. 3.7 simplifies to

$$\hat{H}^{FM} = \frac{1}{2} JzNm^2 - Jzm \sum_i^N \hat{\mathbf{S}}_i^z \tag{3.10}$$

whilst in the AFM configuration, Eq. 3.7 becomes

$$\hat{H}^{AFM} = -\frac{1}{2} JzNm^2 - \frac{1}{2} Jzm \sum_{\langle i,j \rangle}^N (\hat{\mathbf{S}}_j^z - \hat{\mathbf{S}}_i^z) \tag{3.11}$$

where z is the coordination number of each site. In both the FM and AFM spin states, each spin centre, in the MF approximation, is assumed to only align along the z-projected axis. Therefore, Eqs. 3.10 and 3.11 may be further simplified,

$$\begin{aligned} \hat{H}^{FM} &= -\frac{1}{2} JzNm^2 \\ \hat{H}^{AFM} &= \frac{1}{2} JzNm^2 \end{aligned} \tag{3.12}$$

As stated above, the coupling, J may be evaluated from the energy difference between the HS (FM) configuration and lower spin (AFM) configurations. Thus, within the MF approximation, a prescription for the calculation of J is given by the following,

$$\Delta E = E_{FM} - E_{AFM} = -JzNm^2 \tag{3.13}$$

where E_{FM} and E_{AFM} are the total DFT or HF energies of the system, z is the coordination of each spin centre, N is the number of magnetic sites and m is the spin of each magnetic centre. Eq. 3.13 is identical to the formula specified in Refs. [174–176] and provides a mapping that is applicable to both periodic and molecular systems of different dimensions and unit cell size.

As outlined above, whilst the HS configuration of both molecular and periodic systems may be captured within a single determinant framework, the LS state often comprises of a linear combination of states and is multiconfigurational. In order to model such systems

using a DFT or HF approach, the LS state must be approximated as a single determinant configuration. This strategy was pioneered by Noodleman (1981) and is referred to as a broken symmetry (BS) state [177]. The name arises due to the localisation of single electrons of opposite spin on adjacent magnetic centres, *breaking* the symmetry of the singlet state. As a result of this, the BS state is *not* an eigenfunction of the total spin operator, $\langle S^2 \rangle$ and exhibits spin contamination. There are a number of different approaches to spin decontamination of the energies of the BS state [177, 178]. However, the approach formulated by Yamaguchi and coworkers (here referred to as the Yamaguchi formula) has the advantage over other decontamination methods in that it accounts for both strong and weak orbital overlap conditions [179–183]. Thus, Eq. 3.13 may be reformulated so as to include spin decontamination of the energy components according to the Yamaguchi formula. This is given by,

$$JzNm^2 = -\frac{E_{HS} - E_{BS}}{\langle S^2 \rangle_{HS} - \langle S^2 \rangle_{BS}} \tag{3.14}$$

where E_{HS} and E_{BS} refer to the energies of the HS and BS spin states and $\langle S^2 \rangle_{HS}$ and $\langle S^2 \rangle_{BS}$ are the respective spin expectation values. However, it is important to emphasise that the Yamaguchi formula has been derived for the spin contamination of a BS *singlet* state (i.e. a system with two electrons at two magnetic centres). It is less well defined for higher multiplet systems or structures that extend beyond a spin dimer geometry. As a result, whilst Eq. 3.14 has been applied in the evaluation of the exchange interactions in Chapters 4, 5 and 6, for the 2D polymeric metal phthalocyanine sheets, in which calculation of the magnetic coupling necessitates a (2×2) supercell, the energies have not been spin decontaminated. However, spin contamination in transition metal systems is often small and, therefore, it is unlikely that the exclusion of decontamination procedures will result in significant errors final results.

4

The Magnetic Coupling in CoPc and CuPc

In Chapter 1, the magnetic behaviour of transition metal phthalocyanines was discussed. In particular, α-phase cobalt (II) phthalocyanine (α-CoPc) was shown to exhibit exceptionally strong AFM coupling with an evaluated $J/k_B \simeq -100\,\mathrm{K}$ [93]. This contrasted with the coupling measured for the β-phase polymorph (β-CoPc) in which a value of $J/k_B = -1.5\,\mathrm{K}$ was reported [95], suggesting that the strength of the coupling is significantly affected by the stacking geometry of the chain. In addition to this, the coupling interactions measured in both the α and β-phase polymorphs of CuPc - the other spin, $S = 1/2$ first row TMPc - were very weak, with exchange strengths of $J/k_B = -1.2\,\mathrm{K}$ and $J/k_B = 0.0\,\mathrm{K}$, respectively [53]. This is despite the fact that the chain geometries in both systems are identical for each polymorph. Thus, the conclusion that can be drawn from this observation is that the electronic configuration (and in particular the specific singly occupied molecular orbital (SOMO) of each system) plays a crucial role in the strength of the intrachain coupling. For CoPc, the SOMO is a d_{z^2}-derived a_{1g} MO that protrudes out of the plane of the molecule, whilst for CuPc the respective SOMO is a $d_{x^2-y^2}$-derived b_{1g} MO, spatially distributed within

the molecular plane. Consequently, it may be hypothesised that the out-of-plane shape of the CoPc a_{1g} SOMO facilitates a strong KE interaction (see Sec. 3.1.1) whereby the single electrons on adjacent molecules align antiparallel so as to minimise Pauli repulsion and maximise orbital-orbital overlap. In CuPc, the in-plane geometry of the b_{1g} SOMO does not yield any significant orbital overlap resulting in a suppression of the KE interaction. In addition, the increase in the metal-metal distance observed when transitioning from α-CoPc to β-CoPc decreases orbital overlap, also suppressing the strength of the KE interaction. In order to assess the validity of this mechanistic hypothesis, the energy components of the KE interaction can be evaluated for each respective system using single determinant electronic structure methods.

The remainder of this chapter is order as follows: in Sec. 4.1 theoretical information related to the evaluation of the magnetic interactions is outlined; in Sec. 4.2 the computational details used in subsequent calculations is discussed; Sec. 4.3 and Sec. 4.4 present the results related to the single molecule and periodic chains, respectively; finally in Sec. 4.5, conclusions of the chapter are drawn. It is important to highlight that some information within this chapter, including figures and results, has been adapted from a previously published article by the author [184].

4.1 Theoretical Background

The KE interaction may be characterised through the terms of the Hubbard Hamiltonian [172], given by

$$\hat{H} = -t \sum_{\sigma} \sum_{\langle i,j \rangle} (c^{\dagger}_{i\sigma} c_{j\sigma} + h.c) + U \sum_{i} \hat{n}_{i\uparrow} \hat{n}_{i\downarrow} \tag{4.1}$$

where the terms of the Hamiltonian are defined in the previous chapter. As outlined in Sec. 3.4.3, when $U >> t$, the coupling strength arising from *only* the KE interaction is given by,

$$J^{KE} = -\frac{4t^2}{U} \tag{4.2}$$

Both parameters may be extracted from the single particle periodic dispersion spectrum. Using a tight-binding model, t may be approximated as

$$t = \frac{W}{4} \tag{4.3}$$

where W is the width of the magnetic band in the FM configuration. The on-site repulsion, U is obtained by evaluating the energy difference between the occupied and unoccupied bands with each energy taken at the Γ-point.

Whilst J^{KE} relates to the energy arising only from the KE interaction between two magnetic orbitals, it is also important to evaluate the total exchange energy of the system. This value will not only include energy terms from the KE interaction, but also those related to all other exchange effects, including DE and SP. As outlined in Sec. 3.5, within single determinant methodologies, the AFM configuration may be modelled using a BS method in which single electrons of opposite spin are localised onto each alternating metal centre within the periodic chain. In order to obtain this configuration, a dimeric unit cell is adopted. Using the spin-decontaminated mapping strategy given by Eq. 3.14, with $N = 2$, $z = 2$ and $m = 1/2$, the total exchange energy of the chain system is given by

$$J^{BS} = -\frac{E_{HS} - E_{BS}}{\langle S^2 \rangle_{HS} - \langle S^2 \rangle_{BS}} \tag{4.4}$$

where E_{HS} and E_{BS} are the total DFT energies of the HS and BS determinants, and $\langle S^2 \rangle_{HS}$ and $\langle S^2 \rangle_{BS}$ are the respective spin expectation values. The superscript of J^{BS} indicates that it is evaluated using the BS method.

4.2 Computational Details

All-electron spin-polarised DFT calculations are carried out using the CRYSTAL23 [141] solid-state simulation package. Atom centred local gaussian basis sets of double-ζ quality with an additional set of polarisation functions (DZVP) are employed to describe all atoms in each of the systems studied (see Appendix A). The B3LYP global hybrid exchange DF [120, 129] is used. Hybrid exchange functionals have been shown to accurately describe both semiconductor materials with narrow band gaps [185] and correlated systems consisting of localised electrons [186]. Indeed, a number of theoretical studies investigating the magnetic properties of TMPc systems [76, 91, 93, 94] have made use of the B3LYP DF. Although London dispersion forces are believed to play an important role in the intrachain stacking of the molecules, the Grimme pairwise dispersion correction [187–189] - the only dispersion correction available in CRYSTAL - has been previously reported to overestimate the intermolecular forces arising from $\pi - \pi$ stacking interactions [94]. As a result, no dispersion corrections are included. Instead, for each studied system, the available crystal data is used to construct structural models on which single point energy (SPE) calculations are

performed, rendering intrachain geometry optimisations unnecessary. Both single molecule coordinate optimisations and SPE self-consistent field (SCF) calculations are converged to an iterative energy difference of 10^{-7} Ha. Both the Coulomb and exchange integral overlap tolerances are set to 10^{-8}. The convergence of the SCF procedure is expedited by mixing in 30% of the Hamiltonian matrix from the previous cycle into the updated matrix. Additionally, the direct inversion of the iterative subspace (DIIS) convergence accelerator scheme [190, 191] is used[1]. The sampling of k-points in the FBZ is carried out according to the Monkhorst-Pack method [192], making use of a reciprocal space shrinking factor of 10 [193]. This provides a reasonable accuracy to the first-principles calculations without requiring excessive computational resources. The MAE for each system is evaluated using the second variational approach. Here, the SOC interaction is treated as a perturbation to the scalar-relativistic wavefunction [166]. The two-component self-consistent field (2c-SCF) functionality implemented in CRYSTAL23 [167, 194–197] is used to carry out this procedure. The SOC effects are accounted for through the use of sets of "shape consistent" fully

[1]For more information, please refer to Appendix B.2.

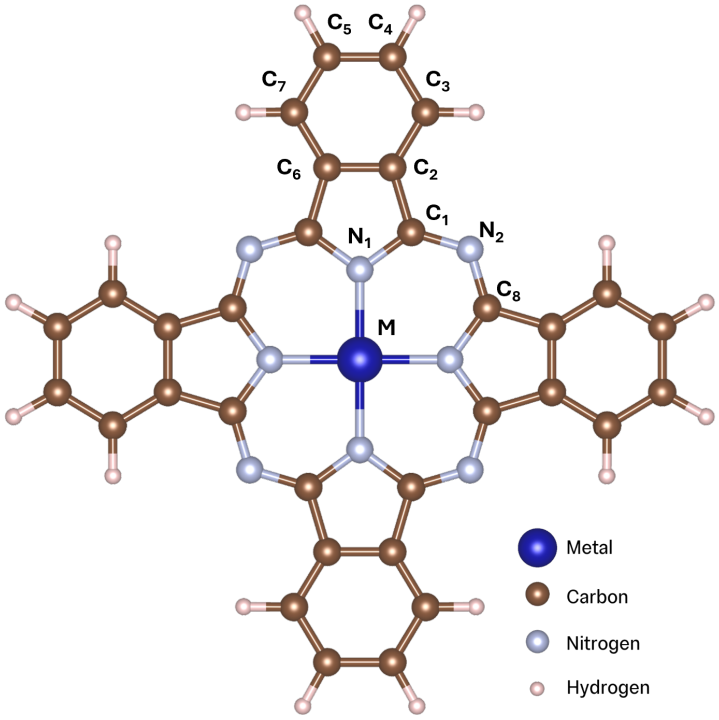

Figure 4.1: Geometry of a metal phthalocyanine molecule with labelled atoms. Atom colours refer to those defined in Fig. 1.2(b). Figure reproduced from Ref. [46] with permission from the authors.

relativistic effective core potentials [198–204]. The dispersion spectrum is evaluated using the CRYSTAL properties executable and visualised with a python-based package [205]. Spin density isosurface plots are generated using the VESTA3 visualisation program [206]. All computations presented in this chapter, as well as the subsequent chapters of this work, are carried out using the Imperial College Research Computing facilities at Imperial College London [207]. Access was granted via internal research computing support.

4.3 Single Molecules

Initial coordinates for the single molecule structure of CoPc are obtained from a deposit on the Cambridge Structural Database (CSD), generated by way of x-ray diffraction measurements of β-phase copper (II) phthalocyanine (CuPc) [208]. For CoPc, the structure is modified, replacing the central Cu for Co.

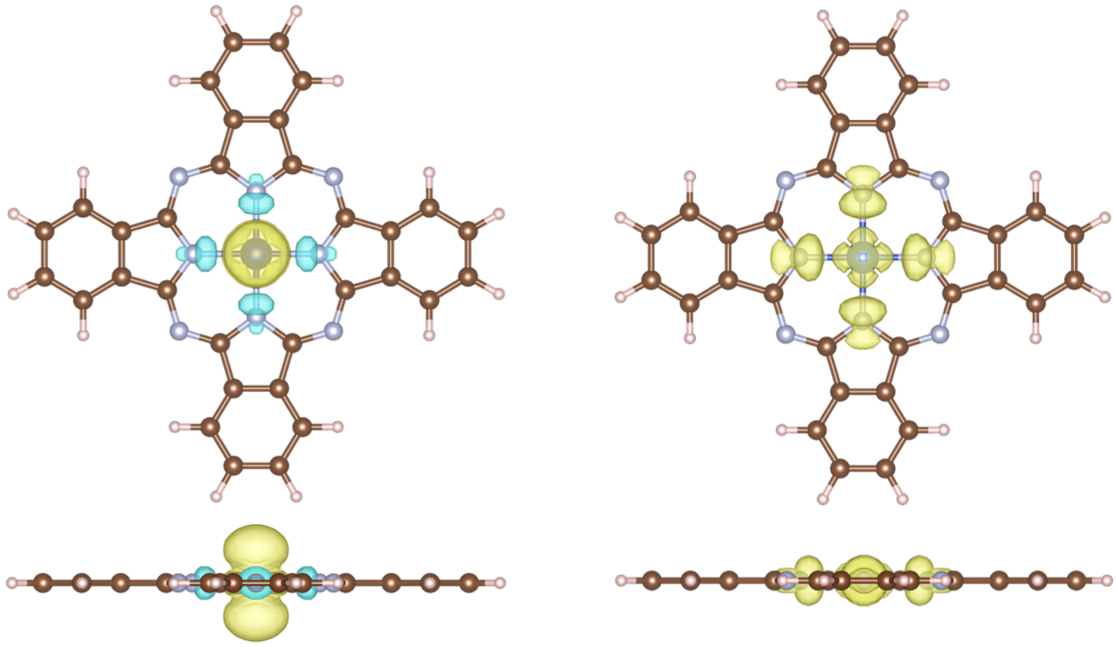

(a) (b)

Figure 4.2: Spin density isosurface plot for the single molecule of (a) CoPc and (b) CuPc. An isovalue of $0.001\,|e|\,\text{Å}^{-3}$ is used. Yellow (blue) shading indicates regions of up-spin (down-spin) electron density.

Bond Lengths			
Label	Calc. [Å]	Exp. [Å]	% Error
M-N1	1.928	1.910	0.94
N1-C1	1.379	1.384	0.36
C1-N2	1.322	1.320	0.14
C1-C2	1.456	1.454	0.13
C2-C3	1.396	1.395	0.06
C3-C4	1.394	1.393	0.07
C4-C5	1.409	1.394	1.07
C2-C6	1.403	1.398	0.36
Bond Angles			
Label	Calc. [°]	Exp. [°]	% Error
M-N1-C1	126.4	127.5	0.88
N1-C1-N2	127.6	127.0	0.45
C1-N2-C8	122.0	122.1	0.08

Table 4.1: Optimised bond lengths and angles (Calc.) for single molecule CoPc, with respective experimental (Exp.) bond lengths and angles obtained from Ref. [209]. Labels refer to those defined in Fig. 4.1.

4.3.1 CoPc

Following the relaxation of the internal coordinates, a planar molecule of D_{4h} symmetry is obtained. The complete set of structural data is shown in Table 4.1. The cobalt-nitrogen ($\mathrm{Co}-\mathrm{N}$) bond lengths are found to be $1.928\,$Å, whilst respective x-ray powder diffraction measurements report a value of $1.910\,$Å [209]. This represents an error of 0.94%. Additionally, the bonding angles defining the shape of the inner phthalocyanine ring are also in agreement with experimental data [209], with the largest error over the three measured angles being 0.88%. With regards to the structure of the outer portion of the complex, close agreement is observed between the calculated bond distances and respective experimental data [209].

Having established an optimised molecular geometry, analysis of the electronic structure of CoPc is subsequently conducted. Due to the equatorial bonding between the metal ion and coordinating nitrogens, the energy of the b_{1g} MO is raised by the crystal field, such that only the a_{1g}, e_g and b_{2g} MOs are occupied first. As a result, the d^7 configuration is expected

Atom	Charge [|*e*|]	Spin [|*e*|]
M	25.599	1.035
N1	7.775	0.000
N2	7.431	0.002
C1	5.620	-0.004
C2	5.939	-0.001
C3	6.119	-0.001
C4	6.091	0.000

Table 4.2: Mulliken population analysis for the charge and spin density in single molecule CoPc. Labels refer to those defined in Fig. 4.1.

Atomic Orbital	Charge [|*e*|]	Spin [|*e*|]
d_{z^2}	1.007	0.954
d_{xz}	1.931	0.011
d_{yz}	1.931	0.011
$d_{x^2-y^2}$	0.691	0.050
d_{xy}	1.951	0.004

Table 4.3: Mulliken population analysis of the spin and charge density for the d AOs in single molecule CoPc.

to form a low-spin complex with total spin, $S = 1/2$. The ground state of the system is found to be ${}^2A_{1g}$, with an unpaired electron residing within the a_{1g} MO. As shown in Table 4.4, taking into account the aforementioned energetic displacement of the b_{1g} MO, the two alternative configurations, in which the single electron resides within the e_g or b_{2g} MOs, are found to be $1.3\,\mathrm{eV}$ and $1.6\,\mathrm{eV}$ higher in energy, respectively. Examination of the AOs constituting the singly occupied a_{1g} eigenstate reveals a dominant contribution from the $3d_{z^2}$ AO of the central Co^{2+} ion alongside limited additional involvement from the coordinating nitrogen (N_1 in Fig. 4.1) p_y and p_x AOs. From analysis of the Mulliken population, the net charge on the central Co atom is shown to be $+1.411\,|e|$ (see Table 4.2), differing from the formal charge of $+2.0\,|e|$. The divergence between these two values highlights the limits of a purely ionic treatment of metal-ligand coordination and indicates that the bonding exhibits a degree of covelancy. In addition to this, MPA reveals $+0.691\,|e|$ localised within the $3d_{x^2-y^2}$ AO, which is formally empty according to the ionic model (see Table 4.3). Previous theoretical evaluations of molecular CoPc have also highlighted the role that

State	Configuration	Relative Energy [eV]
$^2A_{1g}$	$(a_{1g})^1(e_g)^4(b_{2g})^2$	0.0
^2E_g	$(a_{1g})^2(e_g)^3(b_{2g})^2$	1.3
$^2B_{2g}$	$(a_{1g})^2(e_g)^4(b_{2g})^1$	1.6

Table 4.4: Energies of the three electronic configurations in CoPc relative to the ground $^2A_{1g}$ state.

metal-ligand hybridisation plays, evidencing significant anisotropic interactions along the $\mathrm{Co}-\mathrm{N}$ coordinating axes [210]. Regarding the charge density of the ligand structure, MPA indicates an accumulation on the isoindole (N_1) and "bridging" (N_2) nitrogens with values of $-0.775\,|e|$ and $-0.431\,|e|$ respectively, whilst a slight deficit ($+0.380\,|e|$) is present on the carbon pertaining to the inner portion of the ring structure (C_1). The outer components of the ring structure (C_2, C_3 and C_4) present notably smaller magnitudes of charge relative to that of the inner ring. Analysis of the spin density of the system indicates that a population of $+1.035\,|e|$ is localised on the Co^{2+} ion. Inspection of the AO composition of the metal spin density reveals that 92% of this total spin resides within the $3d_{z^2}$ orbital with a population of $+0.954\,|e|$. The singly occupied a_{1g} MO aligns perpendicular to the the molecular plane and, as a result, there is no significant hybridisation between with surrounding ligand-derived MOs. This is also reflected in the negligible spin density population distributed amongst the ligand components (see Table 4.2).

The relative distribution of the eigenstates is depicted in Fig. 4.3(a). The HOMO and LUMO are ligand derived with a_{1u} and e_g symmetry, respectively. The energy gap separating these two electronic levels is measured to be $1.99\,\mathrm{eV}$, in good agreement with respective experimental data that carried out UV-Vis spectroscopic analysis of thin films of CoPc and reported a Q-Band ($n \rightarrow \pi^*$) of $2.10\,\mathrm{eV}$ [57]. The occupied ($a_{1g\uparrow}$) and unoccupied ($a_{1g\downarrow}$) MOs are found $3.26\,\mathrm{eV}$ below and $3.15\,\mathrm{eV}$ above the HOMO, respectively. Evaluation of the difference between these two energy levels yields an estimation of the on-site Coulombic repulsion, $U = 6.41\,\mathrm{eV}$, in good agreement with theoretical DFT+U calculations carried out in Ref. [211], in which a value of $U = 6.0\,\mathrm{eV}$ was found to best fit experimental structural and valence band data for the single molecule. Additionally, the value is consistent with hybrid exchange DFT calculations of single molecule CoPc, carried out by Ref. [94], who calculated a $U \sim 6.0\,\mathrm{eV}$. The relatively large magnitude of U reflects the degree of localisation of the SOMO and offers an explanation as to the stability of the $^2A_{1g}$ ground state, relative to other possible electronic configurations (see Table 4.4).

4.3.2 CuPc

Following a complete optimisation of the single molecule coordinates of CuPc, a planar D_{4h} system is obtained. A full set of geometrical data is presented in Table 4.5. The co-ordinating copper-nitrogen ($\mathrm{Cu}-\mathrm{N}$) bond lengths are found to be 1.956 Å, with respective experimental measurements from x-ray diffraction data reporting a value of 1.939 Å [208]. This represents a percentage error of 0.88%. Furthermore, the bonding angles associated with the structure of the central cavity are in good agreement with experimental data [208], with the largest error over the three measured angles being 0.66%. Close agreement is also found between evaluated and experimentally obtained bonding distances associated with the ligand system, with a maximum error of 1.53%.

Having defined an accurate single molecule geometry for CuPc, the electronic structure of the system is subsequently analysed. A $^2B_{1g}$ ground state is obtained, with the single unpaired electron residing within a $d_{x^2-y^2}$-derived b_{1g} MO. As discussed above, the D_{4h} crystal field raises the b_{1g} MO in energy such that the remaining d-derived MOs will occupy first. As a result of the d^9 electronic state of Cu^{2+}, the a_{1g}, e_g and b_{2g} MOs are expected

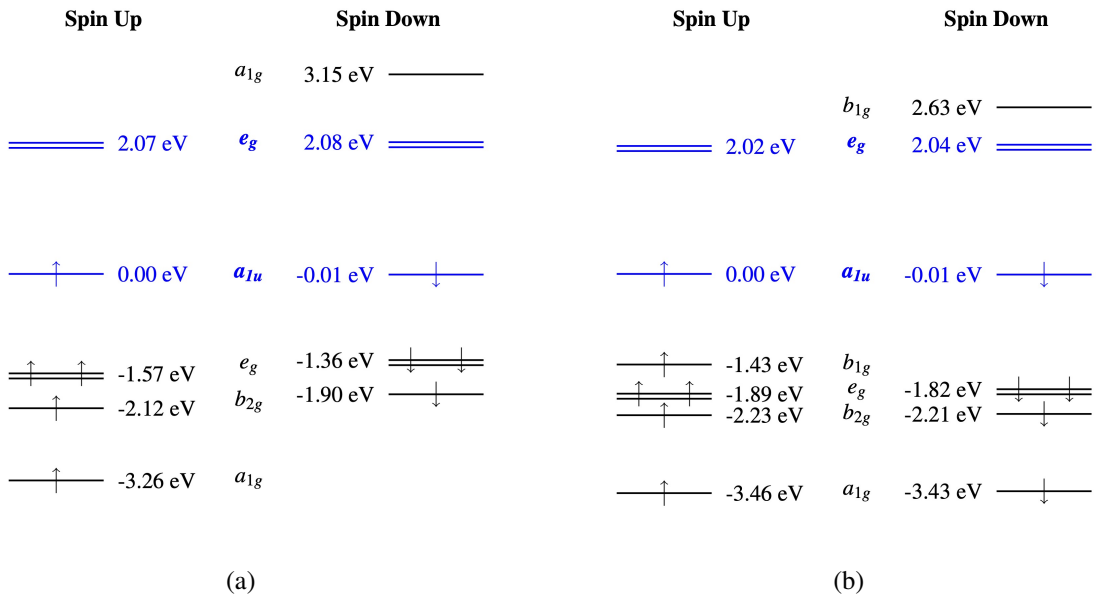

Figure 4.3: Diagrammatic representation of the eigenvalues of the fronter MOs for (a) single molecule CoPc and (b) single molecule CuPc. Black plain-text labels refer to the d-derived MOs, whilst blue bold-text labels refer to the ligand derived MOs. Note that in (a) the b_{1g} MOs are energetically positioned above the unoccupied a_{1g} MO and are omitted for clarity. Fig. 4.3(a) reproduced from Ref. [184] with permission from the authors.

Bond Lengths			
Label	Calc. [Å]	Exp. [Å]	% Error
M-N1	1.956	1.939	0.88
N1-C1	1.375	1.351	1.78
C1-N2	1.326	1.335	0.67
C1-C2	1.459	1.468	0.61
C2-C3	1.396	1.375	1.53
C3-C4	1.394	1.397	0.21
C4-C5	1.409	1.414	0.35
C2-C6	1.406	1.410	0.28
Bond Angles			
Label	Calc. [°]	Exp. [°]	% Error
M-N1-C1	125.9	125.6	0.24
N1-C1-N2	127.7	127.6	0.06
C1-N2-C8	123.0	122.2	0.66

Table 4.5: Optimised bond lengths and angles (Calc.) for single molecule CuPc, with respective experimental (Exp.) bond lengths and angles obtained from Ref. [208]. Labels refer to those defined in Fig. 4.1.

to be fully occupied, with the remaining single electron populating the b_{1g} MO. Through examination of the AO contributions to the b_{1g} SOMO, the metal $3d_{x^2-y^2}$ AO is found to dominate the composition with a spin density of $+0.636\,|e|$ (see Table 4.7). However, as shown in Table 4.6, the isoindole nitrogens (N_1 in Fig. 4.1) also exhibit a non-negligible degree of spin polarisation. Indeed, the sum of polarisation of these four nitrogens is $+0.360\,|e|$, which in conjunction with the polarisation of the metal $d_{x^2-y^2}$ AO, account for 99% of the total spin density. This is to be expected given the alignment of the b_{1g} SOMO along the metal-nitrogen bonding axes, thereby facilitating extensive hybridisation between the two sets of AOs. Through MPA, a charge of $+1.55\,|e|$ on the central Cu atom is evaluated. As observed before in CoPc, there is a discrepancy between the charge calculated from population analysis and the formal $+2.0\,|e|$ charge anticipated according to an ionic model, again, suggestive of a degree of covelancy in the copper-ligand coordination.

Fig. 4.3(b) depicts the energetic distribution of the frontier orbitals for molecular CuPc. As before, the HOMO and LUMO are ligand derived with a_{1u} and e_g symmetry, respectively. The energy gap between the two MOs is measured to be $2.02\,\mathrm{eV}$, in good agreement with

Atom	Charge [|*e*|]	Spin [|*e*|]
M	27.447	0.641
N1	7.815	0.090
N1	7.434	0.002
C1	5.617	-0.005
C2	5.936	0.005
C3	6.123	0.000
C4	6.090	-0.001

Table 4.6: Mulliken population analysis for the charge and spin density in single molecule CuPc. Labels refer to those defined in Fig. 4.1.

Atomic Orbital	Charge [|*e*|]	Spin [|*e*|]
d_{z^2}	1.983	0.000
d_{xz}	1.973	0.002
d_{yz}	1.973	0.002
$d_{x^2-y^2}$	1.399	0.636
d_{xy}	1.964	0.002

Table 4.7: Mulliken population analysis of the spin and charge density for the d AOs in single molecule CuPc.

a UV-Vis spectroscopic study of thin films of CuPc, that reported a Q absorption band between $550 - 750\,\mathrm{nm}$, with a maximum at $\sim 600\,\mathrm{nm}$, corresponding to $\sim 2.0\,\mathrm{eV}$ [212]. The occupied and unoccupied b_{1g} MOs are found $1.43\,\mathrm{eV}$ below and $2.63\,\mathrm{eV}$ above the HOMO respectively. Evaluation of the difference in energy between these two eigenvectors yields $U = 4.06\,\mathrm{eV}$. This value is approximately $2\,\mathrm{eV}$ lower in energy than that of CoPc, reflecting the more extensive hybridisation and resulting diffusion of the CuPc SOMO.

4.4 Periodic Chains

In order to analyse the long range magnetic ordering and electronic structure of the TMPc crystal systems, periodic chain structures are constructed. As outlined in Sec. 1.4, MPc systems crystallise into a 3D array of stacked chains, most commonly adopting a herringbone type arrangement [54], although brickstone packing arrangements have also been reported for CuPc [55]. However, the intrachain metal-metal distance is significantly shorter than that

of its interchain counterpart. Given the distance dependency of the exchange interaction, it is reasonable to hypothesise that the intrachain coupling will dominate the overall interaction. This is also supported by the hybrid exchange DFT study of CoPc carried out in Ref. [94]. As a result, the system required to study the exchange interactions in both CoPc and CuPc is simplified to a single periodic chain system. It is important to note that, as defined in Eq. 3.14, the total exchange interaction energy, J^{BS}, may also be calculated using a molecular dimer. However, this study aims to additionally measure the coupling strength arising from the KE interaction, J^{KE}. This quantity is evaluated using the parameters of the Hubbard Hamiltonian, applied in Eq. 4.2, which are extracted from the dispersion spectrum of the respective periodic chains. The remainder of this section is structured as follows: in Sec. 4.4.1 a detailed description of the unit cell for each system is provided; in Sec. 4.4.2 and Sec. 4.4.3 the results for the periodic chains of CoPc and CuPc, respectively, are presented.

4.4.1 Unit Cell

In order to offer a broad examination of both the CoPc and CuPc systems, the two primary polymorphic phases - the stable β-phase ($\phi \simeq 45°; \psi \simeq 45°$) and meta-stable α-phase ($\phi \simeq 65°; \psi \simeq 0°$) [213, 214] - are constructed and studied.[2] In accordance with x-ray diffraction measurements carried out in Ref. [209] (Ref. [214]), for thin film structures of CoPc (CuPc) the interplanar distance between consecutive molecules is 3.42 Å (3.42 Å). This corresponds to a metal-metal distance of 3.77 Å (4.84 Å) in the α-phase (β-phase). In order to utilise the BS method, a dimeric unit cell is constructed (see Fig. 4.4). The stacking axis of the chain is aligned along the c lattice parameter. The unit cell dimensions of the two polymorphic phases are displayed in Table 4.8. In order to minimise interactions between species in the lateral periodic direction, the dimeric molecular system is placed at the centre of a 60 Å^2 unit cell. For the β-polymorph, the molecular dimer is rotated $45°$ so

[2] Please refer to Chapter 1 for the definition of ϕ and ψ.

Polymorph	a [Å]	b [Å]	c [Å]	α [°]	β [°]	γ [°]
α-phase	60	60	7.54	90	65	90
β-phase	60	60	9.68	90	45	90

Table 4.8: Lattice parameters for the periodic single chain models of the two polymorphic phases of both CoPc and CuPc.

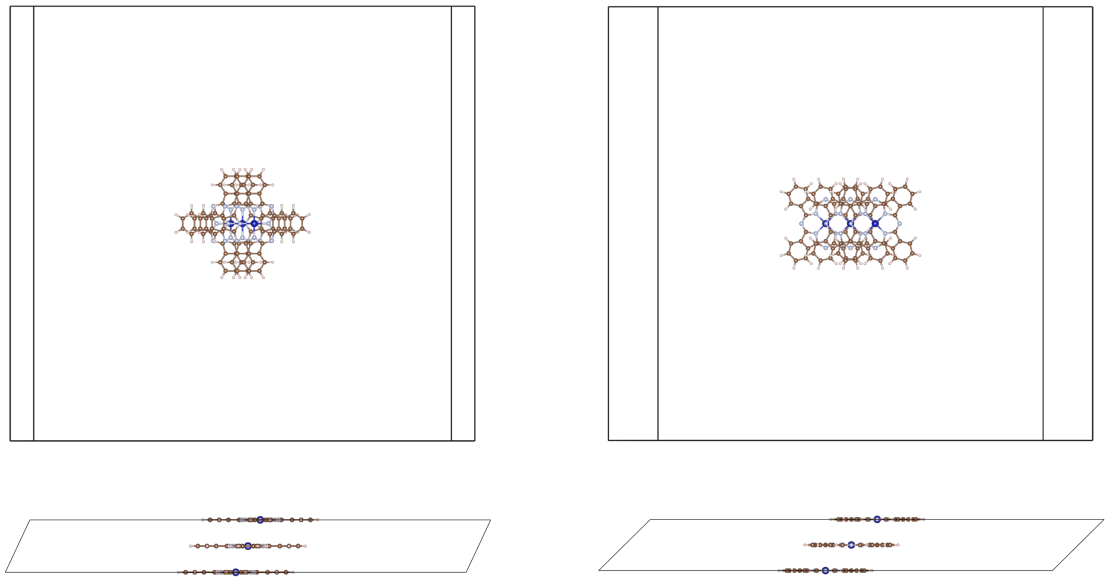

(a) (b)

Figure 4.4: Structural depiction of the dimeric unit cell for the (a) α-phase and (b) β-phase.

as to account for the respective sliding angle (see Fig. 4.4(b)). In all periodic chains of both CoPc and CuPc, the electronic states established in Sec. 4.3 ($^2A_{1g}$ and $^2B_{1g}$, respectively) are used as the initial guess to the density matrix.

4.4.2 CoPc

In Fig. 4.5 (Fig. 4.6), the band structure and spin density are depicted for the AFM and FM configurations for the α-polymorph (β-polymorph) of CoPc. Identification of the singly occupied magnetic bands is realised through analysis of the respective AO contributions. These bands are highlighted in the band plots. Spin density isosurfaces are plotted with an isovalue of $0.001\,|e|$ Å^3.

It is important to note that, the antiparallel (parallel) alignment of the electrons along the chain is captured in an AFM (FM) state, as indicated in respective spin density isosurface plots. For α-CoPc, in the AFM state, the spin density localised on contiguous cobalt centres is found to be of equal magnitude ($1.026\,|e|$) but opposite sign, whilst in the FM state, a spin density of both equal magnitude ($1.028\,|e|$) and sign is found. For β-CoPc, in the AFM state, the spin density on neighbouring cobalt centres is found to be of equal magnitude ($1.030\,|e|$) but opposite sign, whilst in the FM state, the spin density is found to be of both

System	J^{BS} [K]	J^{KE} [K]	J^{Exp} [K]	t [eV]	U [eV]
α-CoPc	-99.1	-176.5	-107.0 [93]	0.15	6.21
β-CoPc	-1.2	-0.6	-1.5 [95]	0.01	6.29
α-CuPc	-0.9	-0.0001	-1.2 [53]	0.0001	4.03
β-CuPc	0.03	-0.002	0.0 [53]	0.0005	4.07

Table 4.9: Full set of exchange energy data for the two polymorphic phases of CoPc and CuPc. J^{BS} refers to the coupling energies obtained using Eq. 4.4; J^{KE} refers to the coupling energies obtained using the values of t and U employed in Eq. 4.2; J^{Exp} refers to respective experimental data for each system.

equal magnitude ($1.029\,|e|$) and sign.

4.4.2.1 α-CoPc

In the α-polymorph of CoPc (α-CoPc), the up-spin (down-spin) band gap is measured to be $1.85\,\mathrm{eV}$ ($1.87\,\mathrm{eV}$)[3]. At the Γ-point ($k = 0$), the singly occupied a_{1g} bands are found at $3.51\,\mathrm{eV}$ below and $2.70\,\mathrm{eV}$ above the Fermi energy (E_F) respectively. Evaluation of the energy difference between the two bands yields an estimate of the on-site Coulombic repulsion, $U = 6.21\,\mathrm{eV}$, in close agreement with the approximation of U calculated from the single molecule energy spectrum. In comparison to the single molecule eigenvalues, both the occupied and unoccupied a_{1g} bands in α-CoPc are found to downwardly shift in energy. This is to be expected given the emergence of an overlap between the SOMOs of neighbouring molecules which acts to lower the respective energy of the eigenvector. Using Eq. 4.3, an estimate of the transfer integral, t, is calculated from the band structure of the FM configuration. The band width, W, of the unoccupied a_{1g} band is found to be $0.6\,\mathrm{eV}$, yielding a $t = 0.15\,\mathrm{eV}$.

With regards to the intrachain magnetic coupling, as outlined above, two distinct procedures are adopted. Using Eq. 4.4, a value of $J^{BS} = -99.1\,\mathrm{K}$ is found in close agreement with experimental data of Ref. [93], in which exchange energies of $J = -78\,\mathrm{K}$, $J = -80\,\mathrm{K}$ and $J = -107\,\mathrm{K}$ were reported for powdered, templated thin-film and non-templated thin-film structures of α-CoPc, respectively. The closer alignment of the evaluated value of J^{BS} with that of the thin-film structures is to be expected given that the respective system contains fewer defects, thereby aligning it more closely with the perfect (defect-free) pe-

[3]Unless specifically stated, band gap data is obtained from the lower energy configuration, whilst the Hubbard parameters are extracted from the FM state of each system.

riodic chain studied here. Additionally, hybrid exchange BS-DFT calculations carried out in Ref. [94], reported a value of $J = -85\,\mathrm{K}$. Here the discrepancy is likely attributed to differences in the respective basis sets.

Using the formalism derived in Eq. 4.2, an estimate of the KE coupling contribution was found with a value of $J^{KE} = -176.5\,\mathrm{K}$. There are clear discrepancies between J^{BS} and J^{KE} for α-CoPc. It is important to emphasise that J^{KE} only takes into account coupling interactions arising from KE pathways, whilst J^{BS} accounts not only for KE, but also for other exchange interactions, including DE. Therefore, the divergence between the two values could be indicative of a considerable DE interaction (approximately half the magnitude of that of the KE). As outlined in Chapter 3, DE acts to align electron spins parallel to one another and, therefore, would compete against KE and, as a result, reduce the magnitude

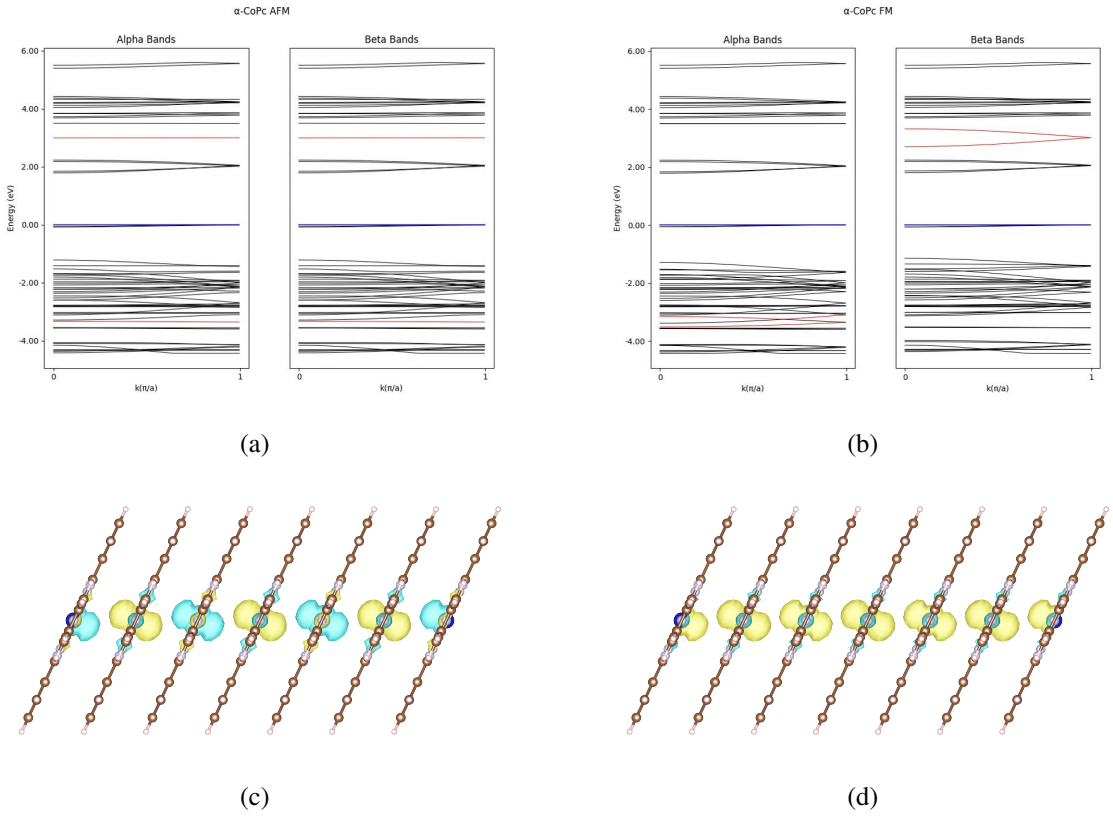

(a) (b)

(c) (d)

Figure 4.5: Plots of the (a) AFM and (b) FM band structures, and (c) AFM and (d) FM spin density isosurfaces for single chain structures of α-CoPc. In (a) and (b), the magnetic a_{1g} bands are highlighted in red. In (c) and (d), an isovalue of $0.001\,|e|\,\text{Å}^{-3}$ is used. Yellow (blue) shading indicates regions of up-spin (down-spin) electron density. Figs. 4.5(a) and 4.5(b) reproduced from Ref. [184] with permission from the authors.

of J^{BS} relative to that of J^{KE}. Alternatively, it is possible that hybridisation of the metal d_{z^2} AO with surrounding ligand orbitals of the inner-portion of the phthalocyanine ring could result in a broadening of the a_{1g} bands, and, thus, increase the computed value of t. Indeed, through inspection of the orbital contributions to the $a_{1g\downarrow}$ band, constructed in FM configuration, a considerable number of ligand AOs are observed. Nevertheless, the discrepancy between J^{KE} and J^{BS} evaluated for α-CoPc, highlights potential limitations in the use of the Hubbard Hamiltonian approach, at least from a quantitative perspective.

Using a second variational approach and employing Eq. 3.1, the MAE is evaluated for the system. Here, θ_0 and τ_0 define the z-cartesian direction which is normal to the molecular plane, whilst $E(\theta, \tau)$ is evaluated for $\theta = 90°$ and $\tau = 0°$[4]. A value of $39\,\mu\mathrm{eV}$ is calculated with an in-plane easy axis and out-of-plane hard axis. This aligns with expectations derived from the molecular electronic structure of CoPc, in which the unpaired electron occupies the d_{z^2}-derived a_{1g} MO[5]. Additionally, the result agrees with a previous theoretical calculation of the MAE of molecular CoPc, utilising a second variational approach, in which an in-plane easy axis was also identified with an anisotropy energy of $60\,\mu\mathrm{eV}$ [215].

4.4.2.2 β-CoPc

The up-spin (down-spin) band gap in the β-CoPc is measured to be $1.91\,\mathrm{eV}$ ($1.93\,\mathrm{eV}$). As with α-CoPc, the band gap of β-CoPc closely aligns with the HOMO-LUMO gap of molecular CoPc, with discrepancies between the two being attributable to intrachain interactions between neighbouring molecules. At the Γ-point, the occupied (unoccupied) a_{1g} band is found $3.18\,\mathrm{eV}$ below ($3.11\,\mathrm{eV}$ above) E_F. Evaluation of the energy between these two bands yields a value of $U = 6.29\,\mathrm{eV}$. Relative to the on-site repulsive term extracted from the band structure of α-CoPc, the value obtained for the β-polymorph more closely agrees with that of the single molecule CoPc ($U = 6.41\,\mathrm{eV}$). The increased overlap and resulting delocalisation of the a_{1g} SOMOs in the α-polymorph likely serves to reduce the energy penalty associated with double occupation of the orbitals (relative to β-CoPc). Nevertheless, it is important to note, that despite this delocalisation, the a_{1g} SOMOs in both polymorphs remain very much localised to their respective metal centres. Employing Eq. 4.3, an estimate of the transfer integral is obtained from the width of the FM unoccupied magnetic band which is measured to be $W = 0.04\,\mathrm{eV}$, yielding a value of $t = 0.01\,\mathrm{eV}$.

[4]For all MAE calculations carried out in this report, the same set of angles are adopted.

[5]The d_{z^2} AO has a z-projected orbital angular momentum number, $m_l = 0$. Therefore, there is no energetic stabilisation gained by the system aligning the magnetic axis perpendicular to the plane of the molecule and consequently, the system is expected to exhibit an in-plane easy axis.

A significant decrease in the magnitude of this value is observed relative to its α-phase counterpart, indicating a marked reduction in the likelihood of an electron transfer event. Given the intrinsic relationship between the magnitude of t and the respective SOMO overlap, this difference is to be expected. In the α-phase, the $\mathrm{Co}-\mathrm{Co}$ distance is $3.77\,\text{Å}$, whilst in the β-phase it is $4.84\,\text{Å}$.

Employing the formula derived in Eq. 4.4, an evaluation of the total exchange energy is computed, yielding a value of $J^{BS} = -1.2\,\mathrm{K}$, in good agreement with the AFM exchange strength of $J = -1.5\,\mathrm{K}$ reported by Ref. [95], who fit $Mvs.H$ data for β-CoPc using the Bonner-Fisher model. The significant reduction in J^{BS} in the β-phase (relative to the α-polymorph) is to be expected given the increased $\mathrm{Co}-\mathrm{Co}$ distance. This results in a reduced SOMO overlap and a commensurate decrease in the energy stabilisation gained from MO delocalisation. This is also supported in the evaluation of the KE contribution using the formula derived in Eq. 4.2, which yields a value of $J^{KE} = -0.68\,\mathrm{K}$. The discrepancy between J^{BS} and J^{KE} indicates that, whilst the coupling in β-CoPc is weak,

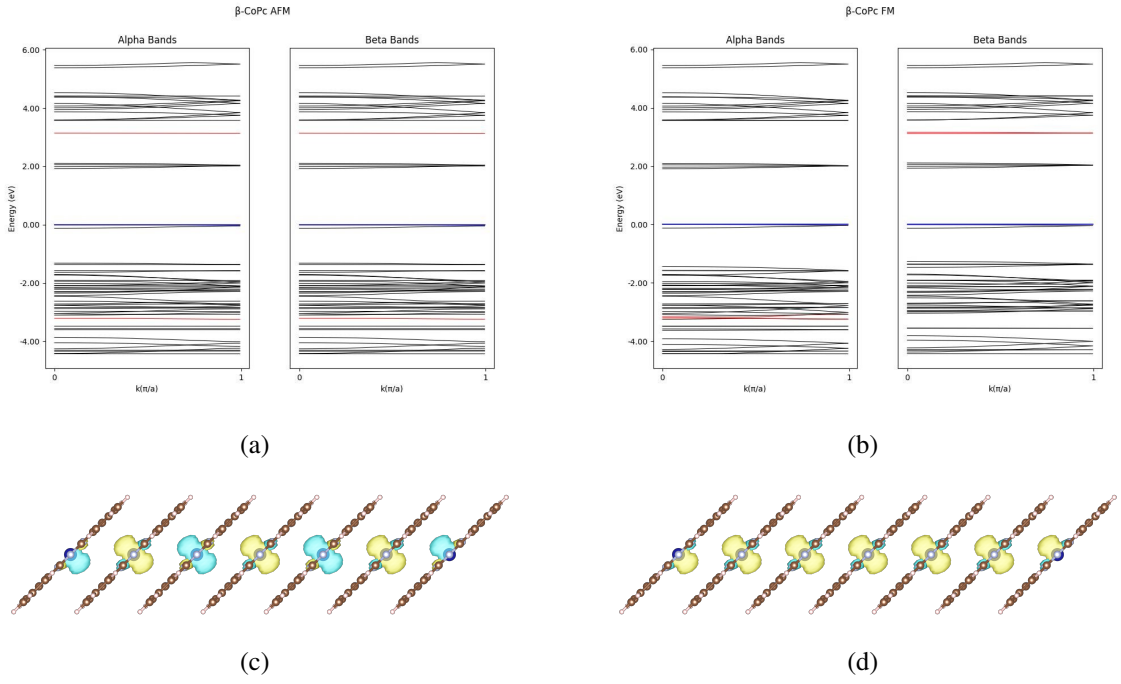

Figure 4.6: Plots of the (a) AFM and (b) FM band structures, and (c) AFM and (d) FM spin density isosurfaces for single chain structures of β-CoPc. In (a) and (b), the magnetic a_{1g} bands are highlighted in red. In (c) and (d), an isovalue of $0.001\,|e|\,\text{Å}^{-3}$ is used. Yellow (blue) shading indicates regions of up-spin (down-spin) electron density. Figs. 4.6(a) and 4.6(b) reproduced from Ref. [184] with permission from the authors.

it can not be entirely accounted for by KE contributions and other exchange pathways may also be present within the system.

Finally, the MAE is evaluated for β-CoPc using a second variational approach, and employing the formula derived in Eq. 3.1. The results indicate an MAE of $40\,\mu\mathrm{eV}$ with an in-plane easy axis and out-of-plane hard axis. The finding is in accordance with expectations derived from the molecular electronic configuration in which the single electron resides within a d_{z^2}-derived MO. Furthermore, the value agrees with the previously cited theoretical evaluation of the MAE of molecular CoPc, in which an MAE of $60\,\mu\mathrm{eV}$ was reported [215].

4.4.3 CuPc

In Fig. 4.7 (Fig. 4.8), plots of the band structure and spin density isosurfaces are depicted for the AFM and FM configurations of the α-polymorph (β-polymorph). Once again, the respective magnetic bands are identified by analysis of AO contributions and highlighted in the plots. The spin density isosurfaces are plotted using an isovalue of $0.001\,|e|\,\mathrm{Å}^3$.

Once again, the antiparallel (parallel) configuration of the single electrons is captured in an AFM (FM) state. In α-CuPc, analysis of the electron density indicates that, in the AFM state, a spin of equal magnitude ($0.638\,|e|$), but opposite sign is located on neighbouring copper atoms, whilst in the FM state, a spin of equal magnitude ($0.638\,|e|$) and sign is found on each copper centre. In β-CuPc, in the AFM state, a spin of equal magnitude ($0.643\,|e|$), but opposite sign is localised on contiguous coppers, whilst in the FM state a spin of equal magnitude ($0.643\,|e|$) and sign is found on the respective metal centres.

4.4.3.1 α-CuPc

In the α-polymorphic phase of CuPc, the up-spin (down-spin) band gap is found to be $1.74\,\mathrm{eV}$ ($1.74\,\mathrm{eV}$). At the Γ-point, the singly occupied b_{1g} magnetic bands are found $1.53\,\mathrm{eV}$ below and $2.50\,\mathrm{eV}$ above E_F. Evaluation of the energy difference between these two bands results in a value of $U = 4.03\,\mathrm{eV}$. This value is in good agreement with the on-site repulsion calculated for the single CuPc molecule ($4.06\,\mathrm{eV}$). Employing Eq. 4.3, the transfer integral, t, is evaluated from the width of the FM unoccupied magnetic band, yielding a value of $t = 0.0001\,\mathrm{eV}$. This value is significantly lower than the quantities extracted from the band structure of both polymorphs of CoPc. This is to be expected given the in-plane geometry of the b_{1g} SOMO, which prevents any meaningful orbital overlap along the chain.

Using the DFT energies of the FM and AFM states and employing Eq. 4.4, the exchange energy of the system is calculated, resulting in a value of $J^{BS} = -0.9\,\mathrm{K}$. This closely agrees with respective experimental data reported in Ref. [53], in which magnetic susceptibility measurements of the system were taken, finding a value of $J = -1.2\,\mathrm{K}$. There is a decrease in the magnitude of this quantity relative to the coupling strengths extracted from both polymorphs of CoPc, again highlighting the importance of the overlap between contiguous SOMOs in facilitating an AFM interaction along the chain.

Using the formalism derived in Eq. 4.2 alongside the Hubbard terms extracted from the band structure and referenced above, a value of $J^{KE} = -0.0001\,\mathrm{K}$ is calculated. The magnitude of this quantity is, again, reflective of the in-plane localisation of the SOMOs in CuPc. Additionally, the discrepancy between J^{BS} and J^{KE} indicates that the exchange interaction in α-CuPc does not proceed via a KE mechanism, but instead through other

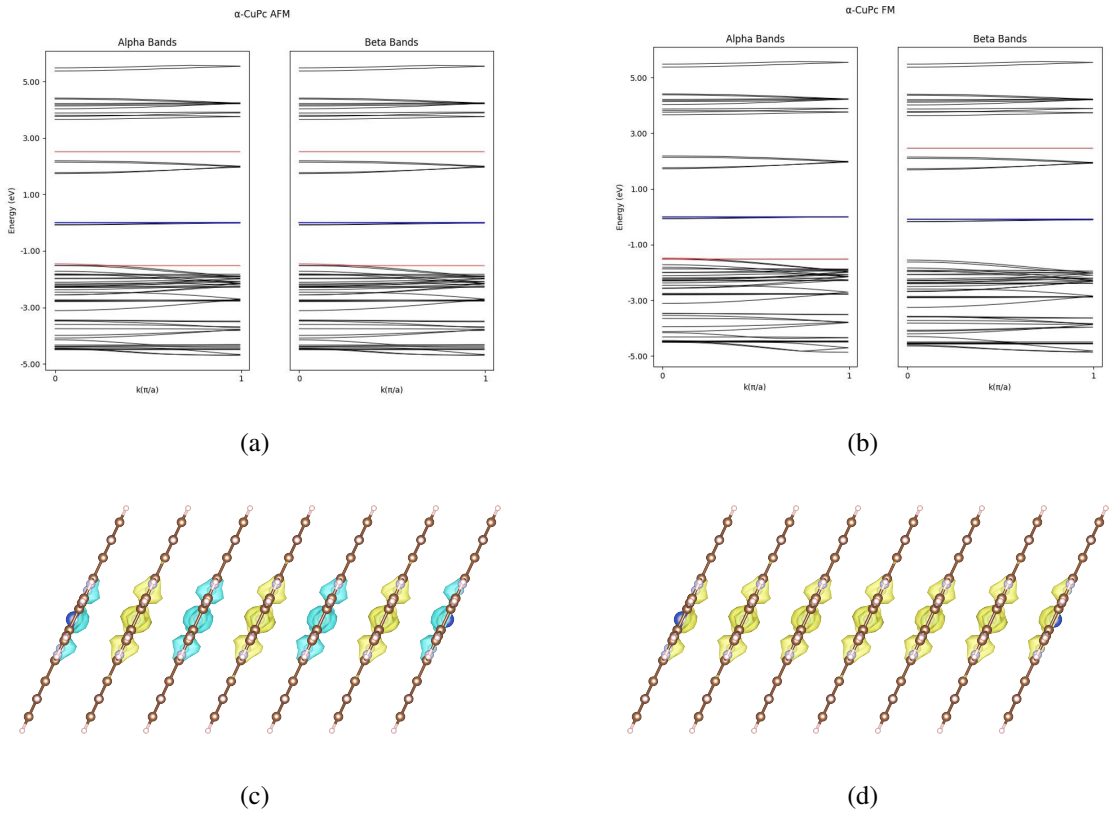

(a) (b)

(c) (d)

Figure 4.7: Plots of the (a) AFM and (b) FM band structures, and (c) AFM and (d) FM spin density isosurfaces for single chain structures of α-CuPc. In (a) and (b), the magnetic b_{1g} bands are highlighted in red. In (c) and (d), an isovalue of $0.001\,|e|$ Å^{-3} is used. Yellow (blue) shading indicates regions of up-spin (down-spin) electron density.

exchange pathways. Given the similarity in MO symmetry and geometrical distribution between the b_{1g} SOMO and frontier ligand derived MOs, it is possible that the coupling interaction (as measured by J^{BS}) occurs due to indirect exchange pathways involving spin polarisation of double occupied orbitals (see Chapter 3). It is important to note, however, that the coupling interaction in α-CuPc is weak, especially with respect to that of α-CoPc. Given the identical crystal chain geometries, the variance in the exchange strength between the two systems highlights the important role that the electronic configuration plays.

Finally, the MAE is evaluated for α-CuPc. As before, a second variational approach is adopted alongside employment of Eq. 3.1. An MAE of $-47\,\mu\mathrm{eV}$ is evaluated indicating an out-of-plane easy axis and in-plane hard axis. This accords with expectations derived from the single molecule electronic structure, in which the $d_{x^2-y^2}$-derived b_{1g} MO was singly occupied. The magnetic quantum number for the $d_{x^2-y^2}$ AO is $m_l = -2$, implying a directional projection of the orbital. As a result, there is an energy stabilisation gained by assuming an out-of-plane easy axis.

4.4.3.2 β-CuPc

In the β-polymorphic phase of CuPc, the up-spin (down-spin) band gap is found to be $1.85\,\mathrm{eV}$ ($1.89\,\mathrm{eV}$). At the Γ-point, the b_{1g} magnetic bands are found to be $1.46\,\mathrm{eV}$ and $2.61\,\mathrm{eV}$ below and above E_F. Calculation of the energy difference between these two bands yields a value of $U = 4.07\,\mathrm{eV}$. As with the α-polymorph, the U value obtained for β-CuPc is in close agreement with that evaluated for molecular CuPc. Utilising Eq. 4.3, an estimate of the transfer integral is obtained from the width of the FM unoccupied magnetic band, with a value of $t = 0.0005\,\mathrm{eV}$. Interestingly, this value is greater than that of the α-polymorph, despite the increase in the metal-metal distance in β-CuPc. To posit a possible explanation for this observance, one must examine the shape and distribution of the b_{1g} SOMO. As outlined in Sec. 4.3.2, the b_{1g} MO is derived from the Cu $3d_{x^2-y^2}$ AO with additional contributions from the $2s$ and $2p$ AOs of the isoindole nitrogens (N_1 in Fig. 4.1). As a result, the respective MO distributes along each of the four metal-nitrogen bonding axes. If consideration is now given to the respective stacking geometries in both the α and β-polymorphs, it is evident that, in the former system, overlap between contiguous SOMOs occurs along only one of the coordinating axes, whilst, in the latter system, due to the sliding angle, $\psi = 45°$, orbital-orbital overlap occurs between two of the isoindole nitrogens of each neighbouring molecule. It is possible that this overlap contributes more than that seen in the α-phase, despite the reduction in ϕ. However, the evaluated t values in both

polymorphs are extremely small (two orders of magnitude smaller than that of β-CoPc), indicative of negligible electron transfer between adjacent b_{1g} MOs.

Application of the total DFT energies of the two magnetic configurations to Eq. 4.4 yield a value of $J^{BS} = 0.03\,\mathrm{K}$, indicating a very weak FM state. Using Eq. 4.2 and the Hubbard parameters extracted from the dispersion spectrum, a value of $J^{KE} = -0.002\,\mathrm{K}$ is calculated. There is clear discrepancy between J^{BS} and J^{KE}, suggesting that the KE pathway is heavily suppressed in β-CuPc and is unlikely to contribute in a significant way to the overall coupling. Given this, it is more likely that the FM ordering, reflected in the evaluated value of J^{BS}, arises from a higher order, indirect exchange pathway, although the exact nature of this interaction is likely to be complex and beyond the investigative ability of monodeterminant methods. Furthermore, the magnitude of the value is small - an order of magnitude less than that of its α-phase counterpart. Therefore, in practice, β-CuPc may be understood to be paramagnetic, as indicated by $J^{Exp} = 0.0\,\mathrm{K}$ [53].

Finally an estimate of the MAE is calculated for β-CuPc. The second variational approach is used alongside Eq. 3.1. An evaluated MAE value of $-41.0\,\mu\mathrm{eV}$ is obtained,

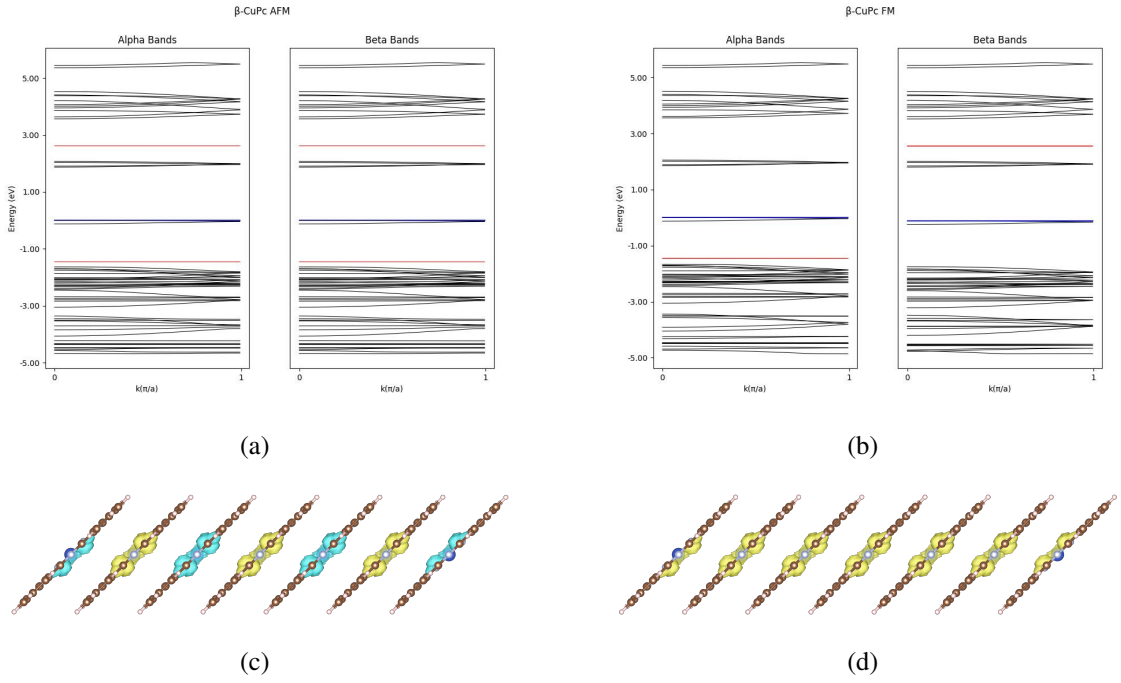

(a) (b)

(c) (d)

Figure 4.8: Plots of the (a) AFM and (b) FM band structures, and (c) AFM and (d) FM spin density isosurfaces for single chain structures of β-CuPc. In (a) and (b), the magnetic b_{1g} bands are highlighted in red. In (c) and (d), an isovalue of $0.001\,|e|$ Å^{-3} is used. Yellow (blue) shading indicates regions of up-spin (down-spin) electron density.

indicating an out-of-plane easy axis and in-plane hard axis, in good agreement with the respective MAE evaluated for α-CuPc.

4.5 Conclusions

In summation, a hybrid exchange BS-DFT methodology has been utilised to study periodic single chain structures of CoPc and CuPc. So as to encompass a broad range of the structural phase space, examination of both the α and β-phase polymorphs of each system was carried out. Previous experimental measurements of the magnetic susceptibility of the two systems evidenced exceptionally strong coupling in α-CoPc with a coupling strength $J = -107.0$ K [93]. This was reproduced well in the theoretical study reported here, with an evaluated $J^{BS} = -99.1$ K. Additionally, good agreement was found between the coupling strengths evaluated in this study for the remaining three systems (β-CoPc, α-CuPc and β-CuPc) and respective experimental data [53, 95]. The large variation in the magnitude of the coupling in α-CoPc and that of the other systems was hypothesised to be due to a strong KE interaction between the d_{z^2}-derived a_{1g} SOMOs of contiguous cobalt centres. The protrusion of the respective MOs perpendicular to the molecular plane facilitated a large overlap with neighbouring orbitals, which resulted in a significant energetic stabilisation gained by aligning their electron spins antiparallel to one another. By mapping the interaction to a Hubbard Hamiltonian and extracting t and U parameters from the dispersion spectrum, an estimate of the KE coupling strength, J^{KE} was determined. For α-CoPc, the value obtained ($J^{KE} = -176.5$ K) was larger than that of J^{BS} and, from this discrepancy, it was inferred that either a significant DE interaction could be present, which would serve to stabilise the parallel configuration and, thus, act to reduce the magnitude of the overall AFM coupling, or the magnitude of the transfer integral, t, was overestimated as a result of metal-ligand orbital hybridisation. A far weaker KE interaction was evaluated in the other studied systems, which was due to a significantly reduced overlap between neighbouring SOMOs. In β-CoPc, this reduction was attributed to an increase in the metal-metal distance between adjacent molecules, whilst in both polymorphs of CuPc, it was ascribed to the in-plane geometry of the $d_{x^2-y^2}$-derived b_{1g} SOMO. Furthermore, whilst agreement was found between the values of J^{BS} and J^{KE} in β-CoPc, indicating the likely dominance of a KE interaction, albeit one very weak in nature, in the two polymorphs of CuPc, the large discrepancy between the two sets of coupling values implied that the weak exchange interactions were due to alternative coupling pathways.

Thus, having attributed the exceptionally strong coupling in α-CoPc to a dominant KE interaction and established that the intensity of this coupling is related to both the electronic structure of the underlying molecular system and the respective intrachain geometry, subsequent steps may now be made to apply modifications with the intention of further increasing the strength of this AFM coupling.

5

The Magnetic Coupling in RhPc

In Chapter 4, a spin-polarised DFT methodology was used to analyse the electronic and magnetic properties of single chain structures of CoPc and CuPc. Evaluation of the coupling in this set of systems evidenced an exceptionally strong exchange interaction in α-CoPc with a calculated $J^{BS} = -99.1\,\mathrm{K}$. The underlying reasoning for this was assigned to a dominant KE interaction arising from the coupling between the out-of-plane a_{1g} SOMOs of neighbouring cobalt centres. This interaction was mapped to a Hubbard Hamiltonian and parametrised by a transfer integral term, t, and an on-site Coulombic repulsion term, U, with the magnitude of the resulting exchange term, J^{KE}, varying as a function of $4t^2/U$, indicating that an increase in the magnitude of J^{KE} could be realised through either an increase in t or a decrease in U. Given this, the following question can be posed: what modifications can be made to the CoPc system in order to facilitate the desired change in either t or U?

In the previous chapter, it was shown that, in going from β-CoPc ($\phi = 45°$) to α-CoPc ($\phi = 65°$), an increase in the relative overlap between neighbouring SOMOs is obtained,

resulting in an increase in t and a commensurate increase in J^{KE}. Therefore, possible geometrically related modifications could be envisaged in which neighbouring molecules are aligned in a cofacial configuration, resulting in the maximal SOMO overlap (provided there is no change in interplanar distance between contiguous molecules). This exact structure was previously reported on in Ref. [94], in which a theoretical treatment of the intrachain exchange interactions in CoPc, using BS hybrid exchange DFT, indicated an AFM coupling of $J/k_B \simeq -400\,\mathrm{K}$ in a cofacial configuration ($\phi = 90°$). However, it is not clear how the self-assembly of the CoPc molecules into this structural configuration could be induced without significant modifications of the chemical structure that may alter the electronic configuration.

The alternative approach would be to transform the system in such a way that a significant decrease in U could be realised without a change in the underlying electronic ground state. To this end, one could envisage the occupation of a more diffuse MO with the same SOMO symmetry as that of CoPc. A possible chemical modification to achieve this would be the replacement of the central Co^{2+} ion for its $4d$ counterpart, Rh^{2+}. It is hypothesised that, should rhodium (II) phthalocyanine (RhPc) exhibit the same $^2A_{1g}$ electronic configuration, then the occupation of a more diffuse $4d_{z^2}$-derived a_{1g} SOMO will result in a decrease in U and a resulting increase in the magnitude of J^{KE}.

It is important to note that the RhPc system discussed in this chapter is purely theoretical and there is no experimental data related to either the molecular system or the crystal structure[1] (although a number of rhodium (III) phthalocyanine based systems [217–220] have been reported in the scientific literature, in which axial ligation of the central metal is present). The aim of the study is to highlight the predictive capabilities of the Hubbard-based model, as described above, and show that specific and directed modifications to the CoPc system can be made in order to increase the strength of the AFM coupling.

The remainder of this chapter is organised as follows: in Sec. 5.1, an outline is given of the computational details used in this study; Sec. 5.2 presents the results related to the RhPc single molecule structure; the periodic single chain RhPc systems are detailed in Sec. 5.3; finally, conclusions are drawn in Sec. 5.4. The information, including results, presented in this chapter has been adapted from a previously published article by the author [184].

[1]Single rhodium (II) phthalocyanine molecules are difficult to isolate experimentally due to their rapid dimerisation with another respective molecule. A previous study has noted that the functionalisation of the ring structure with sterically hindering groups can prevent dimerisation [216], but in doing so likely impacts the self-assembly of the molecules into periodic chain structures.

5.1 Computational Details

The computational methodology applied here is derived from the procedure outlined in Chapter 4. All-electron spin-polarised DFT calculations are carried out using the CRYSTAL23 [141] solid-state simulation package. All atoms are described by atom-centred local GTOs of double-ζ quality with an additional set of polarisation functions (DZVP) (see Appendix A). The B3LYP global hybrid exchange DF is employed [120, 129]. All geometry optimisations and SPE calculations are converged to an iterative energy threshold of $10^{-7}\,\mathrm{Ha}$. To facilitate a more efficient convergence of the SCF procedure, 30% of the previous Hamiltonian matrix is used in the updated matrix. Once again, the DIIS procedure is adopted [190, 191]. For calculations of the single chain periodic systems, k-point sampling of the FBZ is carried out in accordance with the Monkhorst-Pack method [192], using a reciprocal space shrinking factor of 10 [193]. Evaluation of the MAE is conducted using the second variational approach, as implemented in CRYSTAL23 [167, 194–197]. Once again, SOC effects are accounted for through the use of sets of "shape consistent" fully relativistic effective core potentials [198–204]. Band structures are evaluated using the CRYSTAL23 properties executable and visualised using a python-based package [205]. Spin density isosurface plots are constructed using the VESTA3 visualisation program [206].

5.2 Single Molecule

A full geometry relaxation of the internal coordinates of single molecule RhPc is carried out using an initial structure obtained from the optimised single CoPc molecule. The full set of coordinate data may be found in Table 5.1. Following the optimisation of the system, a planar RhPc molecule of D_{4h} symmetry is identified, with rhodium-nitrogen ($\mathrm{Rh}-\mathrm{N}$) bond lengths of $2.013\,\text{Å}$, representing a 4.4% increase relative to those of CoPc. The bonding angle of the "bridging" nitrogens ($\mathrm{N_1}$ in Fig. 4.1) is found to be 125.1° - a 2.5% increase relative to that of CoPc. Therefore, within the DFT geometry optimisation, the system retains its planarity, with the central phthalocyanine cavity expanding in order to accommodate the larger Rh^{2+} ion. As shown in Table 5.1, there are only minor differences in the spatial geometry of the outer portion of the phthalocyanine ring between CoPc and RhPc.

Following the single molecule optimisation, the ground electronic state is identified as ${}^2A_{1g}$, with an unpaired electron occupying the a_{1g} MO. As displayed in Table 5.2, MPA

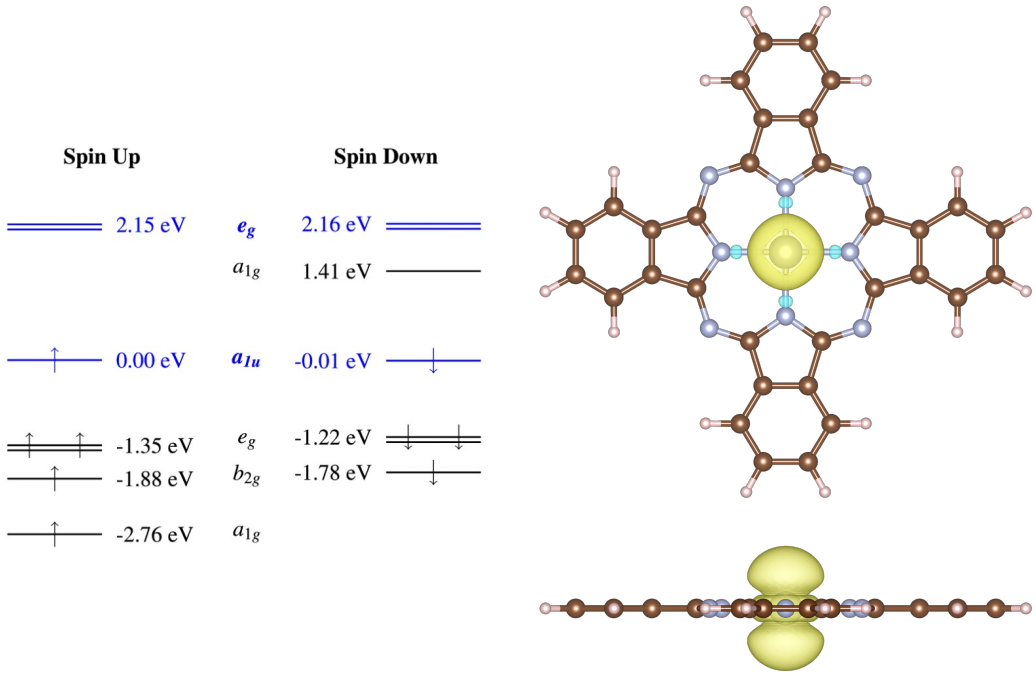

(a) (b)

Figure 5.1: Depiction of (a) eigenvalues of the frontier MOs and (b) spin density isosurface plot for the single molecule RhPc. In (a), black plain-text labels refer to d-derived MOs whilst blue bold-text labels refer to ligand derived MOs. Note that the b_{1g} MOs are energetically positioned above the ligand e_g orbitals and are omitted for clarity. In (b), an isovalue of $0.001\,|e|$ Å^{-3} is used. Yellow (blue) shading indicates regions of up-spin (down-spin) electron density. Fig. 5.1(a) reproduced from Ref. [184] with permission from the authors.

indicates a charge of $+0.925\,|e|$ localised on the central Rh atom. For CoPc, the respective value was $+1.411\,|e|$ implying that in the RhPc system, the metal-ligand bonding exhibits a more covalent character. Given the larger, more diffuse set of $4d$ orbitals in RhPc, an increased overlap between the metal and coordinated ligand orbitals is to be expected. Indeed, an increase of the overlap population between the metal and ligating nitrogens of 108% is observed when transferring from CoPc to RhPc. Furthermore, a charge of $+0.837\,|e|$ is found within the $4d_{x^2-y^2}$ AO, representing an increase of $+0.146\,|e|$ relative to CoPc. This finding further highlights the pronounced covalent character of the metal-ligand bonding. With regards to the charge density distributed amongst the ligand constituents of the phthalocyanine ring, as observed with CoPc (see Chapter 4), there is an accumulation of negative charge density on both the isoindole (N_1 in Fig. 4.1) and "bridging" (N_2) nitrogens

Bond Lengths			
Label	RhPc [Å]	CoPc [Å]	% Difference
M-N1	2.013	1.928	4.42
N1-C1	1.373	1.379	0.44
C1-N2	1.329	1.322	0.53
C1-C2	1.463	1.456	0.48
C2-C3	1.395	1.396	0.07
C3-C4	1.396	1.394	0.14
C4-C5	1.407	1.409	0.14
C2-C6	1.411	1.403	0.79
Bond Angles			
Label	RhPc [°]	CoPc [°]	% Difference
M-N1-C1	124.8	126.4	1.27
N1-C1-N2	127.7	127.6	0.08
C1-N2-C8	125.1	122.0	2.56

Table 5.1: Optimised bond lengths and angles for single molecule RhPc, with respective optimised CoPc bond lengths and angles for comparison. Labels refer to those defined in Fig. 4.1.

of $-0.628\,|e|$ and $-0.424\,|e|$, respectively. This is accompanied by a deficiency of electron density on C_1 with a charge of $+0.377\,|e|$. Once again, there is only minor fluctuations of the charge density on the outer portion of the phthalocyanine ring. Examination of the spin density through MPA, indicates that a population of $+0.988\,|e|$ is centred on the Rh ion, with the majority ($+0.848\,|e|$) concentrated in the $4d_{z^2}$ AO. This finding is in accordance with expectations derived from the CoPc molecular system, in which the spin density was also primarily localised within the Co $3d_{z^2}$ AO.

The energies associated with the frontier MOs are depicted in Fig. 5.1(a). As previously observed with CoPc, the HOMO and degenerate set of LUMOs are ligand-derived, exhibiting a_{1u} and e_g symmetry, respectively. The occupied $a_{1g\uparrow}$ MO is found to be the lowest in energy relative to the other $4d$-derived MOs, located $2.76\,\mathrm{eV}$ below the HOMO. The respective unoccupied $a_{1g\downarrow}$ MO is found $1.41\,\mathrm{eV}$ above the HOMO. Evaluation of the energy difference between the two SOMOs facilitates an estimation of the on-site Coulombic repulsion, $U = 4.17\,\mathrm{eV}$. With respect to the value of U extracted from the single particle energy spectrum of CoPc, a significant decrease in the on-site repulsion is observed here,

Atom	Charge [|*e*|]	Spin [|*e*|]
M	44.085	0.988
N1	7.628	0.008
N2	7.424	0.001
C1	5.623	-0.002
C2	5.953	0.000
C3	6.118	0.000
C4	6.090	0.000

Table 5.2: Mulliken population analysis for the charge and spin density in single molecule RhPc. Labels refer to those defined in Fig. 4.1.

Atomic Orbital	Charge [|*e*|]	Spin [|*e*|]
d_{z^2}	1.068	0.848
d_{xz}	1.904	0.010
d_{yz}	1.904	0.010
$d_{x^2-y^2}$	0.837	0.021
d_{xy}	1.944	0.002

Table 5.3: Mulliken population analysis of the spin and charge density for the d AOs in single molecule RhPc.

reflecting the larger, more diffuse nature of the Rh $4d$ orbitals. Furthermore, the relative decrease is facilitated by both a raising in energy of the $a_{1g\uparrow}$ and a lowering in energy of the $a_{1g\downarrow}$. This results in the placement of the unoccupied $a_{1g\downarrow}$ orbital *in-between* the ligand-derived a_{1u} HOMO and degenerate e_g LUMO. Consequently, the eigenvalue spectrum indicates a differential electronic excitation between the two spin channels. However, it is important to note that the spectrum does not take into account the Coulombic "energy penalty" associated with the double occupation of the a_{1g} MO ($U = 4.17\,\mathrm{eV}$). With the inclusion of this, the total energy corresponding to the $a_{1u\downarrow} \rightarrow a_{1g\downarrow}$ exceeds that of the $a_{1u\downarrow} \rightarrow e_{g\downarrow}$ transition.

5.3 Periodic Chains

Having obtained an optimised molecular structure of RhPc, single periodic chains are subsequently constructed so as to evaluate the intrachain magnetic coupling. As outlined

above, the RhPc system is a purely theoretical system and as a result there is no related experimental crystal data. Thus, in order to provide a valid and robust comparison between the periodic systems analysed in Chapter 4 and the RhPc system here, model chain structures of the two primary polymorphs (α-phase and β-phase) are constructed for the latter complex. In conjunction with this, so as to capture a considerable portion of the geometrical phase space, two additional sets of calculations are carried out on a range of different structural configurations. In the first set, the stacking and sliding angles (ϕ and ψ, respectively) are fixed at their typical α-phase ($\phi = 65°; \psi = 0°$) and β-phase ($\phi = 45°; \psi = 45°$) values, and the interplanar distance is varied from $3.30 - 3.85$ Å in increments of 0.05 Å. In the second set, the interplanar distance is fixed at 3.70 Å and both ϕ and ψ are varied. Here, ϕ is varied from $40 - 75°$[2], whilst ψ is varied from $0 - 45°$; both ranges employ an interval of $5°$.

5.3.1 Unit Cell

In order to account for the larger Rh^{2+} ion relative to that of Co^{2+}, the metal-metal distance in the former complex is adjusted. The magnitude of the distance augmentation is evaluated using the difference in the covalent radii of Co and Rh in their respective single bonds. For $\mathrm{Co} - \mathrm{Co}$, a value of 1.11 Å [221] is obtained, whilst for $\mathrm{Rh} - \mathrm{Rh}$, the respective value is 1.25 Å [221]. The difference between the two yields a value of 0.14 Å. However, the adjustment is required for both metals in the dimeric unit cell, and, therefore, an increase in the interplanar distance of of 0.28 Å in the RhPc system is applied. Following this augmentation, the final interplanar distance in both polymorphs of RhPc is 3.70 Å. This results in a metal-metal distance of 4.08 Å (5.23 Å) and a lattice parameter of 8.16 Å (10.46 Å) for α-RhPc (β-RhPc). Fig. 5.2(a) (Fig. 5.2(b)) presents the dimeric unit cell for α-RhPc (β-RhPc) whilst the respective lattice parameters are shown in Table 5.4. Once again, the

[2]For $\phi > 75°$, in the BS-DFT calculations carried out here, the localised magnetic state of the system is found to transform into a delocalised state. This is not within the region of interest for this particular study. For further information, readers are directed to Appendix C.1.

Polymorph	a [Å]	b [Å]	c [Å]	α [°]	β [°]	γ [°]
α-phase	60	60	8.16	90	65	90
β-phase	60	60	10.46	90	45	90

Table 5.4: Lattice parameters for the periodic single chain models of the two polymorphic phases of RhPc.

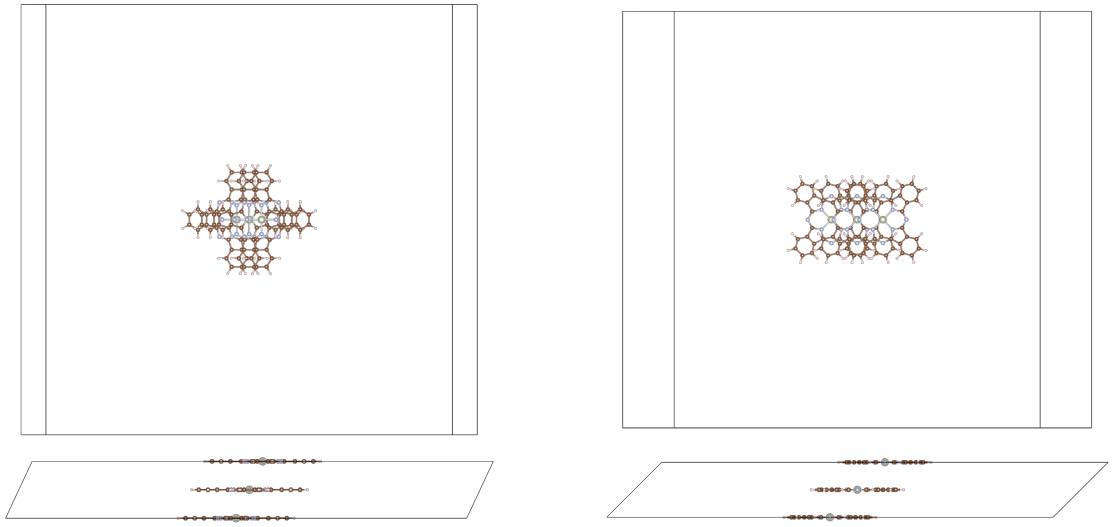

(a) (b)

Figure 5.2: Structural depiction of the dimeric unit cell for the (a) α-phase and (b) β-phase.

cell is constructed such that the periodic stacking direction is aligned along the *c*-axis. The molecular unit is placed in the centre of a $60\,\text{Å}^2$ box to minimise lateral interactions. To account for $\psi = 45°$ in the β-polymorph, the dimeric molecular system is rotated by $45°$.

5.3.2 α-RhPc

Plots of the band structure and spin density isosurface for the α-RhPc periodic chain are displayed in Fig. 5.3. The antiparallel (parallel) alignment of the electrons is captured in an AFM (FM) state, as indicated in the respective spin density isosurface plot in Fig. 5.3(c) (Fig. 5.3(d)). Additionally, in the AFM state, the spin density localised on neighbouring rhodium centres is found to be of equal magnitude ($0.964\,|e|$) but opposite sign, whilst, in the FM state, the spin density of the respective rhodium centres are found to be of equal magnitude ($0.977\,|e|$) and sign.

Examination of the band structure indicates a downwards shift in energy of the unoccupied magnetic bands, relative to that of α-CoPc, resulting in their placement *in-between* the a_{1u} HOMO and e_g LUMO. As a result, the up-spin (down-spin) band gap, in the AFM state, is measured to be $1.28\,\text{eV}$ ($1.27\,\text{eV}$), whilst in the FM state, the respective band gap is found to be $1.96\,\text{eV}$ ($0.94\,\text{eV}$). These energy gaps are much lower in magnitude relative to the $\sim 2.0\,\text{eV}$ band gap observed in the TMPc systems studied in Chapter 4. Interestingly, in the FM configuration, the excitation energy appears to be spin-specific. This suggest

System	J^{BS} [K]	J^{KE} [K]	J^{Exp} [K]	t [eV]	U [eV]
α-CoPc	-99.1	-176.5	-107.0 [93]	0.15	6.21
β-CoPc	-1.2	-0.6	-1.5 [95]	0.01	6.29
α-RhPc	-391.0	-417.8	-	0.19	4.04
β-RhPc	-2.4	-4.5	-	0.02	4.09

Table 5.5: Exchange energy data for the two polymorphic phases of CoPc and RhPc. J^{BS} refers to the coupling energies obtained using Eq. 4.4; J^{KE} refers to the coupling energies obtained using the values of t and U employed in Eq. 4.2; J^{Exp} refers to respective experimental data for the CoPc systems.

that, in the presence of an external magnetic field, a stabilised FM state could exhibit a differential energy spectrum. However, for a highly correlated system, such as that studied here, the electronic transitions are poorly approximated by the eigenvalues, as they do not account for the on-site Coulombic repulsion (U) arising from the double occupation of the a_{1g} band. As a result, it is likely that the first excitation would be the $a_{1u\downarrow} \rightarrow e_{g\downarrow}$ transition.

At the Γ-point, the singly occupied (unoccupied) a_{1g} band is measured to be $3.12\,\mathrm{eV}$ ($0.92\,\mathrm{eV}$) below (above) E_F, yielding a $U = 4.04\,\mathrm{eV}$. This value is reduced in magnitude relative to that calculated from the single molecule energy spectrum, suggesting a degree of delocalisation of the a_{1g} MOs along the chain. Additionally, with comparison to the on-site Coulombic repulsion calculated for α-CoPc ($U = 6.21\,\mathrm{eV}$), the value obtained here is approximately $2.0\,\mathrm{eV}$ less, reflective of the more diffuse nature of the Rh $4d$ orbitals. An estimate of the transfer integral, *t*, is evaluated from the width, *W*, of the unoccupied a_{1g} band which is measured to be $W = 0.76\,\mathrm{eV}$, yielding a value of $t = 0.19\,\mathrm{eV}$. This represents an increase of $0.04\,\mathrm{eV}$ relative to that calculated for α-CoPc. Given the large radial extent of the $4d$ orbitals in Rh, an increase in t is to be expected. However, due to the augmentation of the interplanar distance in α-RhPc (see 5.3.1), only a modest increase in the magnitude of t is observed. The influence of t on the strength of J^{KE} has been explicated in Chapter 4 in the comparison between the two polymorphs of CoPc. The primary focus of this specific study is to highlight the importance of U on J^{KE} and, therefore, efforts have been made to reduce the variance in t between α-CoPc and α-RhPc.

Employing Eq. 4.4, a value of $J^{BS} = -391.0\,\mathrm{K}$ is calculated, representing an increase of approximately 300% with respect to the α-phase of CoPc. Using the Hubbard parameters extracted from the dispersion spectrum and applied in Eq. 4.2, a $J^{KE} = -417.8\,\mathrm{K}$ is measured. In comparison to the coupling strengths calculated for α-CoPc, closer agreement

is observed between the values of J^{BS} and J^{KE} for the system studied here, suggesting that the KE interaction dominates the magnetic coupling. Regarding the magnitude of the evaluated exchange strength, exceptionally strong coupling is observed in α-RhPc, indicating the possibility of magnetic ordering at RT. Additionally, whilst the minor increase in t may have some contribution, the principle reason for the strong coupling is likely as result of the large decrease in U in the RhPc system, which is attributable to the occupation of magnetic bands constructed from a diffuse set of $4d$ orbitals.

Using the second variational approach and employment of Eq. 3.1, an estimate of the MAE is made for α-RhPc. A value of $298\,\mu\text{eV}$ is evaluated, with an in-plane (out-of-plane) easy axis (hard axis). Given the electronic configuration of the system, in which an a_{1g} SOMO is present, these results are in accordance with expectations. Relative to that

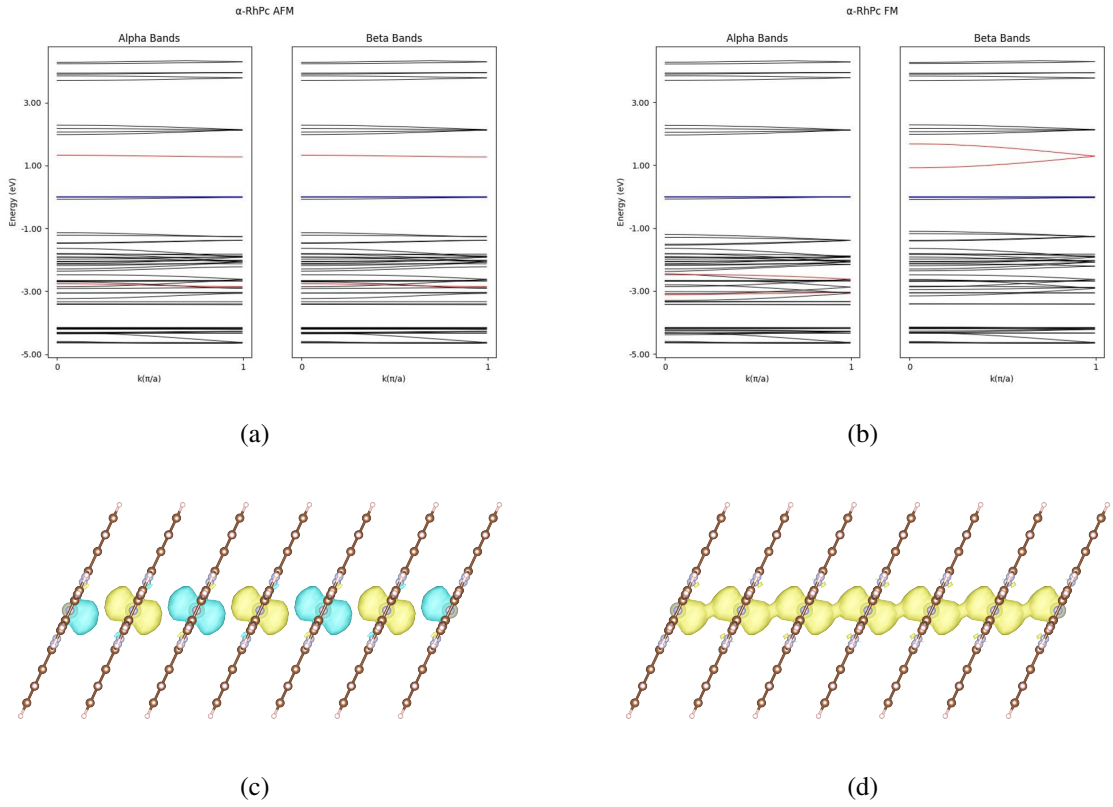

Figure 5.3: Plots of the (a) AFM and (b) FM band structures, and (c) AFM and (d) FM spin density isosurfaces for single chain structures of α-RhPc. In (a) and (b), the magnetic a_{1g} bands are highlighted in red. In (c) and (d), an isovalue of $0.001\,|e|$ Å^{-3} is used. Yellow (blue) shading indicates regions of up-spin (down-spin) electron density. Figs. 5.3(a) and 5.3(b) reproduced from Ref. [184] with permission from the authors.

evaluated for the systems studied in the previous chapter, here, the considerable increase in the MAE may be attributed to the increase in the SOC interaction in the Rh^{2+} ion.

5.3.3 β-RhPc

Fig. 5.4 depicts the band structure and spin density isosurface for the β-RhPc single chain. As for α-RhPc, the antiparallel and parallel alignment of the single electrons is captured in an AFM and FM state, respectively, as indicated in the spin density isosurface plots (Fig. 5.4(c) and Fig. 5.4(d)). In the AFM configuration, the spin density localised to contiguous rhodium centres is found to be of equal magnitude ($0.979\,|e|$) but opposite sign, whilst, in the FM state, the respective spin density on neighbouring metal atoms is of equal magnitude ($0.979\,|e|$) and sign.

As in the α-RhPc system, a downwards shift in the energy of the unoccupied magnetic a_{1g} bands is observed in β-RhPc, once again resulting in their positioning between the a_{1u} HOMO and e_g LUMO. In the AFM configuration, the up-spin (down-spin) band gap is found to be $1.44\,\mathrm{eV}$ ($1.44\,\mathrm{eV}$), whilst, in the FM state, the respective band gap is measured

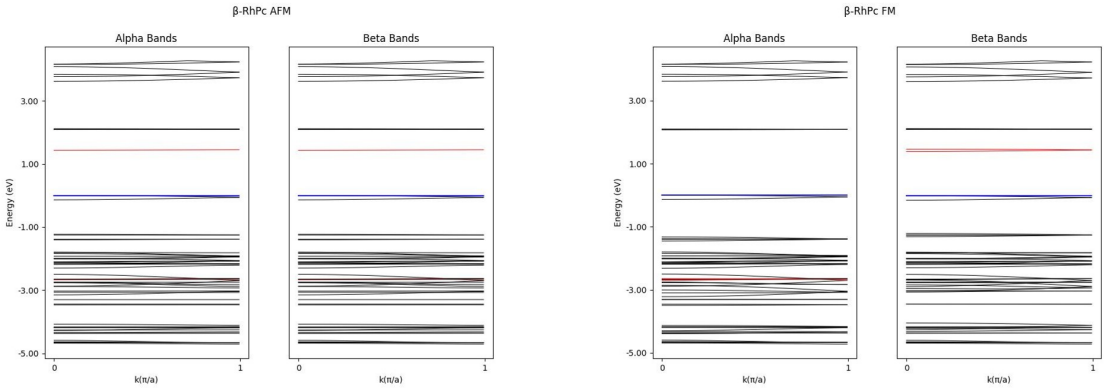

(a) (b)

(c) (d)

Figure 5.4: Plots of the (a) AFM and (b) FM band structures, and (c) AFM and (d) FM spin density isosurfaces for single chain structures of β-RhPc. In (a) and (b), the magnetic a_{1g} bands are highlighted in red. In (c) and (d), an isovalue of $0.001\,|e|\,\text{Å}^{-3}$ is used. Yellow (blue) shading indicates regions of up-spin (down-spin) electron density.

to be $2.08\,\mathrm{eV}$ ($1.41\,\mathrm{eV}$). As was previously observed in α-RhPc, a spin-specific band gap is present in the FM state of the β-polymorph, although, once again, the dispersion spectrum does not take into account the on-site repulsion, U, and therefore the first electronic excitation is also likely to be the $a_{1u\downarrow} \rightarrow e_{g\downarrow}$ transition.

At the Γ-point, the two a_{1g} magnetic bands are measured to be $2.71\,\mathrm{eV}$ and $1.38\,\mathrm{eV}$ below and above E_F, respectively. Evaluation of the energy difference between these two bands yields a $U = 4.09\,\mathrm{eV}$. Once again, this value is lower than that obtained from the single molecule eigenvalues, reflecting the increase in delocalisation of the a_{1g} MOs in the magnetic bands. However, it is important to note that this delocalisation effect is limited, and the MOs constituting the band are still very much localised to their respective metal centres. Using Eq. 4.3, an estimate of t is obtained from the band width of the unoccupied $a_{1g\downarrow}$ band, with a value of $t = 0.02\,\mathrm{eV}$ derived from a $W = 0.08\,\mathrm{eV}$. The reduction in the magnitude of t, relative to α-RhPc, is due to the decrease in the stacking angle, ϕ, which results in a decrease in the overlap between adjacent a_{1g} SOMOs.

Using Eq. 4.4, a $J^{BS} = -2.4\,\mathrm{K}$ is found for β-RhPc, which represents an increase of 100% relative to β-CoPc. Additionally, a value of $J^{KE} = -4.5\,\mathrm{K}$ is evaluated using Eq. 4.2 and the parameters extracted from the dispersion spectrum. Only a slight discrepancy is observed between J^{BS} and J^{KE}, indicating that, whilst the overall coupling is comparatively weak in relation to the α-polymorph of the RhPc system, it is likely that the KE pathway still dominates the mechanism underpinning the AFM ordering. Given this, the comparative weakness in the exchange strength in β-RhPc, may therefore be attributed to the increased metal-metal distance and commensurate decrease in orbital overlap.

Once again, employing the second variational approach, an approximation of the MAE is obtained for β-RhPc. A value of $276\,\mu\mathrm{eV}$ is computed, with an in-plane easy axis and out-of-plane hard axis. Once again, this is in accordance with expectations derived from the single molecule electronic configuration and similar in magnitude to that of α-RhPc.

5.3.4 Additional Chain Geometries

In the first group of chain geometries studied in this section, ϕ and ψ are fixed in the α-phase and β-phase structural geometries, and the interplanar distance is varied form $3.30 - 3.85\,\text{Å}$. For each configuration, J^{BS} and J^{KE} is evaluated. Fig. 5.5 graphically depicts the variation in both of the two polymorphic phases. For both phases, as the distance between adjacent molecules decreases, the magnitude of J^{BS} generally increases. A maximum value of $J^{BS} = -1168.55\,\mathrm{K}$ ($J^{BS} = -13.88\,\mathrm{K}$) is evaluated at an interplanar

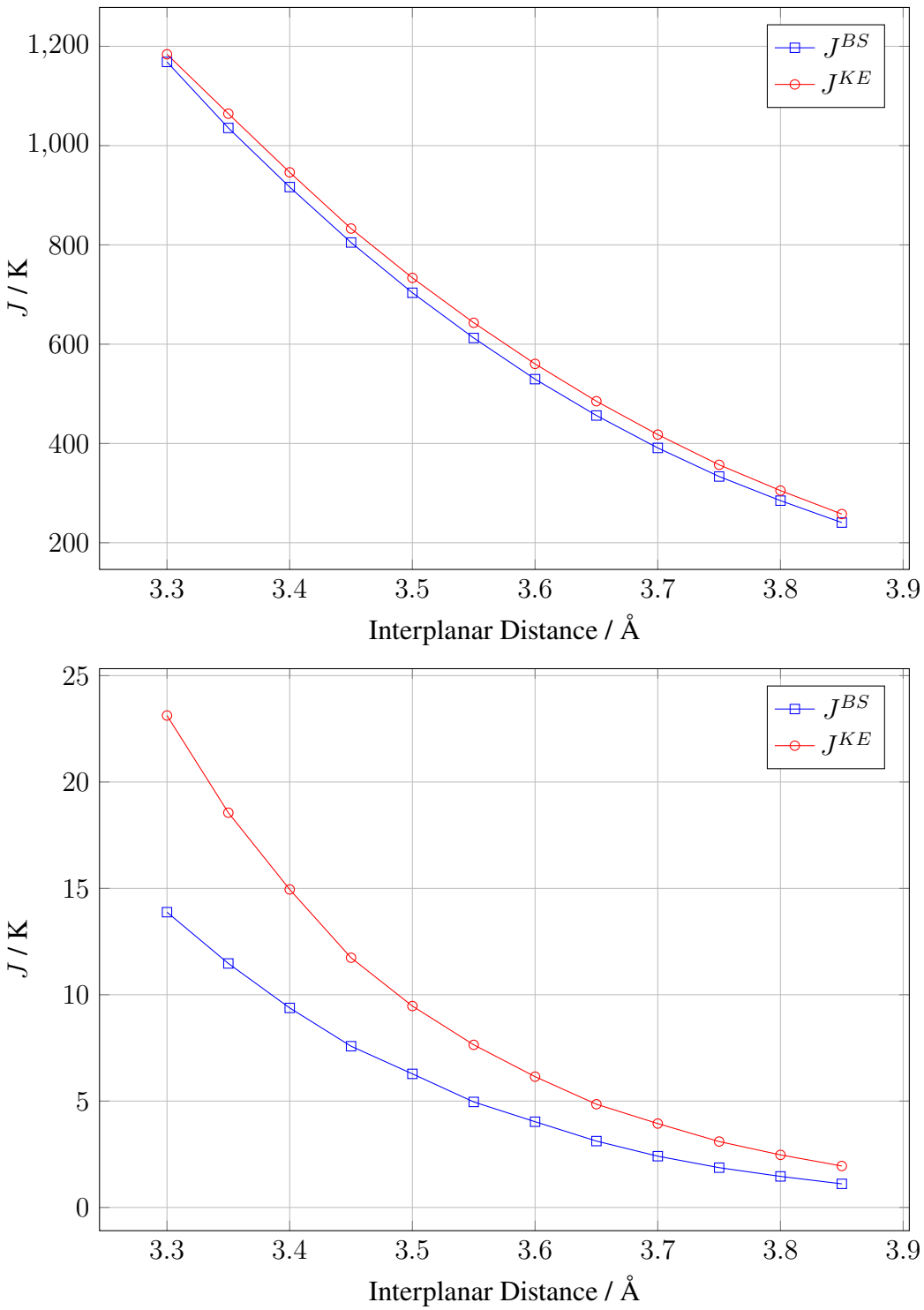

Figure 5.5: Magnitude of J^{BS} and J^{KE} as a function of the interplanar distance for single periodic chains of RhPc in the α-phase configuration ($\phi = 65°; \psi = 0°$) (top panel) and β-phase configuration ($\phi = 45°; \psi = 45°$) (bottom panel).

distance of 3.30 Å, whilst a minimum of $J^{BS} = -240.59\,\mathrm{K}$ ($J^{BS} = -1.11\,\mathrm{K}$) is computed at an interplanar distance of 3.85 Å for the α-phase (β-phase) configuration. Regarding the α-phase, the variation in J^{KE} closely follows that of J^{BS}. This suggests that the dominant mechanism underpinning the magnetic coupling within the chain is derived from a KE interaction. With respect to the β-phase, the magnitude of both J^{BS} and J^{KE} is far lower, once again highlighting the important role the metal-metal distance plays in the coupling strength. Furthermore, the magnitudes of the J^{BS} and J^{KE} are seen to deviate more from one-another, indicating the potential presence of additional contributions to the coupling that are unaccounted for. Despite this, it is clear from the results presented here that the KE mechanism, as parametrised through the Hubbard Hamiltonian, offers an appropriate and informative description of the coupling within single chain structures of RhPc.

In the second set of chain geometries, both ϕ and ψ are systematically augmented for structures in which the interplanar distance is fixed at 3.70 Å, with Fig. 5.6 presenting a graphical depiction of the resulting coupling strengths. Here, only J^{BS} is evaluated for each structure and is included to emphasise the change in the strength of the exchange interactions as the intrachain geometry is modified. The results show that the exchange interaction is particularly dependent upon ϕ, and is seen to increase as the chain geometry approaches

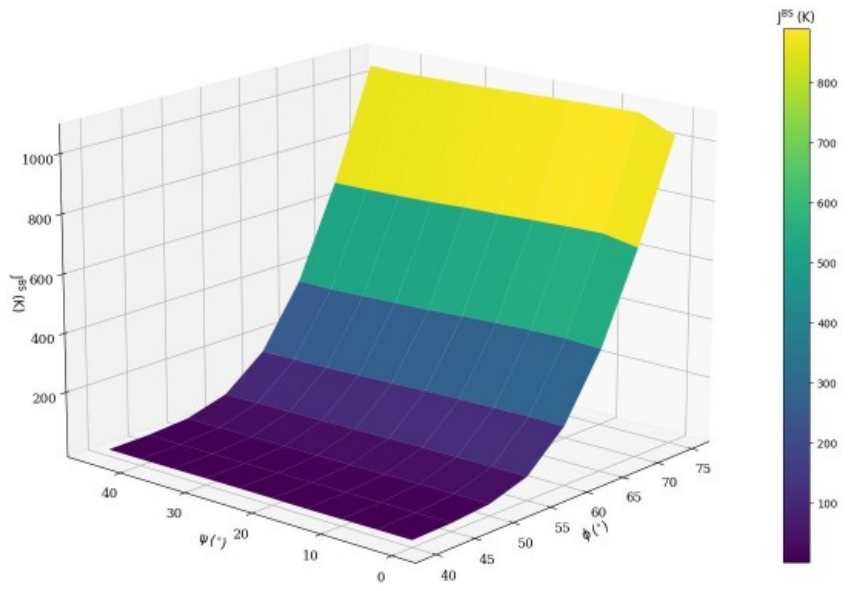

Figure 5.6: Magnitude of J^{BS} as a function of the stacking angle, ϕ, and sliding angle, ψ, for single periodic chains of RhPc at a fixed interplanar distance of 3.70 Å. Figure reproduced from Ref. [184] with permission from the authors.

cofacial alignment ($\phi = 90°$). This is to be expected given the reliance of the strength of the KE interaction on the magnitude of t, and, by extension, the orbital overlap between contiguous SOMOs, which increases commensurately with ϕ. No considerable variance in J^{BS} is observed as ψ is augmented, implying that variations in the intermolecular alignment induced by changes in the sliding angle have only a minor influence on the strength of the exchange interaction (at least within the structural regime analysed in this study).

5.4 Conclusions

It is important to begin with the initial hypothesis outlined in the introductory section of this chapter. In Chapter 4, the results of the BS-DFT analysis of both principle polymorphs (α-phase and β-phase) of CoPc and CuPc, indicated an exceptionally strong AFM coupling in α-CoPc (relative to the other studied systems). The strength of this intrachain exchange was shown to arise from a dominant KE interaction between neighbouring a_{1g} SOMOs located at each cobalt centre. Parameterisation of this KE interaction through the terms of the Hubbard Hamiltonian indicated that, to affect an increase in the strength of the coupling, either t could be raised of U lowered. In this study, by replacing the central Co^{2+} ion of CoPc with its second-row counterpart, Rh^{2+}, it was posited that the more diffuse $4d$ orbitals of the rhodium system would decrease the magnitude of U. Analysis of the magnetic coupling in the two primary polymorphs of this RhPc system, evidenced very strong AFM coupling in α-RhPc. Additionally, with comparison to the magnetic data of α-CoPc, only significant variance in U was observed, with a reduction in magnitude of $\sim 2.0\,\mathrm{eV}$. Furthermore, good agreement was found between J^{BS} and J^{KE}, implying that a dominant KE interaction likely underpins the long range AFM ordering in the system. The variance in t between the α and β-polymorphs, and the resulting difference in coupling strength, served to highlight the additional importance of the intrachain structural geometry in the resulting exchange interactions. The strong correlation observed between the evaluated values of J^{BS} and J^{KE} presented in Sec. 5.3.4, particularly in the α-phase geometries, indicated that not only does the magnitude of the coupling strength vary as a function of $4t^2/U$, but also that DE terms, that were believed to be present in α-CoPc, have been suppressed in the RhPc system.

In considering the intrinsic relationship between chemical structure and emergent magnetic ordering, this study has shown that a simple system modification can result in a substantial augmentation of the strength of this ordering. The prediction of RT AFM ordering in α-RhPc makes the synthesis of a stable molecular structure and its self-assembly into

periodic chains a compelling task for the scientific community. Furthermore, the Hubbard Hamiltonian parameters have been shown to provide valuable predictive capabilities with respect to novel magnetic systems, and it is expected that other systems with stable ordered phases at RT may also be discoverable using such a method.

6

Decomposition of the Exchange Interactions

The relative stability of the FM or AFM configuration of *localised* magnetic moments in both molecular systems and correlated solid-state materials may be explained through the contest between three components underpinning the exchange interaction [222–225]. This was outlined in detail in Sec. 3.1.1, but is briefly reiterated here. The first is the direct exchange (DE) interaction, which always serves to align single electrons in parallel with one another, thereby, preferencing the FM configuration. The second is the kinetic exchange (KE) interaction. By configuring the unpaired electrons into an AFM state, each SOMO may gain a kinetic energy stabilisation through the delocalisation of the tail of its wavefunction onto that of another non-orthogonal singly occupied orbital. Thus, KE acts to align single electrons antiparallel to one another and is, therefore, in direct competition with the DE interaction. The final component is that of spin polarisation (SP) of the core orbitals. The core orbitals of a magnetic system experience a polarising influence from the localised SOMOs that is different in the AFM and FM configurations. In general, electron density of the same spin as that of the moment concentrates closer to the moment, whilst

electrons of the opposite spin diffuse away. This can alter the spatial distribution of the up-spin and down-spin electrons within the system and, in doing so, offer a stabilising effect in either the parallel or antiparallel configurations. The extraction and subsequent comparison of these three energetic contributions can lead to an enhanced comprehension of the mechanism underpinning emergent magnetic ordering in different systems. In doing so, a more directed approach to materials design may be realised.

A methodology has been recently developed to extract the energetic contributions from the aforementioned exchange interactions through the construction and evaluation of a set of single determinant KS-DFT calculations [226–230]. Here, the method is referred to as the *decomposition* procedure. The method has previously been shown to accurately evaluate the respective energetic contributions of the DE, KE and SP interactions in a variety of molecular radicals and bi-nuclear transition metal complexes [227, 228, 231]. In this chapter, the results pertaining to an application of the decomposition scheme to the set of transition metal phthalocyanines systems studied in Chapters 4 and 5 (CoPc, CuPc and RhPc) are presented. Due to computational limitations[1], the periodic single chain structure of the systems are approximated by a molecular dimer. Whilst some discrepancies may arise from this approach, the mapping procedure outlined in Sec. 3.5 provides a formalism for obtaining the correctly scaled, system-dependent coupling energies. Thus the models used here are assumed to provide results suitable for comparison with those of the full periodic system. As examined in detail in Chapters 4 and 5, there is a clear relationship between the intrachain geometry, electronic structure and emergent magnetic ordering in periodic structures of CoPc, CuPc and RhPc. This study, therefore, aims to further develop this understanding by providing a comprehensive model for the mechanistic foundation of the respective exchange interactions in these phthalocyanine systems.

The remainder of this chapter is sectioned as follows: in Sec. 6.1, the decomposition procedure is outlined to provide a mathematical foundation to the methodology; in Sec. 6.2, details related to the computational specifications used in this study are provided; in Sec. 6.3, the decomposition methodology is applied and analysed in detail for the hydrogen molecule; in Sec. 6.4, information and resulting data are presented for the single molecule TMPc structures of the three studied systems; results of the decomposition procedure are provided in Sec. 6.5, whilst concluding remarks are offered in Sec. 6.6. Some information in this

[1] In order to carry out the the decomposition procedure, local self-consistent field (LSCF) functionality is required. This has not been implemented in any version of the CRYSTAL code. Therefore, the molecular code, ORCA, which has an implementation of the LSCF procedure, is used instead. As a result, the periodic single chain structures are approximated as dimeric molecular systems.

chapter, including results, is adapted from a published article by the author [46].

6.1 Decomposition Procedure

Considering a simple centro-symmetric system with two unpaired electrons localised at two separate magnetic centres, the initial step of the decomposition procedure is to generate the restricted open (RO) determinant of the high spin (HS), $M_s = 1$ configuration. This is given by,

$$\Phi_{RO,HS} = \left| \prod_{i}^{N_c} n\overline{n} \prod_{j}^{N_m} gu \right| = \left| \prod_{i}^{N_c} n\overline{n} \prod_{j}^{N_m} ab \right| \tag{6.1}$$

Here, n denotes the doubly occupied, core orbitals of the system, g and u (a and b) are the canonical (localised) singly occupied orbitals and the overline, $\overline{n}$, denotes occupation of the respective orbital by a down-spin electron. N_c and N_m are the total number of core and magnetic electrons, respectively. The localised orbitals are obtained through a rotation of the canonical orbitals,

$$a = \frac{g+u}{\sqrt{2}},\ b = \frac{g-u}{\sqrt{2}} \tag{6.2}$$

Both representations are valid and provide the same description of the system. However, to facilitate the subsequent spin-flip procedures necessitated by the methodology, the localised SOMOs are adopted. The flipping of a spin of one of the unpaired electrons, *without* subsequent optimisation of the resulting MOs, generates the RO, broken symmetry (BS) determinant of the $M_s = 0$ state,

$$\Phi_{RO,BS} = \left| \prod_{i}^{N_c} n\overline{n} \prod_{j}^{N_m} a\bar{b} \right| \tag{6.3}$$

Using the Yamaguchi approach [179–183], and correctly mapping the energy difference between the HS and BS states as defined in Eq. 3.14, in which $N = 2$, $z = 1$ and $m = 1/2$, the energy contribution arising from the DE interaction (J^{DE}) may be calculated using the following formalism,

$$J^{DE} = -\frac{2(E[\Phi_{RO,HS}] - E[\Phi_{RO,BS}])}{\langle S^2 \rangle_{RO,HS} - \langle S^2 \rangle_{RO,BS}} \tag{6.4}$$

where $E[\Phi_{RO,HS}]$ ($E[\Phi_{RO,BS}]$) is the energy of $\Phi_{RO,HS}$ ($\Phi_{RO,BS}$) determinant and $\langle S^2\rangle_{RO,HS}$ ($\langle S^2\rangle_{RO,BS}$) is the respective spin expectation value. In the RO formalism, $\langle S^2\rangle_{RO,HS} = 2$ and $\langle S^2\rangle_{RO,HS} = 1$.

Following this, the energy contribution arising from the KE interaction (J^{KE}) is evaluated. Taking the $\Phi_{RO,BS}$ determinant and selectively relaxing the magnetic orbitals whilst retaining the same set of core (doubly-occupied) orbitals, a new determinant is generated, given by,

$$\Phi_{UFC,BS} = \left| \prod_{i}^{N_c} n\overline{n} \prod_{j}^{N_m} a'\overline{b'} \right| \tag{6.5}$$

Here, UFC stands for "unrestricted frozen core", highlighting the respective formalism used. Optimisation of the magnetic orbitals leads to a new set of MOs (a' and b') the tails of which delocalise onto one another. From a multiconfigurational perspective, the $\Phi_{UFC,BS}$ determinant is formed from the mixing of ionic components of the wavefunction, $|a\overline{a}|$ and $|b\overline{b}|$, into the neutral, $|a\overline{b}|$ component. Evaluation of the energy difference between $\Phi_{UFC,BS}$ and $\Phi_{RO,HS}$ yields J^{KE}, given by,

$$J^{KE} = -\frac{2(E[\Phi_{RO,HS}] - E[\Phi_{UFC,BS}])}{\langle S^2\rangle_{RO,HS} - \langle S^2\rangle_{UFC,BS}} - J^{DE} \tag{6.6}$$

Finally, in order to capture the energy contribution arising from the differential polarisation of the core orbitals (J^{SP}), two determinants are generated. In the first, $\Phi_{RO,HS}$ is employed as the initial reference wavefunction and the core orbitals are selectively relaxed in the presence of the frozen magnetic orbitals. This determinant is given by,

$$\Phi_{UFM,HS} = \left| \prod_{i}^{N_c} n'\overline{n'} \prod_{j}^{N_m} ab \right| \tag{6.7}$$

where UFM indicates an "unrestricted frozen magnetic" formalism is used. The second determinant makes use of $\Phi_{RO,BS}$ and, once again, the core orbitals are selectively relaxed in the field of the frozen magnetic orbitals, generating the following determinant,

$$\Phi_{UFM,BS} = \left| \prod_{i}^{N_c} n'\overline{n'} \prod_{j}^{N_m} a\overline{b} \right| \tag{6.8}$$

Evaluation of the energy difference between the two determinants, given by,

$$J^{SP} = -\frac{2(E[\Phi_{UFM,HS}] - E[\Phi_{UFM,BS}])}{\langle S^2\rangle_{UFM,HS} - \langle S^2\rangle_{UFM,BS}} - J^{DE} \tag{6.9}$$

yields a value of J^{SP}. The cumulative exchange interaction is calculated using the *recomposition* method [232], given by

$$J^{\Sigma} = J^{DE} + J^{KE} + J^{SP} \tag{6.10}$$

Alternatively, the *total* exchange interaction may be evaluated using an unrestricted formalism and calculating the DFT energies of the fully optimised HS ($E[\Phi_{U,HS}]$) and BS ($E[\Phi_{U,BS}]$) determinants. This is given by,

$$J^{Total} = -\frac{2(E[\Phi_{U,HS}] - E[\Phi_{U,BS}])}{\langle S^2\rangle_{U,HS} - \langle S^2\rangle_{U,BS}} \tag{6.11}$$

By evaluating the *difference* between Eq. 6.11 and Eq. 6.10, given by,

$$J^{\Delta} = J^{Total} - J^{\Sigma} \tag{6.12}$$

the relative accuracy of the procedure may be assessed. Here, J^{Δ} captures additional exchange energy contributions not accounted for in J^{Σ}.

6.2 Computational Details

All DFT calculations are carried out using the ORCA molecular simulation package [233, 234]. All atoms are described by all-electron local GTO basis sets of double-ζ quality with an additional set of polarisation functions (DZVP). These basis sets are identical to those used in the studies presented in Chapter 4 and 5 and may be found in Appendix A. The B3LYP hybrid exchange DF [120, 129] is employed for all calculations. The selective optimisation of MOs, used to build the sets of magnetic determinants, is carried out using the local self-consistent field[2] (LSCF) procedure [235]. For both SPE and geometry optimisation calculations, an iterative energy threshold of $10^{-7}\,\mathrm{Ha}$ is adopted. The Pipek-Mezey scheme [236] is used to generate localised MOs. MO and spin density isosurface plots are visualised using the VESTA3 software [206].

6.3 Decomposition of the H_2 Molecule

Before initialising the decomposition procedure for the set of TMPc dimeric systems, the methodology is first applied to an H_2 molecule. This is undertaken in order to better

[2]Please refer to Appendix B.3 for further information related to the LSCF procedure.

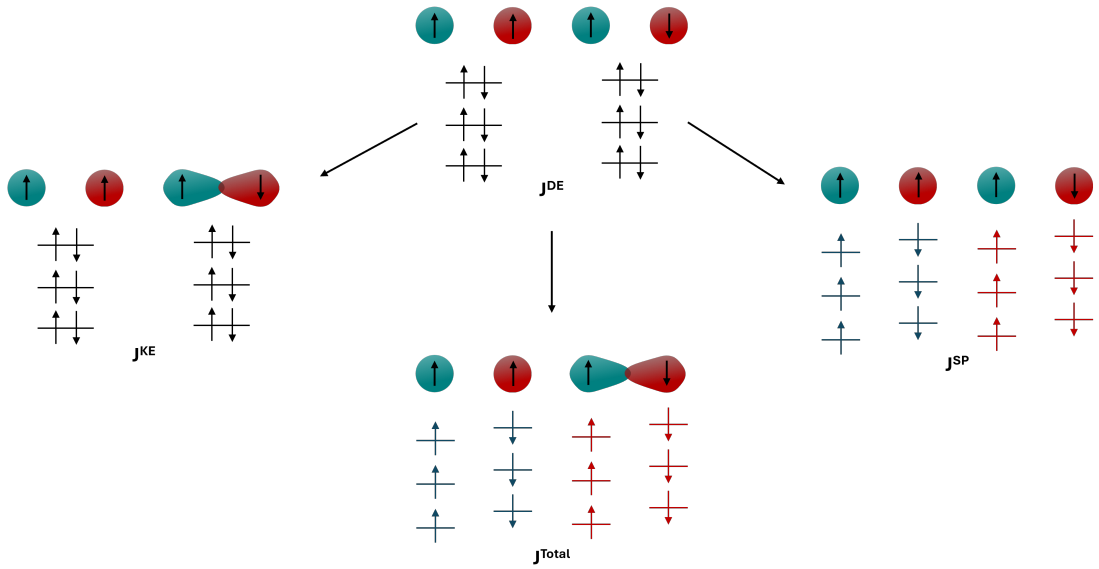

Figure 6.1: Figurative depiction of the decomposition scheme. Green and red spheres represent individual SOMOs localised on adjacent metal centres, whilst core (doubly occupied) MOs are pictured beneath. J^{DE}, J^{KE}, J^{SP} and J^{Total} refer to respective coupling constants as defined in Sec. 6.1. Figure reproduced from Ref. [46] with permission from the authors.

understand any nuances to the process. For H_2, there are two electrons involved in the bonding of the molecule and no additional "core" orbitals. As a result, alongside J^{Total}, only J^{DE} and J^{KE} is evaluated. In order to investigate the role that the magnetic orbital overlap plays, the decomposition is applied to the H_2 molecule over a range of interatomic distances between 0.5 Å and 3.0 Å with a step size of 0.5 Å. So as to maintain continuity with the previous studies discussed in this report, the decomposition procedure is carried out using the Hydrogen basis set employed in Chapters 4 and 5 (see Appendix A.9) and the B3LYP hybrid functional. Fig. 6.3 graphically depicts the variation of J^{DE}, J^{KE}, J^{Σ} (where $J^{\Sigma} = J^{DE} + J^{KE}$) and J^{Total} in H_2 as a function of bonding distance[3].

6.3.1 Direct Exchange

For J^{DE}, the magnitude decreases as the distance between the two H atoms increases. Given the dependence of the exchange integral on inter electronic distance, this decay is

[3]Given the exceptionally large magnitudes for the evaluated decomposition parameters in H_2, units of eV rather than K are used for reader's convenience.

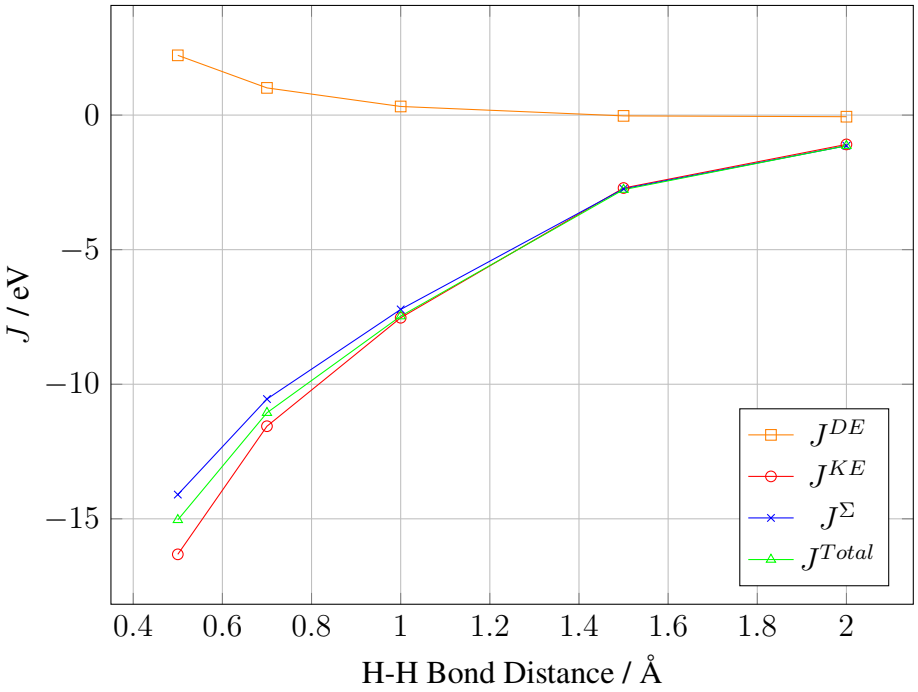

Figure 6.2: Variation in J^{DE}, J^{KE}, J^{Σ} (where $J^{\Sigma} = J^{DE} + J^{KE}$) and J^{Total} as a function of bond distance in H_2. Calculations carried out using the B3LYP functional.

to be expected. At the shortest bond distance of $0.5\,$Å, J^{DE} is measured to be $2.22\,$eV. Interestingly, beyond an H_2 distance of $1.5\,$Å, the value of J^{DE} is negative, albeit with very small magnitudes ($J^{DE} = -0.03\,$eV and $J^{DE} = -0.06\,$eV at bond distances of $1.5\,$Å and $2.0\,$Å, respectively). This suggests that the restricted open broken symmetry determinant ($\Phi_{RO,BS}$) is more stable than that of the restricted open high spin determinant ($\Phi_{RO,HS}$). However, the composition of the MOs in the two determinants are identical - only the specific occupation of the respective orbitals is altered. The LSCF procedure ensures that there is no further optimisation of the wavefunction, and, thus, the SCF procedure converges in a single cycle. In transitioning from the HS configuration, in which the single electrons are localised on each respective H atom, to the BS (or low spin (LS)) configuration, in which *only* the spin of one of the electrons is altered, and the respective orbital shapes remain unchanged, the variation in the expectation value of the Hamiltonian should only amount to the "switching off" of the exchange integral between the two single particles. Thus, $\Phi_{RO,HS}$ should be more stable than $\Phi_{RO,BS}$ irrespective of inter-particle distance, although the energy difference between the two configurations should decrease with increasing distance.

Examination of the DFT components related to the exchange-correlation energy indicates that, for the systems in which J^{DE} is negative, $E_{xc}[\Phi_{RO,HS}] < E_{xc}[\Phi_{RO,BS}]$ (where

the nomenclature here denotes the exchange-correlation energy as function of the respective determinant density). The data related to this is presented in Table 6.1. From the data, it can be seen that, whilst $E_x[\Phi_{RO,HS}] > E_x[\Phi_{RO,BS}]$ for all H_2 systems studied, the magnitude of the difference in the exchange energy between the two determinants decreases as the bonding distance increases. For the correlation energy, $E_c[\Phi_{RO,HS}] < E_c[\Phi_{RO,BS}]$ at all bonding distances. However, with the exception of the system with an interatomic distance of $2.0\,\text{Å}$, for all H_2 systems studied a value of $E_c[\Phi_{RO,HS}] = -0.24\,\text{eV}$ is obtained (the value of $E_c[\Phi_{RO,HS}]$ for the H_2 molecule with an interatomic separation of $2.0\,\text{Å}$ is found to be $-0.23\,\text{eV}$). The result of this is that, for the systems in which the $\text{H}-\text{H}$ distance is greater than $1.5\,\text{Å}$, the total $E_{xc}[\rho]$ energy for $\Phi_{RO,BS}$ is greater than that of $\Phi_{RO,HS}$, despite the exchange portion of the energy ($E_x[\rho]$) being of greater magnitude in the HS configuration.

By separating the B3LYP functional into its individual exchange and correlation energy components, the observed trends presented in Table 6.1 may be understood. The exchange-correlation energy in B3LYP has the following composition,

$$E_{xc}^{B3LYP} = (1-a)E_x^{LSDA} + aE_x^{HF} + bE_x^{B} + (1-c)E_c^{LSDA} + cE_c^{LYP} \tag{6.13}$$

where $a = 0.20$, $b = 0.72$ and $c = 0.81$. E_x^{LSDA} is the LSDA exchange energy, E_c^{LSDA} is the LSDA correlation energy, given by the Vosko, Wilk, Nusair (VWN) correlation functional [237], E_x^{HF} is the Hartree-Fock exact exchange energy, E_x^{B} is the Becke 88 exchange energy [119] and E_c^{LYP} is the Lee, Yang, Parr correlation energy [120]. Given the

$\text{H}-\text{H}$ [Å]	$E_x[\rho]$ [eV]		$E_c[\rho]$ [eV]		$E_{xc}[\rho]$ [eV]	
	$\Phi_{RO,HS}$	$\Phi_{RO,BS}$	$\Phi_{RO,HS}$	$\Phi_{RO,BS}$	$\Phi_{RO,HS}$	$\Phi_{RO,BS}$
0.5	-14.98	-13.73	-0.24	-0.81	-15.22	-14.54
0.7*	-14.55	-13.83	-0.24	-0.68	-14.79	-14.51
1.0	-14.33	-13.98	-0.24	-0.55	-14.57	-14.53
1.5	-13.94	-13.83	-0.24	-0.40	-14.17	-14.23
2.0	-13.65	-13.61	-0.23	-0.32	-13.89	-13.93

Table 6.1: Exchange ($E_x[\rho]$), correlation ($E_c[\rho]$) and total exchange-correlation ($E_{xc}[\rho]$) energy for the RO,HS and RO,BS determinants ($\Phi_{RO,HS}$ and $\Phi_{RO,BS}$, respectively) as a function of interatomic distance in H_2. Calculations carried out using B3LYP. * indicates the optimised $\text{H}-\text{H}$ bonding distance for the singlet ground state.

data shown in Table 6.1, the focus here is placed upon the correlation part of the functional. In B3LYP, the correlation is divided into an LSDA segment, comprising 19% of the overall $E_c[\rho]$, and an 81% portion derived from the LYP functional. Whilst the full form of the functional is complex and beyond the scope of this report[4], there is an important difference in the respective spin-polarisation parameter for each functional. This parameter acts a prefactor and "weights" the correlation energy with respect to the spin polarisation of the system. In the VWN functional this factor has the form,

$$\zeta(\mathbf{r}) = \frac{\rho_{\uparrow}(\mathbf{r}) - \rho_{\downarrow}(\mathbf{r})}{\rho(\mathbf{r})} \tag{6.14}$$

whilst in the LYP functional, this factor is given by,

$$\gamma(\mathbf{r}) = 2\left(1 - \frac{\rho_{\uparrow}^2(\mathbf{r}) + \rho_{\downarrow}^2(\mathbf{r})}{\rho^2(\mathbf{r})}\right) \tag{6.15}$$

where $\rho_{\sigma}(\mathbf{r})$ is the density for spin σ and $\rho(\mathbf{r})$ is the total density. Thus, there is a difference in the treatment of the correlation energy in spin-polarised systems between the VWN and LYP functionals. More specifically, for the case of the HS H_2 system, in which $\int \rho_{\uparrow}(\mathbf{r})d\mathbf{r} = 2$, $\int \rho_{\downarrow}(\mathbf{r})d\mathbf{r} = 0$ and $\int \rho(\mathbf{r})d\mathbf{r} = 2$, Eq. 6.14 yields a value of $\zeta(\mathbf{r}) = 1$, whilst Eq. 6.15 yields a value of $\gamma(\mathbf{r}) = 0$. As a result, in the HS configuration of H_2, there is no LYP contribution to the correlation energy. In $\Phi_{RO,BS}$, in which the system maintains an identical set of MOs as that of $\Phi_{RO,HS}$, $\int \rho_{\uparrow}(\mathbf{r})d\mathbf{r} = 1$, $\int \rho_{\downarrow}(\mathbf{r})d\mathbf{r} = 1$ and $\int \rho(\mathbf{r})d\mathbf{r} = 2$. Here, $\zeta(\mathbf{r}) = 1$ and $\gamma(\mathbf{r}) = 2$. Therefore, it is possible that the observed difference in $E_c[\rho]$ between $\Phi_{RO,HS}$ and $\Phi_{RO,BS}$ may be understood in terms of the contribution from the LYP correlation functional.

In order to further examine this, the same set of H_2 systems are studied using two modified B3LYP functionals. In the first functional (denoted as B3LYP-REF), the portion of E_c^{LYP} is set to 100% ($c = 1$ in Eq. 6.13). In the second functional (denoted as B3VWN-REF), the portion of E_c^{LYP} is set to 0% ($c = 0$ in Eq. 6.13). For these sets of DFT calculations, so as to only capture the energy effects of the LYP functional in relation to the standard B3LYP formalism, the initial wavefunction used in the previous set of B3LYP calculations is also used here. Thus, only the energy and its related components are evaluated for the $\Phi_{RO,HS}$ and $\Phi_{RO,BS}$ determinants and no new wavefunction is optimised. The data related to the B3LYP-REF and B3VWN-REF approaches are presented in Tables 6.2 and 6.3, respectively. It is important to note that the principle aim of the calculations and associated discussion

[4]Readers are directed to Refs. [120, 237] for further information regarding the VWN and LYP correlation functionals.

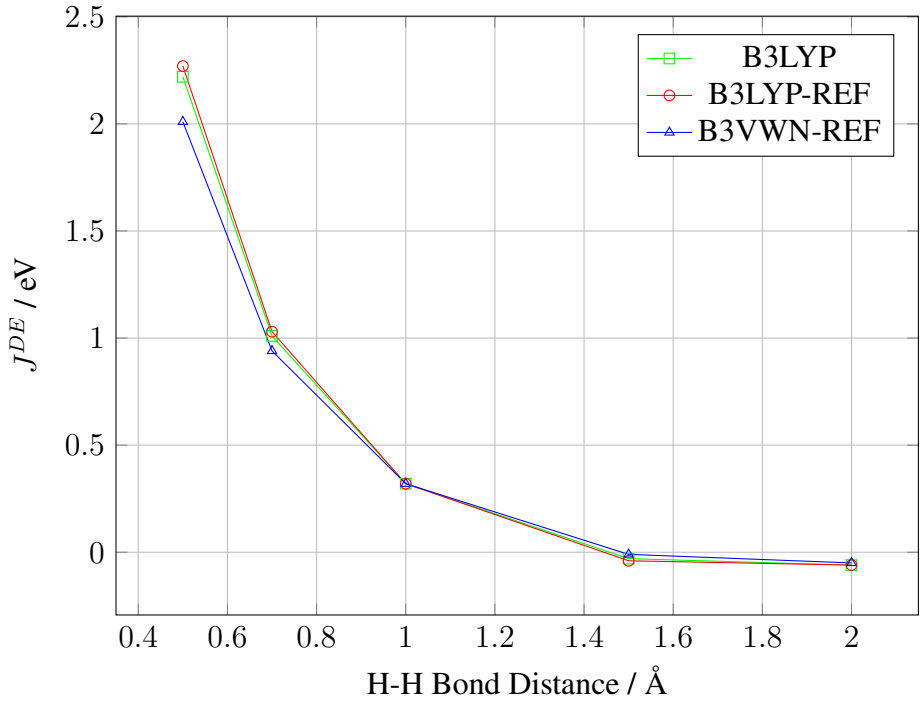

Figure 6.3: Variation in J^{DE} as a function of bond distance in H_2 for calculations carried out using the B3LYP, B3LYP-REF and B3VWN-REF approaches.

presented here is not to dispute the accuracy of the functional description of correlation, but, instead, to highlight potential limitations in the decomposition methodology, particularly related to the evaluation of J^{DE}.

H − H [Å]	$E_x[\rho]$ [eV]		$E_c[\rho]$ [eV]		$E_{xc}[\rho]$ [eV]	
	$\Phi_{RO,HS}$	$\Phi_{RO,BS}$	$\Phi_{RO,HS}$	$\Phi_{RO,BS}$	$\Phi_{RO,HS}$	$\Phi_{RO,BS}$
0.5	-14.98	-13.73	0.00	-0.54	-14.98	-14.27
0.7*	-14.55	-13.83	0.00	-0.43	-14.55	-14.26
1.0	-14.33	-13.98	0.00	-0.31	-14.33	-14.29
1.5	-13.94	-13.83	0.00	-0.16	-13.94	-13.99
2.0	-13.65	-13.61	0.00	-0.08	-13.65	-13.70

Table 6.2: Exchange ($E_x[\rho]$), correlation ($E_c[\rho]$) and total exchange-correlation ($E_{xc}[\rho]$) energy for the RO,HS and RO,BS determinants ($\Phi_{RO,HS}$ and $\Phi_{RO,BS}$, respectively) as a function of interatomic distance in H_2. Calculations carried out using the B3LYP-REF method. * indicates H_2 singlet ground state bonding distance optimised using the B3LYP approach.

Proceeding first with the B3LYP-REF approach in which the proportion of E_c^{LYP} is set to 100%, the magnitude of the $E_c[\Phi_{RO,HS}]$ reduces to $0.00\,\mathrm{eV}$ for all $\mathrm{H}-\mathrm{H}$ bond distances. This is expected given the specific form of the spin-polarisation parameter in Eq. 6.15. Given the identical form of the exchange component of the functional, there is no difference in $E_x[\rho]$ for both $\Phi_{RO,HS}$ and $\Phi_{RO,BS}$ between the B3LYP, B3LYP-REF and B3VWN-REF approaches (see Tables 6.1, 6.2 and 6.3, respectively). $E_c[\Phi_{RO,BS}]$ is markedly reduced in the B3LYP-REF approach (relative to B3LYP) at all bonding distances, suggesting that the E_c^{LYP} functional provides a considerably smaller contribution to the correlation energy than the E_c^{LSDA} functional. Indeed, examination of the data presented in Table 6.3 indicates this to be true, with an increase in $E_c[\rho]$ for both HS and BS configurations using the B3VWN-REF approach (relative to that of B3LYP). However, as was observed in the B3LYP approach (see Table 6.1), whilst there is an increase in the *magnitude* of $E_c[\Phi_{RO,HS}]$, there is a notable absence in the *variance* of the energy as a function of bonding distance, with respect to that of $E_c[\Phi_{RO,BS}]$. In addition to the data presented in the aforementioned tables, J^{DE} is also evaluated for the B3LYP-REF and B3VWN-REF approaches and is graphically presented in Fig. 6.3. As was observed with the initial B3LYP approach, for the H_2 systems, in which $E_{xc}[\Phi_{RO,HS}] > E_{xc}[\Phi_{RO,BS}]$, the evaluated J^{DE} value is negative, indicating that $E[\Phi_{RO,HS}] < E[\Phi_{RO,BS}]$.

To provide an explanation for these observed trends in the correlation energy, the association between the exchange-correlation functional and the homogenous electron gas (HEG) must be examined. In LSDA, the exchange-correlation energy is given by Eq. 2.33,

$\mathrm{H}-\mathrm{H}$ [Å]	$E_x[\rho]$ [eV]		$E_c[\rho]$ [eV]		$E_{xc}[\rho]$ [eV]	
	$\Phi_{RO,HS}$	$\Phi_{RO,BS}$	$\Phi_{RO,HS}$	$\Phi_{RO,BS}$	$\Phi_{RO,HS}$	$\Phi_{RO,BS}$
0.5	-14.98	-13.73	-1.28	-1.95	-16.26	-15.68
0.7*	-14.55	-13.83	-1.27	-1.74	-15.82	-15.57
1.0	-14.33	-13.98	-1.26	-1.57	-15.59	-15.55
1.5	-13.94	-13.83	-1.24	-1.39	-15.18	-15.22
2.0	-13.65	-13.61	-1.23	-1.31	-14.88	-14.92

Table 6.3: Exchange ($E_x[\rho]$), correlation ($E_c[\rho]$) and total exchange-correlation ($E_{xc}[\rho]$) energy for the RO,HS and RO,BS determinants ($\Phi_{RO,HS}$ and $\Phi_{RO,BS}$, respectively) as a function of interatomic distance in H_2. Calculations carried out using the B3VWN-REF method. * indicates H_2 singlet ground state bonding distance optimised using the B3LYP approach.

where $\epsilon_{xc}^{LSDA}(\rho_\uparrow(\mathbf{r}), \rho_\downarrow(\mathbf{r}))$ is the spin-dependent exchange-correlation energy per particle in an HEG. Taking the notation from Ref. [237], this energy can be alternatively represented as $\epsilon_{xc}(r_s, \zeta)$ where r_s is the Wigner-Seitz radius[5] and ζ is as defined in Eq. 6.14. Using this notation, at the boundaries of ζ, paramagnetic and ferromagnetic states may be defined, given by $\epsilon_{xc}^P(r_s)$ and $\epsilon_{xc}^F(r_s)$, respectively. Paramagnetic (ferromagnetic) contributions may also be individually defined for both the exchange and correlation energies, given by $\epsilon_x^P(r_s)$ ($\epsilon_x^F(r_s)$) and $\epsilon_c^P(r_s)$ ($\epsilon_c^F(r_s)$), respectively. Using this notation, both the exchange and correlation energy may be given by

$$\begin{aligned}\epsilon_{x/c}(r_s, \zeta) &= \epsilon_{x/c}^P(r_s) + [\epsilon_{x/c}^F(r_s) - \epsilon_{x/c}^P] f(\zeta) \\ &= \epsilon_{x/c}^P(r_s) + \Delta\epsilon_{x/c}(r_s, \zeta)\end{aligned} \tag{6.17}$$

where

$$f(\zeta) = \frac{(1-\zeta)^{4/3} + (1-\zeta)^{4/3} - 2}{2(2^{1/3} - 1)} \tag{6.18}$$

Within the HEG model, the individual electrons may be understood as occupying a set of orbitals. In the paramagnetic configuration, there are an equal number of occupied up-spin and down-spin orbitals. From a band structure perspective, this may be interpreted as the half-filling of each respective band. Within this configuration, there are many unoccupied orbitals that both the up-spin and down-spin electrons may transition into (without spin-flip processes). This manifests itself as $\epsilon_c^P(r_s)$. However, in the ferromagnetic configuration, the up-spin band is fully occupied and the down-spin band is empty. Consequently no electron transitions into unoccupied orbitals are possible and, thus, the correlation disfavours a ferromagnetic state, preferring instead the paramagnetic configuration. From this, it is possible to understand why the magnitude of $E_c[\Phi_{RO,BS}] > E_c[\Phi_{RO,BS}]$.

As a result of the analysis outlined above, it is clear that the inclusion of correlation effects, inherent in *all* density functionals, is incompatible with a correct evaluation of J^{DE}. To make progress here, the energy components related to the evaluation of J^{DE} may be modified such that only the contributions arising from the exchange interactions

[5] With respect to the homogenous electron gas (HEG), the Wigner-Seitz radius (r_s) defines the radius of sphere that contains a single electron. It is mathematically related to the electron density (ρ) by the following identity:

$$\frac{4}{3}\pi r_s^3 = \frac{1}{\rho} \tag{6.16}$$

A small r_s indicates a high density, with electrons concentrated close to one-another. Conversely, a large r_s indicates a low density with electrons, on-average, positioned further from one another.

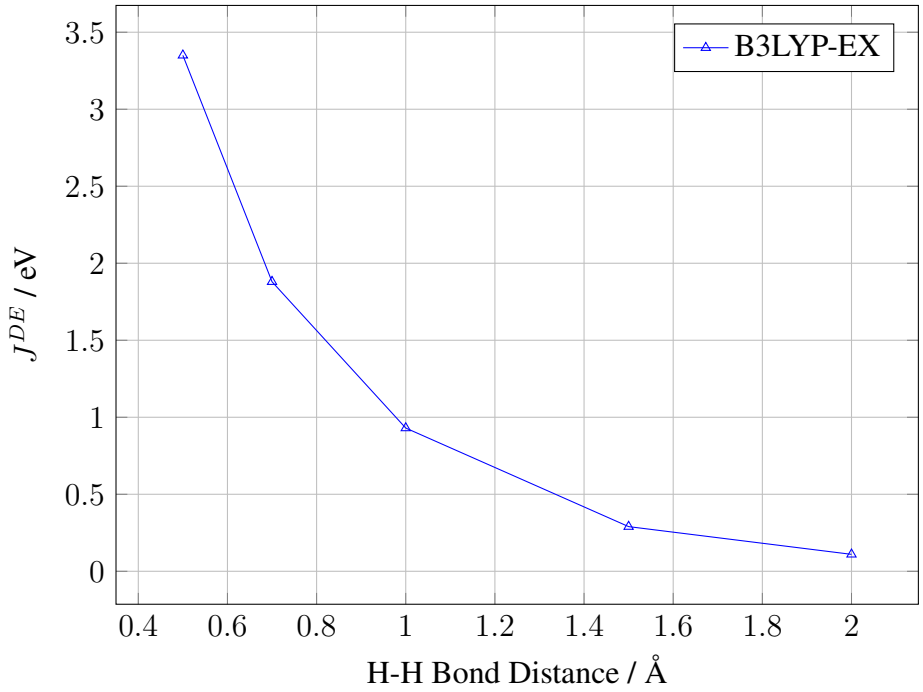

Figure 6.4: Variation in J^{DE} as a function of bond distance in H_2 for calculations carried out using the B3LYP-EX approach.

are included. Thus, within both $E[\Phi_{RO,HS}]$ and $E[\Phi_{RO,BS}]$, $E_c[\rho]$ is removed. It is important to note that this procedure is only carried out for the calculation of J^{DE} using Eq. 6.4. In calculations pertaining to both the construction of the initial wavefunctions and the subsequent evaluations of the remaining decomposition energies, $E_c[\rho]$ is *not* removed from the total energies. Thus, within this methodology, J^{DE} is defined by the DFT *exchange* energy contributions only. This procedure is denoted as the B3LYP-EX approach.

Fig. 6.4 graphically depicts the variation in J^{DE} as a function of the interatomic $\mathrm{H}-\mathrm{H}$ distance using the B3LYP-EX approach. For all bonding distances, J^{DE} is found to be positive, indicating that $E[\Phi_{RO,HS}] > E[\Phi_{RO,BS}]$. The magnitude of J^{DE} is seen to decrease with increasing distance, again in accordance with the short-range, decaying nature of the DE interaction. Thus, the analysis presented here indicates that a quantitative description of the DE interaction is available from single determinant wavefunctions, provided that the energy of these configurations is obtained using the B3LYP-EX approach (i.e. through the removal of correlation energy contributions). This approach is, therefore, used in the subsequent decomposition analysis of the TMPc systems.

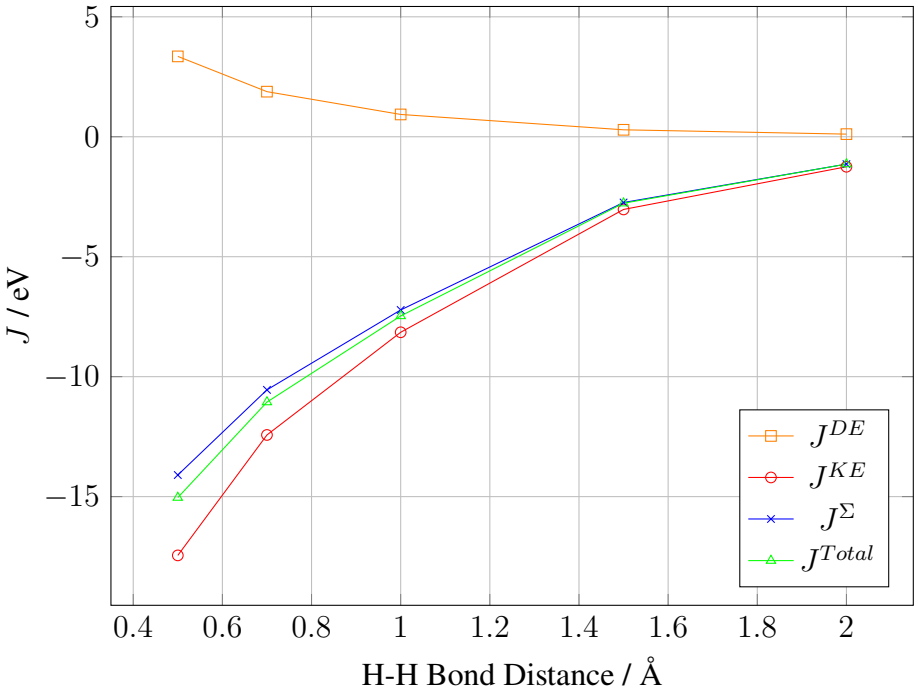

Figure 6.5: Variation in J^{DE}, J^{KE}, J^{Σ} (where $J^{\Sigma} = J^{DE} + J^{KE}$) and J^{Total} as a function of bond distance in H_2. Calculations carried out using the B3LYP-EX approach.

6.3.2 Kinetic Exchange

With regards to the J^{KE}, Fig. 6.3 shows this interaction to be the dominant contribution to the coupling at all bonding distances. However, given the use of the modified B3LYP-EX approach, as justified in the previous section, the values of J^{KE} must be readjusted to incorporate these new values of J^{DE}. Thus, Fig. 6.5 graphically depicts the variation in both J^{DE}, J^{KE}, J^{Σ} and J^{Total} as a function of the $\mathrm{H}-\mathrm{H}$ bonding distances. A maximum (minimum) value of $J^{KE} = -17.45\,\mathrm{eV}$ ($J^{KE} = -1.25\,\mathrm{eV}$) is obtained at interatomic distance of 0.5 Å (2.0 Å). The sign of the interaction indicates that $E[\Phi_{UFC,BS}] > E[\Phi_{RO,HS}]$. Given the covalent nature of the $\mathrm{H}-\mathrm{H}$ bond, the KE interaction is expected to be dominant and can be understood here as the formation of such a bond. Indeed, more generally, in systems in which the coupling is dominated by KE, the interaction may be thought of as the *stabilisation* of a "frustrated" covalent bond - one in which the overlap between the SOMOs is rather weak thus allowing the orbitals to maintain their localised character. However, in the H_2 system, the respective interatomic distance generates a more significant overlap, reorganising the orbitals such that they exhibit a delocalised, covalent character. In $\Phi_{RO,BS}$ the SOMOs are obtained from a $\Phi_{RO,HS}$ determinant that necessitates the maximal separa-

tion of the respective electrons onto each atom so as to minimise the mutual Pauli repulsion. Once this constraint is relaxed in the $\Phi_{UFC,BS}$ determinant, a significant mixing of the two orbitals occurs, accompanied by a substantial energy stabilisation.

In contrast with the evaluation of J^{DE}, here, no functional related issue is observed, with the B3LYP functional correctly capturing the expected physics of the KE interaction. Indeed, here, the inclusion of correlation is likely important in describing the coupling, given its role in covalent bond formation. Therefore, in Eq. 6.6, $E[\Phi_{RO,HS}]$ relates to the *total* energy of the respective determinant, without the removal of $E_c[\rho]$. This is an important distinction to make. Within the decomposition approach, as defined here, J^{DE} describes a specific component of the energy difference between $E[\Phi_{RO,HS}]$ and $E[\Phi_{RO,BS}]$. Thus, in the evaluation of KE interaction, the correlation energy is included within the magnitude of J^{KE}.

6.3.3 Total Exchange

As depicted in Fig. 6.5, minor variance is observed between J^{Σ} and J^{Total}. This suggests that, although the majority of the interaction within the system is captured within J^{DE} and J^{KE}, some degree of reorganisation of the MOs in the fully unrestricted determinants ($\Phi_{U,HS}$ and $\Phi_{U,BS}$) is present, resulting in the inclusion of additional energy terms not captured in the preceding calculations. Examination of the respective energies of each set of determinants indicates that there is negligible difference between $E[\Phi_{RO,HS}]$ and $E[\Phi_{U,HS}]$. This may be expected as the absence of any core (doubly occupied) orbitals dictates that the $\Phi_{RO,HS}$ and $\Phi_{U,HS}$ determinants are identical aside from the unitary transformation used to localise the SOMOs in the former determinant, a condition that is the relaxed in the unrestricted formalism. Thus the energy difference between J^{Total} and J^{Σ} must necessarily arise from the complete relaxation of the BS determinant under unrestricted conditions.

6.3.4 Summary

The decomposition of the H_2 molecule highlights both the utility and limitations of the method. In particular, the evaluation of the DE interaction using DFs, including the global hybrid functional, B3LYP, presents challenges with regards to correctly capturing the interaction. As discussed in Sec. 6.3.1, by a generating set of restricted-open determinants, $\Phi_{RO,HS}$ and $\Phi_{RO,BS}$, using the B3LYP functional, but removing the correlation energy components ($E_c[\rho]$) from $E[\Phi_{RO,HS}]$ and $E[\Phi_{RO,BS}]$ an energy difference evaluation arising

only from the direct exchange interaction between the two SOMOs is calculated. This method is denoted as the B3LYP-EX approach. Once established, the variation in J^{DE} as a function of interatomic distance is in line with expectations, decaying rapidly as the $\mathrm{H}-\mathrm{H}$ distance increased.

The subsequent evaluation of J^{KE} using the B3LYP functional indicates that KE is the dominant contribution to J^{Σ} in H_2, in accordance with expectations related to the covalent bonding in the molecule. Only minor variance between J^{Σ} and J^{Total} is observed indicating that there is very little reorganisation of the MOs beyond the $\Phi_{UFC,BS}$ determinant. However, it is important to note that, whilst the H_2 molecule presents itself as a useful system to study the relative contributions arising from the *direct* interaction between the SOMOs (DE and KE), due to the absence of any doubly occupied (core) orbitals, contributions from the SP (J^{SP}) is not investigated here. In the remainder of this chapter, the decomposition procedure is applied to a set of TMPc dimers, enabling insights into the composition of the magnetic coupling within each system.

6.4 Single TMPc Molecules

Single molecule structures of CoPc, CuPc and RhPc are fully optimised according to the computational conditions outlined in Sec. 6.2, with the full set of associated geometrical data presented in Table 6.4. Spin density isosurface plots for the three structures are displayed in Fig. 6.4.

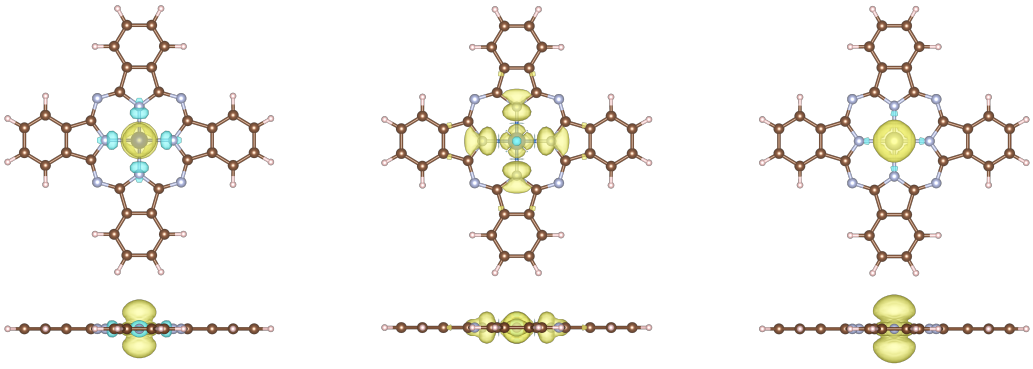

(a) (b) (c)

Figure 6.6: Spin density isosurface plots for single molecule structures of (a) CoPc, (b) CuPc and (c) RhPc. An isovalue of $0.001\ |e|$ Å^{-3} is used. Yellow (blue) shading represents regions of up-spin (down-spin) electron density.

Bond Lengths			
Label	CoPc [Å]	CuPc [Å]	RhPc [Å]
M-N1	1.928	1.957	2.013
N1-C1	1.379	1.375	1.373
C1-N2	1.322	1.326	1.330
C1-C2	1.456	1.459	1.462
C2-C3	1.396	1.396	1.395
C3-C4	1.394	1.394	1.396
C4-C5	1.409	1.409	1.407
C2-C6	1.403	1.406	1.411
Bond Angles			
Label	CoPc [°]	CuPc [°]	RhPc [°]
M-N1-C1	126.4	125.9	124.8
N1-C1-N2	127.6	127.7	127.7
C1-N2-C8	122.0	122.9	125.1

Table 6.4: Optimised bond lengths and angles for single molecule CoPc, CuPc and RhPc. Labels refer to those defined in Fig. 4.1. Note that experimental bond distances and angles for CoPc and CuPc have been omitted for clarity. These respective values may be found in Tables 4.1 and 4.5.

6.4.1 CoPc

Following a full relaxation of the geometrical coordinates, $\mathrm{Co}-\mathrm{N}$ bond distances are measured to be $1.928\,$Å with respective x-ray diffraction data reporting a value of $1.910\,$Å representing an error of 1.4% [209]. The geometrical data associated with the ligand structure (see Table 6.4) is also found to be in good agreement with available experimental references, with a maximum error of 1.1%. In addition, the geometry obtained here closely aligns with that the respective single molecule structure in Chapter 4. This is to be expected given that the same basis set and functional was employed in both sets of calculations.

With regards to the respective electronic structure, a spin $S = 1/2$ ground state is obtained. MPA indicates that a charge of $1.007\,|e|$ is localised within the d_{z^2} AO. The d_{xz}, d_{yz} and d_{xy} AOs are all doubly occupied with Mulliken charges of $1.930\,|e|$, $1.930\,|e|$ and $1.950\,|e|$, respectively. $0.693\,|e|$ is found located within the $d_{x^2-y^2}$ AO, indicating an appreciable metal-ligand hybridisation along the bonding axes. This was also reported in the single molecule calculations of CoPc in Chapter 4 and emphasises the importance of,

MPA Charge			
Atom	CoPc [$\|e\|$]	CuPc [$\|e\|$]	RhPc [$\|e\|$]
M	25.600	27.448	44.089
N1	7.772	7.813	7.625
N2	7.426	7.431	7.420
C1	5.623	5.621	5.623
C2	5.934	5.9343	5.947
C3	6.130	6.130	6.132
C4	6.089	6.089	6.088
MPA Spin			
Atom	CoPc [$\|e\|$]	CuPc [$\|e\|$]	RhPc [$\|e\|$]
M	1.036	0.638	0.988
N1	0.000	0.090	0.008
N2	0.002	0.002	0.001
C1	-0.004	-0.005	-0.002
C2	-0.001	0.005	0.000
C3	-0.001	0.000	0.000
C4	0.000	-0.001	0.000

Table 6.5: Mulliken population analysis of the charge and spin density for the single molecule structures of CoPc, CuPc and RhPc. Labels refer to those defined in Fig. 4.1.

at least partially, treating metal-ligand bonding in a covalent way. With regards to the MPA of the spin density, $1.036\,|e|$ is localised on the metal centre with the majority (92%) within the d_{z^2} AO.

6.4.2 CuPc

Within the fully optimised CuPc single molecule, the $\mathrm{Cu}-\mathrm{N}$ bond lengths are found to be 1.957 Å with respective experimental measurements, obtained from x-ray diffraction data of β-CuPc, of 1.939 Å representing an error of 0.93% [208]. With regards to the coordinate data for the ligand structure (see Table 6.4), a maximum error of 1.8% with respect to the experimental values is found indicating an acceptable accuracy in the optimisation procedure.

A spin, $S = 1/2$ ground state is obtained for the system. MPA indicated that the d_{z^2}, d_{xz}, d_{yz} and d_{xy} AOs are doubly occupied with charges of $1.983\,|e|$, $1.974\,|e|$, $1.974\,|e|$

MPA Charge			
Atomic Orbital	CoPc [$\|e\|$]	CuPc [$\|e\|$]	RhPc [$\|e\|$]
d_{z^2}	1.007	1.983	1.066
d_{xz}	1.930	1.974	1.903
d_{yz}	1.930	1.974	1.903
$d_{x^2-y^2}$	0.693	1.402	0.839
d_{xy}	1.950	1.963	1.941
MPA Spin			
Atomic Orbital	CoPc [$\|e\|$]	CuPc [$\|e\|$]	RhPc [$\|e\|$]
d_{z^2}	0.954	0.001	0.849
d_{xz}	0.011	0.003	0.010
d_{yz}	0.011	0.003	0.010
$d_{x^2-y^2}$	0.050	0.633	0.021
d_{xy}	0.004	0.001	0.002

Table 6.6: Mulliken population analysis of the charge and spin density for d AOs of the single molecule structures of CoPc, CuPc and RhPc.

and $1.950\,|e|$, respectively. A charge of $1.402\,|e|$ is localised in the $d_{x^2-y^2}$ AO, whilst the respective spin density of the orbital is found to be $0.633\,|e|$. Formally, the $d_{x^2-y^2}$ AO should have a charge of $1.00\,|e|$. Thus, the discrepancy between this formal charge and the Mulliken charge from the calculation indicates significant hybridisation along the metal-ligand bonding axes. In addition, the MPA of the spin density highlights the distribution of the unpaired electron density onto the inner portion of the ligand, with $0.090\,|e|$ measured on each of the isoindole nitrogens.

6.4.3 RhPc

With comparison to the geometry of the optimised CoPc, the $\mathrm{Rh}-\mathrm{N}$ bond distances are found to increase by 4.4% with a measured value of $2.013\,\text{Å}$. Additionally, the bonding angles associated with the central cavity are also enlarged to accommodate the larger metal ion. However, there is only minor structural changes with the remaining ligand geometry with a maximum difference (relative to CoPc) of 0.6%.

MPA of the molecular structure indicates a spin $S = 1/2$ ground state, with a charge of $1.066\,|e|$ localised within the metal d_{z^2} AO. The d_{xz}, d_{yz} and d_{xy} AOs are found to be doubly occupied with charges of $1.903\,|e|, 1.903\,|e|$ and $1.941\,|e|$, respectively. As was observed

in the MPA of CoPc, a charge of $0.839\,|e|$ is found to occupy the formally empty $d_{x^2-y^2}$ AO, once again indicating a degree of hybridisation along the metal-ligand bonding axes. A metal ion MPA spin of $0.988\,|e|$ is measured with $0.849\,|e|$ of this density located within the d_{z^2} AO.

6.5 Decomposition of the Exchange Interactions

Having established optimised structures for the three single molecules, dimeric geometries are subsequently formulated within both the α-phase ($\phi = 65°; \psi = 0°$) and β-phase ($\phi = 45°; \psi = 45°$). For both CoPc and CuPc, the interplanar distance is fixed at the experimentally determined value of $3.42\,$Å [209, 214], corresponding to a metal-metal distance of $3.77\,$Å ($4.84\,$Å) in the α-phase (β-phase). For the RhPc dimeric system, the interplanar distance of $3.70\,$Å, determined in Chapter 5, is used. This results in a metal-metal distance of $4.08\,$Å ($5.23\,$Å) in the α-phase (β-phase). In each system, the electronic ground state obtained in the single molecule calculations is used as the reference state for the dimer system. The full set of results for the decomposition study are presented in Table 6.7.

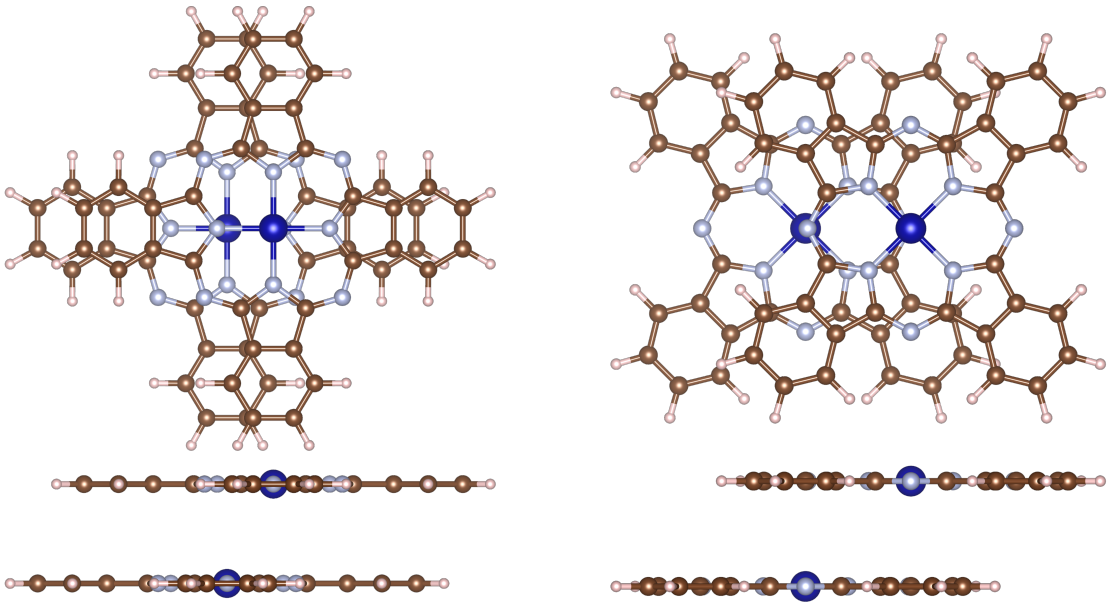

(a) (b)

Figure 6.7: Dimeric molecular geometry of the (a) α-phase and (b) β-phase configurations.

6.5.1 CoPc

As shown in Table 6.7, good agreement is found between the total coupling values and respective experimental data for both the α and β-polymorphic phases. Regarding α-CoPc, a total coupling $J^{Total} = -102.0\,\mathrm{K}$ is obtained, supported well by the $J^{Exp} = -107.0\,\mathrm{K}$ obtained from magnetic susceptibility measurements of the system [93]. The value is also in good agreement with the coupling evaluated from the periodic chain calculations in Chapter 4. Decomposing the exchange interaction into the individual components outlined above reveals a dominant KE contribution of $J^{KE} = -99.9\,\mathrm{K}$, comprising 85% of the cumulative exchange strength, J^{Σ} [6]. In addition to this, an AFM contribution from the SP of the core orbitals of $J^{SP} = -13.4\,\mathrm{K}$ is evaluated, constituting approximately 11% of J^{Σ}. The coupling strength arising from the DE interaction is found to be comparatively weak with a measured value of $J^{DE} = 3.9\,\mathrm{K}$. Comparing the value of J^{DE} calculated here with that estimated from the band structure of α-CoPc in Chapter 4, a significant difference can be observed. Given the exponential decay of the exchange integral with increasing distance, the value of J^{DE} extracted here seems more reasonable than the approximation presented in Chapter 4, and, therefore, indicates an overestimation of the KE contribution from the Hubbard parameters. This could suggest that, despite its clear *qualitative* utility in predicting increases in the coupling as a result of specific chemical modifications, the Hubbard terms provide a poor *quantitative* approximation of the coupling strength, at least for the α-CoPc system, and should not take precedence over the coupling evaluated using the total DFT energies of the two spin states (J^{BS}). This also highlights the utility of the

[6] Here the percentage component of each decomposition contribution is evaluated from the *absolute* sum of the three exchange energies. This takes into account any differences in sign.

System	J^{DE}	J^{KE}	J^{SP}	J^{Σ}	J^{Total}	J^{Exp}
α-CoPc	3.9	-99.9	-13.4	-109.4	-102.0	-107.0 [93]
β-CoPc	0.1	-0.3	-1.0	-1.2	-1.2	-1.5 [95]
α-CuPc	0.4	-0.1	-1.2	-0.9	-1.4	-1.4 [53]
β-CuPc	0.2	-0.1	-0.1	0.0	0.0	0.0 [53]
α-RhPc	42.8	-425.4	-54.1	-436.7	-393.3	-
β-RhPc	1.9	-3.2	-1.8	-3.0	-2.0	-

Table 6.7: Decomposition data for the α and β-phase polymorphs of CoPc, CuPc and RhPc. All values are given in units of temperature (K).

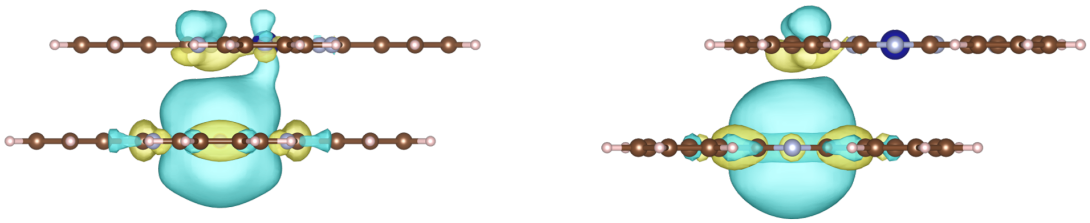

(a) (b)

Figure 6.8: Isosurface plots of the magnetic orbital extracted from the $\Phi_{UFC,BS}$ determinant for (a) α-CoPc and (b) β-CoPc. An isovalue of $0.003\,|e|$ Å^{-3} is used. Blue and yellow shading indicates relative phase. Figures reproduced from Ref. [46] with permission from the authors.

decomposition method over other prescriptions in its ability to define quantitive estimations of the exchange interactions in a consistent and explicit way.

The value of $J^{\Delta} = 7.4\,\mathrm{K}$ indicates that the total exchange coupling is well accounted for by the linear decomposition of the three individual exchange contributions. Furthermore, it emphasises the respective dominance of the KE interaction in the ordering of the α-CoPc system. As discussed in previous chapters, this strong KE term may be rationalised by the large effective orbital overlap between the singly occupied a_{1g} MOs of adjacent molecules, which energetically favours a delocalisation of the respective wavefunctions onto one another. This delocalisation effect is clearly observed in the plot of the magnetic orbital extracted from the $\Phi_{UFC,BS}$ determinant shown in Fig. 6.8(a) in which the wavefunction of the a_{1g} MO is seen to extend onto the adjacent metal centre. Regarding the quite substantial contribution from the SP term, examination of the respective spin density distributions in both the $\Phi_{UFM,BS}$ and $\Phi_{UFM,HS}$ determinants indicates a differential polarisation of the isoindole nitrogens (N_1 in Fig. 4.1). As outlined in Sec. 3.1.1, electron density of the same spin as that of the local magnetic moment will concentrate closer to the moment, whilst that of opposite spin will diffuse away. As shown in the spin density isosurface plot of CoPc (see Fig. 6.6(a)), in the ground state, electron density localised on the isoindole nitrogens is oppositely spin polarised to that of the central metal. Within the α-phase dimeric structures, the metal of each adjacent molecule is aligned axially with one of the nitrogens. In the BS configuration, the spin density of this nitrogen is the same as that of its neighbouring metal centre. However, in the HS configuration, these axially coordinated nitrogens have the opposite spin density to that of the adjacent metal centre. Thus, within this FM state, the metal centre perturbs the electron density of the nitrogen such that a region of positive spin

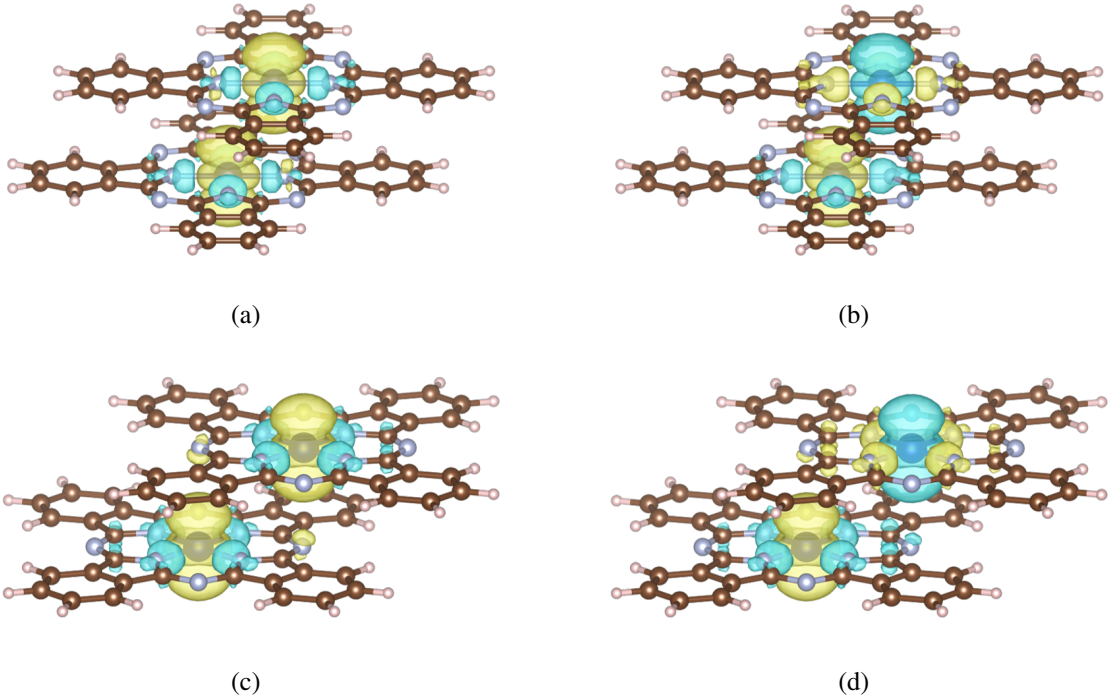

(a) (b)

(c) (d)

Figure 6.9: Spin density isosurface plots of the $\Phi_{UFM,HS}$ determinant for (a) α-CoPc and (c) β-CoPc and, the $\Phi_{UFM,BS}$ determinant for (b) α-CoPc and (d) β-CoPc. An isovalue of $0.0005\,|e|$ Å^{-3} is used. Yellow (blue) shading indicates regions of up-spin (down-spin) electron density. Figures reproduced from Ref. [46] with permission from the authors.

density forms along this axial coordinating axis (see Fig. 6.9(a)). This likely results in a higher energy spatial distribution of the electron density and explains why the contribution from J^{SP} favours antiparallel alignment of the single electrons. Thus, the AFM ordering in α-CoPc arises not only from a significant intrachain KE interaction, but also from a strong SP term, principally arising in the electron distribution of the isoindole nitrogens. It is important to note that elucidation of this intricate combination of energy contributions is not possible with a more basic analysis, such as that presented in Chapter 4, and highlights the diagnostic capabilities of the decomposition approach.

For the β-CoPc dimeric system, a significant reduction in the strength of the total coupling is observed (relative to that of its α-phase counterpart) with a value of $J^{Total} = -1.2\,\mathrm{K}$. This value is in excellent agreement with the respective experimental measurement of $J^{Exp} = -1.5\,\mathrm{K}$ [95] and is in accordance with expectations derived from the calculations carried out in Chapter 4. Additionally, a cumulative decomposition energy of $J^{\Sigma} = -1.2\,\mathrm{K}$ is obtained. With regards to the respective decomposition energies, values of $J^{DE} = 0.1\,\mathrm{K}$ and $J^{KE} = -0.3\,\mathrm{K}$ are obtained, representing 7% and 21% of J^{Σ}, respectively, whilst the

largest contribution is attributed to the SP interaction with an evaluated $J^{SP} = -1.0\,\mathrm{K}$ accounting for 71% of J^{Σ}. Additionally, no variation between J^{Total} and J^{Σ} is observed, suggesting that the exchange interactions within the system are well accounted for by the decomposition analysis. The calculated values of both J^{DE} and J^{KE} are in line with expectations. The increased metal-metal distance in the β-polymorph (relative to α-CoPc) not only results in a decrease in the DE interaction between the two metal centres (the energy of which, as a function of distance, decays rapidly), but also in the respective overlap of the orbitals resulting in a reduction in the kinetic energy stabilisation available to the system. The most consequential energy contribution evaluated for β-CoPc is that pertaining to the SP interaction. This may be expected given the axial proximity of each metal centre to the "bridging" nitrogen (N_2 in Fig. 4.1) of the adjacent molecule. As observed previously for α-CoPc, electron density of the same spin accumulates in the region around each moment. Examination of the spin density isosurface plots for $\Phi_{UFM,HS}$ and $\Phi_{UFM,BS}$ (see Figs. 6.9(c) and 6.9(d), respectively) indicates that, in the former determinant, a region of positive spin density localises on each respective axially coordinated N_2 nitrogen, whilst in the latter system, the density located at the nitrogens is of the same spin as that of its surrounding neighbours and is more spatially diffuse amongst the atoms of the inner ring. As a result of this, it is likely that the electron distribution in the $\Phi_{UFM,BS}$ determinant is of lower energy. However, it is important to note that this stabilisation is significantly weaker than that observed in the α-phase polymorph. Here, the spatial distribution of opposite spin density in the HS configuration is more extensively dispersed amongst the inner ring atoms, whilst in α-CoPc, opposite spin density was localised on the *same* nitrogen atoms, representing a more unstable electron configuration. Nevertheless, the decomposition analysis carried out here indicates that the weak AFM coupling observed in β-CoPc arises due to a dominant SP interaction, with significantly weaker contributions from both the DE and KE terms.

6.5.2 CuPc

For both polymorphic phases of CuPc, excellent agreement is found between the evaluated coupling strengths and the respective experimental measurements. For α-CuPc, a value of $J^{Total} = -1.4\,\mathrm{K}$ is obtained with the respective $J^{Exp} = -1.4\,\mathrm{K}$ [53]. With regards to the linear decomposition of the exchange interactions, a cumulative coupling strength of $J^{\Sigma} = -0.9\,\mathrm{K}$ is calculated, with DE, KE and SP components of $J^{DE} = 0.4\,\mathrm{K}$, $J^{KE} = -0.1\,\mathrm{K}$ and $J^{SP} = -1.2\,\mathrm{K}$, respectively. Both J^{DE} and J^{KE} are in alignment with expectations derived from the respective molecular geometry and spatial distribution of the magnetic orbitals. As

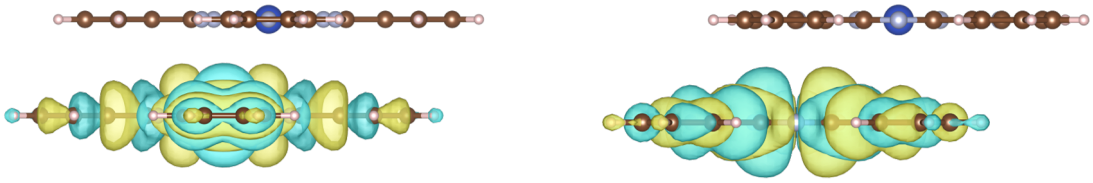

(a) (b)

Figure 6.10: Isosurface plots of the magnetic orbital extracted from the $\Phi_{UFC,BS}$ determinant for (a) α-CuPc and (b) β-CuPc. An isovalue of $0.003\,|e|$ Å^{-3} is used. Blue and yellow shading indicates relative phase. Figures reproduced from Ref. [46] with permission from the authors.

a result of in-plane structure of the $d_{x^2-y^2}$-derived b_{1g} SOMO, the inter-boundary distance (the distance between the outermost extents of each adjacent orbital) is greater in α-CuPc than in α-CoPc. This not only leads to a reduction in the magnitude of the DE coupling between the two orbitals, but also minimises inter-orbital overlap, thus suppressing KE interactions. Thus, the dominant intrachain exchange interaction in α-CuPc arises due to the polarisation of the core orbitals. Once again, this coupling favours AFM alignment of the magnetic moments. Examining the spin density plots of the $\Phi_{UFM,HS}$ and $\Phi_{UFM,BS}$ determinants (Figs. 6.11(a) and 6.11(b), respectively), at an isovalue of $0.0005\,|e|$ Å^{-3}, an isotropic region of electron density with opposite spin to that of the singly occupied b_{1g} MO surrounds the orbital. In the BS configuration, this region localised at each moment is of the same spin as that of the adjacent molecule's axially aligned isoindole nitrogens, whilst in the HS configuration they are of opposite spin to one another. Thus, in the former spin configuration it is possible that a weak exchange interaction between the metal and axial nitrogen is present that does not occur in the HS configuration. Indeed, examination of the individual energy components of both determinants indicates that the magnitude of the DFT exchange energy is marginally greater in the $\Phi_{UFM,BS}$ determinant than in that of the $\Phi_{UFM,HS}$. Thus, from the decomposition analysis, the dominant interaction in the weak AFM coupling of α-CuPc is that of SP.

With regards to β-CuPc, a paramagnetic system is obtained with a $J^{Total} = 0.0\,\mathrm{K}$, in agreement with experimental measurement which also reported a paramagnetic state with $J^{Exp} = 0.0\,\mathrm{K}$ [53]. The cumulative coupling from the decomposition is found to be $J^{\Sigma} = 0.0\,\mathrm{K}$, indicating that the methodology accounts for all exchange interactions in the system. With respect to the individual contributions, values of $J^{DE} = 0.2\,\mathrm{K}$,

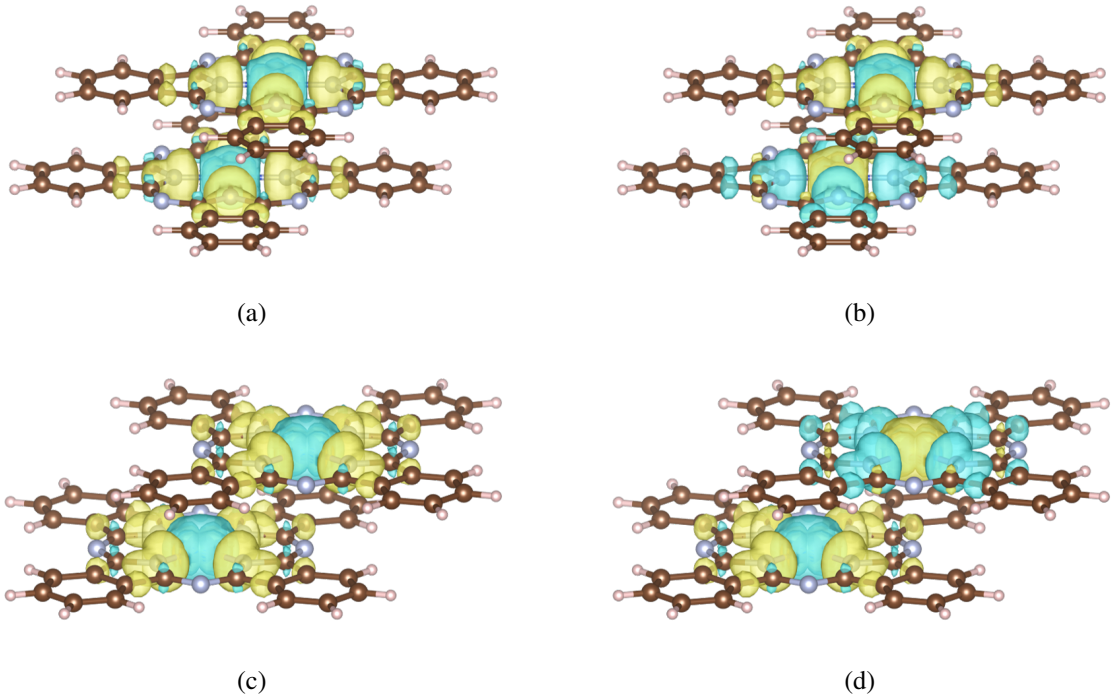

(a) (b)

(c) (d)

Figure 6.11: Spin density isosurface plots of the $\Phi_{UFM,HS}$ determinant for (a) α-CuPc and (c) β-CuPc and, the $\Phi_{UFM,BS}$ determinant for (b) α-CuPc and (d) β-CuPc. An isovalue of $0.0005\,|e|$ Å^{-3} is used. Yellow (blue) shading indicates regions of up-spin (down-spin) electron density. Figures reproduced from Ref. [46] with permission from the authors.

$J^{KE} = -0.1\,\mathrm{K}$ and $J^{SP} = -0.2\,\mathrm{K}$ are obtained. It may be considered unsurprising that the value of J^{KE} is the same as that of α-CuPc given the in-plane spatial distribution of the respective SOMOs. The decrease in J^{DE} (relative to the α-phase) reflects the increased metal-metal distance in the β-polymorph. Regarding the SP interaction, a significant reduction in the respective magnitude of J^{SP}, relative to that of α-CuPc, is observed. Once again, analysing the spin density isosurface plots for the $\Phi_{UFM,HS}$ and $\Phi_{UFM,BS}$ determinants (Figs. 6.11(c) and 6.11(d), respectively), the relative axial alignment of the metal centre with the N_2 of the adjacent molecule does not exhibit a differential exchange effect akin to that observed in α-CuPc. This is likely due to a reduced polarisation of the electron density located on N_2.

6.5.3 RhPc

For the RhPc dimeric system, a significant increase in the magnitude of both the total coupling and linear decomposition components is observed, relative to the respective data

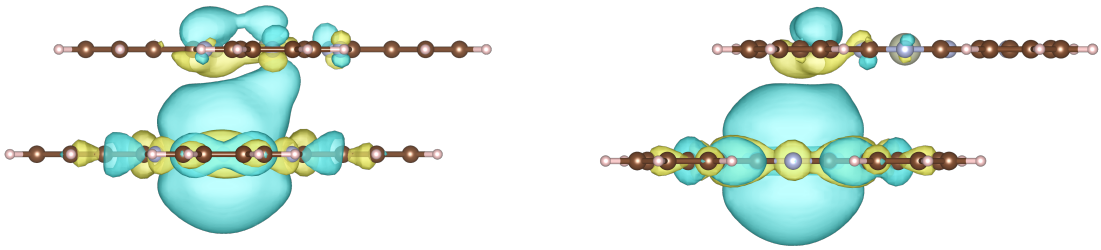

(a) (b)

Figure 6.12: Isosurface plots of the magnetic orbital extracted from the $\Phi_{UFC,BS}$ determinant for (a) α-RhPc and (b) β-RhPc. An isovalue of $0.003\,|e|$ Å^{-3} is used. Blue and yellow shading indicates relative phase.

for the CoPc and CuPc systems. For α-RhPc, a total coupling of $J^{Total} = -393.3\,\mathrm{K}$ is obtained. This is in good agreement with the total coupling $J^{BS} = -391.0\,\mathrm{K}$ evaluated for α-RhPc in Chapter 5 With regards to the decomposition analysis of the system, a $J^{\Sigma} = -436.7\,\mathrm{K}$ is obtained. This results in a value of $J^{\Delta} = 43.4\,\mathrm{K}$ indicating that additional unaccounted for higher-term exchange interactions may be present. Values of $J^{DE} = 42.8\,\mathrm{K}$, $J^{KE} = -425.4\,\mathrm{K}$ and $J^{SP} = -54.1\,\mathrm{K}$ are evaluated for the system. With comparison to the decomposition of α-CoPc, the significant increase in both J^{DE} and J^{KE} is expected given that there is a greater radial extent of the respective a_{1g} SOMOs even despite the increase in the interplanar distance applied to rhodium system. Indeed inspection of the magnetic orbital in the $\Phi_{UFC,BS}$ determinant (see Fig. 6.12(a)) reveals an increase in the delocalisation with far greater mixing of basis functions localised on the adjacent molecule. Interestingly, in contrast to that of α-CoPc, good agreement is obtained for the value of J^{KE} calculated here using the decomposition method and that evaluated in Chapter 5 using the Hubbard parameters extracted from the dispersion plot of the periodic chain. The difference between the two values is $7.6\,\mathrm{K}$. This suggests that the Hubbard parameters may provide a more accurate estimation of the KE interaction in the RhPc system than in the CoPc system. With comparison to the decomposition of α-CoPc, a substantial increase in the magnitude of J^{SP} is observed. Examination of the spin density isosurface plots for the $\Phi_{UFM,HS}$ and $\Phi_{UFM,BS}$ determinants (see Figs. 6.13(a) and 6.13(b), respectively) suggests that the mechanism by which AFM coupling is favoured within this term is similar to that of α-CoPc, where the polarisation of the isoindole nitrogens (N_1) produces a lower energy spin configuration in the antiparallel state relative to its parallel counterpart. However, for the α-RhPc system, the increased radial extent of the a_{1g} SOMOs

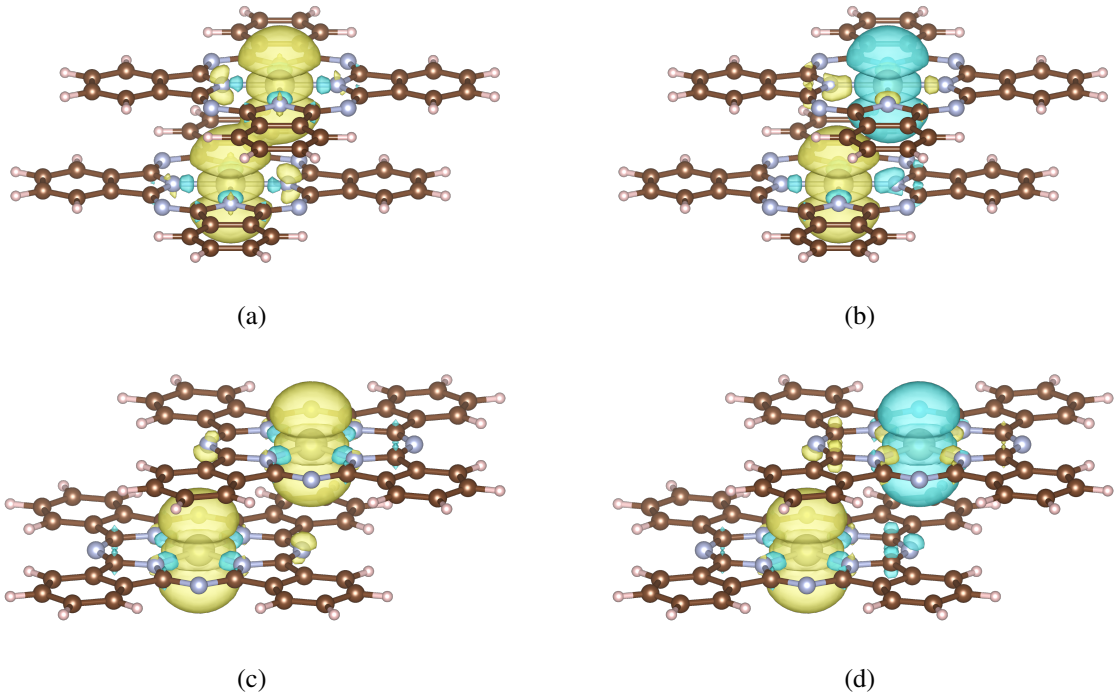

(a) (b)

(c) (d)

Figure 6.13: Spin density isosurface plots of the $\Phi_{UFM,HS}$ determinant for (a) α-RhPc and (c) β-RhPc and, the $\Phi_{UFM,BS}$ determinant for (b) α-RhPc and (d) β-RhPc. An isovalue of $0.0005\,|e|$ Å^{-3} is used. Yellow (blue) shading indicates regions of up-spin (down-spin) electron density.

likely amplifies the effect, thereby increasing the magnitude of the respective value of J^{SP}.

With regards to the decomposition analysis of β-RhPc, a total coupling value of $J^{Total} = -2.0\,\mathrm{K}$ is obtained, whilst a cumulative coupling of $J^{\Sigma} = -3.0\,\mathrm{K}$ is calculated. With comparison to the results obtained in Chapter 5, close agreement is found between J^{Total} and the evaluated $J^{BS} = -2.4\,\mathrm{K}$. However, some discrepancy between the J^{Total} and J^{Σ} is observed here, suggesting that, similarly to its α-phase counterpart, there may be additional exchange terms contributing to the coupling of the system that are unaccounted for in the linear decomposition. For the individual components of the decomposition analysis, values of $J^{DE} = 1.9\,\mathrm{K}$, $J^{KE} = -3.2\,\mathrm{K}$ and $J^{SP} = -1.8\,\mathrm{K}$ are computed. Both J^{DE} and J^{KE} terms are in accordance with expectations: the diffuse nature of the a_{1g} SOMOs results in not only a decrease in the inter-orbital distance but also an enhancement in the orbital overlap (relative to that of β-CoPc). Given the difference in the respective stacking angle, ϕ, between α-RhPc and β-RhPc, the reduction in the magnitudes of the DE and KE terms in the latter system are also consistent with an understanding of the relationship between the structural geometry and exchange mechanism. Interestingly, whilst the SP

term evaluated for β-RhPc indicates a preference for the LS configuration, the difference in its magnitude relative to the value of J^{SP} extracted for β-CoPc is smaller than those of J^{DE} and J^{KE}. Given the enhanced polarising effect in α-RhPc, relative to its CoPc counterpart, it may be expected for this trend to extend to the β-phase system. However, comparing the spin density isosurface plots of β-RhPc (Figs. 6.13(c) and 6.13(d)) with those of β-CoPc (Figs. 6.9(c) and 6.9(d)), a reduction in the polarisation of the ligand structure in both determinants of the former system can be observed. Thus, although there is a clear differential polarisation of the N_2 atom, the decrease in general polarisation may result in the lack of a significant preference for one spin configuration over the other. Nevertheless, despite its small magnitude, the term clearly favours an AFM configuration in line with the expectations derived from the decomposition of β-CoPc.

6.6 Conclusions

Within this chapter, a comprehensive examination of the decomposition method has been carried out. Initially, the procedure was applied to a simple H_2 molecule, facilitating an extensive analysis of its use within DFT and, in particular, alongside the B3LYP DF. The results of the study indicated that an evaluation of the DE coupling constant, J^{DE}, from the total energies of the RO,HS and RO,BS determinants ($\Phi_{RO,HS}$ and $\Phi_{RO,BS}$, respectively) was inconsistent with the underlying assumptions about the FM nature of the interaction. By inspecting the individual energy components of each determinant, it was found that the inclusion of a correlation term within the DF resulted in the destabilisation of the HS configuration (relative to the BS state). Thus the J^{DE} term, as stipulated in the original formulation of the methodology, was not only a measure of the DE interaction, but also included electron correlation terms. In order to account for this and, in doing so, provide a formalism that generated consistent results, the correlation energy component was removed from the total energies of both restricted-open determinants in Eq. 6.4. Subsequent results obtained for both the DE and KE interactions in H_2 were in accordance with expectations. This altered methodology was denoted the B3LYP-EX approach.

Having constructed a consistent decomposition procedure, the method was subsequently applied to dimer structures of CoPc, CuPc and RhPc. The principle aim of this investigation was to assess the utility of such an approach to accurately capture the exchange interactions within each system and, in doing so, provide a detailed description of the mechanisms by which the respective magnetic ordering arises. The results of the study indicated that the

KE interaction dominated in the α-polymorph of both CoPc and RhPc, whilst in α-CuPc, the in-plane geometry of the $d_{x^2-y^2}$-derived b_{1g} SOMOs suppressed J^{KE}, with the AFM coupling of the system instead arising as a result of an SP term. Given the larger, more diffuse nature of the $4d$ orbitals, the increased magnitude of not just J^{KE}, but also J^{DE} and J^{SP} in both polymorphs of RhPc (relative to their CoPc counterparts) was in accordance with expectations. The reduction in the magnitude of both the DE and KE terms in the β-phase of CoPc and RhPc (relative to the α-polymorphs) also agreed well with the previous understanding of the relationship between metal-metal distance (augmented by the system stacking geometry) and coupling strength. One considerable advantage of the decomposition analysis of the TMPc systems over the analysis carried out in Chapters 4 and 5 is the quantitative evaluation of SP interactions within each system. In α-CoPc, the analysis indicated that the strong AFM coupling in the system arises not only as a result of a dominant KE interaction, but also a substantial polarisation of the core orbitals. Furthermore, analysis of the spin density of the respective $\Phi_{UFM,HS}$ and $\Phi_{UFM,BS}$ determinants identified the source of the polarisation as being principally localised on the axially coordinated isoindole nitrogens of each molecule. This had not been previously reported upon and highlights the utility of the methodology.

Whilst the decomposition approach has been successfully applied for a number of bi-nuclear transition metal complexes, the study presented here is the first application of the procedure for a dimeric system in which the magnetic centres reside on two separate molecules. The resulting data not only aligned well with previous experimental and theoretical measurements of the magnetic coupling in each system, but also contributed to a more comprehensive understanding of the interplay between underlying exchange mechanisms. The next logical progression would be to expand the scope of the study to include the remaining magnetic first row TMPcs. The variability in both magnitude and type of coupling observed amongst this group would provide an excellent opportunity to further validate the capabilities of this decomposition approach.

7

The Magnetic Coupling in Polymeric Phthalocyanines

As outlined within the contextual information presented in Chapter 1, an alternative structural form of the TMPc system presents itself as polymeric transition metal phthalocyanines (poly-TMPcs). These systems exist as 2D periodic sheets in which the outer benzene rings of each molecule are shared between itself and its neighbours (see Fig. 7.1). Theoretical characterisations of the materials have revealed a range of magnetic properties, including strong AFM interactions in poly-CrPc and poly-FePc, and significant FM coupling in poly-MnPc [67]. Theoretical evaluations of the set of first row poly-TMPc systems have previously been carried out. However, within these studies, the electronic structure has been calculated using PW basis sets and a GGA+U formalism and, thus, is dependent upon the *ad hoc* choice of the U parameter. No study has made use of hybrid functionals, which have been shown to more accurately capture the electronic structure of highly correlated materials, nor has there been modelling of such systems using GTO-type basis sets. The studies presented in the previous chapters of this report have highlighted the accuracy that hybrid functionals and GTO-type basis sets can achieve with respect to the electronic and magnetic

properties of TMPc systems. In this chapter, the hybrid-exchange BS-DFT methodology is extended to the set of first row poly-TMPcs. The aim of this study is to not only evaluate the precision of the method with respect to previous experimental and theoretical examinations, but also to offer a different approach to the analysis of this group of correlated materials. Furthermore, by including an investigation into this family of systems and, in particular, their magnetic properties, readers will be provided with a more complete picture of the magnetism within metal phthalocyanines.

The remainder of this chapter is divided as follows: in Sec. 7.1, the computational details used in the calculations carried out in this study are outlined; in Sec. 7.2, the general unit cell of the poly-TMPc system is described; Sec. 7.3 presents the results and associated discussion of the electronic structure of each system studied; Sec. 7.4 details the magnetic interactions and properties of each poly-TMPc; finally in Sec. 7.5, concluding remarks for the chapter are offered.

7.1 Computational Details

All-electron spin-polarised DFT calculations are carried out within the CRYSTAL23 [141] solid-state simulation package. All atoms are described by local GTOs of double-ζ quality augmented with a set of polarisation functions (DZVP) (see Appendix A). The B3LYP global hybrid [120, 129] functional is employed throughout. All SPE and geometry optimisation calculations are converged to an iterative energy difference of 10^{-7} Ha. Overlap tolerances for the Coulomb and exchange integrals are set to 10^{-8}. As in the calculations carried out in Chapters 4 and 5, 30% of the previous Fock matrix is mixed into the updated Hamiltonian in order to accelerate convergence. In addition, the DIIS convergence accelerator scheme [190, 191] is used within the SCF process. Sampling of k-points in the FBZ is carried out in accordance with the Monkhorst-Pack method [192], using a shrinking factor of 10 [193]. The dispersion spectrum is calculated in CRYSTAL23 and visualised using a python-based package [205]. Spin density isosurface plots are produced in the VESTA3 visualisation program [206].

7.2 Unit Cell

For all systems studied, the unit cell is derived from the respective optimised single molecules. The initial structure is obtained from the optimised CoPc system in Chap-

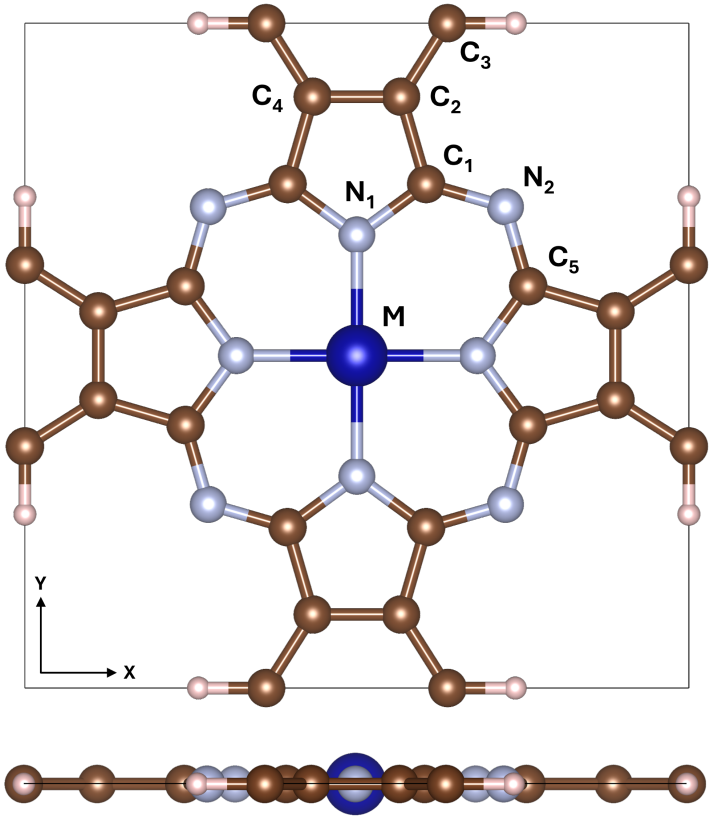

Figure 7.1: Structural geometry of the unit cell for the poly-TMPc systems with labelled atoms. These systems are laterally periodic and extend as a 2D surface. Note that atom colours refer to those defined in Fig. 1.2(b).

ter 4 with replacement of the respective metal prior to coordinate optimisation. Following the full relaxation of the single molecule coordinates the unit cell is constructed as shown in Fig. 7.1. Exploiting the D^1_{4h} square lattice symmetry of the unit cell, a full optimisation of both atomic positions and lattice parameters is then carried out to generate the final optimised polymeric transition metal phthalocyanine (poly-TMPc) unit cells. In Table 7.2 the full set of atom coordinate data is displayed for each system studied, whilst the respective lattice parameter data is presented in Table 7.1. Whilst experimental reference data is not available for all the systems studied here, an experimental evaluation of poly-MnPc sheets reported a square structure with a periodic lattice parameter $(11.0 \pm 0.5\,\text{Å})$ [65], in good agreement with the respective values obtained here. Additionally, a theoretical PW based study employing the PBE functional reported a general poly-TMPc lattice parameter of 10.67 Å [66]. Within the D^1_{4h} symmetry environment, the d AOs transform into MOs of the following symmetry: $a_{1g}(d_{z^2})$, $e_g(d_{xz}, d_{yz})$, $b_{2g}(d_{xy})$ and $b_{1g}(d_{x^2-y^2})$. Given the structural

System	a [Å]	b [Å]	α [°]	β [°]
CoPc	10.64	10.64	90	90
CuPc	10.69	10.68	90	90
MnPc	10.66	10.66	90	90
FePc	10.66	10.66	90	90
CrPc	10.73	10.73	90	90

Table 7.1: Lattice dimensions for the unit cell of each poly-TMPc.

similarity between the poly-TMPc unit cell and the single molecule TMPc, it is justifiable to infer the same energetic splitting of the d-derived MOs due to the ligand crystal field. As a result, the $a_{1g},\ e_g$ and b_{2g} MOs are expected to be fully occupied before subsequent filling of the b_{1g} MO. The ground electronic state of each system is shown in Table 7.3 alongside respective MPA analysis of the spin and charge density. For each system, the band structure and spin density isosurface is plotted. In the dispersion plots, three segments in the two dimensional reciprocal space are sampled: $\Gamma \rightarrow X, X \rightarrow M, M \rightarrow \Gamma$, where, in coordinates of (k_x, k_y), $\Gamma = (0,0), X = (1,0)$ and $M = (1,1)$.

7.3 Electronic Structure

In this section, the electronic structure is examined for each poly-TMPc system. Data related to the ground state configuration and band structure is included, with appropriate discussion. The unit cell structure is used here throughout.

7.3.1 poly-CoPc

In poly-CoPc, an $S = 1/2$ unit cell is generated with the single electron residing within a d_{z^2}-derived a_{1g} band. The metal-nitrogen bond distances are measured to be 1.931 Å, in relatively good agreement with the respective experimental measurements of 1.910 Å evaluated on β-CoPc crystals [209]. Figs. 7.2(a) and 7.5(a) depict the band structure plot and spin density isosurface, respectively. The distribution of the spin density is similar to that of the single molecule structure analysed in Chapter 4. The system is found to converge into an insulating state with an up-spin (down-spin) direct band gap of $0.63\,\mathrm{eV}$ ($0.67\,\mathrm{eV}$) at the M-point in the FBZ. This value is much reduced relative to the system single chain counterpart, reflecting the lateral delocalised nature of the frontier bands. At the Γ-point, the occupied (unoccupied) a_{1g} bands are found $4.26\,\mathrm{eV}$ ($2.14\,\mathrm{eV}$) below (above) E_F, yield-

Bond Lengths					
Label	CoPc [Å]	CuPc [Å]	MnPc [Å]	FePc [Å]	CrPc [Å]
M-N1	1.931	1.958	1.946	1.942	1.986
N1-C1	1.379	1.375	1.393	1.379	1.378
C1-N2	1.322	1.326	1.322	1.325	1.329
C1-C2	1.455	1.457	1.446	1.454	1.458
C2-C3	1.394	1.394	1.394	1.394	1.394
C2-C4	1.416	1.419	1.423	1.419	1.423
Bond Angles					
Label	CoPc [°]	CuPc [°]	MnPc [°]	FePc [°]	CrPc [°]
M-N1-C1	126.3	125.8	126.1	126.2	125.4
N1-C1-N2	127.7	127.7	127.4	127.6	127.4
C1-N2-C5	122.1	123.0	122.9	122.5	124.3

Table 7.2: Structural data for both bond lengths and angles for all poly-TMPc systems studied. Labels refer to those of Fig. 7.1.

ing an estimate of the effective on-site repulsion, $U = 6.40\,\mathrm{eV}$, which closely aligns with that of molecular CoPc. Only a slight variance in the energy of the band across the k-point segments is observed, with a band width of $W = 0.12\,\mathrm{eV}$ ($W = 0.01\,\mathrm{eV}$) in the $a_{1g\uparrow}$ ($a_{1g\downarrow}$) band. The similarity in the relative energies of the a_{1g} bands with respect to those of the single molecule system, reflects the respective shape of the SOMO. Its alignment perpendicular to the molecular plane results in very little lateral interaction with surrounding ligand MOs, and thus similarity in the energetics of these SOMO bands in both the molecular and polymeric configurations should be expected.

7.3.2 poly-CuPc

In poly-CuPc, an $S = 1/2$ unit cell is generated with the single electron found in a $d_{x^2-y^2}$-derived b_{1g} band. As before, plots of the respective band structure and spin density isosurface are generated (see Figs. 7.2(b) and 7.5(b)). Once again, the spin density shows much similarity with that of the single molecule structure with the distribution characterised by a $d_{x^2-y^2}$ orbital shape. An insulating state with an up-spin (down-spin) direct band gap of $0.56\,\mathrm{eV}$ ($0.62\,\mathrm{eV}$) at the M-point is found, representing a sizeable reduction in the energy gap relative to that of the CoPc molecular chain structure. At the Γ-point, the occupied (unoccupied) b_{1g} bands are found $2.48\,\mathrm{eV}$ ($1.66\,\mathrm{eV}$) below (above) E_F resulting in

System	Moment [μ_B]	Metal Spin [e]	Ground State
CoPc	1	1.03	$(a_{1g})^1(e_g)^4(b_{2g})^2$
CuPc	1	0.64	$(a_{1g})^2(e_g)^4(b_{2g})^2(b_{1g})^1$
MnPc	3	3.54	$(a_{1g})^1(e_g)^3(b_{2g})^1$
FePc	2	1.93	$(e_g)^2(b_{2g})^2(a_{1g})^2$
CrPc	4	3.73	$(a_{1g})^1(e_g)^2(b_{2g})^1$

Table 7.3: Total magnetic moment and spin density localised to each metal, and electronic ground state configuration for each poly-TMPc.

$U = 4.14\,\mathrm{eV}$, whilst the band width is measured to be $W = 0.75\,\mathrm{eV}$ ($W = 0.16\,\mathrm{eV}$). The value of U obtained here is in good agreement with that calculated in both the molecular and chain geometries of CuPc (see Chapter 4). Additionally, the variance in band energies here are more significant than that observed in poly-CoPc, reflective of the symmetry of the b_{1g} SOMO which lies within the plane of the molecule. However, interactions here are still relatively minimal as the b_{1g} MOs exhibits σ, rather than π-type bonding, which limits the set of ligand MOs that it may couple with. This is particular evident in the $b_{1g\downarrow}$ band, where ligand bands with similar energy profiles are all π-type MOs with e_g symmetry.

7.3.3 poly-MnPc

For poly-MnPc, the generated unit cell is found to have a spin $S = 3/2$ with three unpaired electrons distributed amongst the a_{1g}, e_g and b_{2g} MOs (see Table 7.3). This is in contrast with the electronic configuration of molecular MnPc obtained from the β-phase crystal structure, in which the e_g MOs are doubly occupied and the overall system exhibits an ${}^4A_{2g}$ ground state (see Table 1.1). The reason for the discrepancy here is the absence of any axial coordinating ligand in the poly-MnPc system, which is believed to stabilise the observed configuration in the periodic single chain structures of MnPc [85]. Spin density isosurface and band structure plots are presented in Figs. 7.3(a) and 7.5(c), respectively. In the up-spin channel, an insulating state is realised with a direct energy band gap of $0.46\,\mathrm{eV}$ located at the M-point in the FBZ. At this crystal momentum value, the valence and conduction bands are of a_{1u} and e_g symmetry, respectively. The valence band is ligand derived, whilst the degenerate pair of conduction bands show contributions from the manganese $d_{xz/yz}$ orbitals, adopting an anti-bonding configuration with the ligand π MOs. In the valence band, the lowest energy state is found at the Γ-point, where the wavefunction is maximally delocalised across the lattice. As the crystal momentum is augmented towards the M-point,

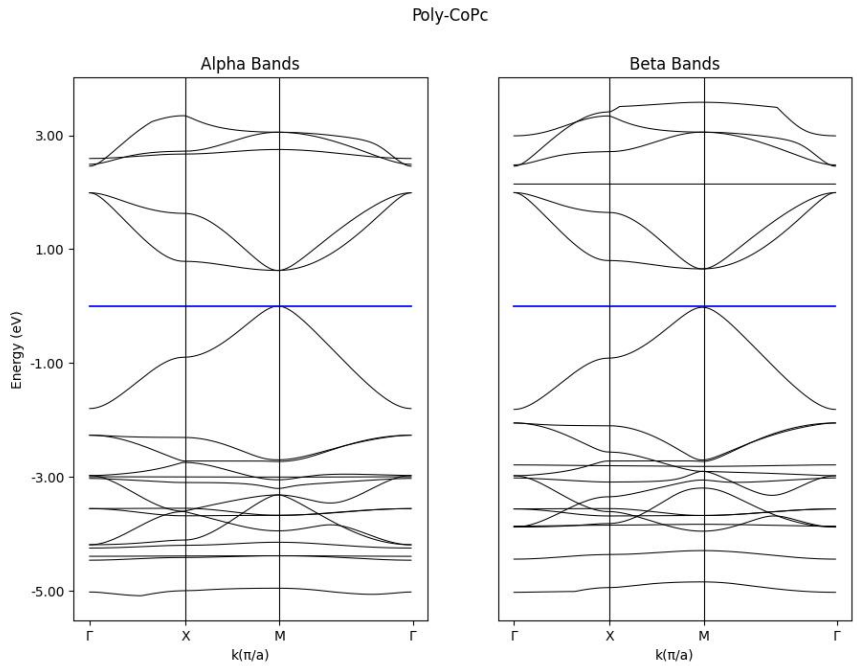

(a)

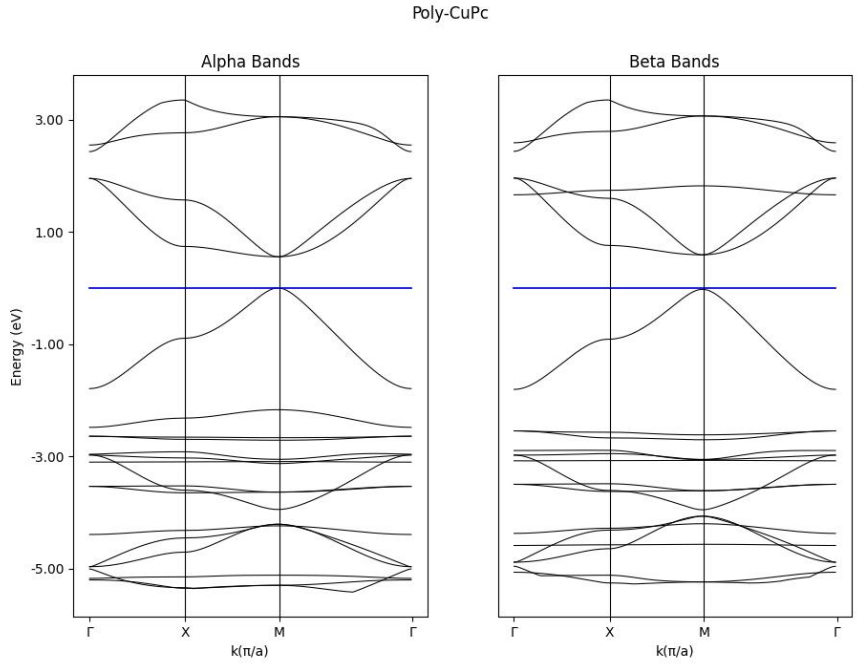

(b)

Figure 7.2: Band structure plots for (a) poly-CoPc and (b) poly-CuPc. E_F is set to $0\mathrm{eV}$ and denoted by a blue highlighted line.

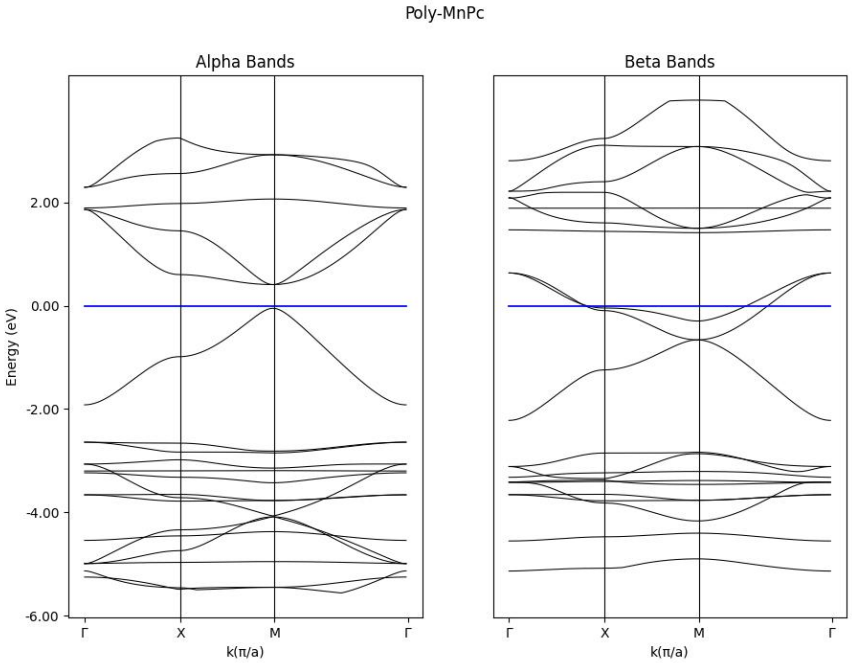

(a)

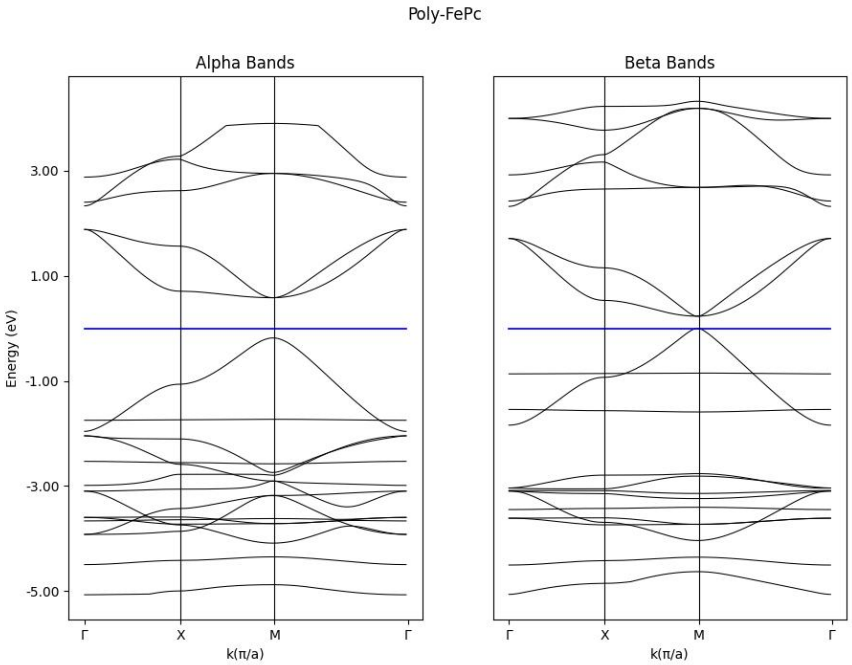

(b)

Figure 7.3: Band structure plots for (a) poly-MnPc and (b) poly-FePc. E_F is set to $0\mathrm{eV}$ and denoted by a blue highlighted line.

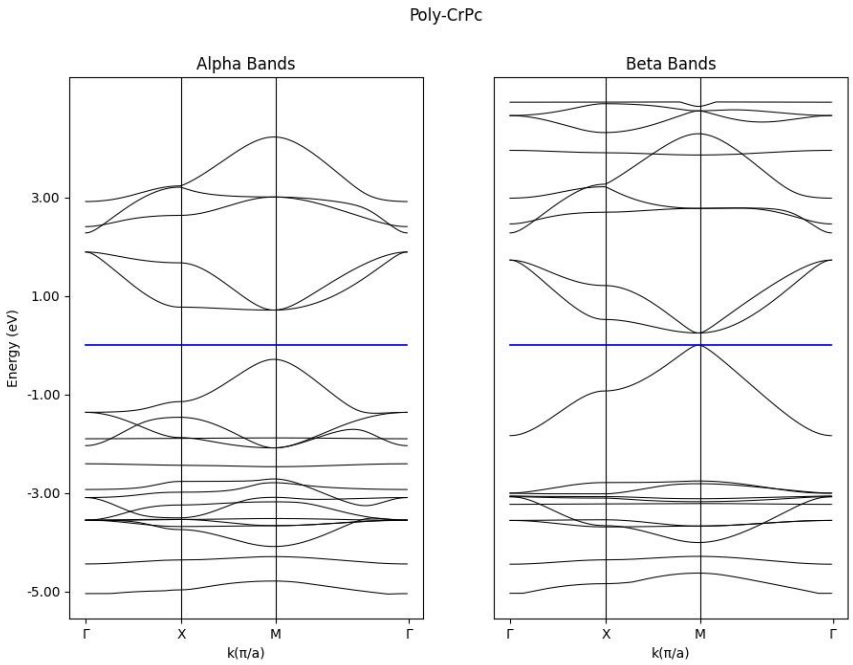

Figure 7.4: Band structure plot for poly-CrPc. E_F is set to $0\,\mathrm{eV}$ and denoted by a blue highlighted line.

the wavefunction becomes more localised and, thus, the relative energy of the band is raised. In the conduction band, the opposite case is observed. The anti-bonding e_g bands are localised at the Γ-point and delocalised at the M-point, thus, generating the observed band shape.

In the down-spin channel, the band structure exhibits half-metallicity with a set of two conducting bands. These bands become conducting as the crystal momentum changes from Γ to X, with the band minima being found at the M-point. Examination of the AO contributions to these bands indicates the presence of manganese $d_{xz/yz}$ AOs. In the square D^1_{4h} symmetry environment, these two d-orbitals are degenerate and "share" the single down-spin electron. Indeed, the MPA indicates that each of the AOs has a spin density of $\sim 0.75\,|e|$, a value slightly larger than the expected $0.5\,|e|$, but nevertheless indicative of a delocalisation of the remaining single electron density across the two AOs. This can also be understood as a "hole" shared between the two orbitals. At the Γ-point the down-spin valence band is of a_{1u} symmetry, with the respective conduction bands characterised by e_g symmetry. As was observed in the up-spin channel, as the crystal momentum changes, the energy of the valence band is raised, whilst that of the conduction band is lowered. However, in the down-spin channel, due to the presence of the hole in the $d_{xz/yz}$ orbitals and

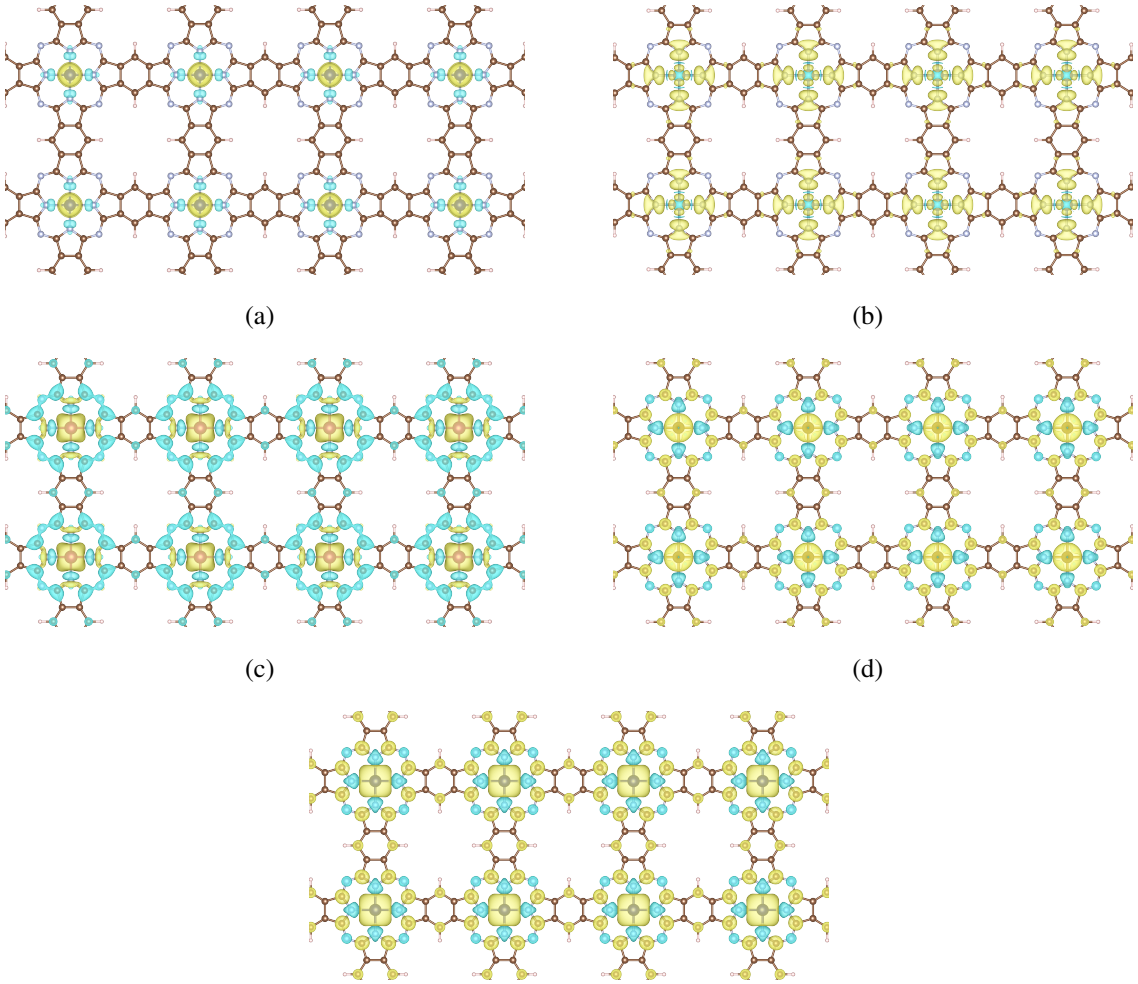

Figure 7.5: Spin density isosurface plots for the unit cell of (a) poly-CoPc, (b) poly-CuPc, (c) poly-MnPc, (d) poly-FePc and (e) poly-CrPc. An isovalue of $0.001\,|e|$ Å^{-3} is used. Yellow (blue) shading indicates regions of up-spin (down-spin) electron density.

their significant hybridisation with the ligand π-conducting electronic levels, the energy of this band falls below E_F and conductance is realised. In the up-spin channel, whilst the phase and shape of the crystalline orbital (CO) of the conducting and valence bands change in a similar way to that of its down-spin counterpart, the full occupation of the two $d_{xz/yz\uparrow}$ orbitals results in no empty levels and, thus, restricts any conductance.

It is important to note that the degeneracy between the e_g orbitals which results in the sharing of the single unpaired electron is most likely due to the high symmetry of the square lattice and lowering of the symmetry may disrupt this degeneracy. However, a theoretical DFT-based study into the electronic structure of the poly-MnPc system found that when

the symmetry restrictions were relaxed and geometry optimisation was carried out, the $\mathrm{Mn-N}$ bond distances in the x-direction were found to change by only $0.007\,\text{Å}$ and the splitting of the degenerate bands was negligible [238]. Thus, the high symmetry geometry of poly-MnPc appears to be a good approximation of the system.

7.3.4 poly-FePc

For the poly-FePc system, an $S = 1$ ground state is obtained with the two single electrons occupying the degenerate $d_{xz/yz}$-derived e_g COs. In the context of the electronic structure of poly-MnPc, the addition of another electron to the system results in the double occupation of both the a_{1g} and b_{2g} COs and the formation of two holes in the degenerate e_g COs. The result of this electronic configuration is the opening of a direct band gap in both spin channels (see Fig. 7.3(b)). In the up-spin channel, this band gap, located at the M-point, is measured to be $0.77\,\mathrm{eV}$ with an a_{1u}-derived valence band and degenerate e_g conduction band. However, in the down-spin channel, the band gap, also situated at the M-point, is found to be significantly smaller in energy with a magnitude of $0.23\,\mathrm{eV}$. The valence and conduction bands at this crystal momentum are also of a_{1u} and e_g symmetry, respectively. Although the valence $a_{1u\downarrow}$ band is found to be marginally higher in energy relative to its up-spin counterpart, the principle variation in energy resulting in the observed difference in band gap size arises from the conduction e_g bands. Examination of the AO contributions to these two sets of conduction bands reveals a difference in the phase of the metal $d_{xz/yz}$ AOs. In the up-spin channel, the $d_{xz/yz}$ AOs are out-of-phase with the ligand π-orbitals resulting in an anti-bonding CO, whilst in the down-spin channel, the respective metal d orbitals are *in-phase* with the delocalised ligand π-system resulting in a lower energy CO. This is likely attributable to the fact that the lower-energy bonding combination of orbitals in the up-spin channel is already occupied given the system's electronic configuration.

Both the a_{1g} and b_{2g} COs are found to be fully occupied and examination of the band structure reveals sets of very flat bands indicating minimal hybridisation with the surrounding ligand structure. For both COs, the down-spin bands are found higher in energy than their up-spin counterparts, likely as a result of the on-site Coulombic repulsion that the pairs of electrons experience when doubly occupying the localised orbitals.

As discussed for poly-MnPc, the observed electronic occupation of poly-FePc likely results from the imposition of D^1_{4h} symmetry environment. However, an identical electronic configuration was obtained for the poly-FePc system within a GGA+U theoretical study, in which the unit cell geometry optimisation was carried out *without* any symmetry constraints

[67]. Should the symmetry restrictions be relaxed, it is possible that the system may exhibit Jahn-Teller distortion, which could result in the reorganisation of the electronic configuration. However, within the study presented here, all poly-TMPc systems, including poly-FePc, are evaluated under a D^1_{4h} symmetry constraint.

7.3.5 poly-CrPc

An $S = 2$ ground state electronic configuration was evaluated for poly-CrPc with four electrons singly occupying the a_{1g}, b_{2g} and degenerate e_g COs. The dispersion plot of the system highlights the presence of a direct band gap in both the spin channels, located at the M-point of the FBZ (see Fig. 7.3.3). In the up-spin channel, this band gap is measured to be $1.00\,\mathrm{eV}$, with an a_{1u}-derived valence band and a degenerate set of e_g conduction bands. In the down-spin channel, a smaller band gap of $0.25\,\mathrm{eV}$ is evaluated, with respective valence and conduction bands of the same symmetry as that of the up-spin channel. As observed in the band structure of poly-FePc, the formation of two holes in the metal e_g COs leads to the in-phase hybridisation of the $d_{xz/yz}$ AOs in the down-spin conduction band lowering its the respective energy relative to that of the up-spin channel, where the occupation of the metal $d_{xz/yz}$ AOs prevents favourable in-phase hybridisation with the delocalised ligand π-system. In the up-spin channel, at the Γ-point the singly occupied a_{1g} and b_{2g} bands are situated $1.90\,\mathrm{eV}$ and $2.41\,\mathrm{eV}$ below E_F, respectively. The bands appear very flat with a width of $0.02\,\mathrm{eV}$ and $0.06\,\mathrm{eV}$, respectively. In the down-spin channel, the unoccupied a_{1g} (b_{2g}) band is located $4.94\,\mathrm{eV}$ ($3.96\,\mathrm{eV}$) above E_F. By evaluating the energy difference between these occupied and unoccupied bands, an estimation of the on-site Coulombic repulsion, U, may be obtained. For the a_{1g} CO, a value of $U = 6.84\,\mathrm{eV}$ is calculated whilst for the b_{2g} CO, a respective value of $U = 6.37\,\mathrm{eV}$ is measured.

7.4 Magnetic Interactions

An evaluation of the magnetic interactions is carried out for each poly-TMPc system. Within the 2D sheets, there are 3 different possible magnetically ordered phases: a ferromagnetic (FM) configuration, a collinear antiferromagnetic (CAF) configuration and a Néel antiferromagnetic (NAF) configuration (see Fig. 7.4).

In order to correctly capture these phases, a (2×2) supercell is used. Total DFT energies of the three magnetic phases are obtained for each studied system. The interactions between the magnetic centres can be captured within the framework of the Ising Hamiltonian. Within

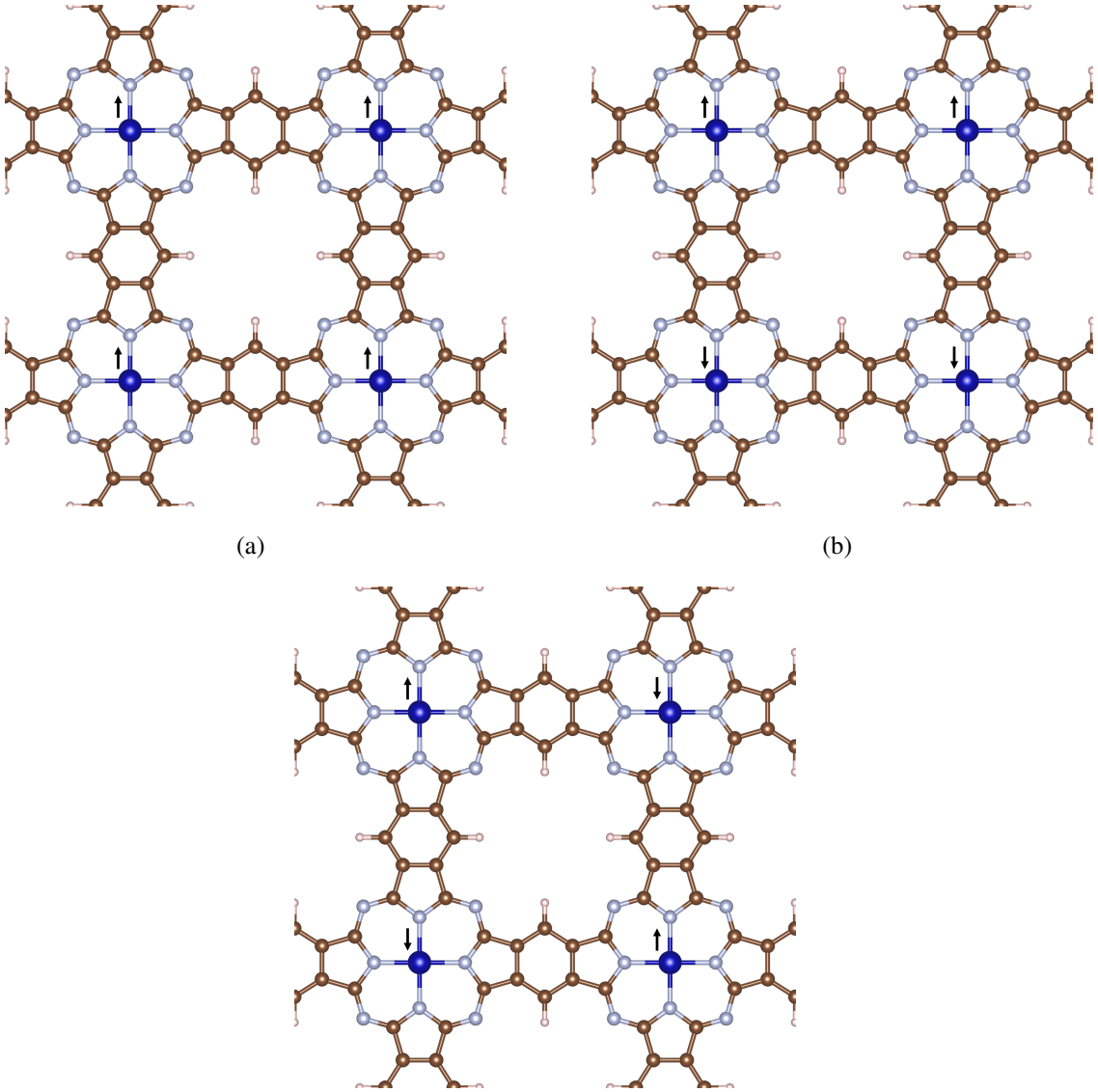

(a) (b)

(c)

Figure 7.6: Graphical depiction of (a) the ferromagnetic (FM) phase, (b) the collinear antiferromagnetic (CAF) phase and (c) the Néel antiferromagnetic (NAF) phase. Arrows indicate the direction of the total magnetic moment at each metal centre.

the (2×2) supercell, two unique coupling interactions are present: one between nearest neighbour magnetic centres and one between next-nearest neighbour magnetic centres (see Fig. 7.7). Thus, the respective Hamiltonian takes the following form,

$$\hat{H} = -J_1 \sum_{\langle i,j \rangle}^{N} \hat{\mathbf{S}}_i \cdot \hat{\mathbf{S}}_j - J_2 \sum_{\langle\langle i,k \rangle\rangle}^{N} \hat{\mathbf{S}}_i \cdot \hat{\mathbf{S}}_k \tag{7.1}$$

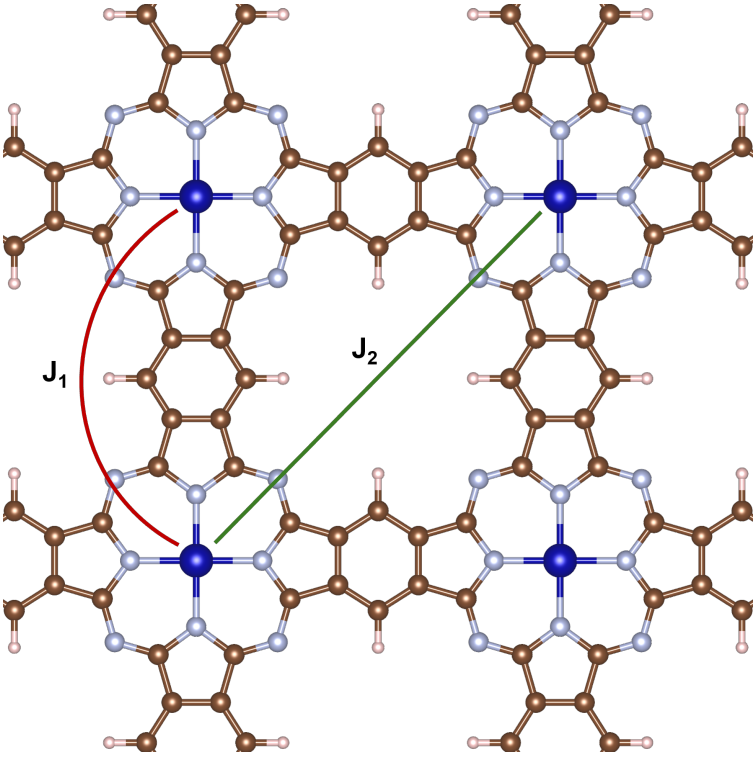

Figure 7.7: Graphical depiction of the two unique coupling interactions in the (2×2) unit cell of a poly-TMPc system. Here J_1 denotes the interaction between nearest neighbour pairs, whilst J_2 captures the interaction between next-nearest neighbour pairs.

where $\hat{\mathbf{S}}_i$ is the i^{th} local spin operator, and $\langle i, j \rangle$ and $\langle\langle i, k \rangle\rangle$ indicate nearest neighbour and next-nearest neighbour pairs, respectively. J_1 and J_2 are the coupling constants for the nearest neighbour and next-nearest neighbour interactions, respectively. Using the procedure derived in Ref. [238], by treating each pair of coupled spins within the MF approximation, additivity of the interactions can be assumed and the energy of each magnetic phase can be represented as follows,

$$\begin{aligned} E^{FM} &= E_0 - 8J_1m^2 - 8J_2m^2 \\ E^{CAF} &= E_0 + 8J_2m^2 \\ E^{NAF} &= E_0 + 8J_1m^2 - 8J_2m^2 \end{aligned} \tag{7.2}$$

where E_0 is the baseline energy of the system excluding any exchange interactions and m is the spin of each site. Here, E^{FM}, E^{NAF} and E^{CAF} are the respective total energies of the (2×2) supercell. J_1 may be simply obtained by evaluating the energy difference between E^{FM} and E^{NAF}.

$$J_1 = -\frac{1}{16m^2}(E^{FM} - E^{NAF}) \tag{7.3}$$

which is obtained identically when the respective energies are mapped to Eq. 3.13. J_2 is obtained by evaluating the energy difference between all three configurations given by,

$$J_2 = -\frac{1}{32m^2}(E^{FM} + E^{NAF} - 2E^{CAF}) \tag{7.4}$$

As outlined in Sec. 3.5, whilst the Yamaguchi spin decontamination procedure provides an effective approach for estimating spin contamination in spin dimer systems (hence its application in the evaluation of the coupling interactions in the systems studied in Chapters 4, 5 and 6), there is little indication that it is suitable for higher dimensional periodic systems. Therefore, the total energies of each magnetic phase in the (2×2) cell are absent of spin decontamination.

Table 7.4 presents the resulting data for the magnetic coupling in each system. For poly-CoPc, the system is weakly AFM with an NAF ground state. This is in accordance with expectations derived from the out-of-plane distribution of the d_{z^2}-derived a_{1g} SOMOs, which results in minimal lateral interactions. This is reflected by the magnitudes of both J_1 and J_2, with the former constant indicative of weak AFM coupling and the latter showing even weaker ferromagnetism. With regards to poly-CuPc, the NAF phase is once again favoured as the lowest energy configuration, with an energy per unit cell of $6.06\,\mathrm{K}$ below that of the FM phase. The CAF phase exhibited a marginally higher energy than the NAF

System	ΔE^{CAF} [K]	ΔE^{NAF} [K]	J_1 [K]	J_2 [K]
CoPc	-0.09	-0.22	-0.22	0.02
CuPc	-3.00	-6.06	-6.06	0.03
MnPc	154.15	297.52	33.06	0.60
FePc	-7.00	-23.10	-5.77	1.12
CrPc	-24.08	-60.75	-3.80	0.39

Table 7.4: Magnetic data for each studied poly-TMPc system. ΔE^{CAF} (ΔE^{NAF}) is the energy difference per unit cell for the CAF (NAF) phase with respect to the FM phase. Note that a positive (negative) value indicates that the FM phase is lower (higher) in energy than the respective CAF or NAF phase. J_1 and J_2 are the respective nearest neighbour and next-nearest neighbour coupling constants. A positive sign indicates FM coupling, a negative sign indicates AFM coupling.

phase, yet remained more stable than the FM phase with a $\Delta E^{CAF} = -3.00\,\mathrm{K}$. The in-plane structural geometry of the b_{1g} SOMOs facilitates a stronger lateral interaction across the lattice than that observed in poly-CoPc. Indeed, inspection of the Mulliken population of both systems indicates that the isoindole nitrogens (N_1 in Fig. 7.1) carry a spin population of $0.090\,|e|$ in poly-CuPc, but lack any polarisation in poly-CoPc. However, the polarisation by the b_{1g} SOMOs only act through the in-plane σ-bonding network and, as a result, does not extend extensively throughout the ligand orbitals. This likely explicates the relative magnitude of the AFM coupling strength. With regards to the values obtained for the coupling constants, the NAF configuration of the spin centres aligns with the AFM nature of J_1 and the FM nature of J_2.

In poly-FePc, a much stronger AFM interaction is observed, with an NAF ground state that resides $23.10\,\mathrm{K}$ below that of the FM phase. The single occupation of the degenerate e_g MOs enables the hybridisation of these respective orbitals with the ligand π-system which in turn increases the extent of the polarisation between magnetic centres. Thus, the coupling between the SOMOs and the π orbitals facilitates a stronger exchange interaction than the respective coupling with σ orbitals. Inspection of the Mulliken population indicates that not only are the orbitals of N_1 polarised but also those orbitals localised on the carbons that constitute the isoindole rings (C_1, C_2 and C_3). The spin density isosurface plots for the three phases studied here may be found in Appendix C.6. Once again, the sign of each coupling constant is in accordance with the NAF ground state, whilst the magnitude of both parameters highlights the relative strength of the AFM interaction between magnetic centres.

For poly-CrPc, a substantial AFM coupling is also observed, with the NAF phase being found at an energy of $60.75\,\mathrm{K}$ below that of the FM phase. With comparison to the coupling observed in poly-FePc, the increased magnitude obtained here is likely due to the increased size of the magnetic moment localised at each metal centre. In poly-CrPc, a moment of $4\,\mu_B$ is obtained, with electrons singly occupying the a_{1g}, b_{2g} and degenerate e_g COs. Analysis of the Mulliken population indicates an increase in the polarisation of the ligand orbitals relative to that of poly-FePc. Once again, the signs of both J_1 and J_2 are consistent with an NAF phase. With regards to the magnitude of the constants, the reduction in their size relative to that of poly-FePc arises as a result of the larger moments located at each metal centre (see Eqs. 7.3 and 7.4).

Finally, for poly-MnPc, the ground state spin configuration is found to be FM with an energy difference of $\Delta E^{CAF} = 154.15\,\mathrm{K}$ and $\Delta E^{NAF} = 297.52\,\mathrm{K}$. To understand

why the system exhibits such a strong FM coupling, analysis of the Mulliken population is carried out. In the electronic configuration of each unit cell of poly-MnPc, the three electrons are shared amongst the degenerate e_g COs. In the single unit cell studied in the previous section, the electrons are distributed equally amongst the two orbitals such that each orbital accommodates $\sim 1.5\,|e|$. In the (2×2) supercell, the degeneracy between the two e_g orbitals is removed, such that each spin centre has a doubly occupied and a singly occupied e_g orbital. Furthermore, at neighbouring sites, the specific e_g orbital singly occupied alternates. Thus at the i^{th} metal site, the occupation is $(e_{gx})^2, (e_{gy})^1$, whilst at the neighbouring j^{th} site the occupation is $(e_{gx})^1, (e_{gy})^2$. The hybridisation of the metal e_g orbitals with those of the ligand results in anisotropic diffusion of the spin density along only one of the lattice directions (see Fig. C.5(a)). Thus at each spin centre, the singly occupied e_g CO is *orthogonal* to its neighbour and, as a result, a strong FM interaction between the hybridised SOMOs is exhibited. The strength of the interaction is likely due to the extensive delocalisation through the ligand π structure which reduces the distance between adjacent orthogonal spin orbitals. This is further reflected in the relative size of nearest neighbour coupling constant, J_1.

Using the MF approach to the Ising model, an estimation of the Curie temperature, T_C, for poly-MnPc may be obtained. Given the substantial difference between J_1 and J_2, only the nearest neighbour interactions are considered. The strategy adopted here is to derive an expression for the average magnetisation, m, of the poly-MnPc system and examine the point at which this magnetisation transitions from a disordered, paramagnetic state to an ordered state. Given that J_1 is normalised to the interaction over one lattice point, the following calculation is also evaluated over a single site. The initial step is to derive an expression for the partition function, Z, for the four spin states $S \in \gamma$ where $\gamma = \{-3/2, -1/2, 1/2, 3/2\}$. This is given by

$$\begin{aligned} Z &= \sum_{S\in\gamma} e^{-\beta H^{MF}} \\ &= \sum_{S\in\gamma} e^{\beta J z m S - \frac{1}{2}\beta J z m} \end{aligned} \tag{7.5}$$

where $\beta = 1/k_B T$, where k_B is the Boltzmann constant and T is the temperature. H^{MF} is derived from the MF approximation to the Ising model (see Eq. 3.10). Factoring out the constant term in the Hamiltonian and expanding the sum, Z is given by

$$Z = e^{-\frac{1}{2}\beta J z m}[e^{-\frac{3}{2}\beta J z m} + e^{-\frac{1}{2}\beta J z m} + e^{\frac{1}{2}\beta J z m} + e^{\frac{3}{2}\beta J z m}] \tag{7.6}$$

Making use of the following identity,

$$\cosh(x) = \frac{e^x + e^{-x}}{2} \tag{7.7}$$

Eq. 7.6 can be simplified to

$$Z = e^{-\frac{1}{2}\beta Jzm}\left[2\cosh\left(\frac{3}{2}\beta Jzm\right) + 2\cosh\left(\frac{1}{2}\beta Jzm\right)\right] \tag{7.8}$$

The average magnetisation, m is given by the following expression

$$m = \sum_{S\in\gamma} S \cdot P(S) \tag{7.9}$$

where $P(S)$ is the Boltzmann probability distribution for each spin, given by

$$P(S) = \frac{e^{\beta JzmS - \frac{1}{2}\beta Jzm}}{Z} \tag{7.10}$$

Thus, evaluating Eq. 7.9, taking note that the constant factor cancels for each summation, and making use of the following identity,

$$\sinh(x) = \frac{e^x - e^{-x}}{2} \tag{7.11}$$

the average magnetisation is given by,

$$m = \frac{3\sinh\left(\frac{3}{2}\omega m\right) - \sinh\left(\frac{1}{2}\omega m\right)}{2\cosh\left(\frac{3}{2}\omega m\right) + 2\cosh\left(\frac{1}{2}\omega m\right)} \tag{7.12}$$

where $\omega = \beta Jz$. Eq. 7.12 is a transcendental equation and thus cannot be solved analytically. However, by plotting both functions graphically for different values of ω, the point at which the transition between paramagnetism and ferromagnetism can be determined. Fig. 7.8 depicts graphical solutions to the above self consistent equation. For $\omega = 0.5$, there is only one point of intersection between the two functions, $m = 0$. This is indicative of a paramagnetic state. For $\omega = 1.5$, there are three intersections between the two plots, $m = 0$ and $m = \pm m_i$ where m_i is a non-zero value. This indicates ferromagnetism. For $\omega = 1.0$, the system exhibits the transition point. For values of $\omega < 1$, the system is paramagnetic; for values of $\omega > 1$, the system is ferromagnetic. From this the following expression may obtained,

$$Jz = k_B T_C \tag{7.13}$$

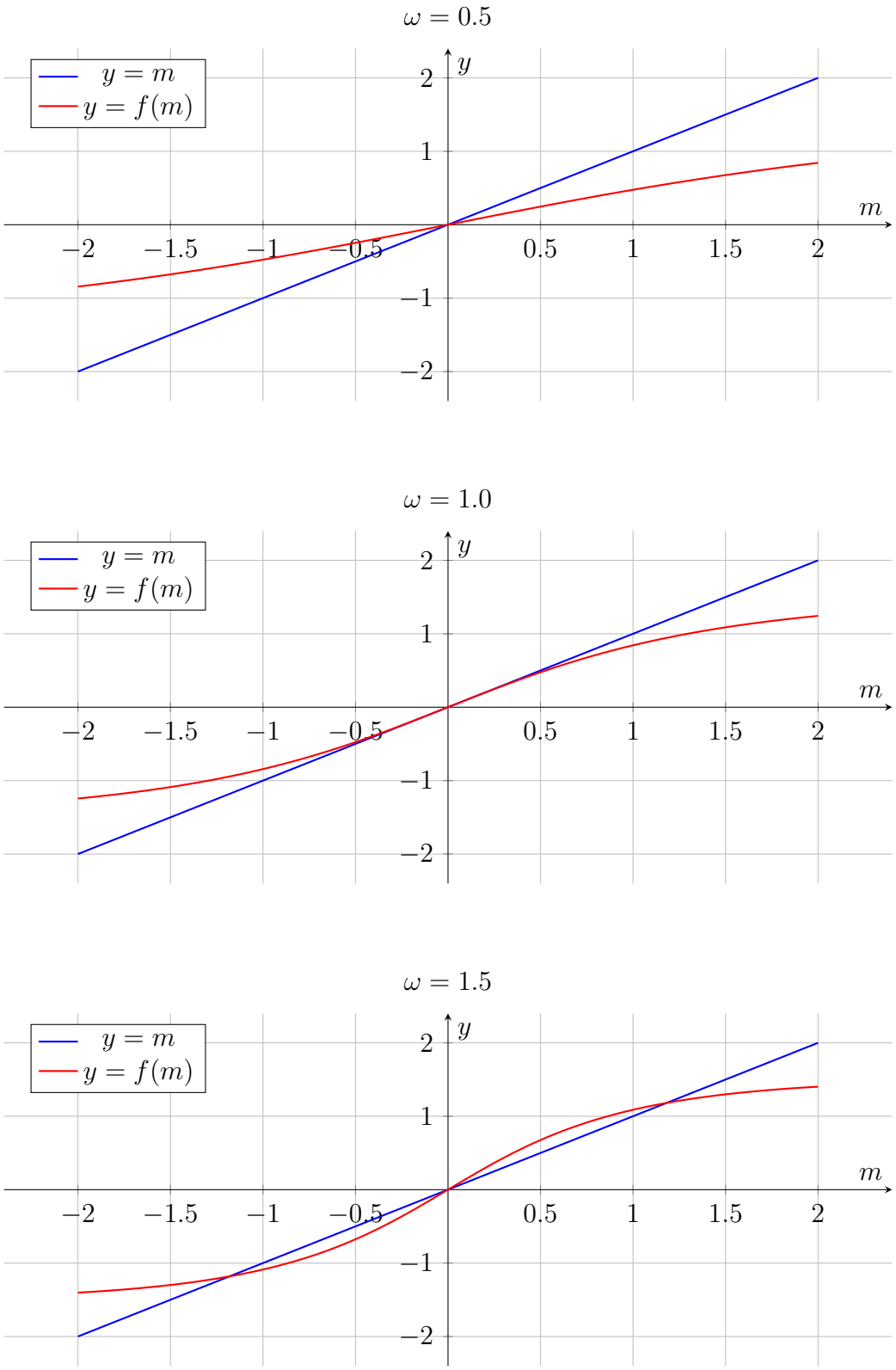

Figure 7.8: Graphical plots of the transcendental average magnetisation equation. $f(m)$ refers to the right hand side of Eq. 7.12.

Thus, using the value of $J_1 = 33.06\,\mathrm{K}$, an approximation of $T_C = 132.24\,\mathrm{K}$ is evaluated. This value is in relatively good agreement with the estimated value of $T_C \sim 150\,\mathrm{K}$ obtained from Monte-Carlo (MC) calculations using a (80×80) supercell [67]. Variation between the two respective values likely arises from differences in the magnitude of the coupling constant. It is important to note that, to the author's knowledge, there is no experimentally measured values of the magnetic properties of poly-MnPc, and, therefore, this study is simply an approximate prediction that the system may exhibit strong ferromagnetism. However, because the MF approach neglects fluctuations, which become increasingly important near the critical temperature, the model has a tendency to overestimate T_C. Nevertheless, the prediction of a strong FM coupling in poly-MnPc presents a valuable opportunity to experimentally investigate its magnetic properties.

7.5 Conclusions

In this chapter, a comprehensive analysis of the electronic and magnetic properties of the family of first row polymeric transition metal phthalocyanines has been carried out. The aim of this study was to provide a thorough analysis of this group of systems and make connections between the respective electronic structure and observed emergent behaviour. In doing so, a more complete picture of the magnetic interactions within phthalocyanine materials has been provided. From the characterisation of the electronic structure of each system, significant variation in the respective band structure was observed. For all systems, the valence and conduction bands were principally derived from the ligand orbitals (although some mixing of relevant d-orbitals were also present). As a result of the delocalised π-system distributed within the poly-phthalocyanine 2D sheet, the band gap between these ligand frontier COs was significantly reduced relative to the approximate $2.0\,\mathrm{eV}$ gap measured in the periodic single chain phthalocyanines. Interestingly, poly-MnPc exhibited a half-metallicity which arose from the specific $(e_g)^3$ occupation of the d-derived orbitals. Here the sharing of the single electron density amongst the e_{gx} and e_{gy} MOs facilitates the formation of a hole distributed amongst the two orbitals that exhibited conducting behaviour at the crystal momentum M-point. However, it is important to note that the unit cell of all poly-TMPc systems was optimised within a D^1_{4h} symmetry environment. Therefore, the study did not include the any effects that Jahn-Teller distortion may have on the respective electronic structure. It was posited that any degeneracy between e_g orbitals may be lifted. In poly-MnPc, this would like result in the suppression of the

half-metallic state.

Having established the ground electronic state of each poly-TMPc system, the magnetic interactions between the spin centres were evaluated. For each system, there are three possible magnetic phases: an FM, CAF and NAF phase. Using a (2×2) supercell, the energy of each phase was measured, facilitating the evaluation of the nearest neighbour and next-nearest neighbour coupling constants (J_1 and J_2, respectively). In contrast to the axial direction of the exchange interactions in the single periodic chains of the TMPc systems studied in Chapters 4, 5 and 6, within the poly-TMPc species, the spin centres may only couple laterally. Thus, unsurprisingly, exceptionally weak coupling was measured in poly-CoPc, where the out-of-plane a_{1g} SOMO suppressed any significant lateral interaction. Poly-CuPc, poly-FePc and poly-CrPc all exhibited relatively strong AFM coupling with a ground NAF phase configuration. The variation in the strength of this coupling was explicated through analysis of the respective ligand orbitals that hybridised with the metal SOMO. Whilst the singly occupation of e_g orbitals in both poly-FePc and poly-CrPc facilitated their respective hybridisation into the delocalised ligand π-system, in poly-CuPc, the in-plane b_{1g} orbitals could only interact with the σ-network which are more localised than the π-system. As a result, in poly-CuPc, the polarisation was not transmitted between spin centres with the same strength as in both poly-FePc and poly-CrPc.

The most intriguing magnetic interactions were observed in poly-MnPc, which exhibited exceptionally strong ferromagnetism, with an energy difference of $\Delta E^{CAF} = 154.15\,\mathrm{K}$. By examining the MPA spin density distribution, this FM interaction was found to be as a result of the differing single occupation of either the metal e_{gx} or e_{gy} MOs on neighbouring spin centres. This generated delocalised metal-ligand e_g SOMOs on adjacent cells that were orthogonal to one-another, thus transmitting a strong DE interaction and suppressing any inter-orbital KE. Following this analysis, an estimation of the Curie transition temperature, T_C, was evaluated using an MF approach. A value of $T_C = 132.4\,\mathrm{K}$ was calculated, which was in relatively good agreement with the value of $T_C \sim 150\,\mathrm{K}$ that was obtained from MC calculations of an (80×80) supercell [67].

From the analysis carried out in this study, polymeric transition metal phthalocyanine systems present themselves as a promising candidate for next-generation molecular electronics, particularly the strongly FM poly-MnPc. Experimental measurement of its magnetic properties appears to offer itself as an interesting challenge with potentially transformative outcomes.

8

Conclusions & Future Work

To begin this final chapter, a brief, holistic summation of the overall contribution of this thesis is offered. As outlined in Chapter 1, the principle aim of this work was to provide deeper insight into the mechanisms underpinning the magnetic behaviour in transition metal phthalocyanines and, in particular, the underlying reasons why strong AFM coupling is observed in α-CoPc but not in its isostructrual counterpart α-CuPc. In understanding the structure-property relationships of the magnetism in these materials, and, thus, the reasoning behind the significant difference in magnetic coupling strength, directed modifications to the systems could then be carried out in order to further strengthen the interaction strength. In order to assess these magnetic interactions, two distinct approaches were developed. In the first approach, the coupling strength was evaluated using BS-DFT calculations on single periodic chain structures of each system. Here, not only was the total coupling evaluated from the energy differences between the FM and AFM configurations, but also the coupling arising only from the kinetic exchange (KE) interaction. This latter term was calculated using Hubbard Hamiltonian parameters extracted from the single particle dispersion spectrum of each system. The second approach used a decomposition procedure in which the three principle components of the exchange interaction - the direct exchange (DE), KE and spin polarisation (SP) - were quantitatively determined through the sequential

relaxation of a set of single Slater determinants. In addition to the analysis of TMPc single chain periodic structures, a supplementary aim of this work was to provide a comprehensive analysis of the electronic and magnetic properties of an analogue of the metal phthalocyanine crystals - the polymeric transition metal phthalocyanine (poly-TMPc). Not only would this provide an in-depth investigation of a more sparsely studied class of phthalocyanine materials, but also ensure that the work presented in this thesis accounted for a group of phthalocyanine systems that show potential within spintronic-based applications.

With regards to the investigation carried out on the magnetic properties in periodic single chain structures of CoPc and CuPc, the calculations successfully reproduced the experimentally observed coupling with substantially stronger AFM interactions in α-CoPc than in α-CuPc. It was reasoned that the out-of-plane geometry of the singly occupied d_{z^2}-derived a_{1g} MO in CoPc facilitated strong inter-orbital coupling (particularly in the α-phase, where the metal-metal distance was reduced relative to that of the β-phase), whilst in CuPc, the in-plane distribution of the $d_{x^2-y^2}$-derived b_{1g} MO suppressed axial inter-orbital interactions between adjacent molecules. By characterising this interaction using Hubbard Hamiltonian parameters, it was predicted that replacing the central cobalt ion with its second-row counterpart, rhodium, would significantly increase the AFM coupling strength. This was due to the occupation of a $4d$ orbital which, owing to its more diffuse nature, would incur a smaller Coulombic penalty when doubly occupied following the electron transfer event that characterises the KE mechanism in this class of materials. Indeed, even after adjusting the metal-metal distance in the novel α-RhPc chain structure to ensure that the inter-orbital overlap — and, by extension, the magnitude of the transfer integral, t — were approximately equal to that of α-CoPc, the strength of both the total coupling and KE interaction were significantly higher. Calculation of the on-site repulsion term, U, showed a decrease of $\sim 2\,\mathrm{eV}$ between CoPc and RhPc, and thus confirmed not only the dominance of the KE interaction in these two systems, but also the predictive capability of such an approach in the design of novel phthalocyanine materials with specific magnetic properties. Indeed, the simple chemical modification carried out here resulted in a hybrid molecular magnetic material that was theoretically predicted to exhibit room temperature magnetism.

In the subsequent chapter, the decomposition procedure was developed and applied to the three systems studied previously - CoPc, CuPc and RhPc. The principle benefit of the method over that utilised in Chapters 4 and 5 was its ability to provide quantitative estimates of the three main components of the exchange interaction between localised magnetic moments. The key findings of this analysis highlighted a dominant KE interaction

in both α-CoPc and α-RhPc, which accounted for the strong AFM coupling in the systems. However, an additional non-negligible SP term was also evaluated in both phthalocyanine systems that had not been previously accounted for. This term was found to arise as a result of the differential polarisation of the axially coordinated isoindole nitrogens of each adjacent molecule. The combination of these terms were found to account for the majority of the total coupling interaction. Interestingly, there was a significant difference in the magnitude between the KE term extracted using the decomposition procedure and that evaluated using the Hubbard Hamiltonian parameters. Given that the value extracted in Chapter 6 appeared to more reasonably align with expectations, it was suggested that the Hubbard parameters, whilst qualitatively useful, may be quantitatively inaccurate. In α-CuPc, the weak AFM coupling was found to arise as a result of a SP term, with both DE and KE interactions minimised due to the orbital geometry of the b_{1g} SOMO. In both polymorphs of CoPc and CuPc, good agreement was found between the total coupling values and the respective experimental data. The conclusions from the study suggested that the decomposition procedure was a powerful investigative tool for analysing the exchange interactions and underlying mechanisms of TMPc systems.

In Chapter 7, a thorough investigation of the group of first-row poly-TMPcs was carried out. Both the electronic structure and magnetic properties of each system were analysed. Of these systems, the most interesting, particularly in relation to potential molecular electronic and spintronic applications, was that of poly-MnPc. The system was found to exhibit half-metallicity, with conduction in its down-spin channel. Additionally, evaluation of the energy of each of the three magnetic phases indicated that the system exhibits strong FM coupling owing to the presence of orthogonal e_g SOMOs localised on adjacent unit cells. Using an MF approach, its Curie transition temperature was estimated to be $T_C = 132.4\,\mathrm{K}$ - a significant value for a hybrid magnetic material. Amongst the other poly-TMPc systems, both poly-CrPc and poly-FePc exhibited strong AFM coupling arising as a result of the hybridisation between the singly occupied metal e_g orbitals and the π MOs of the ligand, which facilitated the strong transmission of the spin polarisation between the adjacent metal centres.

It is important to highlight several limitations to the studies carried out in this work. Firstly, as mentioned above, there were observed discrepancies in α-CoPc between the magnitude of the KE term evaluated using the Hubbard parameters extracted from the single particle dispersion plot and that evaluated using the decomposition method. The significant deviation of the value obtained from the former method suggests that the Hubbard

parameters may not be quantitatively correct. However, comparison of the values calculated for α-RhPc suggest that the discrepancy only occurs in the CoPc system. This may suggest that accuracy of the term is system specific. Given the magnitude of the interaction, relative to that extracted from the decomposition analysis, it is likely that the transfer integral, t, is overestimated from the dispersion plot. One possible reason for this could be the hybridisation of the d_{z^2} orbital with surrounding ligand orbitals which could act to broaden the width of the band and, thus, increase the size of t. Indeed, inspection of the AO contributions to the respective $a_{1g\downarrow}$ band in the FM configuration indicates the inclusion of a significant number of orbitals pertaining to the ligand σ-network, which is absent in the case of RhPc. Secondly, with regards to the decomposition approach, the method is limited to the evaluation of the DE, KE and SP interactions. Whilst the results presented in Chapter 6 suggest that these three terms account for the majority of the total coupling, it is important to note that other higher order terms may also contribute. Nevertheless, this does not detract from the methods utility, particularly given the alignment between the hypothesised exchange mechanisms of the studied systems and the resulting data. An additional limitation to the studies carried out in this report relates to the use of the Yamaguchi formalism for spin decontamination. As outlined in Chapter 3, whilst the formula has been effectively shown to resolve spin contamination issues in BS single determinant wavefunctions of spin dimer systems, it is not well defined for larger systems of a higher dimensional periodic nature (such as 2D poly-TMPcs). The result of this necessitated an inconsistent use of the formula amongst the different studied systems. However, spin contamination is relatively small in transition metal complexes and, therefore, it is unlikely that its absence in the evaluation of the coupling constants in Chapter 7 affected the results significantly.

There are a number of potential subsequent studies, related to this work, that should be undertaken. Firstly, whilst in-depth analyses of the chain structures of CoPc, CuPc and the theoretical RhPc were carried out, the additional first-row TMPc systems were not investigated. A theoretical characterisation of both the electronic structure and magnetic interactions within these remaining species would be desirable. For example, previous experimental measurements of MnPc indicated moderate FM coupling in the system [77,88]. A decomposition analysis of this particular system would be highly insightful and would not only have the potential to yield information about the mechanistic underpinning of the interaction, but also act as a validation test for the capabilities of the method, especially with regards to the evaluation of multiplet based magnetic systems. In relation to the capacity of the decomposition method to capture the exchange interactions in molecular based magnetic

systems, the extension of the procedure to other similar systems would also be beneficial to further its validation. To the author's knowledge, presented in this report is the first use of the method for a system extending beyond a single molecule. Previous uses of the procedure have been only applied to bi-radical molecules. Given that the results obtained in Chapter 6 aligned closely with expectations pertaining to the coupling, it is likely that the method may prove highly effective in better understanding the composition of the exchange interactions in other single chain magnetic systems. However, it is important to highlight that the method may only currently be used within a molecular based code and, therefore, one must be able to approximate any candidate periodic system using a molecular geometry (as has been carried out here). One such possible group of systems are the class of functionalised TMPcs. Like their non-functionalised counterparts these species adopt similar packing arrangements and, thus, may be effectively approximated by a dimeric molecular geometry. The addition of either electronic or steric influencing groups to the peripheral of the ring structure may affect facets of the exchange interaction (although as outlined in Chapter 1, previous studies have indicated that the magnetic behaviour is minimally impacted by the presence of electron withdrawing groups such as fluorine - the most commonly reported electronic substituent used to functionalise phthalocyanines). An analysis of these systems using the decomposition method may prove highly insightful. A natural further extension to the 2D poly-TMPc systems studied in Chapter 7 would be 3D crystals constructed from layers of individual 2D sheets. A previous theoretical study by Park et al. (2022) investigated the magnetic and electronic properties of a *bilayer* of poly-MnPc, indicating the presence of intralayer FM coupling but interlayer AFM coupling [168]. The introduction of axial interlayer interactions alongside the already existing lateral intralayer interactions would likely affect the overall coupling of the system. An analysis of these crystals, similar to that carried out for the 2D systems, would be of great potential interest.

In closing this chapter, and the thesis overall, the principle aims of this body of work - to develop a more refined and sophisticated understanding of the magnetic interactions in the class of transition metal phthalocyanines - has been comprehensively addressed. Not only have the investigations elucidated the exchange mechanism underpinning the exceptionally strong coupling observed in α-CoPc, but have also led to the development of novel theoretical tools that can provide valuable insight into the interactions of other magnetic systems. It is hoped that the findings presented here will contribute to furthering the frontiers of both molecular magnetism and spintronics, and open new avenues for future research within these ever-evolving fields.

Bibliography

[1] Lisa Depraiter and Stephane Goutte. The role and challenges of rare earths in the energy transition. *Resources Policy*, 86:104137, 2023.

[2] TSMC. 3nm technology overview. `https://www.tsmc.com/english/dedicatedFoundry/technology/logic/l_3nm`, 2025. Accessed: 2025-02-13.

[3] David D. Wu Wei Xiong and Jeff H. Y. Yeung. Semiconductor supply chain resilience and disruption: insights, mitigation, and future directions. *International Journal of Production Research*, 0(0):1–24, 2024.

[4] Rahul Pandey, Saurabh Mookerjea, and Suman Datta. Opportunities and challenges of tunnel FETs. *IEEE Transactions on Circuits and Systems I: Regular Papers*, 63(12):2128–2138, 2016.

[5] Mario Norberto Baibich, Jean Marc Broto, Albert Fert, F Nguyen Van Dau, Frédéric Petroff, P Etienne, G Creuzet, A Friederich, and J Chazelas. Giant magnetoresistance of Fe(001)/Cr(001) magnetic superlattices. *Phys. Rev. Lett.*, 61(21):2472, 1988.

[6] G. Binasch, P. Grünberg, F. Saurenbach, and W. Zinn. Enhanced magnetoresistance in layered magnetic structures with antiferromagnetic interlayer exchange. *Phys. Rev. B*, 39:4828–4830, 1989.

[7] Nobel Prize Outreach. Press release. `https://www.nobelprize.org/prizes/physics/2007/press-release/`, 2025. Accessed: 2025-02-13.

[8] Nevill Francis Mott and Ralph Howard Fowler. The electrical conductivity of transition metals. *Proceedings of the Royal Society of London. Series A - Mathematical and Physical Sciences*, 153(880):699–717, 1936.

[9] Nevill F Mott. Electrons in transition metals. *Advances in Physics*, 13(51):325–422, 1964.

[10] Claude Chappert, Albert Fert, and Frédéric Nguyen Van Dau. The emergence of spin electronics in data storage. *Nature Materials*, 6(11):813–823, 2007.

[11] T. Miyazaki and N. Tezuka. Giant magnetic tunneling effect in Fe/Al_2O_3/Fe junction. *Journal of Magnetism and Magnetic Materials*, 139(3):L231–L234, 1995.

[12] Yoshinori Nagamine, Hiroki Maehara, Koji Tsunekawa, David D. Djayaprawira, Naoki Watanabe, Shinji Yuasa, and Koji Ando. Ultralow resistance-area product of $0.4\Omega(\mu m)^2$ and high magnetoresistance above 50% in CoFeB/MgO/CoFeB magnetic tunnel junctions. *Applied Physics Letters*, 89(16):162507, 2006.

[13] Puja Dey, Jitendra Nath Roy, Puja Dey, and Jitendra Nath Roy. Tunnelling magnetoresistance (TMR). *Spintronics: Fundamentals and Applications*, pages 103–125, 2021.

[14] W. H. Butler, X.-G. Zhang, T. C. Schulthess, and J. M. MacLaren. Spin-dependent tunneling conductance of Fe/MgO/Fe sandwiches. *Phys. Rev. B*, 63:054416, 2001.

[15] J. Mathon and A. Umerski. Theory of tunneling magnetoresistance of an epitaxial Fe/MgO/Fe(001) junction. *Phys. Rev. B*, 63:220403, 2001.

[16] T. Kishi, H. Yoda, T. Kai, T. Nagase, E. Kitagawa, M. Yoshikawa, K. Nishiyama, T. Daibou, M. Nagamine, M. Amano, S. Takahashi, M. Nakayama, N. Shimomura, H. Aikawa, S. Ikegawa, S. Yuasa, K. Yakushiji, H. Kubota, A. Fukushima, M. Oogane, T. Miyazaki, and K. Ando. Lower-current and fast switching of a perpendicular tmr for high speed and high density spin-transfer-torque MRAM. In *2008 IEEE International Electron Devices Meeting*, pages 1–4, 2008.

[17] Supriyo Datta and Biswajit Das. Electronic analog of the electro-optic modulator. *Applied Physics Letters*, 56(7):665–667, 1990.

[18] Junsaku Nitta and Tobias Bergsten. Electrical manipulation of spin precession in an ingaas-based 2deg due to the rashba spin-orbit interaction. *IEEE Transactions on Electron Devices*, 54(5):955–960, 2007.

[19] Gul Faroz Ahmad Malik, Mubashir Ahmad Kharadi, Farooq Ahmad Khanday, and Nusrat Parveen. Spin field effect transistors and their applications: A survey. *Microelectronics Journal*, 106:104924, 2020.

[20] Priti J. Rajput, Sheetal U. Bhandari, and Girish Wadhwa. A review on—spintronics an emerging technology. *Silicon*, 14(15):9195–9210, 2022.

[21] Vinod Kumar Joshi. Spintronics: A contemporary review of emerging electronics devices. *Engineering Science and Technology, an International Journal*, 19(3):1503–1513, 2016.

[22] Pojen Chuang, Sheng-Chin Ho, L. W. Smith, F. Sfigakis, M. Pepper, Chin-Hung Chen, Ju-Chun Fan, J. P. Griffiths, I. Farrer, H. E. Beere, G. A. C. Jones, D. A. Ritchie, and Tse-Ming Chen. All-electric all-semiconductor spin field-effect transistors. *Nature Nanotechnology*, 10(1):35–39, 2015.

[23] Hyun Cheol Koo, Jae Hyun Kwon, Jonghwa Eom, Joonyeon Chang, Suk Hee Han, and Mark Johnson. Control of spin precession in a spin-injected field effect transistor. *Science*, 325(5947):1515–1518, 2009.

[24] Shengwei Jiang, Lizhong Li, Zefang Wang, Jie Shan, and Kin Fai Mak. Spin tunnel field-effect transistors based on two-dimensional Van der Waals heterostructures. *Nature Electronics*, 2(4):159–163, 2019.

[25] Masafumi Tamura, Yasuhiro Nakazawa, Daisuke Shiomi, Kiyokazu Nozawa, Yuko Hosokoshi, Masayasu Ishikawa, Minuro Takahashi, and Minoru Kinoshita. Bulk ferromagnetism in the β-phase crystal of the p-nitrophenyl nitronyl nitroxide radical. *Chem. Phys. Lett.*, 186(4):401–404, 1991.

[26] Juan M. Manriquez, Gordon T. Yee, R. Scott McLean, Arthur J. Epstein, and Joel S. Miller. A room-temperature molecular/organic-based magnet. *Science*, 252(5011):1415–1417, 1991.

[27] D. Gatteschi, Roberta Sessoli, and Jacques Villain. *Molecular nanomagnets*. Mesoscopic physics and nanotechnology; 5. Oxford University Press, Oxford, 2006.

[28] R. Sessoli, D. Gatteschi, A. Caneschi, and M. A. Novak. Magnetic bistability in a metal-ion cluster. *Nature*, 365(6442):141–143, 1993.

[29] Ayuk M Ako, Ian J Hewitt, Valeriu Mereacre, Rodolphe Clérac, Wolfgang Wernsdorfer, Christopher E Anson, and Annie K Powell. A ferromagnetically coupled Mn_{19} aggregate with a record S=83/2 ground spin state. *Angewandte Chemie*, 118(30):5048–5051, 2006.

[30] Wei-Peng Chen, Jared Singleton, Lei Qin, Agustín Camón, Larry Engelhardt, Fernando Luis, Richard E. P. Winpenny, and Yan-Zhen Zheng. Quantum monte carlo simulations of a giant $Ni_{21}Gd_{20}$ cage with a S=91 spin ground state. *Nature Communications*, 9(1):2107, 2018.

[31] Conrad A. P. Goodwin, Fabrizio Ortu, Daniel Reta, Nicholas F. Chilton, and David P. Mills. Molecular magnetic hysteresis at 60 Kelvin in dysprosocenium. *Nature*, 548(7668):439–442, 2017.

[32] Naoto Ishikawa, Miki Sugita, Tadahiko Ishikawa, Shin-ya Koshihara, and Youkoh Kaizu. Lanthanide double-decker complexes functioning as magnets at the single-molecular level. *J. Am. Chem. Soc.*, 125(29):8694–8695, 2003.

[33] Rashmi Bagai and George Christou. The drosophila of single-molecule magnetism: $[Mn_{12}O_{12}(O_2Cr)_{16}(H_2O)_4]$. *Chemical Society Reviews*, 38(4):1011–1026, 2009.

[34] Nicholas F. Chilton. Molecular magnetism. *Annual Review of Materials Research*, 52:79–101, 2022.

[35] Lapo Bogani and Wolfgang Wernsdorfer. Molecular spintronics using single-molecule magnets. *Nature Materials*, 7(3):179–186, 2008.

[36] A Chiesa, P Santini, E Garlatti, F Luis, and S Carretta. Molecular nanomagnets: a viable path toward quantum information processing? *Reports on Progress in Physics*, 87(3):034501, 2024.

[37] Roy J. Glauber. Time-dependent statistics of the Ising model. *Journal of Mathematical Physics*, 4(2):294–307, 1963.

[38] A. Caneschi, D. Gatteschi, N. Lalioti, C. Sangregorio, R. Sessoli, G. Venturi, A. Vindigni, A. Rettori, M. G. Pini, and M. A. Novak. Glauber slow dynamics of the magnetization in a molecular Ising chain. *Europhysics Letters*, 58(5):771, 2002.

[39] Lapo Bogani, Alessandro Vindigni, Roberta Sessoli, and Dante Gatteschi. Single chain magnets: where to from here? *J. Mater. Chem.*, 18:4750–4758, 2008.

[40] Tian-Fu Liu, Dan Fu, Song Gao, Yuan-Zhu Zhang, Hao-Ling Sun, Gang Su, and Yong-Jiang Liu. An azide-bridged homospin single-chain magnet: [Co(2,2'-bithiazoline)$(N_3)_2]_n$. *J. Am. Chem. Soc.*, 125(46):13976–13977, 2003.

[41] Luminita Marilena Toma, Liviu Dan Toma, Fernando S. Delgado, Catalina Ruiz-Pérez, Jorunn Sletten, Joan Cano, Juan Modesto Clemente-Juan, Francesc Lloret, and Miguel Julve. Trans-dicyanobis(acetylacetonato)ruthenate(III) as a precursor to build novel cyanide-bridged Ru(III)-M(II) bimetallic compounds [M=Co and Ni]. *Coordination Chemistry Reviews*, 250(17):2176–2193, 2006.

[42] Rodrigue Lescouëzec, Jacqueline Vaissermann, Catalina Ruiz-Pérez, Francesc Lloret, Rosa Carrasco, Miguel Julve, Michel Verdaguer, Yves Dromzee, Dante Gatteschi, and Wolfgang Wernsdorfer. Cyanide-bridged Iron(III)–Cobalt(II) double zigzag ferromagnetic chains: Two new molecular magnetic nanowires. *Angewandte Chemie International Edition*, 42(13):1483–1486, 2003.

[43] Kevin Bernot, Lapo Bogani, Andrea Caneschi, Dante Gatteschi, and Roberta Sessoli. A family of rare-earth-based single chain magnets: Playing with anisotropy. *J. Am. Chem. Soc.*, 128(24):7947–7956, 2006.

[44] K. Bernot, L. Bogani, R. Sessoli, and D. Gatteschi. [Tm(III)$(hfac)_3$(NiTPhOPh)]$_\infty$: A new member of a lanthanide-based single chain magnets family. *Inorganica Chimica Acta*, 360(13):3807–3812, 2007.

[45] Neil B McKeown. *Phthalocyanine materials: synthesis, structure and function*. Number 6. Cambridge university press, 1998.

[46] James Broadhurst, Giuseppe Mallia, and Nicholas Harrison. The quantum origin of magnetic coupling in molecular crystals for spintronics. *The Journal of Chemical Physics*, 162(24):244708, 2025.

[47] A. Braun and J. Tcherniac. Über die produkte der einwirkung von acetanhydrid auf phthalamid. *Berichte der deutschen chemischen Gesellschaft*, 40(2):2709–2714, 1907.

[48] Henri de Diesbach and Edmond von der Weid. Quelques sels complexes des o-dinitriles avec le cuivre et la pyridine. *Helvetica Chimica Acta*, 10(1):886–888, 1927.

[49] R. P. Linstead. 212. Phthalocyanines. Part I. A new type of synthetic colouring matters. *J. Chem. Soc.*, pages 1016–1017, 1934.

[50] Peter Gregory. Industrial applications of phthalocyanines. *Journal of porphyrins and phthalocyanines*, 4(4):432–437, 2000.

[51] Hai Wang, Soumaya Mauthoor, Salahud Din, Jules A. Gardener, Rio Chang, Marc Warner, Gabriel Aeppli, David W. McComb, Mary P. Ryan, Wei Wu, Andrew J. Fisher, Marshall Stoneham, and Sandrine Heutz. Ultralong copper phthalocyanine nanowires with new crystal structure and broad optical absorption. *ACS Nano*, 4(7):3921–3926, 2010.

[52] M. Brinkmann, P. Turek, and J. André. EPR study of the x, α and β structures of lithium phthalocyanine. *J. Mater. Chem.*, 8:675–685, 1998.

[53] S. Heutz, C. Mitra, W. Wu, A. J Fisher, A. Kerridge, M. Stoneham, A. H Harker, J. Gardener, H. H. Tseng, T. S Jones, C. Renner, and G. Aeppli. Molecular thin films: A new type of magnetic switch. *Advanced Materials*, 19(21):3618–3622, 2007.

[54] Rosemary R. Cranston and Benoît H. Lessard. Metal phthalocyanines: thin-film formation, microstructure, and physical properties. *RSC Adv.*, 11:21716–21737, 2021.

[55] Amy C. Cruickshank, Christian J. Dotzler, Salahud Din, Sandrine Heutz, Michael F. Toney, and Mary P. Ryan. The crystalline structure of copper phthalocyanine films on ZnO(1100). *J. Am. Chem. Soc.*, 134(35):14302–14305, 2012.

[56] Christian G. Claessens, Uwe Hahn, and Tomás Torres. Phthalocyanines: From outstanding electronic properties to emerging applications. *The Chemical Record*, 8(2):75–97, 2008.

[57] R Seoudi, GS El-Bahy, and ZA El Sayed. Ultraviolet and visible spectroscopic studies of phthalocyanine and its complexes thin films. *Optical Materials*, 29(2-3):304–312, 2006.

[58] Wei Wu, L. A. Rochford, S. Felton, Zhenlin Wu, J. L. Yang, S. Heutz, G. Aeppli, T. S. Jones, N. M. Harrison, and A. J. Fisher. Magnetic properties of copper hexadecaphthalocyanine (F_{16}CuPc) thin films and powders. *Journal of Applied Physics*, 113(1):013914, 2013.

[59] Wei Chen, Shuang Chen, Shi Chen, Yu Li Huang, Han Huang, Dong Chen Qi, Xing Yu Gao, Jing Ma, and Andrew Thye Shen Wee. Orientation-controlled charge transfer at CuPc/F_{16}CuPc interfaces. *Journal of Applied Physics*, 106(6):064910, 2009.

[60] H. Brinkmann, C. Kelting, S. Makarov, O. Tsaryova, G. Schnurpfeil, D. Wöhrle, and D. Schlettwein. Fluorinated phthalocyanines as molecular semiconductor thin films. *Physica Status Solidi(A*, 205(3):409–420, 2008.

[61] Yu Jiang, Minzhi Li, Xu Liang, John Mack, Martijn Wildervanck, Tebello Nyokong, Mingfeng Qin, and Weihua Zhu. Lipophilic M(α, α-OC_5H_{11})$_8$ phthalocyanines (M = H_2 and Ni(II)): synthesis, electronic structure, and their utility for highly efficient carbonyl reductions. *Dalton Trans.*, 44:18237–18246, 2015.

[62] Lyudmila A. Lapkina Yuliya G. Gorbunova and Aslan Yu. Tsivadze. Supramolecular systems constructed from crownphthalocyaninates. *Journal of Coordination Chemistry*, 56(14):1223–1232, 2003.

[63] Yasuyuki Yamada, Katsuhiko Nawate, Tomoaki Maeno, and Kentaro Tanaka. Intramolecular strong electronic coupling in a discretely h-aggregated phthalocyanine dimer connected with a rigid linker. *Chem. Commun.*, 54:8226–8228, 2018.

[64] Mathieu Abel, Sylvain Clair, Oualid Ourdjini, Mireille Mossoyan, and Louis Porte. Single layer of polymeric fe-phthalocyanine: An organometallic sheet on metal and thin insulating film. *J. Am. Chem. Soc.*, 133(5):1203–1205, 2011.

[65] M. Koudia and M. Abel. Step-by-step on-surface synthesis: from manganese phthalocyanines to their polymeric form. *Chem. Commun.*, 50:8565–8567, 2014.

[66] Yun-Peng Wang, Xiang-Guo Li, Shuang-Long Liu, James N. Fry, and Hai-Ping Cheng. Magnetic phase transition induced by electrostatic gating in two-dimensional square metal-organic frameworks. *Phys. Rev. B*, 97:115419, 2018.

[67] Jian Zhou and Qiang Sun. Magnetism of phthalocyanine-based organometallic single porous sheet. *J. Am. Chem. Soc.*, 133(38):15113–15119, 2011.

[68] Biswanath Mukherjee and Moumita Mukherjee. Programmable memory in organic field-effect transistor based on lead phthalocyanine. *Organic Electronics*, 10(7):1282–1287, 2009.

[69] R. Zeis, T. Siegrist, and Ch. Kloc. Single-crystal field-effect transistors based on copper phthalocyanine. *Applied Physics Letters*, 86(2):022103, 2005.

[70] Luis Martín-Gomis, Fernando Fernández-Lázaro, and Ángela Sastre-Santos. Advances in phthalocyanine-sensitized solar cells (PcSSCs). *J. Mater. Chem. A*, 2:15672–15682, 2014.

[71] Wei Wu, N. M. Harrison, and A. J. Fisher. p-orbital nanomagnetism in an organic chain magnet. *Phys. Rev. B*, 88:180404, 2013.

[72] Yang Song, Chuan-Kui Wang, Gang Chen, and Guang-Ping Zhang. A first-principles study of phthalocyanine-based multifunctional spintronic molecular devices. *Phys. Chem. Chem. Phys.*, 23:18760–18769, 2021.

[73] Wenkai Zhao, Dongqing Zou, Chuan-Lu Yang, and Zhaopeng Sun. Spin transport properties and spin logic gates in manganese phthalocyanine-based molecular combinational circuits. *J. Mater. Chem. C*, 5:8862–8868, 2017.

[74] L. L. Tao and J. Wang. Giant magnetoresistance and perfect spin filter effects in manganese phthalocyanine based molecular junctions. *Nanoscale*, 9:12684–12689, 2017.

[75] Mirko Cinchetti, Kathrin Heimer, Jan-Peter Wüstenberg, Oleksiy Andreyev, Michael Bauer, Stefan Lach, Christiane Ziegler, Yongli Gao, and Martin Aeschlimann. Determination of spin injection and transport in a ferromagnet/organic semiconductor heterojunction by two-photon photoemission. *Nature Materials*, 8(2):115–119, 2009.

[76] Wei Wu, N. M. Harrison, and A. J. Fisher. Suitability of chromium phthalocyanines to test haldane's conjecture: First-principles calculations. *Phys. Rev. B*, 88(22):224417, 2013.

[77] C. G. Barraclough, R. L. Martin, S. Mitra, and R. C. Sherwood. Paramagnetic Anisotropy, Electronic Structure, and Ferromagnetism in Spin, S=32 Manganese(II) Phthalocyanine. *J. Chem. Phys.*, 53(5):1638–1642, 1970.

[78] Philip Coppens, Liang Li, and Nai Jui Zhu. Electronic ground state of iron (II) phthalocyanine as determined from accurate diffraction data. *J. Am. Chem. Soc.*, 105(19):6173–6174, 1983.

[79] T. Kroll, V. Yu Aristov, O. V. Molodtsova, Yu A. Ossipyan, D. V. Vyalikh, B. Büchner, and M. Knupfer. Spin and orbital ground state of Co in cobalt phthalocyanine. *J. Phys. Chem. A*, 113(31):8917–8922, 2009.

[80] Fabrizio Evangelista, Vincenzo Carravetta, Giovanni Stefani, Branislav Jansik, Michele Alagia, Stefano Stranges, and Alessandro Ruocco. Electronic structure of copper phthalocyanine: An experimental and theoretical study of occupied and unoccupied levels. *J. Chem. Phys.*, 126(12):124709, 2007.

[81] C. Ercolani, C. Neri, and P. Porta. Synthesis and x-ray data of a stable in air crystalline modification of chromium (II) phthalocyanine (Cr-α-Pc). *Inorganica Chimica Acta*, 1:415–418, 1967.

[82] A. B. P. Lever. 336. The magnetic behaviour of transition-metal phathalocyanines. *J. Chem. Soc.*, pages 1821–1829, 1965.

[83] Wei Wu, A. Kerridge, A. H. Harker, and A. J. Fisher. Structure-dependent exchange in the organic magnets Cu(II)Pc and Mn(II)Pc. *Phys. Rev. B*, 77:184403, 2008.

[84] Bryce E Williamson, Thomas C VanCott, Michael E Boyle, G Christian Misener, Martin J Stillman, and Paul N Schatz. Determination of the ground state of manganese phthalocyanine in an argon matrix using magnetic circular dichroism and absorption spectroscopy. *J. Am. Chem. Soc.*, 114(7):2412–2419, 1992.

[85] Meng-Sheng Liao, John D. Watts, and Ming-Ju Huang. Dft study of unligated and ligated manganese (II) porphyrins and phthalocyanines. *Inorganic Chemistry*, 44(6):1941–1949, 2005.

[86] Samaresh Mitra, AK Gregson, William E Hatfield, and Robert R Weller. Single-crystal magnetic study on ferromagnetic manganese (II) phthalocyaninate. *Inorganic Chemistry*, 22(12):1729–1732, 1983.

[87] J. Crangle. *Solid state magnetism.* Edward Arnold, 1991.

[88] Hiroyuki Yamada, Toshihiro Shimada, and Atsushi Koma. Preparation and magnetic properties of manganese (II) phthalocyanine thin films. *J. Chem. Phys.*, 108(24):10256–10261, 1998.

[89] Michael D. Kuz'min, Roland Hayn, and Vincent Oison. Ab initio calculated XANES and XMCD spectra of Fe(II) phthalocyanine. *Phys. Rev. B*, 79:024413, 2009.

[90] Huayan Xia, Lihong Li, Mei Fang, Tim S. Jones, and Junliang Yang. Molecular-orientation-dependent magnetic properties of iron phthalocyanine (FePc) thin films and microwires. *Organic Electronics*, 121:106870, 2023.

[91] Wei Wu, A. J. Fisher, and N. M. Harrison. Theoretical modeling of the electronic structure and exchange interactions in a Cu(II)Pc one-dimensional chain. *Phys. Rev. B*, 84:024427, 2011.

[92] Jill C. Bonner and Michael E. Fisher. Linear magnetic chains with anisotropic coupling. *Phys. Rev.*, 135:A640–A658, 1964.

[93] Michele Serri, Wei Wu, Luke R. Fleet, Nicholas M. Harrison, Cyrus F. Hirjibehedin, Christopher W. M. Kay, Andrew J. Fisher, Gabriel Aeppli, and Sandrine Heutz. High-temperature antiferromagnetism in molecular semiconductor thin films and nanostructures. *Nature Communications*, 5(1):3079, 2014.

[94] W. Wu, A. J. Fisher, and N. M. Harrison. Electronic structure and exchange interactions in cobalt-phthalocyanine chains. *Phys. Rev. B*, 88(2):024426, 2013.

[95] Z. Wang, M. Lee, E.S. Choi, J. Poston, and M.S. Seehra. Low temperature, high magnetic field investigations of the nature of magnetism in the molecular semiconductor β-cobalt phthalocyanine ($C_{32}H_{16}CoN_8$). *Journal of Magnetism and Magnetic Materials*, 407:83–86, 2016.

[96] Xi Chen, Ying-Shuang Fu, Shuai-Hua Ji, Tong Zhang, Peng Cheng, Xu-Cun Ma, Xiao-Long Zou, Wen-Hui Duan, Jin-Feng Jia, and Qi-Kun Xue. Probing superexchange interaction in molecular magnets by spin-flip spectroscopy and microscopy. *Phys. Rev. Lett.*, 101:197208, 2008.

[97] John B. Goodenough. Theory of the role of covalence in the perovskite-type manganites [La, M(II)]MnO_3. *Phys. Rev.*, 100:564–573, 1955.

[98] Junjiro Kanamori. Superexchange interaction and symmetry properties of electron orbitals. *Journal of Physics and Chemistry of Solids*, 10(2):87–98, 1959.

[99] P. W. Anderson. Antiferromagnetism. theory of superexchange interaction. *Phys. Rev.*, 79:350–356, 1950.

[100] Nicola Marzari, Andrea Ferretti, and Chris Wolverton. Electronic-structure methods for materials design. *Nature Materials*, 20(6):736–749, 2021.

[101] Sabrina C. Shen, Eesha Khare, Nicolas A. Lee, Michael K. Saad, David L. Kaplan, and Markus J. Buehler. Computational design and manufacturing of sustainable materials through first-principles and materiomics. *Chemical Reviews*, 123(5):2242–2275, 2023.

[102] John A Keith, Valentin Vassilev-Galindo, Bingqing Cheng, Stefan Chmiela, Michael Gastegger, Klaus-Robert Muller, and Alexandre Tkatchenko. Combining machine learning and computational chemistry for predictive insights into chemical systems. *Chemical Reviews*, 121(16):9816–9872, 2021.

[103] Julia Westermayr, Michael Gastegger, Kristof T. Schütt, and Reinhard J. Maurer. Perspective on integrating machine learning into computational chemistry and materials science. *J. Chem. Phys.*, 154(23):230903, 2021.

[104] Attila Szabo and Neil S. Ostlund. *Modern Quantum Chemistry : Introduction to Advanced Electronic Structure Theory*. Dovere, Mineola, N.Y, 1996 - 1989.

[105] Richard L. Liboff. *Introductory Quantum Mechanics*. Addison-Wesley, Reading, Mass., 3rd edition, 1998.

[106] Maria Fyra. *Computational Approaches in Physics*. [IOP release 3]. Morgan Claypool Publishers, San Rafael, California, 2016.

[107] Sérgio Filipe Sousa, Pedro Alexandrino Fernandes, and Maria João Ramos. General performance of density functionals. *J. Phys. Chem. A*, 111(42):10439–10452, 2007.

[108] J. Grant Hill, James A. Platts, and Hans-Joachim Werner. Calculation of intermolecular interactions in the benzene dimer using coupled-cluster and local electron correlation methods. *Phys. Chem. Chem. Phys.*, 8:4072–4078, 2006.

[109] Thomas Gasevic, Markus Bursch, Qianli Ma, Stefan Grimme, Hans-Joachim Werner, and Andreas Hansen. The p-block challenge: assessing quantum chemistry methods for inorganic heterocycle dimerizations. *Phys. Chem. Chem. Phys.*, 26:13884–13908, 2024.

[110] Zohreh Amanollahi, Lukas Lampe, Moritz Bensberg, Johannes Neugebauer, and Milica Feldt. On the accuracy of orbital based multi-level approaches for closed-shell transition metal chemistry. *Phys. Chem. Chem. Phys.*, 25:4635–4648, 2023.

[111] Jorge. Kohanoff. *Electronic structure calculations for solids and molecules : theory and computational methods*. Cambridge University Press, Cambridge, 2006.

[112] NM Harrison. An introduction to density functional theory. *Nato Science Series Sub Series III Computer and Systems Sciences*, 187:45–70, 2003.

[113] Klaus Capelle. A bird's-eye view of density-functional theory. *Brazilian Journal of Physics*, 36(4a):1318–1343, 2006.

[114] P. Hohenberg and W. Kohn. Inhomogeneous electron gas. *Phys. Rev.*, 136:B864–B871, 1964.

[115] W. Kohn and L. J. Sham. Self-consistent equations including exchange and correlation effects. *Phys. Rev.*, 140:A1133–A1138, 1965.

[116] D. M. Ceperley and B. J. Alder. Ground state of the electron gas by a stochastic method. *Phys. Rev. Lett.*, 45:566–569, 1980.

[117] J. P. Perdew and Alex Zunger. Self-interaction correction to density-functional approximations for many-electron systems. *Phys. Rev. B*, 23:5048–5079, 1981.

[118] John P. Perdew. Accurate density functional for the energy: Real-space cutoff of the gradient expansion for the exchange hole. *Phys. Rev. Lett.*, 55:1665–1668, 1985.

[119] A. D. Becke. Density-functional exchange-energy approximation with correct asymptotic behavior. *Phys. Rev. A*, 38:3098–3100, 1988.

[120] Chengteh Lee, Weitao Yang, and Robert G. Parr. Development of the Colle-Salvetti correlation-energy formula into a functional of the electron density. *Phys. Rev. B*, 37(2):785–789, 1988.

[121] John P. Perdew, Kieron Burke, and Matthias Ernzerhof. Generalized gradient approximation made simple. *Phys. Rev. Lett.*, 77:3865–3868, 1996.

[122] Stefan Kurth, John P. Perdew, and Peter Blaha. Molecular and solid-state tests of density functional approximations: LSD, GGAs, and meta-GGAs. *International Journal of Quantum Chemistry*, 75(4-5):889–909, 1999.

[123] Carlo Adamo, Matthias Ernzerhof, and Gustavo E. Scuseria. The meta-GGA functional: Thermochemistry with a kinetic energy density dependent exchange-correlation functional. *J. Chem. Phys.*, 112(6):2643–2649, 2000.

[124] Jianmin Tao, John P Perdew, Viktor N Staroverov, and Gustavo E Scuseria. Climbing the density functional ladder: Nonempirical meta–generalized gradient approximation designed for molecules and solids. *Physical review letters*, 91(14):146401, 2003.

[125] Jianwei Sun, Adrienn Ruzsinszky, and John P Perdew. Strongly constrained and appropriately normed semilocal density functional. *Phys. Rev. Lett.*, 115(3):036402, 2015.

[126] Yan Zhao and Donald G. Truhlar. A new local density functional for main-group thermochemistry, transition metal bonding, thermochemical kinetics, and noncovalent interactions. *J. Chem. Phys.*, 125(19):194101, 2006.

[127] J. Harris. Adiabatic-connection approach to Kohn-Sham theory. *Phys. Rev. A*, 29:1648–1659, 1984.

[128] Axel D Becke. A new mixing of Hartree-Fock and local density-functional theories. *J. Chem. Phys.*, 98(2):1372–1377, 1993.

[129] Axel D. Becke. Density-functional thermochemistry. III. The role of exact exchange. *J. Chem. Phys.*, 98(7):5648–5652, 1993.

[130] Aliaksandr V. Krukau, Oleg A. Vydrov, Artur F. Izmaylov, and Gustavo E. Scuseria. Influence of the exchange screening parameter on the performance of screened hybrid functionals. *J. Chem. Phys.*, 125(22):224106, 2006.

[131] Thomas M. Henderson, Artur F. Izmaylov, Gustavo E. Scuseria, and Andreas Savin. The importance of middle-range Hartree-Fock-type exchange for hybrid density functionals. *J. Chem. Phys.*, 127(22):221103, 2007.

[132] Thomas M. Henderson, Artur F. Izmaylov, Gustavo E. Scuseria, and Andreas Savin. Assessment of a middle-range hybrid functional. *Journal of Chemical Theory and Computation*, 4(8):1254–1262, 2008.

[133] Carlo Adamo and Vincenzo Barone. Toward reliable density functional methods without adjustable parameters: The PBE0 model. *J. Chem. Phys.*, 110(13):6158–6170, 1999.

[134] Larry A. Curtiss, Krishnan Raghavachari, Paul C. Redfern, and John A. Pople. Assessment of Gaussian-2 and density functional theories for the computation of enthalpies of formation. *J. Chem. Phys.*, 106(3):1063–1079, 1997.

[135] Hai Xiao, Jamil Tahir-Kheli, and III Goddard, William A. Accurate band gaps for semiconductors from density functional theory. *J. Phys. Chem. Lett.*, 2(3):212–217, 2011.

[136] J. Muscat, A. Wander, and N.M. Harrison. On the prediction of band gaps from hybrid functional theory. *Chem. Phys. Lett.*, 342(3):397–401, 2001.

[137] O. Madelung. *Introduction to Solid-State Theory*. Springer series in Solid-State sciences. Springer, Berlin, 1996 - 1978.

[138] Felix Bloch. Über die quantenmechanik der elektronen in kristallgittern. *Zeitschrift für physik*, 52(7):555–600, 1929.

[139] Richard M. Martin. *Electronic structure : basic theory and practical methods*. Cambridge University Press, Cambridge, UK ;, 1st pbk, ed., with corrections. edition, 2008.

[140] Eva. Perlt. *Basis Sets in Computational Chemistry*. Lecture Notes in Chemistry, 107. Springer International Publishing, Cham, 1st edition, 2021.

[141] Alessandro Erba, Jacques K Desmarais, Silvia Casassa, Bartolomeo Civalleri, Lorenzo Donà, Ian J Bush, Barry Searle, Lorenzo Maschio, Loredana Edith-Daga, Alessandro Cossard, et al. CRYSTAL23: A program for computational solid state physics and chemistry. *Journal of Chemical Theory and Computation*, 19(20):6891–6932, 2022.

[142] Frank. Jensen. *Introduction to computational chemistry*. John Wiley Sons, Chichester, England ;, 2nd ed. edition, 2007.

[143] H. Bernhard Schlegel. Geometry optimization. *WIREs Computational Molecular Science*, 1(5):790–809, 2011.

[144] C. G. Broyden. The convergence of a class of double-rank minimization algorithms 1. general considerations. *IMA Journal of Applied Mathematics*, 6(1):76–90, 1970.

[145] C. G. Broyden. The convergence of a class of double-rank minimization algorithms: 2. the new algorithm. *IMA Journal of Applied Mathematics*, 6(3):222–231, 1970.

[146] R. Fletcher. A new approach to variable metric algorithms. *The Computer Journal*, 13(3):317–322, 1970.

[147] Donald Goldfarb. A family of variable-metric methods derived by variational means. *Mathematics of computation*, 24(109):23–26, 1970.

[148] David F Shanno. Conditioning of Quasi-Newton methods for function minimization. *Mathematics of computation*, 24(111):647–656, 1970.

[149] Walter A. Harrison. *Electronic Structure and the Properties of Solids: The Physics of the Chemical Bond*. Dover Books on Physics. Dover Publications, Newburyport, 2012.

[150] R. S. Mulliken. Electronic Population Analysis on LCAO–MO Molecular Wave Functions. I. *J. Chem. Phys.*, 23(10):1833–1840, 1955.

[151] Per-Olov Löwdin. On the Non-Orthogonality Problem Connected with the Use of Atomic Wave Functions in the Theory of Molecules and Crystals. *J. Chem. Phys.*, 18(3):365–375, 1950.

[152] Joachim Stohr and Hans Christoph Siegmann. *Magnetism : from fundamentals to nanoscale dynamics*. Springer series in Solid-State Sciences, 152. Springer, Berlin, 2006.

[153] William Lowrie and Andreas Fichtner. *Fundamentals of geophysics*. Cambridge University Press, Cambridge, 3rd edition, 2020.

[154] William Gilbert. *De Magnete, Magneticisque Corporibus, et de Magno Magnete Tellure*. Peter Short, London, 1600.

[155] Roberto De Andrade Martins. Resistance to the discovery of electromagnetism: Ørsted and the symmetry of the magnetic field. *Volta and the History of Electricity*, pages 245–266, 2003.

[156] J Clerk Maxwell. A treatise on electricity and magnetism. *Clarendon Press Google Scholar*, 2:3408–3425, 1873.

[157] Neils Bohr. II. The Doctor's Dissertation. In L. Rosenfeld and J. Rud Nielsen, editors, *Early Work (1905–1911)*, volume 1 of *Niels Bohr Collected Works*, pages 163–393. Elsevier, 1972.

[158] H. J Van Leeuwen. Problemes de la théorie électronique du magnétisme. *J. Phys. Radium*, 2(12):361–377, 1921.

[159] Stephen Blundell. *Magnetism in condensed matter*. Oxford master series in condensed matter physics. Oxford University Press, Oxford, 2001.

[160] Joachim Stohr and Hans Christoph Siegmann. *Magnetism : from fundamentals to nanoscale dynamics*. Springer series in solid-state sciences, 152. Springer, Berlin, 2006.

[161] Robert M. White. *Quantum theory of magnetism : magnetic properties of materials*. Springer series in solid-state sciences ; 32. Springer, Berlin, 3rd edition, 2007.

[162] M. A. Ruderman and C. Kittel. Indirect exchange coupling of nuclear magnetic moments by conduction electrons. *Phys. Rev.*, 96:99–102, 1954.

[163] Tadao Kasuya. A Theory of Metallic Ferro- and Antiferromagnetism on Zener's Model. *Progress of Theoretical Physics*, 16(1):45–57, 1956.

[164] Kei Yosida. Magnetic properties of Cu-Mn alloys. *Phys. Rev.*, 106:893–898, 1957.

[165] Giulia C. De Fusco, Leonardo Pisani, Barbara Montanari, and Nicholas M. Harrison. Density functional study of the magnetic coupling in $V(TCNE)_2$. *Phys. Rev. B*, 79:085201, 2009.

[166] DD Koelling and BN Harmon. A technique for relativistic spin-polarised calculations. *Journal of Physics C: Solid State Physics*, 10(16):3107, 1977.

[167] Jacques K. Desmarais, Jean-Pierre Flament, and Alessandro Erba. Spin-orbit coupling from a two-component self-consistent approach. I. generalized Hartree-Fock theory. *J. Chem. Phys.*, 151(7), 2019.

[168] Haechan Park, Shuanglong Liu, James N. Fry, and Hai-Ping Cheng. First-principles study of bilayer polymeric manganese phthalocyanine. *Phys. Rev. B*, 105:195408, 2022.

[169] W. Heisenberg. Zur theorie des ferromagnetismus. *Zeitschrift für Physik*, 49(9):619–636, 1928.

[170] Paul Adrien Maurice Dirac and Ralph Howard Fowler. On the theory of quantum mechanics. *Proceedings of the Royal Society of London. Series A, Containing Papers of a Mathematical and Physical Character*, 112(762):661–677, 1926.

[171] J. H van Vleck. Electric and magnetic susceptibilities, Univ. Press, 1932.

[172] J. Hubbard and Brian Hilton Flowers. Electron correlations in narrow energy bands. *Proceedings of the Royal Society of London. Series A. Mathematical and Physical Sciences*, 276(1365):238–257, 1963.

[173] Assa. Auerbach. *Interacting electrons and quantum magnetism*. Graduate texts in contemporary physics. Springer-Verlag, New York ;, 1994.

[174] David Muñoz, Ibério de P. R. Moreira, and Francesc Illas. Effective t-J model hamiltonian parameters of monolayered cuprate superconductors from ab initio electronic structure calculations. *Phys. Rev. B*, 65:224521, 2002.

[175] Yen-Sheng Su, T. A. Kaplan, S. D. Mahanti, and J. F. Harrison. Crystal Hartree-Fock calculations for La_2NiO_4 and La_2CuO_4. *Phys. Rev. B*, 59:10521–10529, 1999.

[176] Christopher Lane, James W. Furness, Ioana Gianina Buda, Yubo Zhang, Robert S. Markiewicz, Bernardo Barbiellini, Jianwei Sun, and Arun Bansil. Antiferromagnetic ground state of La_2CuO_4: A parameter-free ab initio description. *Phys. Rev. B*, 98:125140, 2018.

[177] Louis Noodleman. Valence bond description of antiferromagnetic coupling in transition metal dimers. *J. Chem. Phys.*, 74(10):5737–5743, 1981.

[178] Alessandro Bencini and Dante Gatteschi. Xα-SW calculations of the electronic structure and magnetic properties of weakly coupled transition-metal clusters. The $[Cu_2Cl_6]_2$ dimers. *J. Am. Chem. Soc.*, 108(19):5763–5771, 1986.

[179] K Yamaguchi, Y Takahara, and T Fueno. Applied quantum chemistry. *Reidel, Dordrecht*, 155, 1986.

[180] T Soda, Y Kitagawa, T Onishi, Y Takano, Y Shigeta, H Nagao, Y Yoshioka, and K Yamaguchi. Ab initio computations of effective exchange integrals for H–H,

H–He–H and Mn_2O_2 complex: comparison of broken-symmetry approaches. *Chem. Phys. Lett.*, 319(3-4):223–230, 2000.

[181] Yu Takano, Shigehiro Kubo, Taku Onishi, Hiroshi Isobe, Yasunori Yoshioka, and Kizashi Yamaguchi. Theoretical studies on the magnetic interaction and reversible dioxygen binding of the active site in hemocyanin. *Chem. Phys. Lett.*, 335(5-6):395–403, 2001.

[182] K. Yamaguchi, F. Jensen, A. Dorigo, and K. N. Houk. A spin correction procedure for unrestricted Hartree-Fock and Møller-Plesset wavefunctions for singlet diradicals and polyradicals. *Chem. Phys. Lett.*, 149(5):537–542, 1988.

[183] Kohei Tada, Shingo Tanaka, Takashi Kawakami, Yasutaka Kitagawa, Mitsutaka Okumura, and Kizashi Yamaguchi. Spin contamination errors on spin-polarized density functional theory/plane-wave calculations for crystals of one-dimensional materials. *Applied Physics Express*, 12(11):115506, 2019.

[184] James Broadhurst, Giuseppe Mallia, and Nicholas Harrison. A prediction of high temperature magnetic coupling in transition metal phthalocyanines. *J. Chem. Phys.*, 161(11):114703, 2024.

[185] Hai Xiao, Jamil Tahir-Kheli, and III Goddard, William A. Accurate band gaps for semiconductors from density functional theory. *J. Phys. Chem. Lett.*, 2(3):212–217, 2011.

[186] Richard L. Martin and Francesc Illas. Antiferromagnetic exchange interactions from hybrid density functional theory. *Phys. Rev. Lett.*, 79(8):1539–1542, 1997.

[187] Stefan Grimme, Jens Antony, Stephan Ehrlich, and Helge Krieg. A consistent and accurate ab initio parametrization of density functional dispersion correction (DFT-D) for the 94 elements H-Pu. *J. Chem. Phys.*, 132(15):154104, 2010.

[188] Stefan Grimme, Stephan Ehrlich, and Lars Goerigk. Effect of the damping function in dispersion corrected density functional theory. *Journal of Computational Chemistry*, 32(7):1456–1465, 2011.

[189] Stefan Grimme, Andreas Hansen, Jan Gerit Brandenburg, and Christoph Bannwarth. Dispersion-corrected mean-field electronic structure methods. *Chemical Reviews*, 116(9):5105–5154, 2016.

[190] P. Pulay. Convergence acceleration of iterative sequences. the case of SCF iteration. *Chem. Phys. Lett.*, 73(2):393–398, 1980.

[191] P. Pulay. Improved SCF convergence acceleration. *Journal of Computational Chemistry*, 3(4):556–560, 1982.

[192] Hendrik J. Monkhorst and James D. Pack. Special points for brillouin-zone integrations. *Phys. Rev. B*, 13:5188–5192, Jun 1976.

[193] R Dovesi, VR Saunders, C Roetti, R Orlando, CM Zicovich-Wilson, F Pascale, B Civalleri, K Doll, NM Harrison, IJ Bush, et al. CRYSTAL23. 2023.

[194] Jacques K. Desmarais, Jean-Pierre Flament, and Alessandro Erba. Fundamental role of fock exchange in relativistic density functional theory. *J. Phys. Chem. Lett.*, 10(13):3580–3585, 2019.

[195] Jacques K. Desmarais, Jean-Pierre Flament, and Alessandro Erba. Adiabatic connection in spin-current density functional theory. *Phys. Rev. B*, 102(23):235118, 2020.

[196] Jacques K. Desmarais, Jean-Pierre Flament, and Alessandro Erba. Spin-orbit coupling in periodic systems with broken time-reversal symmetry: Formal and computational aspects. *Phys. Rev. B*, 101(23):235142, 2020.

[197] Jacques K. Desmarais, Jean-Pierre Flament, and Alessandro Erba. Spin-orbit coupling from a two-component self-consistent approach. II. non-collinear density functional theories. *J. Chem. Phys.*, 151(7), 2019.

[198] Luis Fernandez Pacios and P. A. Christiansen. Ab initio relativistic effective potentials with spin-orbit operators. I. Li through Ar. *J. Chem. Phys.*, 82(6):2664–2671, 1985.

[199] M. M. Hurley, Luis Fernandez Pacios, P. A. Christiansen, R. B. Ross, and W. C. Ermler. Ab initio relativistic effective potentials with spin-orbit operators. II. K through Kr. *J. Chem. Phys.*, 84(12):6840–6853, 1986.

[200] L. A. LaJohn, P. A. Christiansen, R. B. Ross, T. Atashroo, and W. C. Ermler. Ab initio relativistic effective potentials with spin–orbit operators. III. Rb through Xe. *J. Chem. Phys.*, 87(5):2812–2824, 1987.

[201] R. B. Ross, J. M. Powers, T. Atashroo, W. C. Ermler, L. A. LaJohn, and P. A. Christiansen. Ab initio relativistic effective potentials with spin–orbit operators. IV. Cs through Rn. *J. Chem. Phys.*, 93(9):6654–6670, 1990.

[202] Richard B. Ross, Sanjukta Gayen, and Walter C. Ermler. Ab initio relativistic effective potentials with spin–orbit operators. V. Ce through Lu. *J. Chem. Phys.*, 100(11):8145–8155, 1994.

[203] W. C. Ermler, R. B. Ross, and P. A. Christiansen. Ab initio relativistic effective potentials with spin-orbit operators.VI. Fr through Pu. *International Journal of Quantum Chemistry*, 40(6):829–846, 1991.

[204] Clinton S. Nash, Bruce E. Bursten, and Walter C. Ermler. Ab initio relativistic effective potentials with spin-orbit operators. VII. Am through element 118. *J. Chem. Phys.*, 106(12):5133–5142, 1997.

[205] James Broadhurst. CRYSTALProjectTools. `https://github.com/JamesB686/CRYSTALProjectTools`, 2024.

[206] Koichi Momma and Fujio Izumi. VESTA3 for three-dimensional visualization of crystal, volumetric and morphology data. *Journal of Applied Crystallography*, 44(6):1272–1276, 2011.

[207] Imperial College Research Computing Service. DOI: 10.14469/hpc/2232.

[208] C. J. Brown. Crystal structure of β-copper phthalocyanine. *J. Chem. Soc. A*, pages 2488–2493, 1968.

[209] Paolo Ballirano, Ruggero Caminiti, Claudio Ercolani, Adriana Maras, and Maria Antonietta Orrù. X-ray powder diffraction structure reinvestigation of the α and β forms of cobalt phthalocyanine and kinetics of the $\alpha \rightarrow \beta$ phase transition. *J. Am. Chem. Soc.*, 120(49):12798–12807, 1998.

[210] Jing Zhou, Linjuan Zhang, Zhiwei Hu, Changyang Kuo, Hengjie Liu, Xiao Lin, Yu Wang, Tun-Wen Pi, Jianqiang Wang, and Shuo Zhang. The significant role of covalency in determining the ground state of cobalt phthalocyanines molecule. *AIP Advances*, 6(3):035306, 2016.

[211] Satadeep Bhattacharjee, Barbara Brena, Rudra Banerjee, Heiko Wende, Olle Eriksson, and Biplab Sanyal. Electronic structure of Co-phthalocyanine calculated by GGA+U and hybrid functional methods. *Chemical Physics*, 377(1-3):96–99, 2010.

[212] A.A.M. Farag. Optical absorption studies of copper phthalocyanine thin films. *Optics Laser Technology*, 39(4):728–732, 2007.

[213] Akitaka Hoshino, Yoshiko Takenaka, Masahiro Izukashi, Hidehito Yoshida, and Hideki Miyaji. Epitaxial growth of copper and cobalt phthalocyanines on KCl. *Japanese Journal of Applied Physics*, 43(7R):4344, 2004.

[214] Akitaka Hoshino, Yoshiko Takenaka, and Hideki Miyaji. Redetermination of the crystal structure of α-copper phthalocyanine grown on KCl. *Acta Crystallographica Section B*, 59(3):393–403, 2003.

[215] Soumyajyoti Haldar, Sumanta Bhandary, Hakkim Vovusha, and Biplab Sanyal. Comparative study of electronic and magnetic properties of iron and cobalt phthalocyanine molecules physisorbed on two-dimensional MoS_2 and graphene. *Phys. Rev. B*, 98:085440, 2018.

[216] David G. DeWit. Reactivity of mononuclear rhodium (II) compounds. *Coordination Chemistry Reviews*, 147:209–246, 1996.

[217] Tamer Ezzat Youssef and Hanan H. Mohamed. Synthesis and photophysicochemical properties of novel mononuclear rhodium (III) phthalocyanines. *Polyhedron*, 30(12):2045–2050, 2011.

[218] G. Ferraudi, S. Oishi, and S. Muraldiharan. The photochemical properties of rhodium (III) phthalocyanine cation radicals. *J. Phys. Chem.*, 88(22):5261–5264, 1984.

[219] Tebello Nyokong. Cyclic voltammetry and spectroelectrochemistry of rhodium phthalocyanines. *J. Chem. Soc., Dalton Trans.*, pages 1359–1365, 1994.

[220] S Muralidharan and G Ferraudi. Sequential biphotonic processes in rhodium (III) phthalocyanines. *J. Phys. Chem.*, 87(24):4877–4881, 1983.

[221] Pekka Pyykkö and Michiko Atsumi. Molecular single-bond covalent radii for elements 1–118. *Chemistry – A European Journal*, 15(1):186–197, 2009.

[222] Carmen Jiménez Calzado, Jesús Cabrero, Jean Paul Malrieu, and Rosa Caballol. Analysis of the magnetic coupling in binuclear complexes. I. Physics of the coupling. *J. Chem. Phys.*, 116:2728–2747, 2002.

[223] Carmen Jiménez Calzado, Jesús Cabrero, Jean Paul Malrieu, and Rosa Caballol. Analysis of the magnetic coupling in binuclear complexes. II. Derivatio of valence effective Hamiltonians from ab initio CI and DFT calculations. *J. Chem. Phys.*, 116:3985–4000, 2002.

[224] Carmen Jiménez Calzado, Celestino Angeli, David Taratiel, Rosa Caballol, and Jean-Paul Malrieu. Analysis of the magnetic coupling in binuclear systems. III. The role of the ligand to metal charge transfer excitations revisited. *J. Chem. Phys.*, 131:1–14, 2009.

[225] Ph De Loth, Ph Cassoux, JP Daudey, and JP Malrieu. Ab initio direct calculation of the singlet-triplet separation in cupric acetate hydrate dimer. *J. Am. Chem. Soc.*, 103(14):4007–4016, 1981.

[226] Grégoire David, Georges Trinquier, and Jean-Paul Malrieu. Consistent spin decontamination of broken-symmetry calculations of diradicals. *J. Chem. Phys.*, 153(19), 2020.

[227] Grégoire David, Gwenhaël Duplaix-Rata, and Boris Le Guennic. What governs magnetic exchange couplings in radical-bridged dinuclear complexes? *Phys. Chem. Chem. Phys.*, 26(11):8952–8964, 2024.

[228] Grégoire David, Nathalie Guihéry, and Nicolas Ferré. What are the physical contents of Hubbard and Heisenberg Hamiltonian interactions extracted from broken symmetry DFT calculations in magnetic compounds? *Journal of Chemical Theory and Computation*, 13(12):6253–6265, 2017.

[229] Esther Coulaud, Nathalie Guihéry, Jean-Paul Malrieu, Denis Hagebaum-Reignier, Didier Siri, and Nicolas Ferré. Analysis of the physical contributions to magnetic couplings in broken symmetry density functional theory approach. *J. Chem. Phys.*, 137(11), 2012.

[230] Esther Coulaud, Jean-Paul Malrieu, Nathalie Guihéry, and Nicolas Ferré. Additive decomposition of the physical components of the magnetic coupling from broken

symmetry density functional theory calculations. *Journal of Chemical Theory and Computation*, 9(8):3429–3436, 2013.

[231] Gwenhaël Duplaix-Rata, Boris Le Guennic, and Grégoire David. Revisiting magnetic exchange couplings in heterodinuclear complexes through the decomposition method in KS-DFT. *Phys. Chem. Chem. Phys.*, 25(20):14170–14178, 2023.

[232] Grégoire David, Nicolas Ferré, and Boris Le Guennic. Consistent evaluation of magnetic exchange couplings in multicenter compounds in KS-DFT: The recomposition method. *Journal of Chemical Theory and Computation*, 19(1):157–173, 2023.

[233] Frank Neese. The ORCA program system. *Wiley Interdisciplinary Reviews: Computational Molecular Science*, 2(1):73–78, 2012.

[234] Frank Neese. Software update: the ORCA program system, version 4.0. *Wiley Interdisciplinary Reviews: Computational Molecular Science*, 8(1):e1327, 2018.

[235] Xavier Assfeld and Jean-Louis Rivail. Quantum chemical computations on parts of large molecules: the ab initio local self consistent field method. *Chem. Phys. Lett.*, 263(1):100–106, 1996.

[236] János Pipek and Paul G. Mezey. A fast intrinsic localization procedure applicable for abinitio and semiempirical linear combination of atomic orbital wave functions. *J. Chem. Phys.*, 90(9):4916–4926, 1989.

[237] Seymour H Vosko, Leslie Wilk, and Marwan Nusair. Accurate spin-dependent electron liquid correlation energies for local spin density calculations: a critical analysis. *Canadian Journal of Physics*, 58(8):1200–1211, 1980.

[238] Yun-Peng Wang, Xiang-Guo Li, Shuang-Long Liu, James N. Fry, and Hai-Ping Cheng. Magnetic phase transition induced by electrostatic gating in two-dimensional square metal-organic frameworks. *Phys. Rev. B*, 97:115419, 2018.

[239] Mike Towler. TCM CRYSTAL Resources Page. `https://vallico.net/mike_towler/crystal.html`, 2022.

[240] CRYSTAL. CRYSTAL Basis Set Libary. `https://www.crystal.unito.it/basis_sets.html`, 2022.

[241] Daniel Vilela Oliveira, Joachim Laun, Michael F. Peintinger, and Thomas Bredow. Bsse-correction scheme for consistent gaussian basis sets of double- and triple-zeta valence with polarization quality for solid-state calculations. *Journal of Computational Chemistry*, 40(27):2364–2376, 2019.

[242] Joachim Laun, Daniel Vilela Oliveira, and Thomas Bredow. Consistent gaussian basis sets of double- and triple-zeta valence with polarization quality of the fifth period for solid-state calculations. *Journal of Computational Chemistry*, 39(19):1285–1290, 2018.

[243] Nicolas Ferré and Xavier Assfeld. Application of the local self-consistent-field method to core-ionized and core-excited molecules, polymers, and proteins: True orthogonality between ground and excited states. *J. Chem. Phys.*, 117(9):4119–4125, 2002.

[244] Marjory C. Clement, Xiao Wang, and Edward F. Valeev. Robust Pipek–Mezey orbital localization in periodic solids. *Journal of Chemical Theory and Computation*, 17(12):7406–7415, 2021.

[245] Florian Weigend and Reinhart Ahlrichs. Balanced basis sets of split valence, triple zeta valence and quadruple zeta valence quality for H to Rn: Design and assessment of accuracy. *Phys. Chem. Chem. Phys.*, 7:3297, 2005.

A

Basis Sets

All sets of GTO basis functions used in the studies presented in this report are disclosed below. For each set, the exponent, α_i, and coefficient, c_i are given. All basis sets are optimised for the use in periodic systems and have been obtained from Refs. [239, 240]. Each metal basis set has been modified to include a set of polarisation functions, the exponent of which has been sourced from Refs. [241, 242].

A.1 Cobalt

Shell	α_i	c_i	
$1s$		s	
	341701.0000	0.000227	
	48850.0000	0.001929	
	10400.9000	0.01110	
	2718.9900	0.05010	
	819.6610	0.1705	
	283.8780	0.3692	
	111.0170	0.4033	
	46.4757	0.1433	
$2sp$		s	p
	855.5580	-0.0054	0.0088
	206.5040	-0.0684	0.0620
	69.0516	-0.1316	0.2165
	27.2653	0.2616	0.4095
	11.5384	0.6287	0.3932
	4.2017	0.2706	0.2250
$3sp$		s	p
	51.5542	0.0182	-0.0287
	18.9092	-0.2432	-0.0937
	7.7251	-0.8490	0.2036
	3.5428	0.8264	1.4188
$4sp$		s	p
	1.4914	1.0	1.0
$5sp$		s	p
	0.6031	1.0	1.0

Shell	α_i	c_i
$3d$		d
	29.9009	0.0617
	8.1164	0.2835
	2.6433	0.5290
	0.8869	0.4976
$4d$		d
	0.3011	1.0
$4f$		f
	1.903	1.0

A.2 Copper

Shell	α_i	c_i	
$1s$		s	
	398000.0000	0.0002270	
	56670.0000	0.001929	
	12010.0000	0.01114	
	3139.0000	0.05013	
	947.2000	0.1703	
	327.6800	0.3693	
	128.3900	0.4030	
	53.6300	0.1437	
$2sp$		s	p
	1022.0000	-0.00487	0.008500
	238.9000	-0.06740	0.06063
	80.0000	-0.12420	0.2118
	31.8600	0.24660	0.3907
	13.3300	0.67200	0.3964
	4.4420	0.28900	0.2610
$3sp$		s	p
	54.7000	0.01190	-0.0288
	23.2600	-0.14600	-0.0741
	9.9200	-0.75000	0.1820
	4.0130	1.03100	1.2800
$4sp$		s	p
	1.5820	1.0	1.0
$5sp$		s	p
	0.5590	1.0	1.0

Shell	α_i	c_i
$3d$		d
	48.5400	0.03100
	13.5500	0.16200
	4.5200	0.37800
	1.4700	0.45900
$4d$		d
	0.4300	1.0
$4f$		f
	2.2330	1.0

A.3 Manganese

Shell	α_i	c_i	
$1s$		s	
	292601.0000	0.0002270	
	42265.0000	0.001900	
	8947.2900	0.01110	
	2330.3200	0.05010	
	702.0470	0.1705	
	242.9070	0.3691	
	94.9550	0.4035	
	39.5777	0.1437	
$2sp$		s	p
	732.1400	-0.00530	0.00860
	175.5510	-0.06730	0.06120
	58.5093	-0.12930	0.21350
	23.1290	0.25350	0.40180
	9.7536	0.63450	0.40120
	3.4545	0.27140	0.22220
$3sp$		s	p
	38.3890	0.01570	-0.03110
	15.4367	-0.25350	-0.09690
	6.1781	-0.86480	0.25630
	2.8235	0.93370	1.65520
$4sp$		s	p
	1.2086	1.0	1.0
$5sp$		s	p
	0.4986	1.0	1.0

Shell	α_i	c_i
$3d$		d
	22.5929	0.07080
	6.1674	0.3044
	2.0638	0.5469
	0.7401	0.5102
$4d$		d
	0.2490	1.0
$4f$		f
	1.3260	1.0

A.4 Iron

Shell	α_i	c_i	
$1s$		s	
	315379.0000	0.0002270	
	45690.0000	0.001900	
	9677.3000	0.01110	
	2520.8800	0.05010	
	759.7460	0.17050	
	262.9640	0.36924	
	102.8010	0.40330	
	42.9733	0.14340	
$2sp$		s	p
	798.2620	-0.005200	0.008500
	191.1620	-0.06800	0.06080
	63.6885	-0.13140	0.21140
	25.3625	0.25170	0.39440
	10.7338	0.64330	0.39800
	3.7640	0.28250	0.22510
$3sp$		s	p
	48.1434	0.01220	-0.02150
	17.4579	-0.22780	-0.08500
	6.9972	-0.88010	0.20100
	3.0791	0.97550	1.30240
$4sp$		s	p
	1.3137	1.0	1.0
$5sp$		s	p
	0.5625	1.0	1.0

Shell	α_i	c_i
$3d$		d
	30.4821	0.05830
	8.6920	0.25910
	3.1008	0.51620
	1.1709	0.56560
$4d$		d
	0.4345	1.0
$4f$		f
	1.1980	1.0

A.5 Chromium

Shell	α_i	c_i	
$1s$		s	
	235200.0000	0.0002700	
	35040.0000	0.002110	
	7806.0000	0.01139	
	2134.0000	0.04860	
	669.2000	0.1591	
	235.9000	0.3555	
	90.5200	0.4231	
	35.8800	0.1482	
$2sp$		s	p
	735.0000	-0.004730	0.008430
	176.1000	-0.05930	0.06100
	57.6500	-0.13530	0.23040
	21.8400	0.23750	0.47430
	8.9870	0.67310	0.46060
	3.4600	0.24870	0.16960
$3sp$		s	p
	33.8400	0.01100	-0.02790
	11.7200	-0.42070	-0.08120
	5.4140	-0.86730	0.22110
	2.5020	0.96750	1.03300
$4sp$		s	p
	1.1590	1.0	1.0
$5sp$		s	p
	0.5035	1.0	1.0

Shell	α_i	c_i
$3d$		d
	30.5700	0.03077
	8.4030	0.16040
	2.8340	0.39070
	1.0020	0.47880
$4d$		d
	0.3538	1.0
$4f$		f
	1.1470	1.0

A.6 Rhodium

Shell	α_i	c_i	
$1s$		s	
	3327036.5000	0.00004870	
	504400.2500	0.0003740	
	109039.9766	0.002220	
	27491.2148	0.01120	
	7823.6880	0.04680	
	2479.1201	0.1561	
	875.4503	0.3524	
	343.9631	0.4257	
	142.4540	0.1756	
$2sp$		s	p
	9588.2295	-0.000358	0.001020
	2212.8999	-0.006610	0.009440
	672.0008	-0.05610	0.05650
	235.2685	-0.1475	0.2182
	92.8736	0.1718	0.4557
	41.4345	0.6463	0.4181
	19.5677	0.3549	0.1498
$3sp$		s	p
	209.0530	0.005860	-0.01480
	78.4767	-0.03690	-0.07380
	33.1303	-0.3331	0.05780
	14.3868	0.07110	0.9320
	6.6341	0.9490	1.278
	3.1265	0.3807	0.4098
$4sp$		s	p
	5.1562	-3.958	-0.08240
	2.4297	1.387	0.5389
	1.0561	9.333	0.9554

Shell	α_i	c_i	
$5sp$		s	p
	0.4449	1.0	1.0
$6sp$		s	p
	0.1541	1.0	1.0
$3d$		d	
	309.6160	0.01020	
	92.1470	0.07300	
	34.2798	0.2521	
	13.9996	0.4467	
	5.9303	0.3753	
	2.4421	0.0888	
$4d$		d	
	3.7762	0.1650	
	1.4392	0.4744	
	0.5509	0.4719	
$5d$		d	
	0.2017	1.0	
$4f$		f	
	1.0950	1.0	

A.7 Carbon

Shell	α_i	c_i	
$1s$		s	
	30475.2488	0.01835	
	4573.6952	0.1404	
	1039.4869	0.6884	
	292.1016	2.3218	
	92.8666	4.6794	
	31.6393	3.6231	
$2sp$		s	p
	78.6827	-0.1193	0.6900
	18.8129	-1.6085	3.1642
	5.4425	11.4346	7.4431
$3sp$		s	p
	0.1687	1.0	1.0
$3d$		d	
	0.8000	1.0	

A.8 Nitrogen

Shell	α_i	c_i	
$1s$		s	
	41735.1000	0.01835	
	6274.5800	0.1399	
	1429.0200	0.6859	
	402.3430	0.2322	
	128.2020	0.4691	
	43.9044	0.3605	
$2sp$		s	p
	11.6264	-1.1496	0.6758
	2.7163	-1.6912	3.2391
	0.7722	11.4585	7.4089
$3sp$		s	p
	0.2120	1.0	1.0
$3d$		d	
	0.8000	1.0	

A.9 Hydrogen

Shell	α_i	c_i
$1s$		s
	187.3114	0.03349
	28.2539	2.3473
	6.4012	8.1376
$2s$		s
	0.1612	1.0
$2p$		p
	1.1000	1.0

B

Mathematical Formalisms

A number of important concepts and derivations are presented below in order to compliment, where necessary, information in the main of body of work.

B.1 Two Component SCF Procedure

In the two-component SCF (2c-SCF) procedure, the electronic Schrödinger equation is reformulated so as to account for relativistic effects that arise due to the finite (and constant) speed of light. This reformulated equation is known as the *electronic Dirac equation*[1] and facilitates the calculation of spin-orbit coupling (SOC) and scalar relativistic effects. Here, the one-component (1c) eigenfunctions of the Schrödinger equation are replaced by 2c eigenfunctions within a so-called Pauli spinor basis, given by

$$\psi_i(\mathbf{r}) = \sum_{\mu} c^{\alpha}_{i,\mu} \begin{pmatrix} \phi_\mu(\mathbf{r}) \\ 0 \end{pmatrix} + c^{\beta}_{i,\mu} \begin{pmatrix} 0 \\ \phi_\mu(\mathbf{r}) \end{pmatrix} \tag{B.1}$$

where $c^{\sigma}_{i,\mu}$ are the (complex) coefficients of the AO, $\phi_\mu(\mathbf{r})$, for the i^{th} MO. The consequence of this formulation is that the 1×1 Hamiltonian operator in the Schrödinger basis, $\mathbf{H}$, is transformed into a 2×2 operator in the Pauli spinor basis.

$$\mathbf{H} = \begin{pmatrix} \mathbf{H}^{\alpha\alpha} & \mathbf{H}^{\alpha\beta} \\ \mathbf{H}^{\beta\alpha} & \mathbf{H}^{\beta\beta} \end{pmatrix} \tag{B.2}$$

Generalisation of this treatment to the HF or KS approximations results in a complex set of equations, given by

$$\begin{pmatrix} \mathbf{F}^{\alpha\alpha} & \mathbf{F}^{\alpha\beta} \\ \mathbf{F}^{\beta\alpha} & \mathbf{F}^{\beta\beta} \end{pmatrix} \begin{pmatrix} \mathbf{c}^{\alpha} \\ \mathbf{c}^{\beta} \end{pmatrix} = \begin{pmatrix} \mathbf{S}^{\alpha\alpha} & \mathbf{0} \\ \mathbf{0} & \mathbf{S}^{\beta\beta} \end{pmatrix} \begin{pmatrix} \mathbf{c}^{\alpha} \\ \mathbf{c}^{\beta} \end{pmatrix} \epsilon \tag{B.3}$$

where $\mathbf{F}^{\sigma\sigma'}$ are the respective Fock or KS operators, $\mathbf{c}^{\sigma}$ are the coefficients for the eigenvectors, $\mathbf{S}^{\sigma\sigma}$ is the overlap matrix and ϵ are the respective eigenvalues.

For periodic calculations, such as those carried out in the CRYSTAL program, the MOs are transformed into crystalline orbitals (COs) composed of a linear combination of Bloch functions, again within a 2c formulation,

$$\psi_i(\mathbf{r}, \mathbf{k}) = \sum_{\mu} c^{\alpha}_{i,\mu}(\mathbf{k}) \begin{pmatrix} \phi_\mu(\mathbf{r}, \mathbf{k}) \\ 0 \end{pmatrix} + c^{\beta}_{i,\mu}(\mathbf{k}) \begin{pmatrix} 0 \\ \phi_\mu(\mathbf{r}, \mathbf{k}) \end{pmatrix} \tag{B.4}$$

[1] The full Dirac equation takes into account both electronic and positronic energy contributions, labelled as the "Large" and "Small" components, respectively. However, in quantum chemistry calculations, only the electronic portion of the energy is of relevance and, as such, only information related to the 2c-SCF procedure is included here.

where $\phi_n(\mathbf{r}, \mathbf{k})$ are the one-electron Bloch functions as defined in Sec. 2.5.3. Eq. B.3 is reformulated to reflect the $\mathbf{k}$ dependence. For additional information, readers are directed to Refs. [141, 167, 193–197].

B.2 Direct Inversion of the Iterative Subspace

The direct inversion of the iterative subspace (DIIS) scheme, originally formulated by Péter Pulay [190, 191], is a convergence accelerator algorithm implemented in many quantum simulation programs, including both the CRYSTAL and ORCA software packages. The scheme attempts to accelerate the convergence of the SCF procedure by defining the Fock (or Kohn-Sham) Hamiltonian ($\mathbf{F}$) as a matrix generated from a *linear combination* of Hamiltonian matrices from the previous cycles [141], rather than constructing a new Hamiltonian from the density matrix of the cycle before. Thus, the Hamiltonian at cycle n is defined as,

$$\overline{\mathbf{F}}_n = \sum_{i=1}^{n} c_i \mathbf{F}_i \tag{B.5}$$

where the overline of $\overline{\mathbf{F}}_n$ indicates that it has been generated according to the DIIS scheme. The coefficients c_i are obtained by solving the following set of linear equations,

$$\begin{pmatrix} e_{11} & e_{12} & \cdots & e_{1n} & -1 \\ e_{21} & e_{22} & \cdots & e_{2n} & -1 \\ \vdots & \vdots & \ddots & \vdots & \vdots \\ e_{n1} & e_{n2} & \cdots & e_{nn} & -1 \\ -1 & -1 & \cdots & -1 & 0 \end{pmatrix} \begin{pmatrix} c_1 \\ c_2 \\ \vdots \\ c_n \\ \lambda \end{pmatrix} = \begin{pmatrix} 0 \\ 0 \\ \vdots \\ 0 \\ -1 \end{pmatrix} \tag{B.6}$$

under the constraint,

$$\sum_{i=1}^{n} c_i = 1 \tag{B.7}$$

Here, λ is a Lagrange multiplier and $e_{nm} = \langle \mathbf{e_n} | \mathbf{e_m} \rangle$, where $\mathbf{e_n}$ is the commutator of the Fock ($\mathbf{F}$) and density ($\mathbf{P}$) matrices at cycle n [191], given by

$$\mathbf{e_n} = [\mathbf{F}_n, \mathbf{P}_n] = \mathbf{F}_n \mathbf{P}_n - \mathbf{P}_n \mathbf{F}_n \tag{B.8}$$

B.3 Local Self Consistent Field Procedure

The local self consistent field (LSCF) procedure was originally developed by Assfeld & Rivail [235] for quantum mechanics/molecular mechanics (QM/MM) applications, however, the method has been generalised to fully *ab initio* approaches. The method facilitates the optimisation of a subset of MOs within the field of a different subset of "frozen" MOs (i.e. MOs that are not optimised during the SCF procedure). The details regarding the procedure outlined below have been drawn from Refs. [235, 243] and readers are directed to these publications for further information.

The total quantum system is described by a set of MOs. Within this set, two subsets of orbitals may be defined: a set of frozen orbitals (FOs), and a set variational orbitals (VOs) that are to be optimised during the SCF procedure. A basis set of N AOs are used to describe the orbitals of all atoms in the system. Each FO, denoted as $|\psi_i\rangle$, may be expanded within this set of AOs, as

$$|\psi_i\rangle = \sum_{\mu}^{N} c_{\mu i}|\phi_\mu\rangle \tag{B.9}$$

where $|\phi_\mu\rangle$ is an AO and $c_{\mu i}$ is the respective coefficient. The key principle that underpins the LSCF procedure is the requirement that the VOs are orthogonal to the set of FOs. In order to ensure this, the VOs are developed on a set of basis functions that are themselves orthogonal to the FOs. To achieve this, the set of FOs are first mutually orthogonalised[2], generating a set of new orthogonalised frozen orbitals (OFOs), denoted as $|\psi_i'\rangle$.

The set of N AOs are then orthogonalised to the OFOs through the following transformation,

$$|\phi_\mu'\rangle = \left[1 - \sum_{i}^{M} S_{\mu i}^2\right]^{-1/2} \left[|\phi_\mu\rangle - \sum_{i}^{M} |\psi_i'\rangle\langle\psi_i'|\phi_\mu\rangle\right] \tag{B.10}$$

where

$$S_{\mu i} = \sum_{\lambda}^{N} d_{\lambda i} S_{\mu\lambda} \tag{B.11}$$

Here, the original set of N AOs are projected out of the subspace defined by the OFOs and normalised. However, if the original basis set was linearly independent, there will be M linear dependencies (arising from their involvement in the M FOs) within

[2] In Ref. [235], the authors stipulate the use the Löwdin symmetric orthogonalisation scheme [151].

this new orthonormalised set of basis functions. Therefore, a canonical orthogonalisation procedure [104] is subsequently carried out generating a set of $(N - L)$ functions, denoted as $\{|\tilde{\phi}_\mu\rangle\}$, that are mutually orthogonal, linearly independent and orthogonal to the set of OFOs [235].

The SCF process to optimise the set of VOs proceeds in a similar way to that of a standard SCF calculation. However, once the Fock (or Kohn-Sham) matrix, $\mathbf{F}$, has been defined using a trial density matrix $\mathbf{P}$[3], which itself is defined on the original set of AOs, $\{|\phi_\mu\rangle\}$, a unitary transformation of $\mathbf{F}$ in the set of $\{|\tilde{\phi}_\mu\rangle\}$ is carried out. This defines a new matrix, $\tilde{\mathbf{F}}$, which is diagonalised to obtain an eigenvector matrix, $\tilde{\mathbf{C}}$. This set of eigenvectors are then transformed in the set of $\{|\phi_\mu\rangle\}$, generating a matrix $\mathbf{C}$ which is used to compute $\mathbf{P}^V$ - the density matrix corresponding to the set of VOs. This algorithm is executed iteratively until self consistency is achieved.

B.4 Pipek-Mezey Localisation Procedure

The primary aim of any orbital localisation procedure is to find a set of orbitals $\{|\phi\rangle\}$ that have been transformed by a unitary operator such that they satisfy some localisation criteria. In the Pipek-Mezey procedure [236], the localised orbitals are obtained through the maximisation of a localisation quantity, D, given by,

$$D = \sum_a \sum_i (Q_i^a)^2 \tag{B.12}$$

where a and i index the constituent atoms and MOs of the system and Q_i^μ is the gross atomic Mulliken charge associated with the i^{th} MO on the a^{th} atom (see Sec. 2.7.2). This parameter may be regarded as a measure of the mean delocalisation of the MO over the set of atoms. Thus, the stationary points of this function correspond to the maximally localised orbitals, with respect to the atomic positions [244]. In practice, these stationary points are obtained by deriving a set unitary transformations that act on the MOs, maximising D [236].

[3]The total density matrix $\mathbf{P}$ is defined as $\mathbf{P} = \mathbf{P}^V + \mathbf{P}^F$, where $\mathbf{P}^V$ is the density matrix defined by the set of VOs and $\mathbf{P}^F$ is the density matrix defined by the set of FOs.

C

Supplementary Data

Presented in this appendix is additional data and figures related to the studies carried out in this report.

C.1 Delocalised Magnetic State in RhPc Chains

As noted in Chapter 5, within the additional set of RhPc chain geometries analysed in Sec. 5.3.4, configurations in which the stacking angle, $\phi > 75°$, are omitted from the results due to the generation of a delocalised magnetic state. Here, a brief analysis of the underlying reasons for this observed behaviour is provided. The aim is to offer the reader clarity with regards to the boundaries of ϕ selected for the study.

To initiate the discussion here, two chain geometries of RhPc that reside on the boundary between a localised and delocalised magnetic state are selected and directly compared. The structural parameters defining the geometry of these chains are presented in Table C.1. A critical facet related to the correct evaluation of the coupling interaction in single determinant BS-DFT calculations is the preservation of equivalent electronic configurations (within a suitable numerical accuracy) between the two respective states. This ensures that the difference between the two species *only* relates to the "flipping" of one unpaired electron. Any substantial electron reorganisation in either system introduces additional energy terms, unrelated to the exchange interaction. Thus, this establishes a prerequisite for any accurate assessment of the coupling within the BS-DFT method.

For Chain A, equivalent localised magnetic states[1] are obtained in both the FM (HS) and AFM (BS) configurations. However, for Chain B, there is an inequivalence in the spin states between the two configurations. As shown in Table C.2, in the AFM state of Chain B, a Mulliken charge of $1.077\,|e|$ is found within the metal d_{z^2} AO, whilst, for the FM state, a respective charge of $1.355\,|e|$ is computed. Clearly the numerical discrepancy in the MPA between these two configurations exceeds the acceptable difference that is typically observed between different spin states within the BS-DFT method and indicates that there

[1]Here, the term 'equivalent state" indicates that the occupation of the frontier MOs (as analysed from the Mulliken population) in both the HS and BS configurations is equivalent (within a numerical accuracy), with the only difference between the two arising as a result of the reversal of the spin of one unpaired electron.

Structure	$\mathrm{M}-\mathrm{M}$ [Å]	ϕ [°]	ψ [°]
Chain A	3.83	75.0	0.0
Chain B	3.76	80.0	0.0

Table C.1: Structural parameters defining two RhPc periodic chains. Here, $\mathrm{M}-\mathrm{M}$ is the metal-metal distance between adjacent molecules, ϕ is the stacking angle and ψ is the sliding angle. Please refer to Fig. 1.3 for the definition of these two latter parameters.

Chain A		
Atomic Orbital	FM State	AFM State
d_{z^2}	1.087	1.077
d_{xz}	1.889	1.903
d_{yz}	1.905	1.905
$d_{x^2-y^2}$	0.843	0.843
d_{xy}	1.944	1.944
Chain B		
Atomic Orbital	FM State	AFM State
d_{z^2}	1.355	1.077
d_{xz}	1.848	1.904
d_{yz}	1.849	1.906
$d_{x^2-y^2}$	0.788	0.845
d_{xy}	1.936	1.945

Table C.2: Mulliken population analysis of the charge density localised in the d AOs for the FM (HS) and AFM (BS) states of Chain A and Chain B.

is an inequivalence.

Exanimation of the MPA of the FM state of Chain B indicates that, whilst the charge density localised within the d_{z^2} AO increases, there is a significant decrease in the respective spin density, relative to that observed in the AFM state. In the former configuration (FM), a spin density of $0.548\,|e|$ is computed, whilst in the latter configuration (AFM), the spin density is found to be $0.787\,|e|$. This is also complemented by the total spin density of each metal centre, with values of $0.623\,|e|$ and $0.917\,|e|$ in the FM and AFM states, respectively.

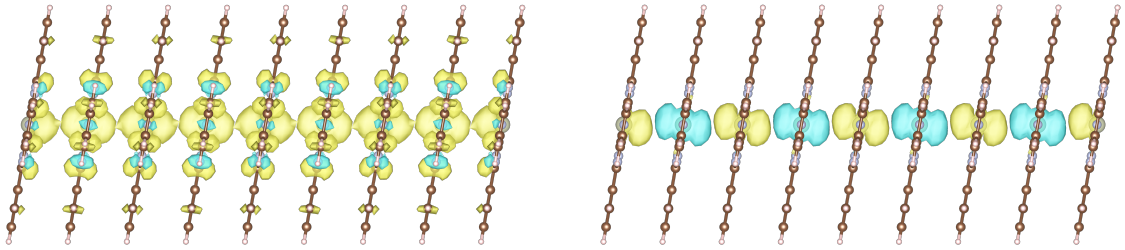

(a) (b)

Figure C.1: Spin density isosurface plots for the (a) FM and (b) AFM configurations of Chain B. An isovalue of $0.001\,|e|$ Å^{-3} is used.

Thus, in the AFM configuration, the system can be understood to be in a well localised state with approximately a single electron occupying the SOMO of each metal centre. However, in the FM configuration, the single electron spin density is delocalised across not only the metal centre but also the phthalocyanine ring. This is likely due to the increased interaction between adjacent d_{z^2}-derived orbitals as ϕ increases. For configurations in which $\phi > 75°$, the Pauli repulsion between same spin orbitals induces a reorganisation of the single electron density within the phthalocyanine. This effect is observed within the FM state of Chain B, as depicted in Fig. C.1(a). Due to the absence of any Pauli repulsion in the AFM configuration, no reorganisation of the spin density is required within the system. As a result of this effect, the stacking angle range studied in Sec. 5.3.4 is truncated at $\phi = 75°$.

C.2 H_2 Basis Set Analysis

An analysis of the affect of the basis set on the value of J^{DE} in the H_2 molecule is carried out. Three basis sets are selected for this study: the DZVP basis set (see Appendix A.9), the def2-SVP basis set [245] and the def2-TZVP basis set [245]. Both the DZVP and def2-SVP basis sets are of double-ζ quality. However, the latter set contains a more diffuse s-function. The def2-TZVP basis set is one of triple-ζ quality, with an outer s-function even more diffuse than that of the def2-SVP. Thus, if the value of J^{DE} in H_2 is dependent upon the relative overlap of the orbitals, it is expected that the def2-TZVP basis set should provide positive quantities at all interatomic distances. As shown in the graphical depiction of the related data (see Fig. C.2), negative measurements of J^{DE} are obtained for all three basis sets at $\mathrm{H}-\mathrm{H}$ distances of $1.5\,\text{Å}$ and $2.0\,\text{Å}$, indicating that the basis set size does *not* establish the correct sign for the DE interaction.

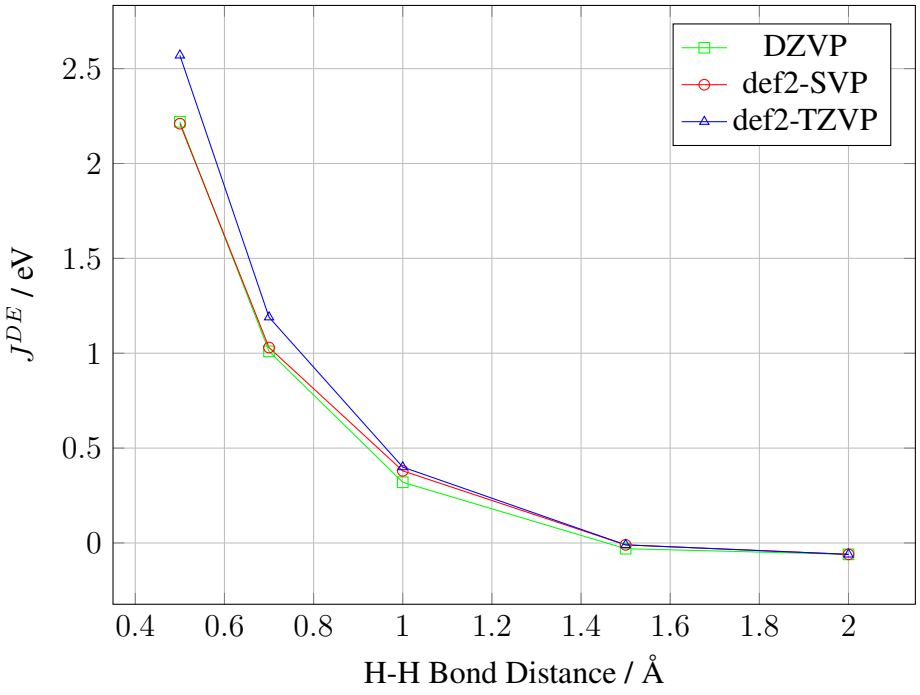

Figure C.2: Variation in J^{DE} as a function of bond distance in H_2 for calculations carried out using the B3LYP approach alongside the DZVP (see Appendix A.9), def2-SVP [245] and def2-TZVP [245] basis sets.

C.3 Poly-TMPc Spin Density Isosurfaces

Figures of the spin density isosurfaces for each magnetic phase of all the first-row poly-TMPcs studied in Chapter 7.

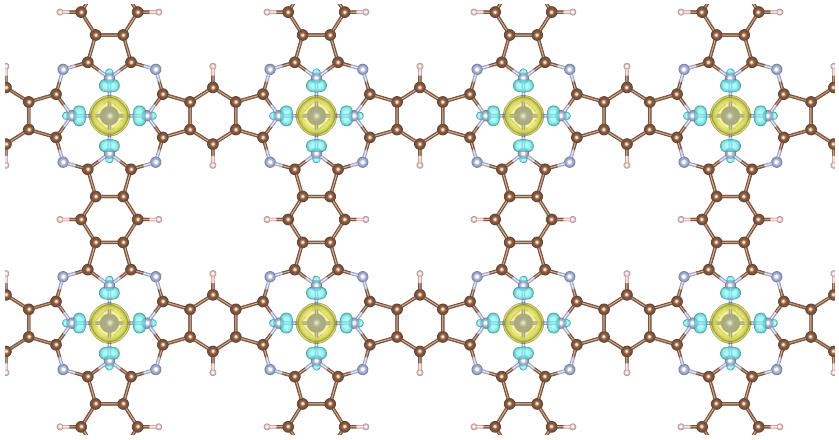

(a)

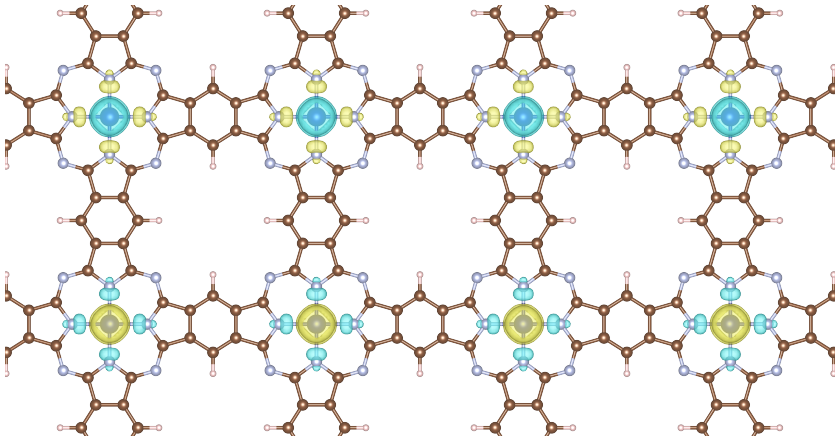

(b)

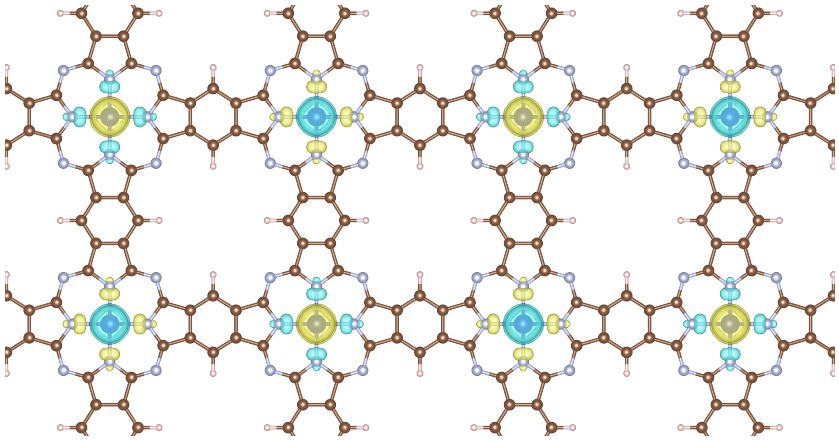

(c)

Figure C.3: Spin density isosurface plots for poly-CoPc in (a) the FM phase, (b) the CAF phase and (c) the NAF phase. An isovalue of $0.001\,|e|$ Å^{-3} is used. Yellow (blue) shading indicates regions of up-spin (down-spin) electron density.

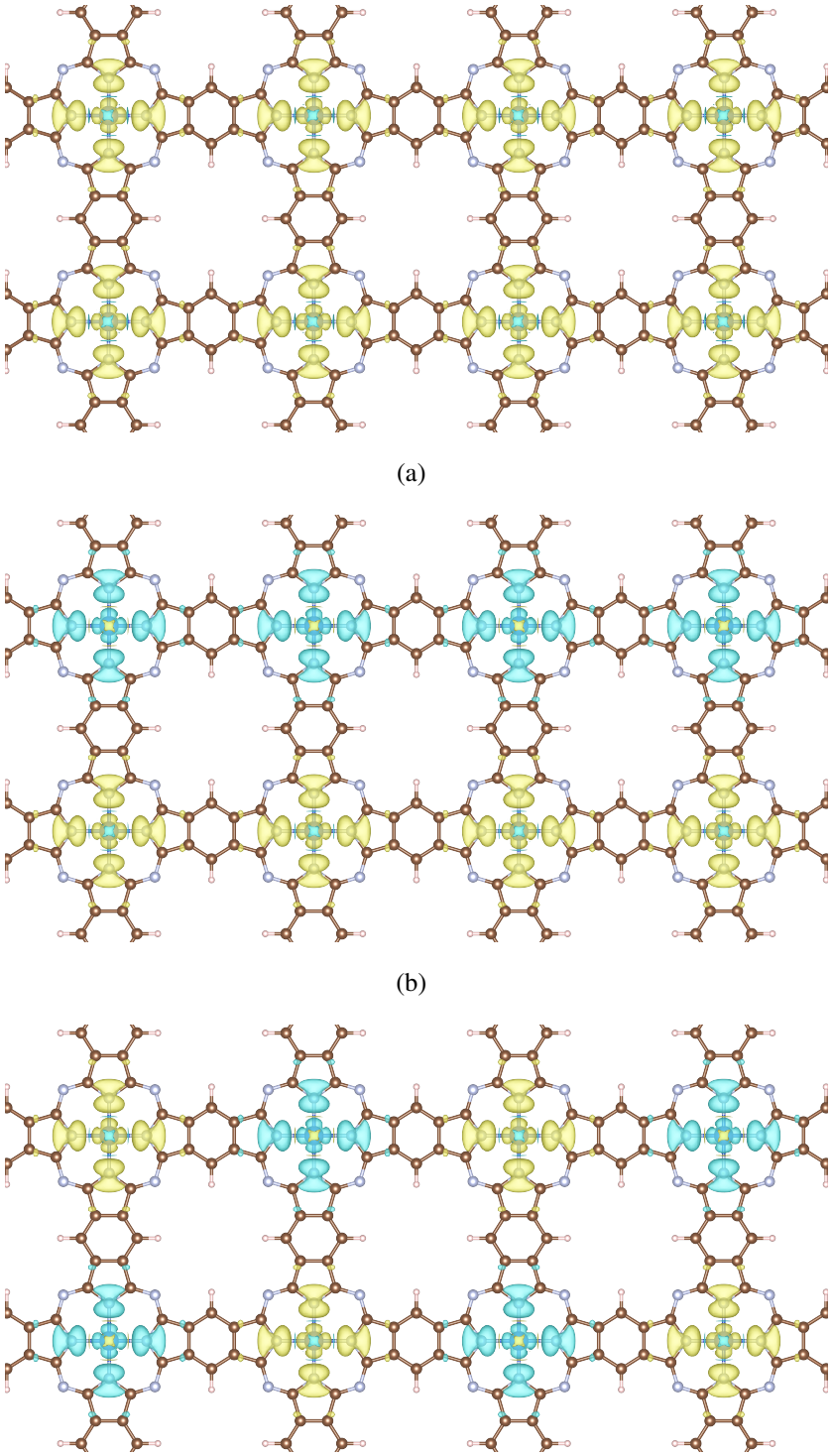

(a)

(b)

(c)

Figure C.4: Spin density isosurface plots for poly-CuPc in (a) the FM phase, (b) the CAF phase and (c) the NAF phase. An isovalue of $0.001\,|e|$ Å^{-3} is used. Yellow (blue) shading indicates regions of up-spin (down-spin) electron density.

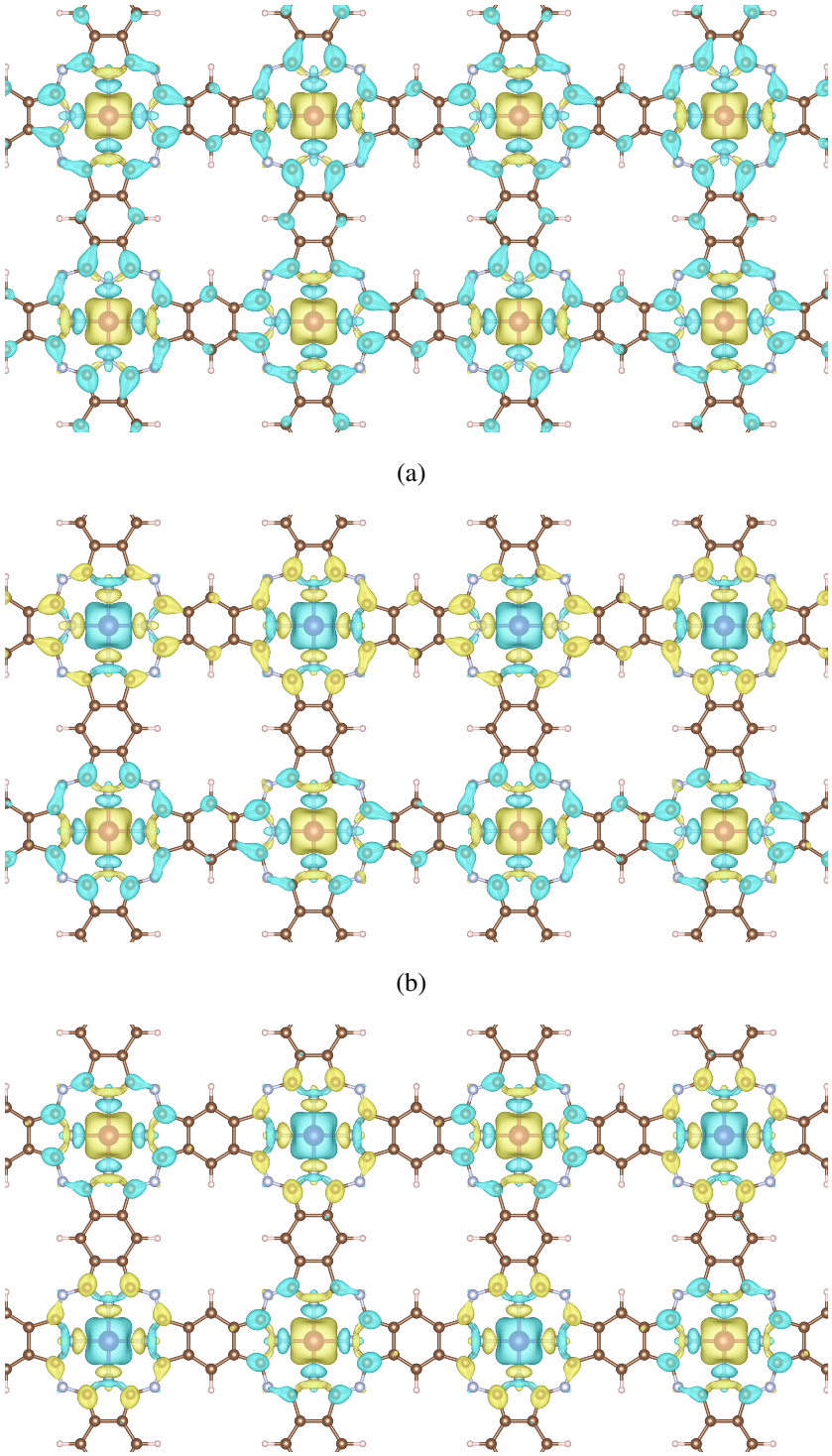

(a)

(b)

(c)

Figure C.5: Spin density isosurface plots for poly-MnPc in (a) the FM phase, (b) the CAF phase and (c) the NAF phase. An isovalue of $0.001\,|e|$ Å^{-3} is used. Yellow (blue) shading indicates regions of up-spin (down-spin) electron density.

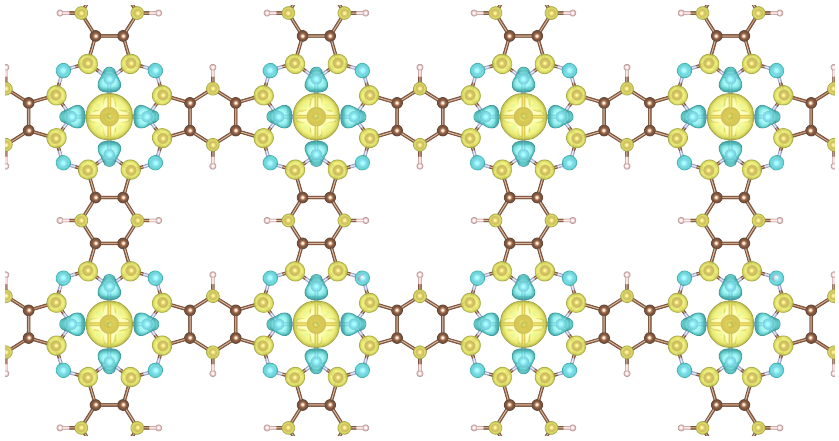

(a)

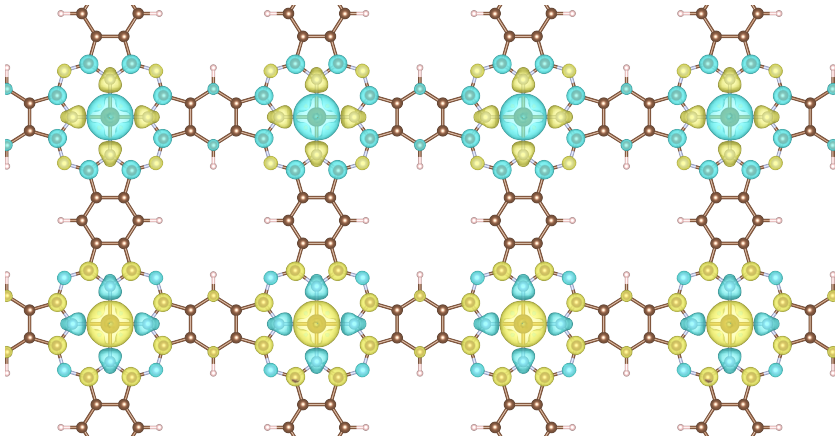

(b)

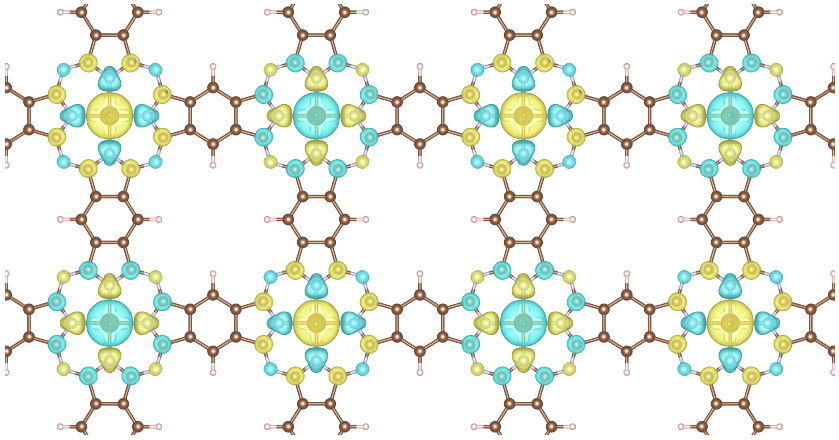

(c)

Figure C.6: Spin density isosurface plots for poly-FePc in (a) the FM phase, (b) the CAF phase and (c) the NAF phase. An isovalue of $0.001\,|e|$ Å^{-3} is used. Yellow (blue) shading indicates regions of up-spin (down-spin) electron density.

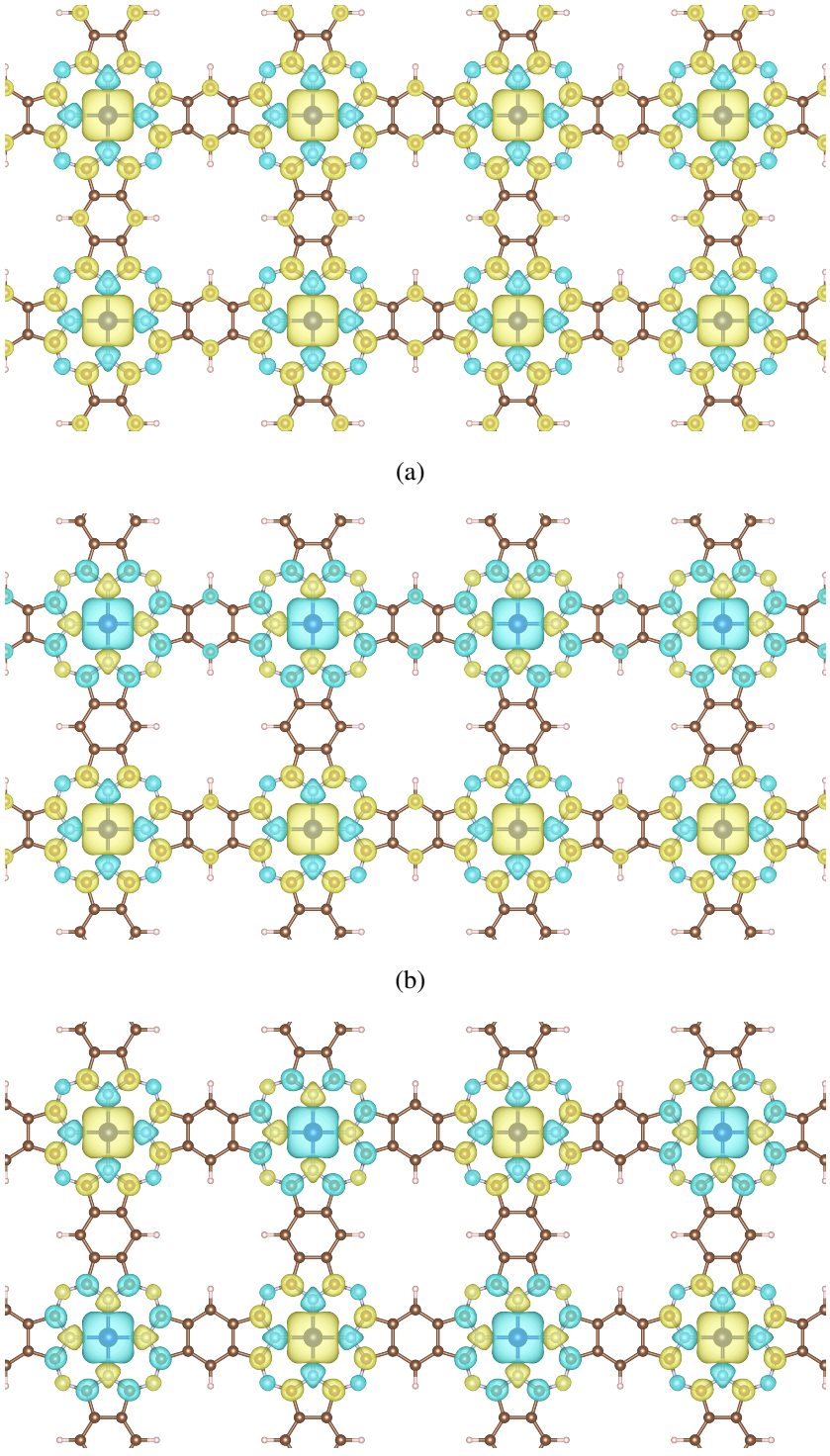

(a)

(b)

(c)

Figure C.7: Spin density isosurface plots for poly-CrPc in (a) the FM phase, (b) the CAF phase and (c) the NAF phase. An isovalue of $0.001\,|e|$ Å^{-3} is used. Yellow (blue) shading indicates regions of up-spin (down-spin) electron density.